Interactions between mantle plumes and mid-ocean ridges: Constraints from geophysics, geochemistry, and geodynamical modeling

by

Jennifer E. Georgen

B.A., University of Virginia, 1995

Submitted in partial fulfillment of the requirements for the degree of
Doctor of Philosophy
at the
MASSACHUSETTS INSTITUTE OF TECHNOLOGY
and the
WOODS HOLE OCEANOGRAPHIC INSTITUTION

September, 2001

Signature of Author: _____

Massachusetts Institute of Technology/
Woods Hole Oceanographic Institution
Joint Program in Oceanography
August, 2001

Certified by: _____

Jian Lin
Thesis Supervisor

Accepted by: _____

Timothy L. Grove
Chairman, Joint Committee in Marine Geology and Geophysics
Massachusetts Institute of Technology/Woods Hole Oceanographic Institution

Interactions between mantle plumes and mid-ocean ridges: Constraints from geophysics, geochemistry, and geodynamical modeling

by
Jennifer E. Georgen

Submitted in partial fulfillment of the requirements for the degree of Doctor of Philosophy
at the Massachusetts Institute of Technology
and the Woods Hole Oceanographic Institution
September, 2001

ABSTRACT

This thesis studies interactions between mid-ocean ridges and mantle plumes using geophysics, geochemistry, and geodynamical modeling. Chapter 1 investigates the effects of the Marion and Bouvet hotspots on the ultra-slow spreading, highly-segmented Southwest Indian Ridge (SWIR). Gravity data indicate that both Marion and Bouvet impart high-amplitude mantle Bouguer anomaly lows to the ridge axis, and suggest that long-offset transforms may diminish along-axis plume flow. Building upon this observation, Chapter 2 presents a series of 3D numerical models designed to quantify the sensitivity of along-axis plume-driven mantle flow to transform offset length, spreading rate, and mantle viscosity structure. The calculations illustrate that long-offset transforms in ultra-slow spreading environments may significantly curtail plume dispersion. Chapter 3 investigates helium isotope systematics along the western SWIR as well as near a global array of hotspots. The first part of this study reports uniformly low $^3He/^4He$ ratios of 6.3–7.3 R/R_a along the SWIR from 9°-24°E, compared to values of 8±1 R_a for normal mid-ocean ridge basalt. The favored explanation for these low values is addition of (U+Th) into the mantle source by crustal and/or lithospheric recycling. Although high $^3He/^4He$ values have been observed along the SWIR near Bouvet Island to the west, there is no evidence for elevated $^3He/^4He$ ratios along this section of the SWIR. The second part of Chapter 3 investigates the relationship between $^3He/^4He$ ratios and geophysical indicators of plume robustness for nine hotspots. A close correlation between a plume's flux and maximum $^3He/^4He$ ratio suggests a link between plume upwelling strength and origination in the deep, relatively undegassed mantle. Chapter 4 studies 3D mantle flow and temperature patterns beneath oceanic ridge-ridge-ridge triple junctions (TJs). In non-hotspot-affected TJs with geometry similar to the Rodrigues TJ, temperature and upwelling velocity along the slowest-spreading of the three ridges are predicted to increase within a few hundred kilometers of the TJ, to approach those of the fastest-spreading ridge. Along the slowest-spreading branch in hotspot-affected TJs such as the Azores, a strong component of along-axis flow directed away from the TJ is predicted to advect a hotspot thermal anomaly away from its deep-seated source.

Thesis Supervisor: Jian Lin
Title: Associate Scientist, Woods Hole Oceanographic Institution

Table of Contents

Biographical Sketch

The author was born on January 4, 1974, in Corpus Christi, Texas. Raised in Virginia, she entered the University of Virginia in 1992, where she graduated from the Department of Environmental Sciences with a B.A. with honors in 1995. In the fall of 1995, she entered the Massachusetts Institute of Technology/Woods Hole Oceanographic Institution Joint Program in Oceanography to study marine geology and geophysics. She received her degree in 2001.

Acknowledgments

Two hundred pages of thesis, 18 gigabytes of files, and six years of graduate school are not the product of a single person. Many people have contributed to the pages contained within this document. Jian Lin, my advisor, has patiently and methodically guided me through the steps from student to young scientist. Jian's generosity as an advisor quickly became apparent through our long meetings and late-night e-mail sessions. Older graduate students nearly always counsel those thinking of entering a Ph.D. program that the single most important factor in picking a graduate school is to find a good advisor. I feel very fortunate to have found a fantastic one.

I also owe much thanks to the members of my graduate school committees, Bob Detrick, Henry Dick, Mark Kurz, Marcia McNutt, and Maria Zuber. Henry and I shared interests in strange portions of the mid-ocean ridge system, like triple junctions and ultra-slow spreading ridges, as well as numerous interesting conversations. I gratefully thank Mark Kurz for allowing me to indulge my curiosity and venture beyond the computer lab to do helium isotope analyses. I'm certain Mark must have been more than a little surprised by the young geophysics student who appeared on his doorstep wanting to make $^{3}He/^{4}He$ measurements, and I truly appreciate his scientific generosity and collaboration.

My education at WHOI and MIT benefited from contributions from numerous people. The weekly tectonics and geodynamics discussion group provided a terrific forum for airing out ideas-in-progress, and I thank all of its members over the years. I would also like to thank Brian Tucholke, Debbie Smith, Ken Sims, Dick Von Herzen, Peter Clift, Nobu Shimizu, Ralph Stephen, Maurice Tivey, Rob Evans, Alan Chave, and Hans Schouten for wonderfully stimulating courses, seminars, cruises, and discussions.

I am truly grateful to my fellow Joint Program students. In my first year as a grad student, Garrett Ito and Javier Escartin patiently led me through the particulars of Unix, Matlab, and GMT, and since then they have been valued collaborators. Alberto Saal was endlessly willing to answer my infinite geochemistry questions, element by element and isotope by isotope. My experience in the Joint Program was uniquely enhanced by Mark Behn. Late-night DIAL room conversations with Mark not only kept my thesis going, but they also contributed greatly to the preservation of my sanity during grad school. In addition to being a fellow JP student, Carrie Tuit was a terrific and flexible housemate, somehow managing to understand the concept of a microwave curfew and why her somewhat strange housemate wanted to make dinner at midnight. Judith Wells's nighttime perambulations around the halls of Clark made for many welcome nocturnal visits, and our analyses of the scientific writing process helped me to understand that it was all right if I only cleared a paragraph an hour. The presence of folks like Allegra Hosford, Mike Braun, Sheri White, Stefan Hussenoeder, Kelsey Jordahl, Kirsten Laarkamp, Debbie Hassler, and Albert Fisher enriched my graduate school experience.

Finally, I would like to thank my family, Mom, Dad, and David. It is impossible to express how much they have supported me throughout graduate school and my entire education. I think they had some idea of what was ahead of them when the rock collections started appearing in the basement in elementary school, but I hope that they have enjoyed being a part of my journey to become a geologist as much as I have.

Funding was provided by the National Science Foundation through grants OCE-9811924 and OCE-9907630, and by a National Defense Science and Engineering Graduate Fellowship.

Chapter 1: Introduction

Many of the most prominent bathymetric anomalies on the ocean floor are attributable to mantle plumes. Plumes occur in a number of geologic settings, from intraplate (e.g., Hawaii), to near a mid-ocean ridge (e.g., Azores, Bouvet, Marion, Galapagos), to atop a spreading center (e.g., Iceland). In all of these settings, plumes fundamentally alter the character of normal oceanic crust and lithosphere, imparting geological, geophysical and geochemical anomalies which can be used to infer underlying plume geodynamics.

The phenomenology of mantle plumes has been explored for many decades. For example, *Morgan* [1971, 1972] proposed that hotspots are deep-seated upwelling anomalies which create quasi-linear, time-transgressive tracks on overriding lithospheric plates. Similarly, many studies have addressed the physics of mantle flow at mid-ocean ridges. Investigations of ridge processes in the vicinity of a mantle plume can probe the geodynamics of both the plume and the ridge. Early geochemical studies around Iceland and the Azores (e.g., *Hart et al.* [1973]; *Schilling* [1975]; *White and Schilling* [1978]) investigated the length scale over which plume material can be transported along-axis, addressing questions such as the balance between horizontal plate-driven flow and vertical plume upwelling in the distribution of plume-affected mantle. Building on these geochemical results, as well as observations of bathymetric and gravity anomalies around hotspots [*Vogt*, 1976; *Ito and Lin*, 1995; *Small*, 1995], laboratory and numerical models have explored the governing variables of plume-ridge interaction, including spreading rate, plume flux, layered mantle viscosity structure, lithospheric slope, and thermal erosion of the lithosphere [*Ribe and Christensen*, 1994; *Feighner and Richards*, 1995; *Feighner et al.*, 1995; *Ribe et al.*, 1995; *Ribe*, 1996; *Ito et al.*, 1997, 1999]. In this thesis, we investigate

the influence of plate boundary geometry on ridge-hotspot interactions, using the combined approaches of geophysical data analysis, geochemistry, and geodynamical modeling.

In Chapter 1, we extend the study of plume-ridge interactions to the Southwest Indian Ridge (SWIR). Crustal accretion processes along the SWIR are affected by two near-ridge hotspots, Marion and Bouvet. Bouvet is located approximately 300 km to the east of the Bouvet Triple Junction in the western portion of the SWIR, while Marion is east of the long-offset Andrew Bain Fracture Zone in the central portion of the SWIR. We use gravity and bathymetry data to calculate mantle Bouguer and residual mantle Bouguer anomaly [*Kuo and Forsyth,* 1988; *Lin et al.*, 1990] for the entirety of the western Indian Ocean, and then use these calculations to delineate the sections of the SWIR affected by these two hotspots.

Investigation of ridge-hotspot interactions at the SWIR is important for two reasons. First, numerical and laboratory modeling experiments suggest that one of the fundamental controls on dispersion of plume material along a mid-ocean ridge is spreading rate. With a half-rate of ~0.8 cm/yr along most of its length, the SWIR is the slowest-spreading accessible portion of the global mid-ocean ridge system. Only the ice-covered Arctic ridges are slower. Thus, the SWIR is an important end-member test of scaling relationships involving spreading rate. Second, the SWIR is highly segmented; many transform offsets exist in the vicinity of Marion and Bouvet. Earlier analytical studies, such as *Vogt and Johnson* [1975] and *Sleep* [1996], suggest that transform offsets may limit or diminish along-axis flow originating from a mantle plume. Therefore, we examine along-axis gravity and bathymetry trends along the SWIR for evidence of this "transform damming" effect.

Whereas Chapter 1 uses observational data to argue for the importance of transform offsets in governing plume-ridge interactions, Chapter 2 quantitatively evaluates the effects

of ridge offsets in a series of three-dimensional numerical models. We model plume-driven flow beneath a segmented ridge system, through a 3D mantle domain with temperature- and pressure-dependent viscosity. Our calculations cover a range of spreading rates (from ultra-slow to fast), offset lengths (from 0 to 250 km), and mantle viscosity structures to determine the sensitivity of along-axis flux to the presence of transform offsets. We then compare the numerical model predictions to observed bathymetric anomalies of several plume-ridge systems, including Marion/SWIR, Iceland/Mid-Atlantic Ridge, and Galapagos/Galapagos Spreading Center, to illustrate the role of large transform faults in controlling the spatial extent of plume-ridge interactions.

Since hotspot plumes affect not only the geological and geophysical characteristics of ridge systems, but also the geochemistry, Chapter 3 investigates helium isotopic anomalies for the western SWIR as well as the northern Mid-Atlantic Ridge. Because the source of primordial ^{3}He is believed to be the relatively undegassed lower mantle, the ratio of ^{3}He to ^{4}He can be used as an indicator of deep-seated mantle plumes [*Kurz et al.*, 1982a]. For example, oceanic islands such as Iceland have ^{3}He/^{4}He ratios ranging up to 37, normalized to the atmospheric ratio (R_a) [*Hilton et al.*, 2000]. For comparison, normal mid-ocean ridge basalt has ^{3}He/^{4}He ratios averaging 8±1 R_a [*Kurz and Jenkins*, 1981; *Kurz et al.*, 1982b; *Poreda et al.*, 1993]. The first portion of Chapter 3 presents new helium isotope data for the western SWIR, between 9°E and 24°E. Studying helium isotopic variation along this portion of the SWIR is valuable for a number of reasons. First, this investigation is the first systematic study of helium isotope ratios along an ultra-slow spreading ridge. Second, the study region can be divided into two supersegments, one oriented at a highly oblique angle to the regional spreading direction (9°-16°E) and the other more orthogonal to the spreading direction (16°-25°E). Because of its extreme obliquity, the 9°-16°E supersegment has an extremely low effective spreading rate of approximately

0.5 cm/yr. Therefore, this significant change in ridge geometry permits investigation of the sensitivity of helium isotopic ratios to changes in upwelling rate and mantle temperature at extremely low spreading rates. Third, earlier geochemical studies suggest that the western, oblique supersegment is affected by the Bouvet plume, more than 700 km away [*le Roex et al.*, 1992]. Since the Bouvet plume has relatively high $^3He/^4He$ ratios of approximately 12-13 R_a, it is possible to use helium isotopic ratios to trace the influence of Bouvet on the oblique supersegment.

The second portion of Chapter 3 examines the relationship between $^3He/^4He$ ratios and geophysical indicators of plume influence for a global array of plumes. More specifically, we investigate the correlation between the maximum helium isotopic ratio and bathymetric anomaly, gravity anomaly, waist width, and inferred plume flux for Iceland, Azores, Tristan, Reunion, Bouvet, Galapagos, Easter, and Amsterdam-St. Paul. Such investigations yield insight into the coupled geodynamical-geochemical behavior of mantle plumes, and support the hypothesis that robust, high-flux plumes might tend to originate in the deep, relatively undegassed mantle.

The geodynamics of mantle flow and heat transfer beneath oceanic ridge-ridge-ridge triple junctions is the subject of Chapter 4. Triple junctions in ridge-ridge-ridge configuration reflect unusual regions of crustal and lithospheric creation, compared to normal spreading systems with divergence of only two plates. We use a three-dimensional finite element numerical model to investigate how mantle flow dynamics beneath a triple junction differs from that beneath the simpler system of a single straight ridge. We initially model a triple junction with geometry resembling the Rodrigues and Galapagos triple junctions, to explore large-scale flow and heat transfer around a triple junction that is not affected by a nearby mantle plume. For each of the three ridge branches, we quantify how the presence of the other two ridge systems affects axial temperature and upwelling velocity

as a function of along-ridge distance from the triple junction. We then investigate a plume-affected triple junction, such as near the Azores Triple Junction, and explore how the 3D mantle flow beneath a triple junction can advect plume anomalies. Together, the results of this thesis work argue for the strong influence of plate boundary geometry on hotspot-ridge interactions.

References

Feighner, M.A. and M.A. Richards, The fluid dynamics of plume-ridge and plume-plate interactions: An experimental investigation, *Earth Planet. Sci. Lett.*, 129, 171-182, 1995.

Feighner, M.A., L.H. Kellogg, and B.J. Travis, Numerical modeling of chemically buoyant mantle plumes at spreading ridges, *Geophys. Res. Lett.*, 22, 715-718, 1995.

Hart, S.R., J.G. Schilling, and J.L. Powell, Basalts from Iceland and along the Reykjanes Ridge: Strontium isotope geochemistry, *Nature*, 246, 104-107, 1973.

Hilton, D.R., M.F. Thirwall, R.N. Taylor, B.J. Murton, and A. Nichols, Controls on magmatic degassing along the Reykjanes Ridge with implications for the helium paradox, *Earth Planet. Sci. Lett.*, 183, 43-50, 2000.

Ito, G. and J. Lin, Oceanic spreading center-hotspot interactions: Constraints from along-isochron bathymetric and gravity anomalies, *Geology*, 23, 657-660, 1995.

Ito. G., J. Lin, and C.W. Gable, Interaction of mantle plumes and migrating mid-ocean ridges: Implications for the Galapagos plume-ridge system, *J. Geophys. Res.,* 102, 15403-15417, 1997.

Ito, G., Y. Shen, G. Hirth, and C.J. Wolfe, Mantle flow, melting, and dehydration of the Iceland mantle plume, *Earth Planet. Sci. Lett.,* 165, 81-96, 1999.

Kuo, B.Y and D.W. Forsyth, Gravity anomalies of the ridge-transform system in the South Atlantic between 31 and 34.5°S: Upwelling centers and variations in crustal thickness, *Mar. Geophys. Res.,* 10, 205-232, 1988.

Kurz, M.D. and W.J. Jenkins, The distribution of helium in oceanic basalt glasses, *Earth Planet. Sci. Lett.*, 53, 41-54, 1981.

Kurz, M.D., W.J. Jenkins, and S.R. Hart, Helium isotope systematics of oceanic islands and mantle heterogeneity, *Nature*, 297, 43-47, 1982a.

Kurz, M.D., W.J. Jenkins, J.G. Schilling, and S.R. Hart, Helium isotopic variations in the mantle beneath the central North Atlantic Ocean, *Earth Planet. Sci. Lett.*, 58, 1-14, 1982b.

le Roex, A.P., H.J.B. Dick, and R.T. Watkins, Petrogenesis of anomalous K-enriched MORB from the Southwest Indian Ridge: 11°53'E to 14°38'E, *Contrib. Mineral. Petrol.*, 110, 253-268, 1992.

Lin, J., G.M. Purdy, H. Schouten, J.-C. Sempere, and C. Zervas, Evidence from gravity data for focused magmatic accretion along the Mid-Atlantic Ridge, *Nature*, 344, 627-632, 1990.

Morgan, W.J., Convection plumes in the lower mantle, *Nature*, 230, 42-43, 1971.

Morgan, W.J., Deep mantle convection plumes and plate motions, *Am. Assoc. Petr. Geol. Bull.*, 56, 203-213, 1972.

Poreda, R.J. and J.G. Schilling, Helium isotope ratios in Easter Microplate basalts, *Earth Planet. Sci. Lett.*, 119, 319-329, 1993.

Ribe, N.M. and U.R. Christensen, Three-dimensional modeling of plume-lithosphere interaction, *J. Geophys. Res.*, 99, 669-682, 1994.

Ribe, N.M., U.R. Christensen, and J. Theissing, The dynamics of plume-ridge interaction, 1: ridge-centered plumes, *Earth Planet. Sci. Lett.*, 134, 155-168, 1995.

Ribe, N.M., The dynamics of plume-ridge interaction 2. Off-ridge plumes, *J. Geophys. Res.*, 101, 16195-16024, 1996.

Schilling, J.-G., Azores mantle blob: Rare earth evidence, *Earth Planet. Sci. Lett.*, 25, 103-115, 1975.

Sleep, N.H., Lateral flow of hot plume material ponded at sublithospheric depths, *J. Geophys. Res.*, 101, 28,065-28,083, 1996.

Small, C., Observations of ridge-hotspot interactions in the Southern Ocean, *J. Geophys. Res.*, 100, 17931-17946, 1995.

Vogt, P.R. and G. L. Johnson, Transform faults and longitudinal flow below the midoceanic ridge, *J. Geophys. Res.*, 80, 1399-1428, 1975.

Vogt, P.R., Plumes, subaxial pipe flow, and topography along the mid-oceanic ridge, *Earth Planet. Sci. Lett.*, 29, 309-325, 1976.

White, W.M. and J.-G. Schilling, The nature and origin of geochemical variation in Mid-Atlantic Ridge basalts from the central north Atlantic, *Geochim. Cosmochem. Acta*, 42, 1501-1516, 1978.

ELSEVIER

Chapter 2

Reprinted with permission of Elsevier Science.

EPSL

Earth and Planetary Science Letters 187 (2001) 283–300

www.elsevier.com/locate/epsl

Evidence from gravity anomalies for interactions of the Marion and Bouvet hotspots with the Southwest Indian Ridge: effects of transform offsets

Jennifer E. Georgen [a,*], Jian Lin [b], Henry J.B. Dick [b]

[a] *MIT-WHOI Joint Program in Oceanography, Woods Hole Oceanographic Institution, Woods Hole, MA 02543, USA*
[b] *Department of Geology and Geophysics, Woods Hole Oceanographic Institution, Woods Hole, MA 02543, USA*

Received 15 July 2000; received in revised form 13 February 2001; accepted 23 February 2001

Abstract

The ultra-slow spreading Southwest Indian Ridge (SWIR) presents a unique environment to study the interactions between hotspots and ridges with highly segmented geometry. Using recently available satellite free-air gravity and shipboard bathymetry data, we obtain mantle Bouguer (MBA) and residual mantle Bouguer anomalies (RMBA) by removing from free-air gravity the attractions of seafloor topography, sediment thickness variations, a reference crust, and theoretically predicted effects of lithospheric cooling. The Bouvet hotspot, previously observed to be associated with anomalous bathymetry and geochemistry near the Bouvet triple junction, has an MBA axial gravity low of ~100 mGal, implying pronounced localized crustal thickening. Off-axis, the RMBA lows along previously calculated Bouvet hotspot tracks are variable in amplitude, suggesting the possibilities that Bouvet flux varies in time or that hotspot magmatism is enhanced by proximity to a spreading center. Along-axis geophysical anomalies suggest that the Marion hotspot has a significant effect on accretionary processes in the central portion of the SWIR. Importantly, the Marion axial anomaly appears to be compartmentalized between the Andrew Bain and Discovery II fracture zones, implying that transform offsets play a significant role in governing the distribution of plume material in a highly segmented, ultra-slow spreading system.

Keywords: Bouguer anomalies; hot spots; Southwest Indian Ridge; transform faults; mid-ocean ridges

1. Introduction

The accretion of oceanic crust along the global mid-ocean ridge system is influenced greatly by the presence of nearby mantle plumes. Most studies of ridge–hotspot interactions have focused on the Atlantic and eastern Pacific ocean basins, where relatively abundant data are available. In contrast, comparatively poor coverage of conventional underway geophysical data has hindered the investigation of hotspots in the southern oceans. Recently released satellite-derived gravity [1], however, permits the inclusion of southern ocean hotspots in global studies of plume–ridge

* Corresponding author. Tel.: +1-508-289-2581; Fax: +1-508-457-2187; E-mail: jgeorgen@mit.edu
E-mail: jlin@whoi.edu
E-mail: hdick@whoi.edu

0012-821X/01/$ – see front matter
PII: S0012-821X(01)00293-X

interaction. Moreover, recent compilation of the GEBCO digital database [2] represents a major improvement in bathymetric data coverage in the southern oceans. This study combines ship-track bathymetry and satellite gravity to determine gravity anomalies for the western Indian and southern Atlantic oceans. We use mantle Bouguer anomaly (MBA) and residual MBA (RMBA) to characterize the interactions of the Marion and Bouvet hotspots with the Southwest Indian Ridge (SWIR) and to provide constraint for Marion and Bouvet hotspot tracks. Further, we place Marion and Bouvet in a global context by comparing them with other spreading center–plume systems, and consider the important role of transform faults in plume–ridge interactions at this ultra-slow spreading rate.

2. Geological setting

The SWIR extends ~8000 km from the Bouvet triple junction (BTJ) in the west to the Rodrigues triple junction (RTJ) in the east (Fig. 1). The SWIR is among the world's slowest spreading ridges, with a full spreading rate close to ~13–16 mm/yr along most of its length. Marion Island, which is located on 28 Ma crust about 250 km from the SWIR [3], marks the current position of the Marion/Prince Edward plume (hereafter referred to as the Marion plume) [4,5]. Bouvet Island lies on 7 Ma crust [3], approximately 300 km to the east of the BTJ and 55 km from the nearest segment of the SWIR. Several recent papers have investigated whether Bouvet Island or Spiess Seamount, located between the BTJ and Bouvet Island, is the position of the Bouvet plume (e.g. [6–8]). However, this question has not yet been resolved, so we will place the plume at Bouvet Island unless otherwise noted.

The configuration of the SWIR varies significantly along its strike, and the ridge may be divided into a number of subsections based on geometry and spreading history (Fig. 1). The first subsection extends from the BTJ to 10°E and is characterized by short ridge segments and closely spaced transforms. This geometry is more or less mirrored by conjugate sections on the eastern American–Antarctic Ridge (AAR). The second subsection consists of a 400-km-long length of ridge between 10°E and 15°E. This stretch lies at a oblique angle to the regional spreading direction, resulting in a confused segmentation pattern and very low effective spreading rate. The third subsection, between 15°E and 25°E, was the focus of a detailed geophysical survey by Grindlay et al. [9] where SeaBeam multibeam bathymetry, magnetics, and gravity data revealed that the ridge consists of a series of short (~45 km) segments separated by non-transform offsets. The 720-km-long Andrew Bain FZ and 150-km-long Du Toit FZ, which were also studied in the survey of Grindlay et al. [10], significantly displace the trend of the SWIR and constitute a fourth subsection. Between the Marion and Gallieni FZs, the fifth subsection, axial depth is relatively shallow and the segmentation pattern is somewhat irregular. In contrast, offsets between the Gallieni and Atlantis II FZs, subsection six, may be traced considerable distances off-axis in the satellite gravity map (Fig. 1). Subsection seven, the portion of ridge between Melville FZ and the RTJ, is characterized by marked obliquity accommodated by second-order segmentation, and has been created since 45 Ma by eastward migration of the RTJ [11]. An increase in axial depth from 49°E to the RTJ, as well as a relative lack of fresh volcanic activity as seen in TOBI sidescan sonar images, likely reflects amagmatic extension [12–14].

The highly segmented nature of the SWIR in the vicinity of Marion and Bouvet provides a unique opportunity to explore plume–ridge interactions at an ultra-slow spreading ridge. Prior studies of plume–ridge interactions have often focused on systems with relatively straight ridges. For example, both the Galapagos/Cocos–Nazca spreading center (CNSC) and the Iceland/Reykjanes Ridge systems have been extensively modeled (e.g. [15–19]), yet the CNSC is offset by only a few major (>50 km) discontinuities near the Galapagos plume (e.g. [20]), and the Reykjanes Ridge south of Iceland is characterized by en echelon segments [21]. Long offsets in the SWIR such as the Andrew Bain FZ may exert important control on the dispersal of the Marion plume.

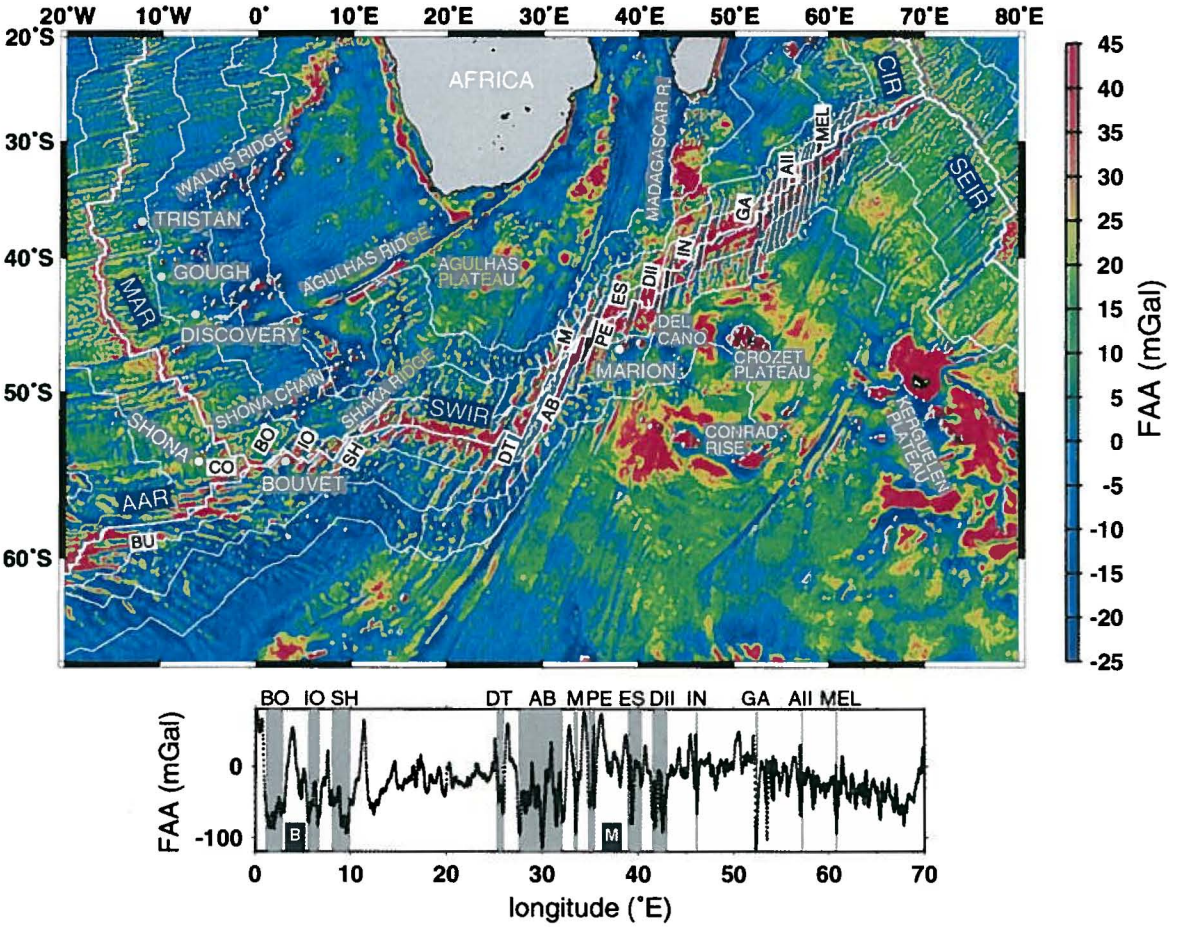

Fig. 1. Regional FAA map for the SWIR and part of the Southern Atlantic Ocean (data from [1]). Thick white lines mark the location of ridge axes: SWIR = Southwest Indian Ridge, SEIR = Southeast Indian Ridge, CIR = Central Indian Ridge, MAR = Mid-Atlantic Ridge, AAR = American–Antarctic Ridge. Locations of significant seafloor features are labeled in white lettering; positions of hotspots are marked with filled white circles. The names of prominent fracture zones are labeled as BU = Bullard FZ, CO = Conrad FZ, BO = Bouvet FZ, IO = Islas Orcadas FZ, SH = Shaka FZ, DT = Du Toit FZ, AB = Andrew Bain FZ, M = Marion FZ, PE = Prince Edward FZ, ES = Eric Simpson FZ, DII = Discovery II FZ, IN = Indomed FZ, GA = Gallieni FZ, AII = Atlantis II FZ, and MEL = Melville FZ. Thin white lines are 25, 50, and 75 Ma isochrons [3]. Gravity data are plotted at 5′ spacing and an artificial illumination has been imposed on the grid from the NW. Lower panel shows FAA along the axis of the SWIR. Regions covering fracture zones are shaded, and the positions of the Marion and Bouvet hotspots are indicated with M and B, respectively.

3. Gravity analysis

3.1. Data sources

The primary bathymetry data source of this study was the recently released GEBCO digital database [2,22]. The GEBCO-97 database offers the position of bathymetric contours with depth values spaced at an interval of ~1–2 km along the contours, which we projected onto a 5′ grid (Fig. 2). The GEBCO-97 dataset, a compilation of accumulated shiptrack data from many sources, represents a major improvement in data coverage over any previous bathymetric database of the southern oceans. Note that shiptrack coverage is relatively dense along the ridge axis, especially near Marion and Bouvet islands (Fig. 2). To guard against overinterpretation of the GEBCO

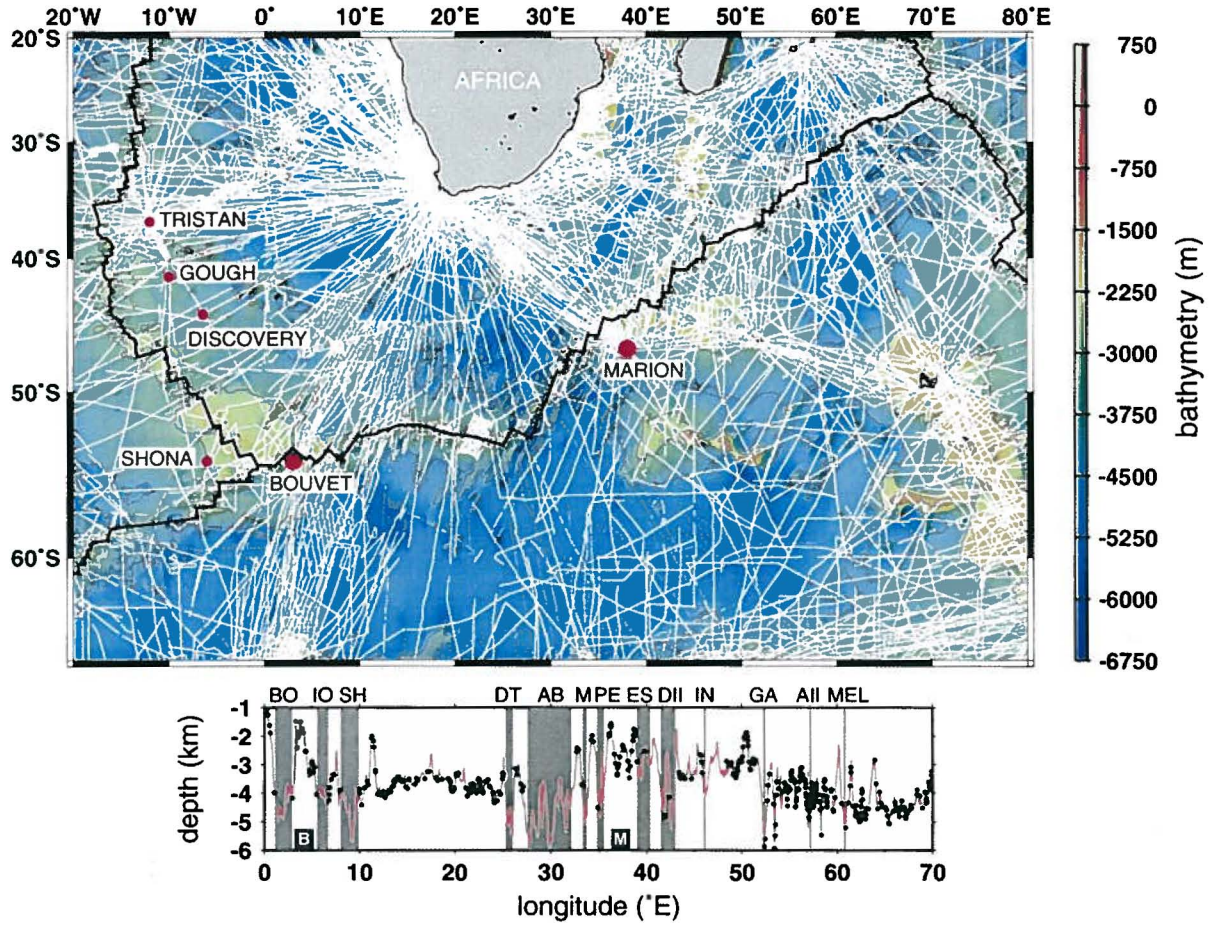

Fig. 2. Bathymetry map for the southwest Indian Ocean based on the GEBCO-97 database [2]. Thin white lines indicate shiptrack coverage of the bathymetry data in the GEBCO-97 compilation, and red dots mark the locations of hotspots. Grid spacing is 5′, contour interval is 1500 m, and artificial illumination is from the NW. Lower panel shows SWIR axial bathymetry (pink line). Depths constrained by shiptrack lines crossing spreading segments are indicated with black dots, regions covering fracture zones are shaded, and fracture zones and hotspots are labeled as in Fig. 1.

dataset, maps of gravity anomalies calculated using the GEBCO data (e.g. Figs. 3 and 5) were also projected on a 5′ grid and all nodes lacking shiptrack control within a 15′ radius were masked.

We extracted free-air anomaly (FAA) gravity data from the 2′ grid spacing global database calculated by Sandwell and Smith [1] from declassified Geosat and ERS-1 altimetry (Fig. 1). Neumann et al. [23] showed that the 3′ grid that preceded the current 2′ database is coherent with bathymetry to wavelengths as short as 27.5 km for the Mid-Atlantic Ridge between 31° and 36°S. Similarly, Rommevaux-Jestin et al. [12] found reasonably good correspondence between shipboard and satellite FAA for wavelengths greater than 30–50 km for the eastern SWIR. We analyze this further below.

Sediment thickness data were extracted from a preliminary global database comprising digitized isopach maps gridded with 5′ spacing [24]. Sediment thickness is less than 1000 m for most of the region. Maximum thicknesses occur within 5° of the African margin (5000 m) and in the southeastern portion of Fig. 2, east of 50°E and south of 60°S (4000 m).

We used the digital age grid of Mueller et al. [3]

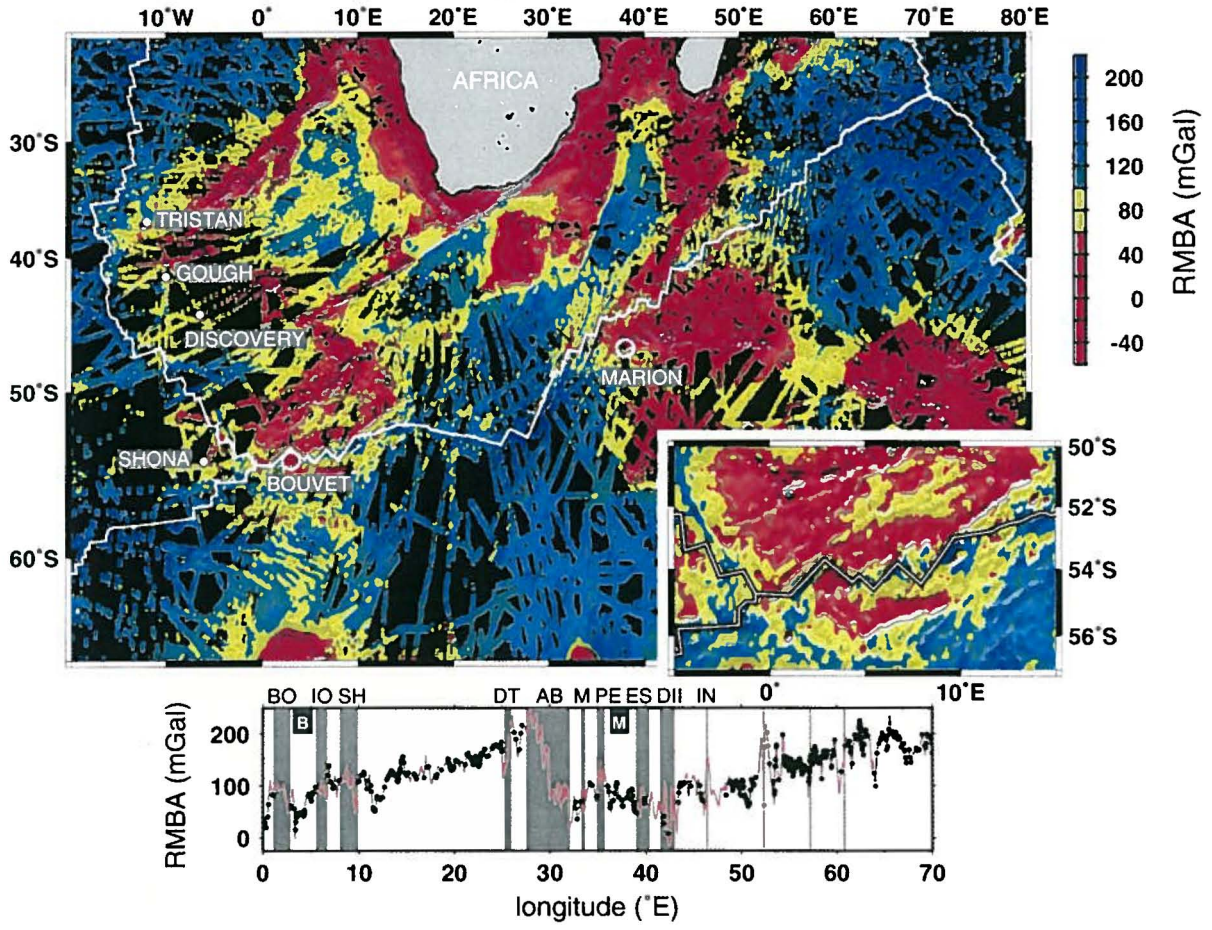

Fig. 5. Map of RMBA, created by subtracting from MBA the effects of lithospheric cooling based on an age-correction model. Masking is the same as in Fig. 3. Artificial illumination is imposed from the NW. Grid spacing is 5′ and contour interval is 100 mGal. Inset shows RMBA in the immediate vicinity of the BTJ, without shiptrack masking. The lower panel displays along-axis RMBA (pink line) with RMBA values constrained by shiptrack crossings of the SWIR shown in black dots. Regions covering fracture zones are shaded and fracture zones and hotspots are labeled as in Fig. 1.

determined the root-mean-square (RMS) difference between the filtered data (Fig. 4b). The RMS difference decreases quickly with cutoff wavelength, reaching a value of approximately 5 mGal for a cutoff wavelength of 125 km. This suggests that intermediate- to long-wavelength features, such as hotspot swells, are resolved reasonably accurately in the present study.

The second step in gravity data reduction was removal of the effects of lithospheric cooling. We calculated a three-dimensional (3D) mantle temperature field based on crustal age from the Mueller et al. [3] database. For computational ease, the plate cooling model [25] with temperature of 1350°C at the base of a 100-km lithosphere was used for crustal ages >1 Ma, while the half-space solution [26] was employed for ages <1 Ma. The gravity signals of this 3D mantle temperature field were then calculated and integrated down to 100 km depth to yield a theoretical estimation of the contribution of 3D lithospheric cooling to MBA (e.g. [27,28]), assuming a coefficient of thermal expansion of 3.5×10^{-5} K^{-1}. An along-axis profile of the age-based thermal correction is shown in Fig. 6a. Subtraction of lithospheric cooling from MBA yielded RMBA (Fig. 5). RMBA re-

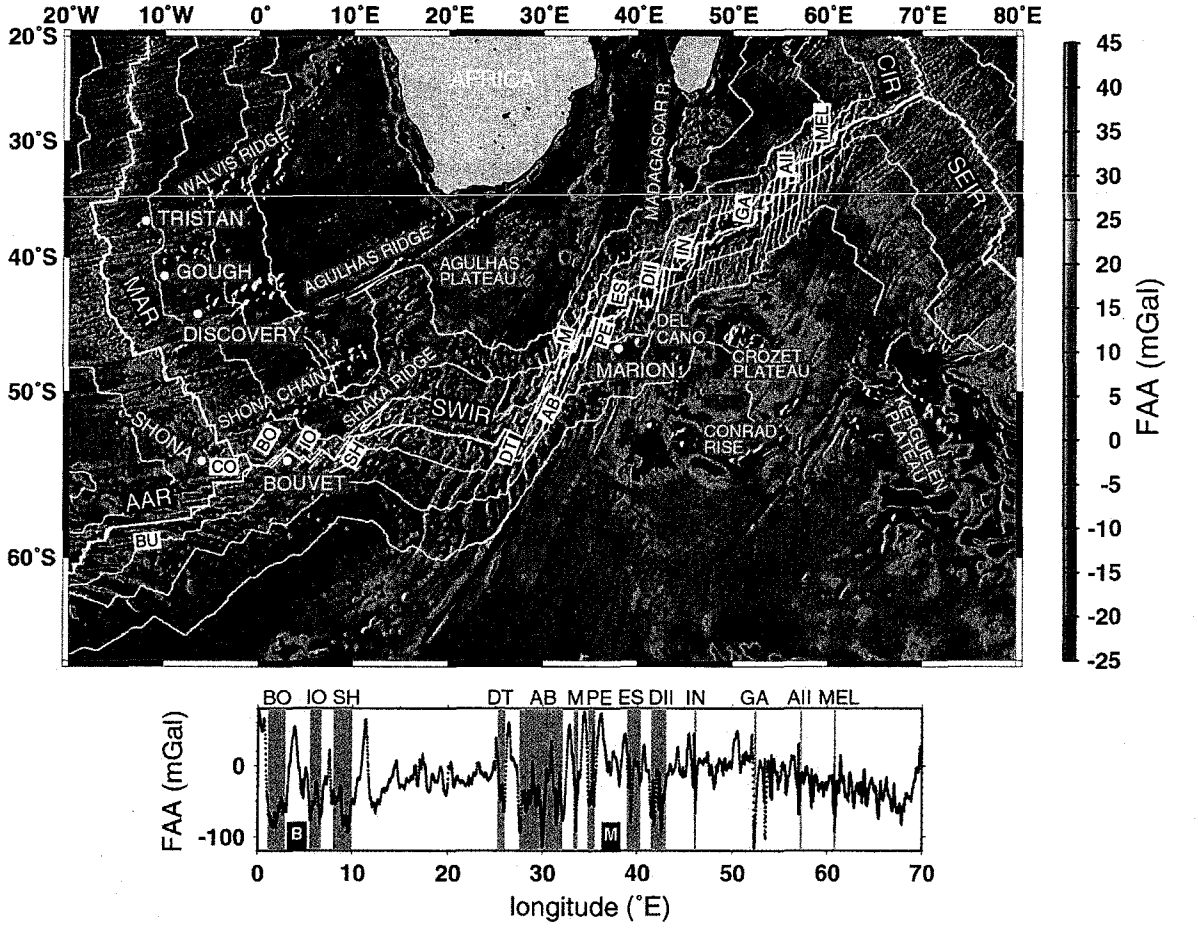

Fig. 1. Regional FAA map for the SWIR and part of the Southern Atlantic Ocean (data from [1]). Thick white lines mark the location of ridge axes: SWIR = Southwest Indian Ridge, SEIR = Southeast Indian Ridge, CIR = Central Indian Ridge, MAR = Mid-Atlantic Ridge, AAR = American–Antarctic Ridge. Locations of significant seafloor features are labeled in white lettering; positions of hotspots are marked with filled white circles. The names of prominent fracture zones are labeled as BU = Bullard FZ, CO = Conrad FZ, BO = Bouvet FZ, IO = Islas Orcadas FZ, SH = Shaka FZ, DT = Du Toit FZ, AB = Andrew Bain FZ, M = Marion FZ, PE = Prince Edward FZ, ES = Eric Simpson FZ, DII = Discovery II FZ, IN = Indomed FZ, GA = Gallieni FZ, AII = Atlantis II FZ, and MEL = Melville FZ. Thin white lines are 25, 50, and 75 Ma isochrons [3]. Gravity data are plotted at 5′ spacing and an artificial illumination has been imposed on the grid from the NW. Lower panel shows FAA along the axis of the SWIR. Regions covering fracture zones are shaded, and the positions of the Marion and Bouvet hotspots are indicated with M and B, respectively.

3. Gravity analysis

3.1. Data sources

The primary bathymetry data source of this study was the recently released GEBCO digital database [2,22]. The GEBCO-97 database offers the position of bathymetric contours with depth values spaced at an interval of ~1–2 km along the contours, which we projected onto a 5′ grid (Fig. 2). The GEBCO-97 dataset, a compilation of accumulated shiptrack data from many sources, represents a major improvement in data coverage over any previous bathymetric database of the southern oceans. Note that shiptrack coverage is relatively dense along the ridge axis, especially near Marion and Bouvet islands (Fig. 2). To guard against overinterpretation of the GEBCO

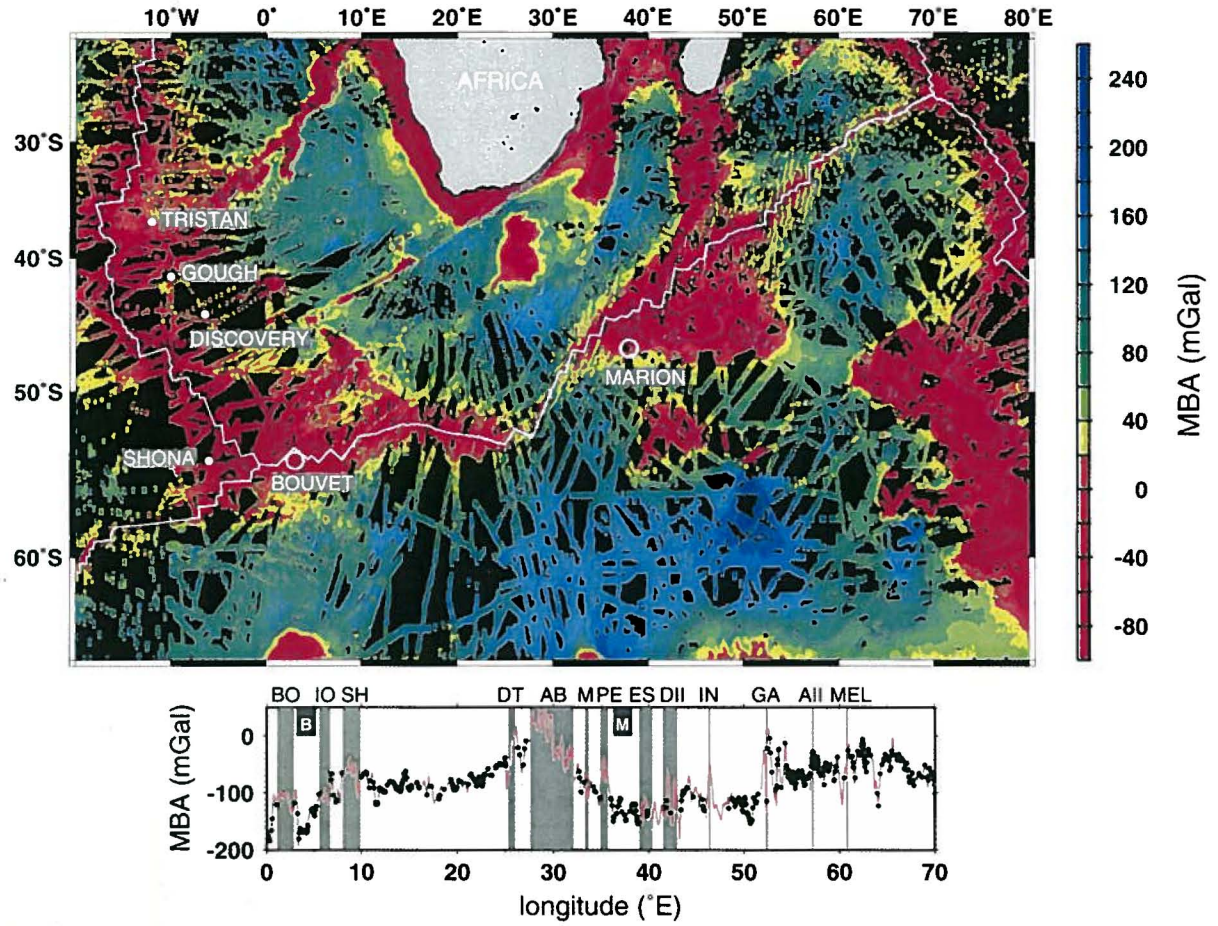

Fig. 3. Map of MBA, calculated by subtracting from FAA the gravitational effects of the water–sediment, sediment–crust, and crust–mantle interfaces assuming a constant 5-km-thick reference crust. The densities for seawater, sediment, crust, and mantle are assumed to be 1030, 2300, 2800, and 3300 kg/m^3, respectively. Grid nodes without shiptrack control within a 15′ radius are masked with black. Grid spacing is 5′ and contour interval is 100 mGal. Artificial illumination is imposed from the NW. Lower panel shows MBA along the axis of the SWIR (pink line). MBA values constrained by shiptrack crossings of the ridge are indicated with black dots, regions covering fracture zones are shaded, and fracture zones and hotspots are labeled as in Fig. 1.

for gravity thermal corrections (Fig. 1). Age error estimations for more than two-thirds of the seafloor in the area of study are <3 Myr [3]. Errors of such magnitude would have little effect on the calculated thermal correction for RMBA, described below. For young (<25 Ma) crust, age errors of up to 5–8 Ma occur in isolated areas [3], such as the Bouvet FZ, the oblique section of ridge between 10°E and 15°E, and the Du Toit FZ. Such errors would translate to approximately 20 mGal in the RMBA thermal correction. Off-axis (>25 Ma), large errors (>8 Ma) are also associated with the seafloor around the Shona Chain and between the Shona Chain and Shaka Ridge [3]. Such crustal age errors could correspond to RMBA thermal correction errors of up to 25 mGal.

3.2. Data analysis

The free-air gravity map shown in Fig. 1 contains signals from seafloor topography, sediments, and crust and mantle density anomalies. To reveal the more subtle crust and mantle anomalies, we

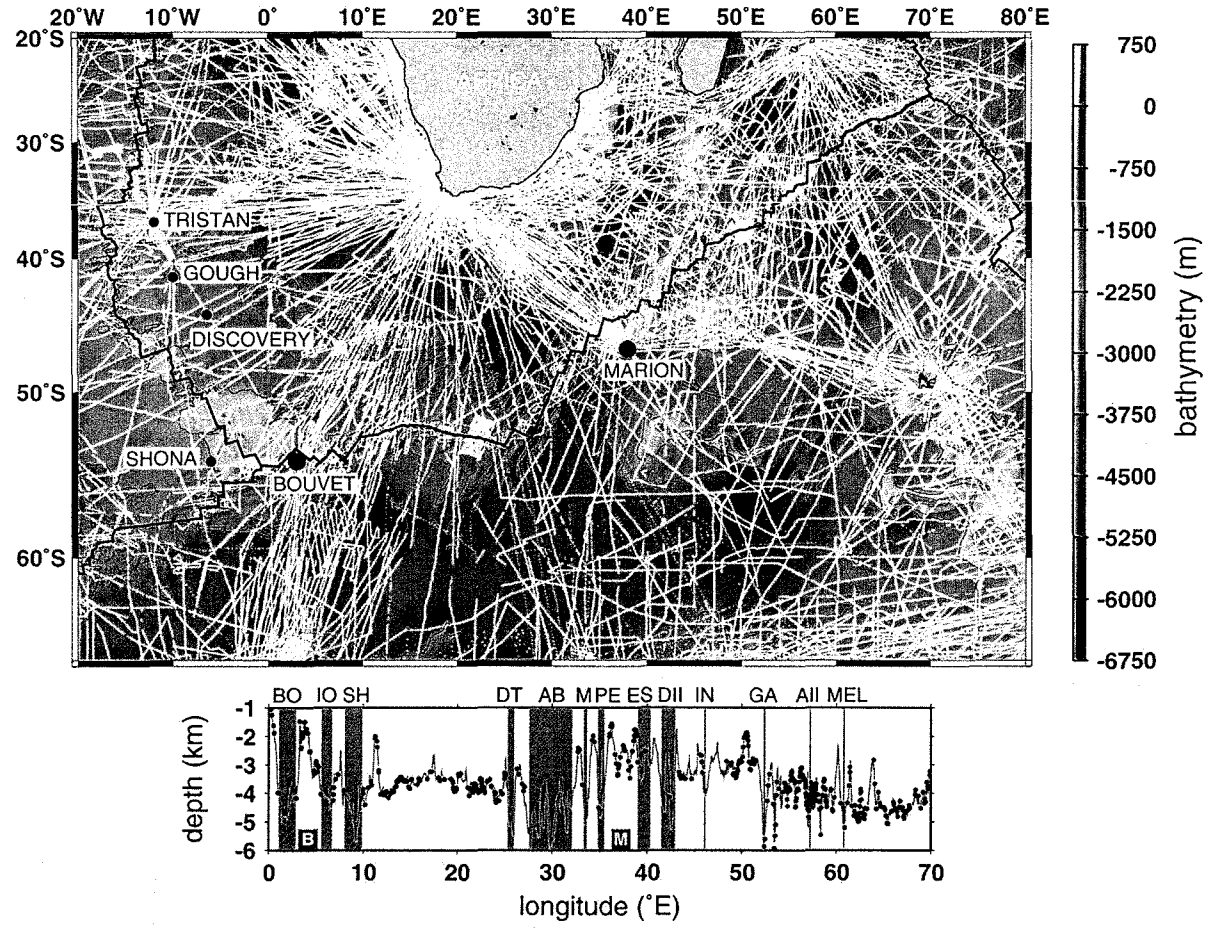

Fig. 2. Bathymetry map for the southwest Indian Ocean based on the GEBCO-97 database [2]. Thin white lines indicate shiptrack coverage of the bathymetry data in the GEBCO-97 compilation, and red dots mark the locations of hotspots. Grid spacing is 5′, contour interval is 1500 m, and artificial illumination is from the NW. Lower panel shows SWIR axial bathymetry (pink line). Depths constrained by shiptrack lines crossing spreading segments are indicated with black dots, regions covering fracture zones are shaded, and fracture zones and hotspots are labeled as in Fig. 1.

dataset, maps of gravity anomalies calculated using the GEBCO data (e.g. Figs. 3 and 5) were also projected on a 5′ grid and all nodes lacking shiptrack control within a 15′ radius were masked.

We extracted free-air anomaly (FAA) gravity data from the 2′ grid spacing global database calculated by Sandwell and Smith [1] from declassified Geosat and ERS-1 altimetry (Fig. 1). Neumann et al. [23] showed that the 3′ grid that preceded the current 2′ database is coherent with bathymetry to wavelengths as short as 27.5 km for the Mid-Atlantic Ridge between 31° and 36°S. Similarly, Rommevaux-Jestin et al. [12] found reasonably good correspondence between shipboard and satellite FAA for wavelengths greater than 30–50 km for the eastern SWIR. We analyze this further below.

Sediment thickness data were extracted from a preliminary global database comprising digitized isopach maps gridded with 5′ spacing [24]. Sediment thickness is less than 1000 m for most of the region. Maximum thicknesses occur within 5° of the African margin (5000 m) and in the southeastern portion of Fig. 2, east of 50°E and south of 60°S (4000 m).

We used the digital age grid of Mueller et al. [3]

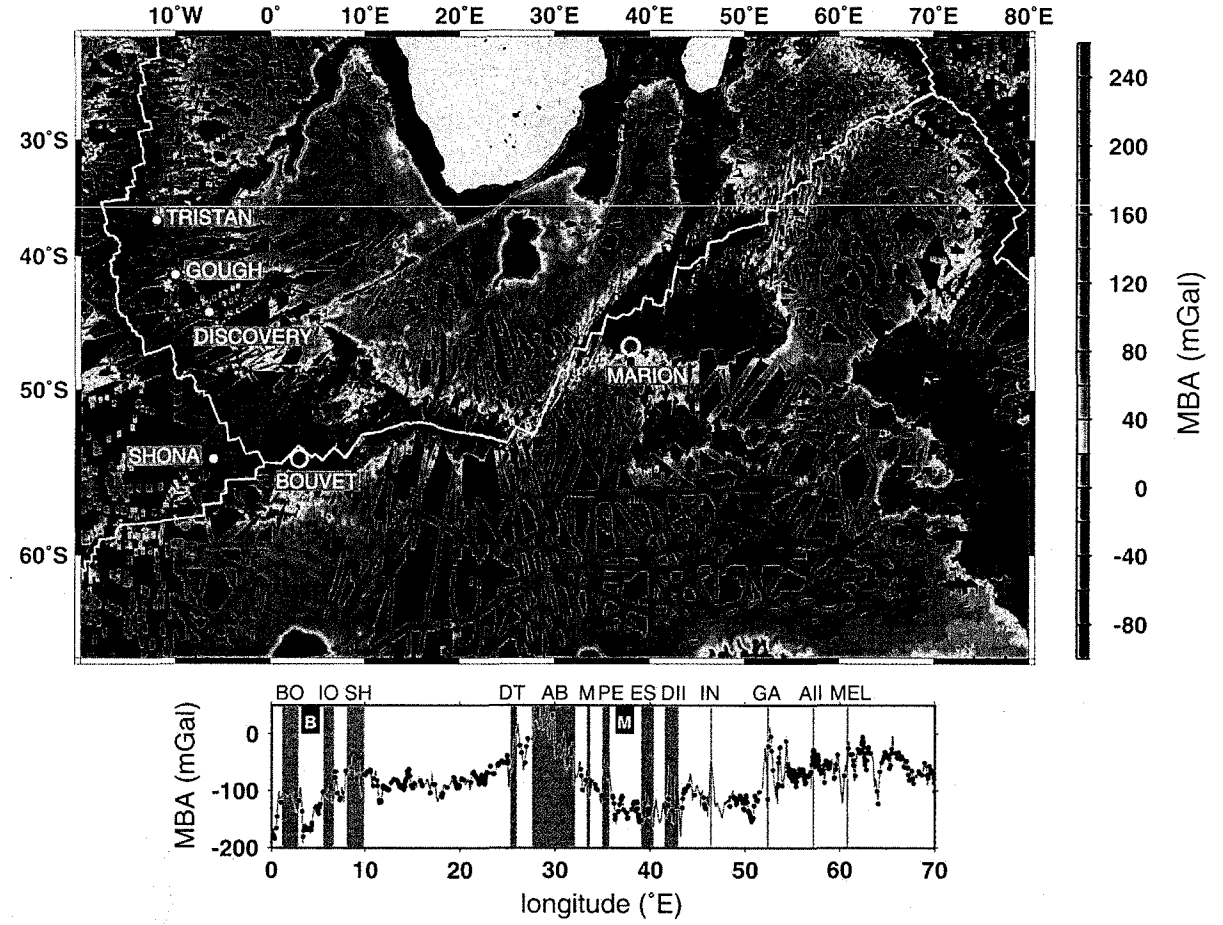

Fig. 3. Map of MBA, calculated by subtracting from FAA the gravitational effects of the water–sediment, sediment–crust, and crust–mantle interfaces assuming a constant 5-km-thick reference crust. The densities for seawater, sediment, crust, and mantle are assumed to be 1030, 2300, 2800, and 3300 kg/m^3, respectively. Grid nodes without shiptrack control within a 15′ radius are masked with black. Grid spacing is 5′ and contour interval is 100 mGal. Artificial illumination is imposed from the NW. Lower panel shows MBA along the axis of the SWIR (pink line). MBA values constrained by shiptrack crossings of the ridge are indicated with black dots, regions covering fracture zones are shaded, and fracture zones and hotspots are labeled as in Fig. 1.

for gravity thermal corrections (Fig. 1). Age error estimations for more than two-thirds of the seafloor in the area of study are <3 Myr [3]. Errors of such magnitude would have little effect on the calculated thermal correction for RMBA, described below. For young (<25 Ma) crust, age errors of up to 5–8 Ma occur in isolated areas [3], such as the Bouvet FZ, the oblique section of ridge between 10°E and 15°E, and the Du Toit FZ. Such errors would translate to approximately 20 mGal in the RMBA thermal correction. Off-axis (>25 Ma), large errors (>8 Ma) are also associated with the seafloor around the Shona Chain and between the Shona Chain and Shaka Ridge [3]. Such crustal age errors could correspond to RMBA thermal correction errors of up to 25 mGal.

3.2. Data analysis

The free-air gravity map shown in Fig. 1 contains signals from seafloor topography, sediments, and crust and mantle density anomalies. To reveal the more subtle crust and mantle anomalies, we

subtracted from FAA the theoretical gravity effects of the water–sediment, sediment–crust, and crust–mantle interfaces assuming a constant density 5-km-thick model crust. The densities for seawater, sediment, crust, and mantle were assumed to be 1030, 2300, 2800, and 3300 kg/m^3, respectively. The resulting MBA map is shown in Fig. 3.

The results of our MBA calculations are compared with those of the detailed geophysical survey of Grindlay et al. [9] along the SWIR axis between 15.5°E and 25°E (Fig. 4a). The MBA results of Grindlay et al. [9] were obtained using high-resolution multibeam bathymetry and shipboard gravity data that were collected in early 1996 and were not included in the GEBCO-97 database. Although differing in detail, the two studies yield intermediate- to long-wavelength trends that are very similar (Fig. 4a). To quantify this similarity, we applied lowpass filters with varying cutoff wavelengths to both profiles and

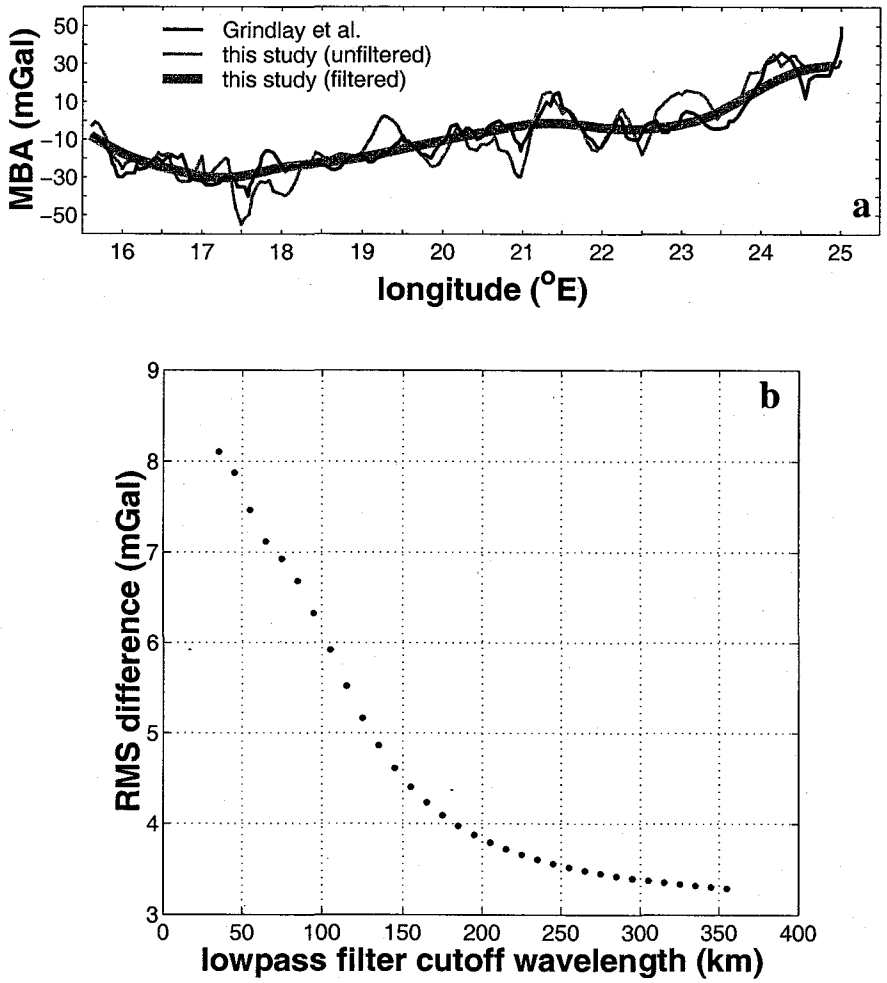

Fig. 4. (a) Comparison of axial MBA profiles for 15.5°E–25°E between the results of Grindlay et al. [9] and this study. Filtered profile is generated by applying 125-km cutoff lowpass filter to axial data sampled every 10 km. Note the general long-wavelength agreement between the two profiles despite differences in detail. (b) RMS difference between lowpass-filtered profiles from Grindlay et al. [9] and this study as a function of lowpass cutoff wavelength. Differences were taken every 10 km along the profile and filtered used a Hanning window.

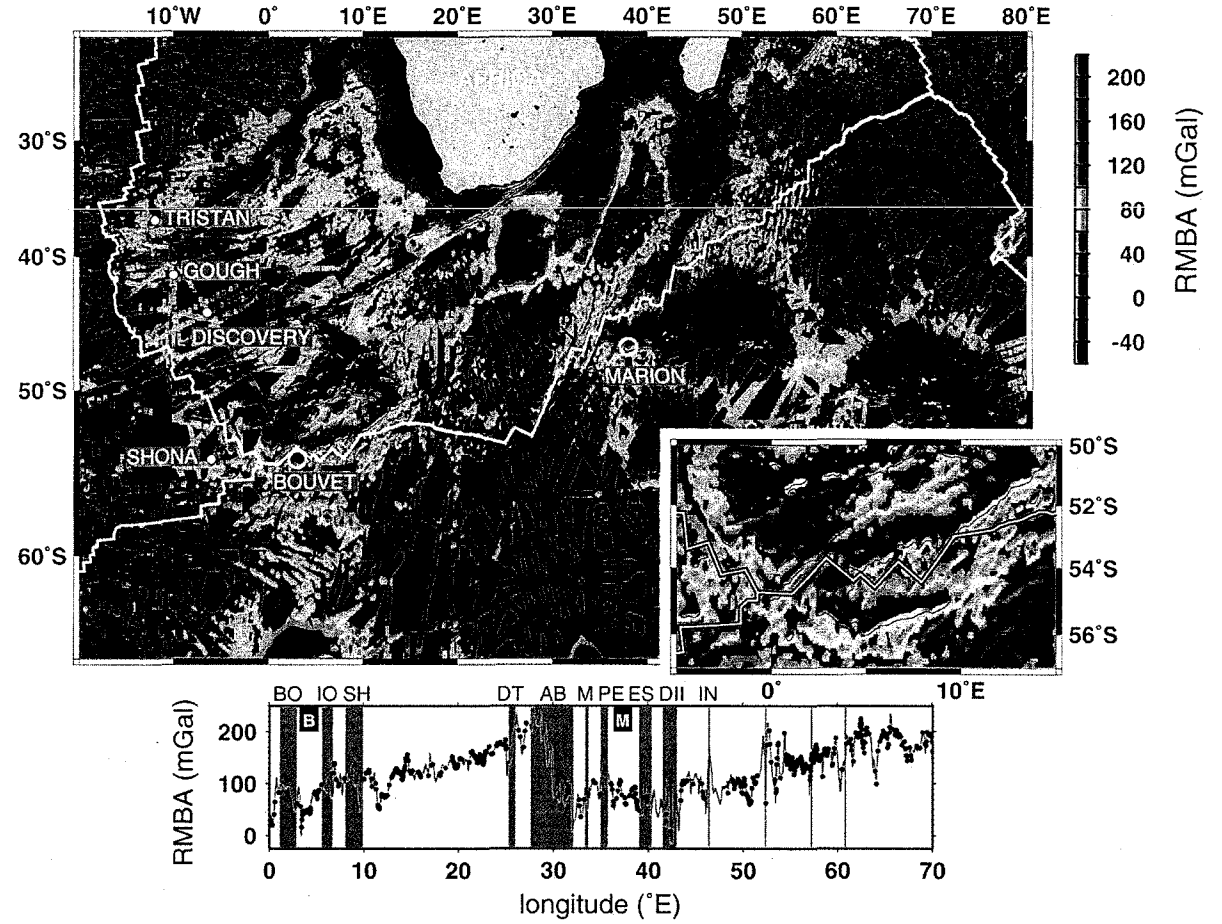

Fig. 5. Map of RMBA, created by subtracting from MBA the effects of lithospheric cooling based on an age-correction model. Masking is the same as in Fig. 3. Artificial illumination is imposed from the NW. Grid spacing is 5′ and contour interval is 100 mGal. Inset shows RMBA in the immediate vicinity of the BTJ, without shiptrack masking. The lower panel displays along-axis RMBA (pink line) with RMBA values constrained by shiptrack crossings of the SWIR shown in black dots. Regions covering fracture zones are shaded and fracture zones and hotspots are labeled as in Fig. 1.

determined the root-mean-square (RMS) difference between the filtered data (Fig. 4b). The RMS difference decreases quickly with cutoff wavelength, reaching a value of approximately 5 mGal for a cutoff wavelength of 125 km. This suggests that intermediate- to long-wavelength features, such as hotspot swells, are resolved reasonably accurately in the present study.

The second step in gravity data reduction was removal of the effects of lithospheric cooling. We calculated a three-dimensional (3D) mantle temperature field based on crustal age from the Mueller et al. [3] database. For computational ease, the plate cooling model [25] with temperature of 1350°C at the base of a 100-km lithosphere was used for crustal ages >1 Ma, while the half-space solution [26] was employed for ages <1 Ma. The gravity signals of this 3D mantle temperature field were then calculated and integrated down to 100 km depth to yield a theoretical estimation of the contribution of 3D lithospheric cooling to MBA (e.g. [27,28]), assuming a coefficient of thermal expansion of 3.5×10^{-5} K^{-1}. An along-axis profile of the age-based thermal correction is shown in Fig. 6a. Subtraction of lithospheric cooling from MBA yielded RMBA (Fig. 5). RMBA re-

flects deviations in crustal structure and/or mantle temperature from the reference model. Areas with low RMBA may result from the combined effects of thicker crust, lower density crust, and/or higher temperature mantle than surrounding regions.

The Phipps Morgan and Forsyth [29] model, which calculates mantle flow patterns based on ridge-transform geometry, was not used to determine the thermal correction for several reasons. First, unlike the age-based approach, the Phipps Morgan and Forsyth [29] model requires constant spreading rate both along the ridge and over time, which is an assumption clearly violated here given the large area under consideration. Also, the crus-

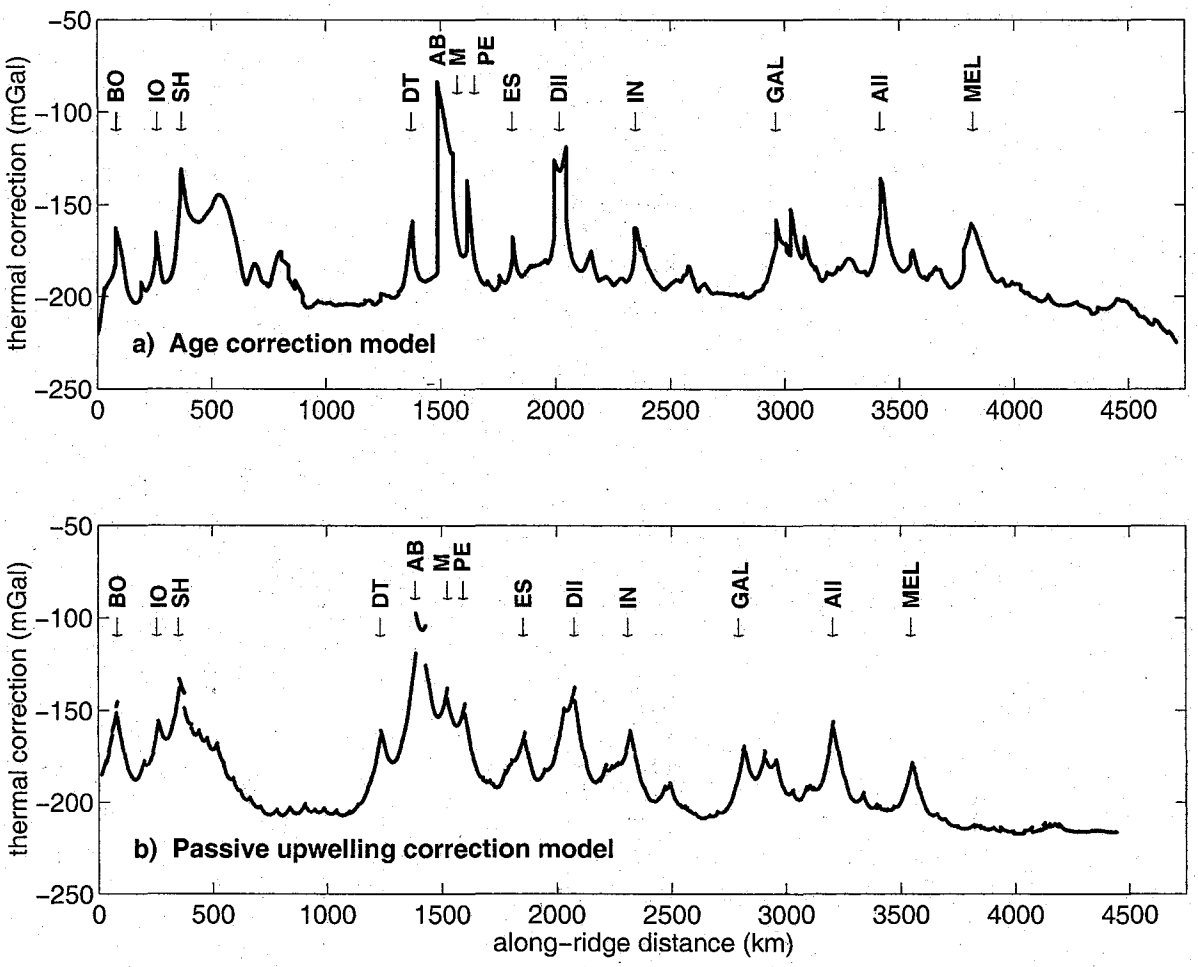

Fig. 6. Along-axis profiles of gravity thermal corrections calculated using (a) the age model and (b) the passive upwelling model. The age method assumes thermal cooling based on crustal age [3]. Mantle flow patterns in the passive upwelling model are calculated based on ridge-transform geometry, following [29]. The thermal structure resulting from the calculated 3D mantle flow field is then translated into density, assuming a coefficient of thermal expansion of 3.4×10^{-5} K^{-1}. Finally, the FFT technique of Parker [45] is used to calculate gravity. The discrepancy in length between the two profiles results from orthogonalizing SWIR ridge segments and transforms before input into the passive upwelling code, a requirement of the Phipps Morgan and Forsyth [29] technique. Because the passive upwelling method takes into account the 3D nature of flow around transform faults, its predicted thermal corrections near long-offset transforms are broader than those calculated by the age method. However, the age method is more appropriate for the large area addressed by this study because it allows for non-constant spreading rates and can determine the gravity signal around a triple junction.

tal age method permits calculation of the 3D thermal structure for the BTJ and RTJ, which have more complex geometry than that allowed by the Phipps Morgan and Forsyth [29] approach. The use of crustal age rather than passive flow modeling for the calculation of thermal correction, however, may lead to an underestimation of the thermal effects associated with large fracture zones such as the Andrew Bain FZ, because the effects of reduced upwelling and lateral asthenospheric flow were not considered. For example, Fig. 6 shows thermal corrections calculated using both the age and passive upwelling approaches. The age-based method yields corrections that are much more localized around individual offsets, rather than the broader correction of the passive upwelling model. This effect is particularly pronounced for the closely spaced transforms around the Andrew Bain FZ. However, the maximum values of the thermal corrections at the Andrew Bain FZ are similar in the two models (Fig. 6).

4. Regional and along-axis gravity anomalies

4.1. Regional gravity patterns

MBA varies significantly in the western Indian Ocean (Fig. 3). The most positive value of MBA in the region, 272 mGal, occurs southeast of the Crozet Plateau (50.83°E, 52.58°S). The Kerguelen Plateau has the lowest MBA value, −321 mGal (at 69.08°E, 48.66°S). Prominent MBA lows are also found in the vicinity of all oceanic plateaus and hotspot features including Tristan, Walvis Ridge, Gough, Discovery, Agulhas Ridge, Agulhas Plateau, Madagascar Ridge, Del Cano Plateau, Crozet Plateau, and Conrad Rise. A broad, irregular low is roughly centered on the BTJ.

All prominent MBA lows persist in the RMBA map (Fig. 5), indicating that these MBA features are not artifacts of lithospheric cooling effects. The most positive RMBA values are found near the RTJ (294 mGal at 58.75°E, 30.67°S), along the AAR (276 mGal at 9.75°W, 57.92°S), and along the Andrew Bain FZ (274 mGal at 30.08°E, 51.25°S). The most negative RMBA values correspond to the Crozet Plateau (−231 mGal at 50.5°E, 46.2°S) and the Kerguelen Plateau (−294 mGal at 69.08°E, 48.66°S).

4.2. Along-axis gravity

MBA shows pronounced intermediate- to long-wavelength trends along the SWIR (Fig. 3). From west to east, MBA values increase from a regional low at Bouvet Island (−181 mGal) to a high at the Andrew Bain FZ (62 mGal). Similarly, MBA values increase eastward from a regional low near Marion Island (−124 mGal) to a high west of the Melville FZ. An along-axis profile of RMBA shows intermediate- to long-wavelength trends similar to those of MBA (Fig. 5). The lowest RMBA value west of the Andrew Bain FZ occurs near Bouvet Island (26 mGal) while the maximum occurs at ~27°E (195 mGal). To the east, RMBA values generally increase from a low near Marion Island (40 mGal) to a high near the RTJ (~200 mGal).

4.3. Marion

Strict definition of the amplitude and wavelength of the Marion axial gravity anomaly is difficult. Along-axis profiles show short-wavelength variations that are not observed along other hotspot-affected ridges (e.g. the Galapagos spreading center [20]) which may be a function of a number of effects, including the ultra-slow spreading rate, frequent ridge offsets, and relatively sparser data coverage. Broad MBA and RMBA anomalies bracket the central SWIR between the Andrew Bain and Gallieni FZs (Figs. 3 and 5). However, we advocate limiting the Marion plume's eastern boundary to the Discovery II FZ, for several reasons. First, the ridge segment bounded by the dual-offset Discovery II transform faults has locally high MBA. Second, we postulate that the long-offset (350 km) Discovery II transform system is sufficiently long to displace segments to the east out of the range of Marion plume influence, an idea that we develop more thoroughly in a later section. The limited number of shiptrack crossings of SWIR spreading segments near Marion prevents us from assigning an anomaly amplitude.

To the west of Marion, a prominent RMBA high occurs in the vicinity of the Marion and Prince Edward FZs, and further to the west is the pronounced Andrew Bain FZ RMBA high (Fig. 7b). Local surveys of the segments between the Prince Edward and Marion FZs, and the Marion and Andrew Bain FZs, found evidence for extremely robust magmatism, uncharacteristic of slow spreading segments bounded by well-developed transform offsets [10]. It is likely that this robust magmatism is due to the Marion plume. For this reason, we interpret the Marion hotspot axial gravity anomaly to be between the Andrew Bain and Discovery II FZs. This yields an along-axis anomaly of 510 km without counting intervening transform offsets, or 1100 km including the transform faults. Meanwhile we attribute the axial bathymetric high and MBA low between the Indomed and Gallieni FZs to another source. Although the exact cause is unclear at this point, such bathymetric and MBA anomalies could be due to (1) the lack of significant offset in this length of ridge (Fig. 1) and thus less transform cooling effect, (2) remnant effects from the creation of the Del Cano Plateau, or (3) excess volcanism due to another off-axis plume source, such as the Crozet hotspot. However the latter option, linkage to the Crozet hotspot, would require a ridge–hotspot conduit of more than 1000 km from the Crozet Plateau to the SWIR.

Geochemical data, although sparse, also suggest that the Marion effect may be localized. For example, Mahoney et al. [30] noted that the SWIR immediately west of the Prince Edward FZ shows no plume characteristics: it has low $^{87}Sr/^{86}Sr$, high $^{143}Nd/^{144}Nd$, and low $^{206}Pb/^{204}Pb$. In contrast, the segment of ridge between the Prince Edward FZ and the Eric Simpson FZ is distinguished by low Ba/Nb and Zr/Nb, which are characteristics that Mahoney et al. [30] attribute to the Marion plume. These data limit the along-axis length of the geochemical effects of Marion to about 250 km. The adjacent ridge between the Eric Simpson FZ and the Discovery II FZ has high Ba/Nb, low ε_{Nd}, high $^{87}Sr/^{86}Sr$ and unusually low $^{206}Pb/^{204}Pb$. Although Mahoney et al. [30] do not advocate the addition of this length of SWIR to the range of Marion geochemical influence, it is interesting to note that the spreading centers between the Prince Edward and Discovery II FZs show both pronounced negative RMBA anomalies and anomalous geochemistry. Further geochemical sampling and more shiptrack geophysical data will help to resolve some of the questions surrounding the Marion plume.

4.4. Bouvet

Employing isotope and incompatible element data, le Roex et al. [31,32] find evidence for ba-

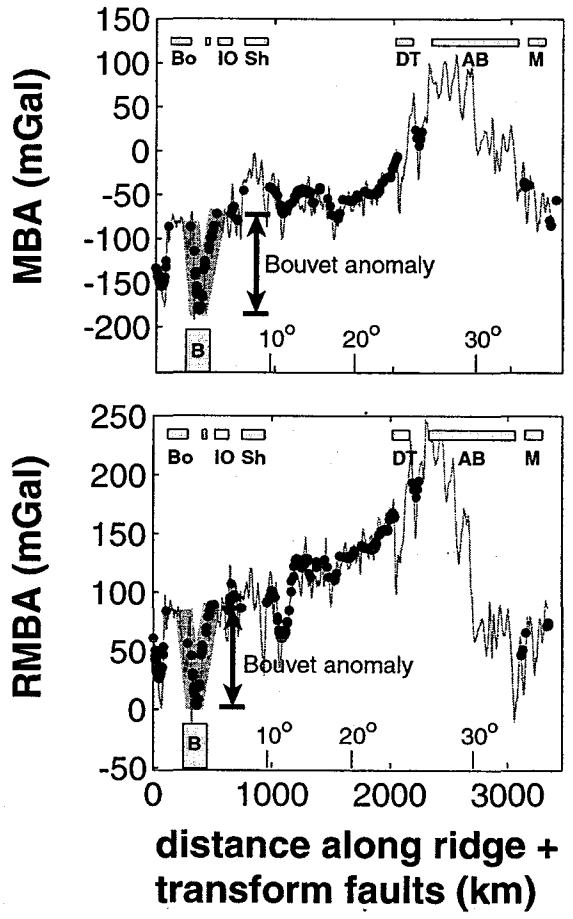

Fig. 7. Along-axis profiles of SWIR MBA and RMBA in the vicinity of the Bouvet plume. As in Figs. 3 and 5, black dots mark the locations constrained by shiptrack crossings of SWIR ridge segments. The location of Bouvet (B) is indicated with a vertical gray bar. Thick, dark gray lines near the Bouvet hotspot indicate the estimated amplitude and wavelength of the plume anomaly.

salts related to the Bouvet hotspot along the SWIR from the BTJ to 14°E. Values of $^{87}Sr/^{86}Sr$ and $^{143}Nd/^{144}Nd$ are highly scattered from the BTJ to ~14°E, and Zr/Nb data suggest that enriched, transitional, and normal MORB are juxtaposed throughout the length of the affected region. Le Roex et al. [31] and Dick [33] suggested that since the ultra-slow spreading SWIR represents a relatively cold thermal regime, magma chambers along the SWIR are both small and short-lived, allowing the persistence of local geochemical heterogeneities originating from the Bouvet plume.

Gravity calculations, on the other hand, suggest a considerably more localized anomaly. A high-amplitude (~100–125 mGal) MBA low is found between the Bouvet and Islas Orcadas FZs (Fig. 7a), yielding an along-axis distance, excluding transform offsets, of 260 km. Another pronounced MBA low between the BTJ and Bouvet FZ, of ~75–80 mGal amplitude, is associated with Spiess Seamount, possibly also reflecting the Bouvet plume.

A long-wavelength gradient between the Shaka and Andrew Bain FZs is a pronounced feature of the axial RMBA profile (Fig. 7b). However, it is unlikely that this extended gradient should be attributed to Bouvet. Some component of the gradient is attributable to underestimation of the transform effect by the age-based thermal correction method, as compared to the passive upwelling-based method (Fig. 6). More important, limited rock dredging sampling of the section of ridge between 15°E and 25°E shows little or no plume influence [34].

It is interesting to note that there is a high degree of symmetry in plate boundary geometry between the SWIR and the AAR in the vicinity of the BTJ (Fig. 1). The relatively long-offset Bouvet FZ on the SWIR is the conjugate of the Conrad FZ on the AAR, while the Shaka FZ is analogous to the Bullard FZ. Spreading rates along the two ridges are also similar, with a 0.9 cm/yr half-rate for the AAR. In addition, le Roex et al. [35] found a juxtaposition of enriched, transitional, and normal MORB along the AAR to approxi-

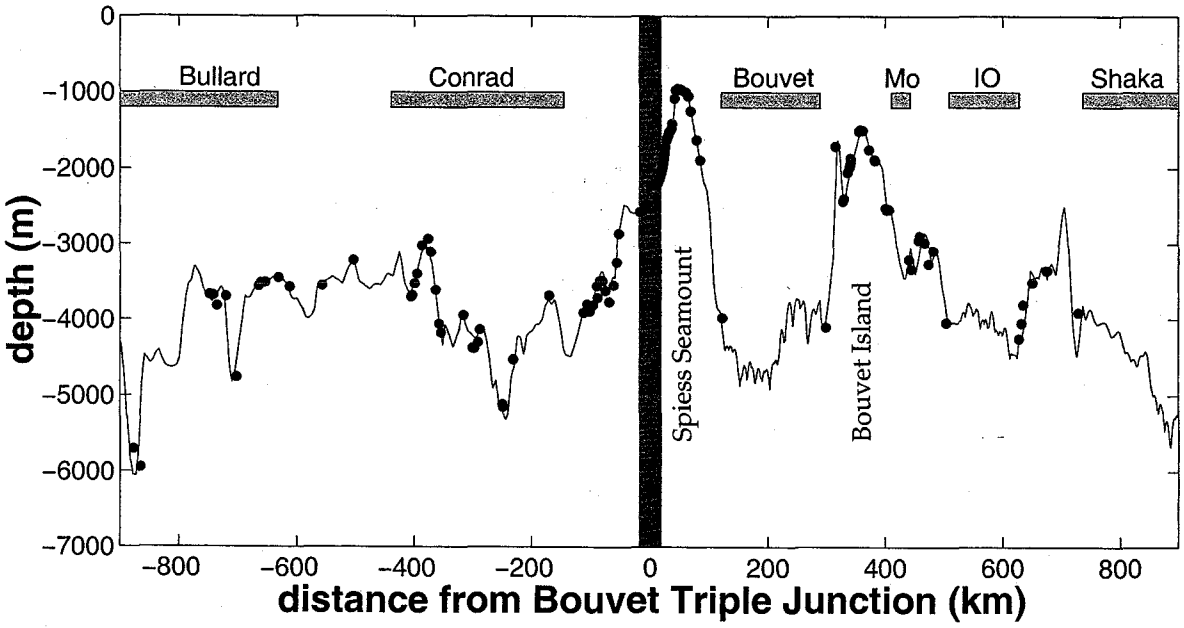

Fig. 8. Axial bathymetric profile along the American–Antarctic (distances < 0 km) and Southwest Indian (distances > 0 km) ridges, from the data source of [2]. Positions of Bullard, Conrad, Bouvet, Moshesh (Mo), Islas Orcadas (IO), and Shaka fracture zones are indicated; BTJ is shown with a vertical gray bar at a distance of 0 km. Black dots show locations where shiptracks cross ridge axes.

mately 18°W. However, although spreading rate, ridge geometry, and geochemistry are similar, bathymetric profiles of the SWIR and AAR are not (Fig. 8). While both ridges show rugged topography, Bouvet Island and Spiess Seamount represent bathymetric anomalies along the SWIR that are not paralleled in the AAR. The geochemical similarity, but bathymetric discrepancy, between the AAR and SWIR may support the notion that geochemical heterogeneity is an inherent feature of south Atlantic mantle, independent of the Bouvet plume source. Another possible explanation of the discrepancy is that complex 3D mantle flow patterns associated with the BTJ may have redistributed the geochemical anomalies represented by the Bouvet plume over a broad area. Geodynamical modeling of upwelling in the vicinity of the BTJ would be necessary to evaluate this mechanism.

5. Hotspot tracks

A prominent linear RMBA low extends from Marion Island along the Madagascar Ridge (Figs. 5 and 9a). RMBA profiles taken along shiptracks across this roughly N–S striking low are shown in Fig. 9b. The profiles are aligned so that RMBA minima fall at zero distance. The location of each of these minima is marked on Fig. 9a and connection of the minima forms an off-axis trace of RMBA lows which follow closely the calculated hotspot track for Marion based on the plate reconstruction of Duncan and Richards [36], lending support to the association of thickened crust with hotspot tracks. In general, RMBA anomaly amplitude is greater for profiles on older crust than younger, which may suggest a decrease in Marion flux over time. However, other explanations are also possible. For example, seismic and gravity studies of the Madagascar Ridge (Fig. 1) suggest it is divided into two provinces, with strongly anomalous crust to the north of 31°S and more normal oceanic crust to the south [37]. Correspondingly, RMBA profiles 4 and 5, to the north of 31°S, are considerably higher amplitude than profiles 1 and 2, both south of 31°S.

Based on a plate reconstruction model of Morgan [5], Hartnady and le Roex [38] presented a solution for the Bouvet hotspot track that extends from southern Africa to the west of the Agulhas Plateau until its intersection with the northeastern Shaka Ridge (Fig. 9a). Hartnady and le Roex [39] also proposed an alternative track based on a single rotation about a 64 Ma pole (Fig. 9a). Connecting the local minima in along shiptrack RMBA yields a line that agrees well with the Morgan-based track for relatively recent times ($< \sim 30$ Ma) and is a little south and east of the Hartnady and le Roex [38] track for earlier periods (Fig. 9a).

Shiptrack RMBA anomaly profiles across the Bouvet track are shown in Fig. 9c. Interestingly, amplitude anomalies are relatively large for profiles 1–4 and 8 and 9, for the most recent and earliest time periods, respectively, but considerably smaller for profiles 5–7 (Fig. 9c). This result confirms Morgan's [5] observation that portions of the Bouvet hotspot track lack bathymetric expression, suggesting at least three possibilities for Bouvet plume history, although other explanations are also possible. First, Bouvet may not rep-

→

Fig. 9. (a) Simplified map of RMBA, with regions which have RMBA less than 50 mGal shaded gray. The dashed gray line emanating from Bouvet shows a hotspot track calculated by Hartnady and le Roex [38] using finite reconstruction poles from Morgan [5]. The solid gray line from Bouvet shows a track based on rotation about a single, 64 Ma pole [38]. Solid gray line striking roughly N–S is the Marion hotspot track given in Duncan and Richards [36], shifted slightly so zero-age plume location corresponds with Marion Island. Numbered black lines crossing hotspot tracks indicate the locations of RMBA profiles, extracted along shiptrack lines, shown in b and c. Black lines connect local minima in the individual RMBA profiles, with the locations of the local minima shown as white diamonds. (b) Profiles of filtered (thick gray lines) and unfiltered (thin black lines) RMBA along shiptracks crossing the Madagascar Ridge. Profiles are aligned so that local minima fall at roughly zero distance. Crustal ages and age error estimates [3] are provided for each profile, as are thin black lines indicating the definition of ΔRMBA. ΔRMBA amplitudes are shown to the right of the profiles. (c) RMBA profiles along shiptracks to the northeast of Bouvet Island. 'S. Track?' in profile 1 may be a portion of the Bouvet track to the south of the SWIR, resulting from ridge–hotspot interactions. Profiles 8 and 9 cross the southernmost extent of the Agulhas Plateau.

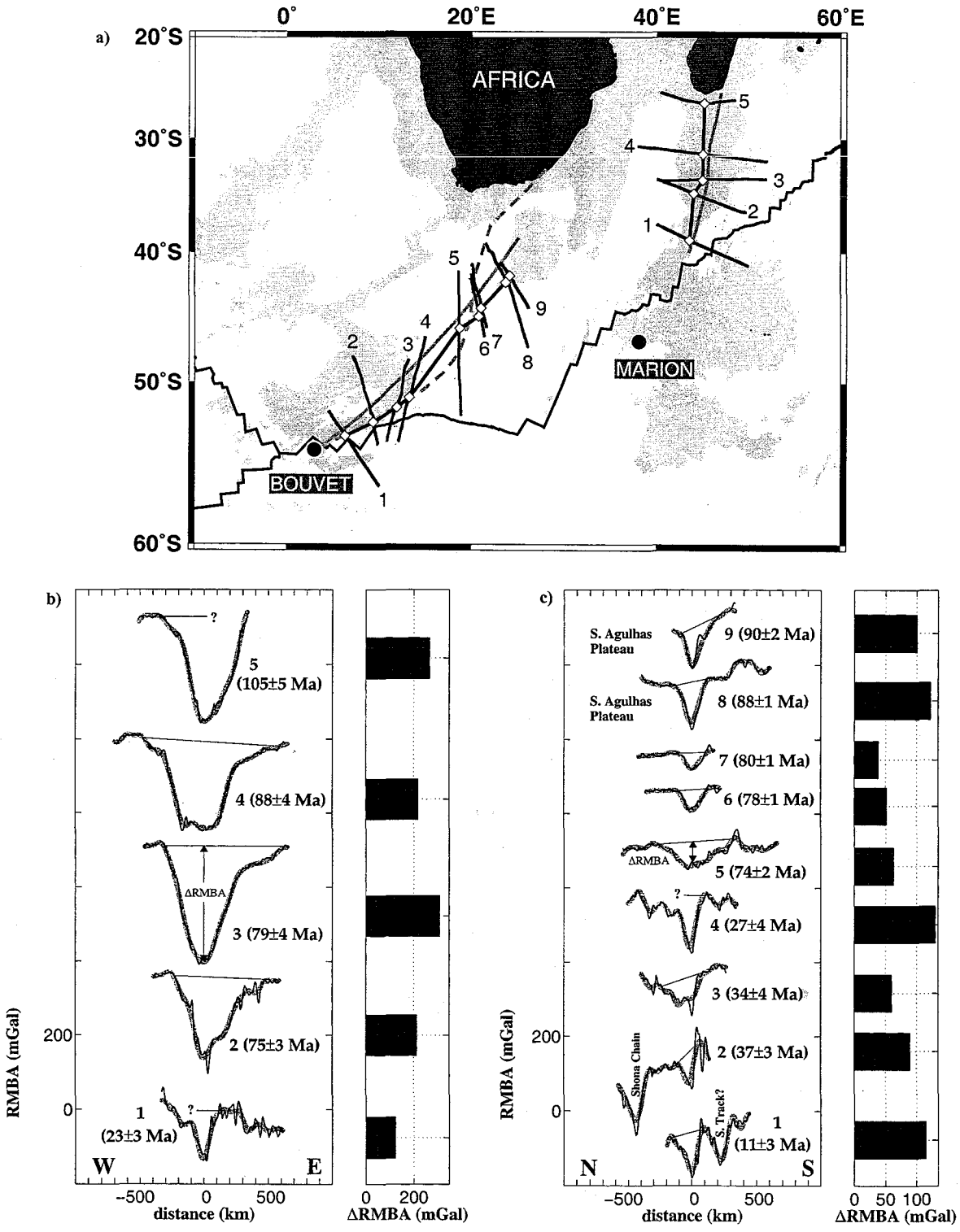
a)
0°
20°E
40°E
60°E
20°S
30°S
40°S
50°S
60°S
AFRICA
BOUVET
MARION
b)
RMBA (mGal)
200
0
W
E
?
5
(105±5 Ma)
4 (88±4 Ma)
ΔRMBA
3 (79±4 Ma)
2 (75±3 Ma)
1
(23±3 Ma)
-500
0
500
distance (km)
0
200
ΔRMBA (mGal)
c)
S. Agulhas Plateau
9 (90±2 Ma)
S. Agulhas Plateau
8 (88±1 Ma)
7 (80±1 Ma)
6 (78±1 Ma)
ΔRMBA
5 (74±2 Ma)
4 (27±4 Ma)
3 (34±4 Ma)
Shona Chain
2 (37±3 Ma)
S. Track?
1
(11±3 Ma)
N
S
0 50 100

resent a long-lived, deep-seated melting anomaly, but instead a more localized, shallow geochemical heterogeneity tapped relatively recently ($< \sim 30$ Ma) by the SWIR. In this scenario, little or no off-axis expression of the hotspot would be expected. Second, the flux of the Bouvet plume may fluctuate on 10 Myr time scales. Third, it is possible that there is a close relationship between Bouvet plume volcanism and a nearby triple junction. Martin [39] suggests that the paleolocation of the Bouvet plume was coincident with a triple junction at the Agulhas Plateau sometime in the range of 80–100 Ma (Fig. 9c). It may only be through coincidence with a spreading center, or a triple junction and its unusual mantle upwelling patterns, that the weak Bouvet plume develops a bathymetric or gravimetric expression. Further paleomagnetic reconstruction work detailing the position of the triple junction between 90 Ma and the present would be required to examine this possibility more thoroughly.

To the south of the SWIR, a linear RMBA low strikes NW–SE between approximately 3°E and 10°E, roughly mirroring the low anomaly to the north of the ridge (Fig. 5, inset). The easternmost portion of such conjugate lows, at approximately 10°E, may have been created when Bouvet-related volcanism first began along the SWIR (i.e. when the plume first started supplying material to the ridge). Taken together, the northern and southern lows form an RMBA 'wake' which converges on the present-day location of the plume, much like the Carnegie and Cocos ridges for the Galapagos plume.

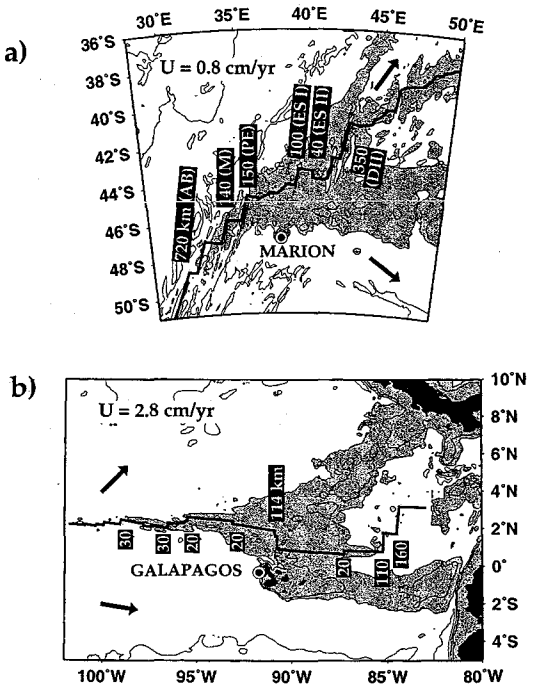

Fig. 10. (a) Bathymetry for the Marion plume region, with depths shallower than 3 km shaded. Selected fracture zones are labeled as in Fig. 1, with transform offsets in km. Arrows indicate absolute plate motion direction [46], U is half-spreading rate, and contours are drawn at 1.5, 3.0, and 4.5 km depth. (b) Bathymetry of the Galapagos archipelago, with depths shallower than 2.75 km shaded. As in (a), selected ridge offset distances are given in km. Contours mark 1.75, 2.75, and 3.75 km depth, and arrows indicate absolute plate motion [46].

6. Plume–ridge interactions

To examine the effects of ridge offset on ridge–hotspot interactions, we compare the Marion/SWIR and Galapagos/CNSC systems depicted in Fig. 10. These maps, which have the same scale, show that the Marion and Galapagos systems have roughly the same ridge–hotspot separation distance, 250 km and 200 km, respectively. However, the CNSC spreads at more than three times the rate of the SWIR (2.8 cm/yr versus 0.8 cm/yr half-rate, respectively). Further, over the region in Fig. 10, the cumulative ridge offset along the SWIR is 1520 km, again approximately three times the CNSC cumulative offset distance (560 km).

6.1. Plume dispersion along a segmented ridge

Transform offsets may play an important role in ridge–hotspot interactions. Fig. 11 shows two possible scenarios for the ridgeward transport of plume material for ridge geometries that resemble the Galapagos and Marion systems: (1) diffuse plume dispersion (Fig. 11a,b), as suggested by the numerical modeling of Ito et al. [15–17], Ribe [18], and Ribe et al. [19]; and (2) channelized along-axis flow (Fig. 11c,d), following Morgan

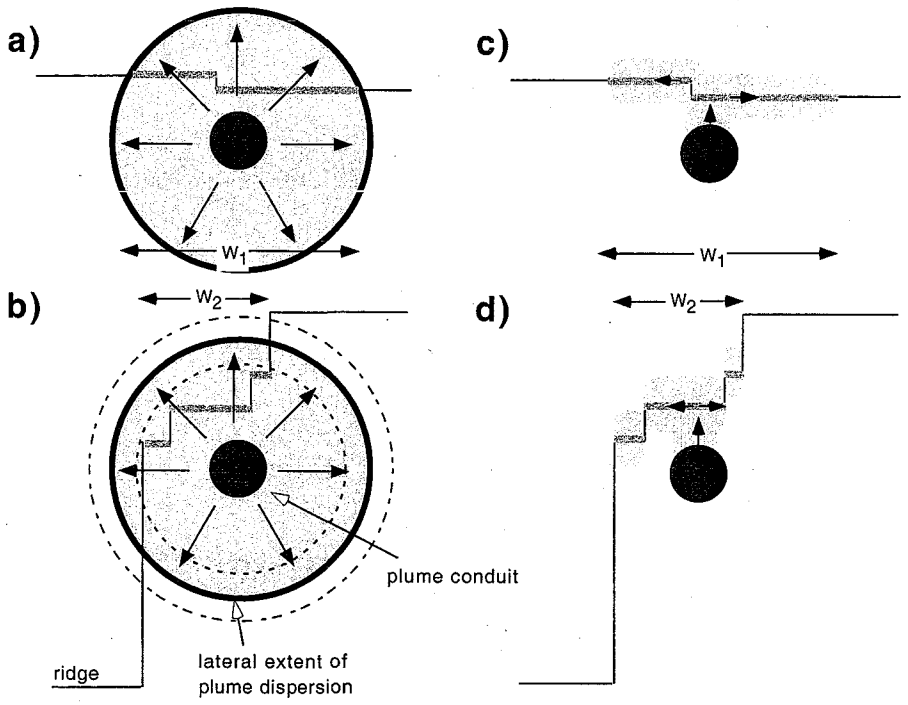

Fig. 11. Schematic cartoons of plume–ridge interaction with a segmented ridge. (a) Broad dispersion of plume material at a depth below the onset of melting, for a ridge with only a single, small transform offset. Dark gray circle represents the plume conduit, light gray shading depicts dispersal of plume material, arrows indicate plume dispersal direction, and thin black lines denote ridge geometry. Ridge segments with a plume signature are emphasized with thick, medium gray shading. The length of ridge affected by plume 1, or waist width, is W_1. (b) As in (a), but for a highly segmented ridge. Although the plume's lateral extent is the same as in (a), the resulting waist width W_2 is less than W_1. Note ambiguity in inferring plume dispersion from W_2, since both smaller (dashed) and larger (dash–dot) circles will produce the same W_2. (c) Schematic illustration of the channelized along-axis plume dispersion model for the same ridge geometry as in (a). Arrows indicate flow directed from plume to ridge, and subsequent dispersion along-axis, at depths within the partial melting zone. The resulting waist width is W_1. (d) As for (c), but for a highly segmented ridge. Note that long-offset transforms act as thermal and mechanical barriers and prevent along-axis dispersion, resulting in a W_2 that is less than W_1.

[40], Vogt and Johnson [41], Vogt [42], and Sleep [43]. In the scenario of diffuse flow (Fig. 11a,b), a plume upwells vertically to a depth below the region of partial melting, and then spreads radially. The style of plume–ridge interaction will differ depending on ridge-transform geometry. If the ridge offset is small (Fig. 11a), the plume waist width will reflect well the width of the plume anomaly. For highly segmented geometry (Fig. 11b), however, transform faults offset the ridge out of the area of plume influence, thereby decreasing the waist width. The true lateral extent and flux of the plume will be ambiguous, because plumes with a somewhat smaller or larger areal extent will result in the same waist width.

In the other end-member geometry of channelized along-axis flow (Fig. 11c,d), mantle flows directly from plume to ridge, with subsequent along-axis distribution within or above the melting zone. Here, transform offsets may act as thermal and mechanical barriers to along-axis plume dispersion. Longer offsets compartmentalize hotspot material more effectively than shorter discontinuities. In this case, the plume waist width is also related to ridge geometry, with waist width for a more segmented ridge always less than or equal to that of a straight ridge. Importantly, therefore, both the diffuse dispersion and channelized along-axis flow models imply that ridge segmentation acts to decrease plume waist width.

6.2. Marion and Galapagos

The present paucity of geophysical and geochemical data for the Marion region, and particularly the lack of seismic data, makes it difficult to distinguish between the diffuse and channelized plume dispersion models. Here we note that two prominent transform faults disrupt the SWIR in the vicinity of Marion, Andrew Bain (total offset of 720 km) and Discovery II (total offset of 350 km) (Fig. 10a). These transforms appear to bracket the along-axis MBA and RMBA anomalies for Marion (Figs. 3 and 5). Therefore, we postulate that these two transform systems are long enough to limit Marion's waist width, or to act as 'transform terminators'. We do not presently have enough data to conclusively determine if Andrew Bain and Discovery II limit Marion's waist width by offsetting the SWIR out of Marion's influence (diffuse plume model) or damming along-axis flow (channelized plume model).

In contrast to Marion, there are few significant ridge discontinuities along the CNSC near the Galapagos (Fig. 10b). No discontinuities greater than 35 km exist to the west of the Galapagos Islands, suggesting that the western half-width of the Galapagos anomaly reflects the original plume width. The eastern CNSC also has few discontinuities between the Galapagos Islands and ~85°W; however, a 110-km transform at 85°W may terminate the Galapagos anomaly. Taken together, the Marion/SWIR and Galapagos/CNSC examples illustrate the important influence of transform offsets in limiting the lateral extent of plume–ridge interaction at a variety of spreading rates. Since ultra-slow spreading ridges tend to be more highly segmented, the transform effect may be most pronounced along the SWIR. The effects of transform offset length and spreading rate on along-axis flow from a ridge-centered plume are quantitatively evaluated through numerical modeling in a separate study [44].

7. Conclusions

The main results of this study of ridge–hotspot interactions along the SWIR include the following:

1. The Bouvet hotspot, approximately 300 km east of the BTJ and 55 km from the nearest spreading segment along the SWIR, imparts a high-amplitude (~100 mGal) mantle Bouguer gravity anomaly low to the SWIR, implying considerable crustal thickening, anomalously warm mantle, or a combination of both. However, the Bouvet anomaly is quite localized between the Bouvet and Islas Orcadas FZs. In comparison, the Marion MBA low is broader, and likely limited to the stretch of ridge between the Andrew Bain and Discovery II FZs.
2. There is little off-axis indication of a Bouvet hotspot track in crust ~30–90 Ma, suggesting the possibilities that the flux of the hotspot changes with time, or that the hotspot melting anomaly is enhanced when it is close to a plate boundary. In contrast, a well-defined residual gravity low, striking north–south along the Madagascar Ridge, corresponds closely with published Marion hotspot tracks.
3. Long-offset transforms, characteristic of ultra-slow spreading centers, may play an important role in influencing ridge–hotspot interactions. Transforms may either act as thermal and mechanical barriers to along-axis plume transport, or displace ridge segments out of a hotspot-affected region. We postulate that the Andrew Bain and Discovery II FZs, with offsets of 720 and 350 km, respectively, act as 'transform terminators' for the Marion plume.

Acknowledgements

We are grateful to R. Fisher, J. Sclater, and A. Goodwillie for providing the GEBCO-97 bathymetric data of the southern oceans and to J. Madsen, N. Grindlay, C. Rommevaux-Jestin, and M. Cannat for providing reprints of their manuscripts. Constructive reviews by Roger Searle and an anonymous reviewer improved the manuscript. We benefited greatly from discussion with M. Cannat, B. Detrick, J. Escartin, G. Ito, and B.

West. This work was supported by a National Defense Science and Engineering Graduate (NDSEG) Fellowship to J.G. and NSF Grants OCE-9811924 and OCE-9907630. Woods Hole Oceanographic Institution contribution number 10311.*[FA]*

References

[1] D.T. Sandwell, W.H.F. Smith, Marine gravity anomaly from Geosat and ERS 1 satellite altimetry, J. Geophys. Res. 102 (1997) 10039–10054.
[2] IOC, IHO, and BODC, GEBCO-97: The 1997 Edition of the GEBCO Digital Atlas, 1997.
[3] R.D. Mueller, W.R. Roest, J.-Y. Royer, L.M. Gahagan, J.G. Sclater, Digital isochrons of the world's ocean floor, J. Geophys. Res. 102 (1997) 3211–3214.
[4] R.A. Duncan, Hotspots in the southern oceans – an absolute frame of reference for motion of the Gondwana continents, Tectonophysics 74 (1981) 29–42.
[5] W.J. Morgan, Hotspot tracks and the early rifting of the Atlantic, Tectonophysics 94 (1982) 123–139.
[6] M. Ligi, E. Bonatti, G. Bortoluzzi, G. Carrara, P. Fabretti, D. Penitenti, D. Gilod, A.A. Peyve, S. Skolotnev, N. Turko, Death and transfiguration of a triple junction in the south Atlantic, Science 276 (1997) 243–245.
[7] M.D. Kurz, A.P. leRoex, H.J.B. Dick, Isotope geochemistry of the oceanic mantle near the Bouvet triple junction, Geochim. Cosmochim. Acta 62 (1998) 841–852.
[8] N.C. Mitchell, R.A. Livermore, Spiess Ridge: An axial high on the slow spreading Southwest Indian Ridge, J. Geophys. Res. 103 (1998) 15457–15471.
[9] N.R. Grindlay, J. Madsen, C. Rommevaux-Jestin, J. Sclater, A different pattern of ridge segmentation and mantle Bouguer gravity anomalies along the ultra-slow spreading Southwest Indian Ridge (15°30′E to 25°E), Earth Planet. Sci. Lett. 161 (1998) 243–253.
[10] N.R. Grindlay, J. Madsen, C. Rommevaux, J. Sclater, S. Murphy, Southwest Indian Ridge 15°E–35°E: A geophysical investigation of an ultra-slow spreading mid-ocean ridge system, InterRidge News 5 (1996) 7–12.
[11] P. Patriat, D. Sauter, M. Munschy, L. Parson, A survey of the Southwest Indian Ridge axis between Atlantis II Fracture Zone and the Indian Ocean Triple Junction: Regional setting and large scale segmentation, Mar. Geophys. Res. 19 (1997) 457–480.
[12] C. Rommevaux-Jestin, C. Deplus, P. Patriat, Mantle Bouguer anomaly along an ultra-slow spreading ridge: Implications for accretionary processes and comparison with results from central Mid-Atlantic Ridge, Mar. Geophys. Res. 19 (1997) 481–503.
[13] C. Mevel, K. Tamaki, The FUJI scientific party, Imaging an ultra-slow spreading ridge: first results of the FUJI cruise on the SWIR (R/V Marion Dufresne, 7/10–3/11/97), InterRidge News 7 (1998) 29–32.
[14] M. Cannat, C. Rommevaux-Jestin, D. Sauter, C. Deplus, V. Mendel, Formation of the axial relief at the very slow spreading Southwest Indian Ridge (49 degrees to 69 degrees E), J. Geophys. Res. 104 (1999) 22825–22843.
[15] G. Ito, J. Lin, C.W. Gable, Dynamics of mantle flow and melting at a ridge-centered hotspot: Iceland and the Mid-Atlantic Ridge, Earth Planet. Sci. Lett. 144 (1996) 53–74.
[16] G. Ito, J. Lin, C.W. Gable, Interaction of mantle plumes and migrating mid-ocean ridges: Implications for the Galapagos plume–ridge system, J. Geophys. Res. 102 (1997) 15403–15417.
[17] G. Ito, Y. Shen, G. Hirth, C.J. Wolfe, Mantle flow, melting, and dehydration of the Iceland mantle plume, Earth Planet. Sci. Lett. 165 (1999) 81–96.
[18] N.M. Ribe, U.R. Christensen, J. Theißing, The dynamics of plume–ridge interaction, 1: Ridge-centered plumes, Earth Planet. Sci. Lett. 134 (1995) 155–168.
[19] N.M. Ribe, The dynamics of plume–ridge interaction, 2: Off-ridge plumes, J. Geophys. Res. 101 (1996) 16024–16195.
[20] G. Ito, J. Lin, Mantle temperature anomalies along the present and paleoaxes of the Galapagos spreading center as inferred from gravity analysis, J. Geophys. Res. 100 (1995) 3733–3745.
[21] B. Appelgate, A.N. Shor, The northern Mid-Atlantic and Reykjanes Ridges: Spreading center morphology between 55°50′N and 63°00′N, J. Geophys. Res. 99 (1994) 17935–17956.
[22] R.L. Fisher, A.M. Goodwillie, The physiography of the Southwest Indian Ridge, Mar. Geophys. Res. 19 (1997) 451–455.
[23] G.A. Neumann, D.W. Forsyth, D. Sandwell, Comparison of marine gravity from shipboard and high-density satellite altimetry along the Mid-Atlantic Ridge, 30.5°–35.5°S, Geophys. Res. Lett. 20 (1993) 1639–1642.
[24] D. Divens, Total sediment thickness of the world's oceans, National Oceanic and Atmospheric Administration, US Department of Commerce, Boulder, CO, 1996 (information available on the Web at http://www.ngdc.noaa.gov/mgg/sedthick/sedthick.html).
[25] B. Parsons, J.G. Sclater, An analysis of the variation of ocean floor bathymetry and heat flow with age, J. Geophys. Res. 82 (1977) 803–827.
[26] D.L. Turcotte, E.R. Oxburgh, Finite amplitude convection cells and continental drift, J. Fluid Mech. 28 (1967) 29–42.
[27] B.Y. Kuo, D.W. Forsyth, Gravity anomalies of the ridge-transform system in the South Atlantic between 31 and 34.5°S: Upwelling centers and variations in crustal thickness, Mar. Geophys. Res. 10 (1988) 205–232.
[28] J. Lin, G.M. Purdy, H. Schouten, J.-C. Sempere, C. Zervas, Evidence from gravity data for focused magmatic accretion along the Mid-Atlantic Ridge, Nature 344 (1990) 627–632.
[29] J. Phipps Morgan, D.W. Forsyth, 3-D flow and temper-

ature perturbations due to transform offset: effects on oceanic crustal and upper mantle structure, J. Geophys. Res. 93 (1988) 2955–2966.

[30] J. Mahoney, A.P. le Roex, Z. Peng, R.L. Fisher, J.H. Natland, Southwestern limits of Indian Ocean ridge mantle and the origin of low $^{206}Pb/^{204}Pb$ mid-ocean ridge basalt: Isotope systematics of the central Southwest Indian Ridge (17°–50°E), J. Geophys. Res. 97 (1992) 19771–19790.

[31] A.P. le Roex, H.J.B. Dick, A.J. Erlank, A.M. Reid, F.A. Frey, S.R. Hart, Geochemistry, mineralogy and petrogenesis of lavas erupted along the Southwest Indian Ridge between the Bouvet Triple Junction and 11 degrees east, J. Petrol. 24 (1983) 267–318.

[32] A.P. le Roex, H.J.B. Dick, R.T. Watkins, Petrogenesis of anomalous K-enriched MORB from the Southwest Indian Ridge: 11°53′E to 14°38′E, Contrib. Mineral. Petrol. 110 (1992) 253–268.

[33] H.J.B. Dick, Abyssal peridotites, very slow spreading ridges, and ocean ridge magmatism, in: A.D. Saunders, M.J. Norry (Eds.), Magmatism in the Ocean Basins, Geological Society special publication No. 42, 1989, pp. 71–105.

[34] H.J.B. Dick, A.P. leRoex, J. Madsen, N.R. Grindlay, Constraints on mantle melting, diapirism and melt flow at ultra-slow spreading ridges: observations from petrological and geophysical data from the Southwest Indian Ridge 15 to 25 degrees east, EOS Trans. AGU 78 (Suppl.) (1997) F682–F683.

[35] A.P. le Roex, H.J.B. Dick, A.M. Reid, F.A. Frey, A.J. Erlank, S.R. Hart, Petrology and geochemistry of basalts from the American–Antarctic Ridge, Southern Ocean: Implications for the westward influence of the Bouvet mantle plume, Contrib. Mineral. Petrol. 90 (1985) 367–380.

[36] R.A. Duncan, M.A. Richards, Hotspots, mantle plumes, flood basalts, and true polar wander, Rev. Geophys. 29 (1991) 31–50.

[37] J. Goslin, M. Recq, R. Schlich, Structure profonde du plateau de Madagascar: relations avec le plateau de Crozet, Tectonophysics 76 (1981) 75–97.

[38] C.J.H. Hartnady, A.P. le Roex, Southern Ocean hotspot tracks and the Cenozoic absolute motion of the African, Antarctic, and South American plates, Earth Planet. Sci. Lett. 75 (1985) 245–257.

[39] A.K. Martin, Plate reorganisations around Southern Africa, hot-spots and extinctions, Tectonophysics 147 (1987) 309–316.

[40] W.J. Morgan, Rodriguez, Darwin, Amsterdam, ..., A second type of hotspot island, J. Geophys. Res. 83 (1978) 5355–5360.

[41] P.R. Vogt, G.L. Johnson, Transform faults and longitudinal flow below the midoceanic ridge, J. Geophys. Res. 80 (1975) 1399–1428.

[42] P.R. Vogt, Plumes, subaxial pipe flow, and topography along the mid-oceanic ridge, Earth Planet. Sci. Lett. 29 (1976) 309–325.

[43] N. Sleep, Lateral flow of plume material ponded at sublithospheric depths, J. Geophys. Res. 101 (1996) 28065–28083.

[44] J. Georgen, J. Lin, The effects of transform offsets on reducing along-ridge plume flux: Implications for ridge–hotspot interactions, EOS Trans. AGU 81 (Suppl.) (2000) F1129.

[45] R.L. Parker, The rapid calculation of potential anomalies, Geophys. J. R. Astron. Soc. 31 (1972) 447–455.

[46] A.E. Gripp, R.G. Gordon, Current plate velocities relative to the hotspots incorporating the NUVEL-1 global plate motion model, Geophys. Res. Lett. 17 (1990) 1109–1112.

Chapter 3

The effects of transform faults on along-axis flow of plume material: Implications for plume-ridge interaction

Jennifer E. Georgen and Jian Lin

Abstract

We explore a potentially important variable in controlling ridge-hotspot interaction, the effect of transform offsets in limiting along-axis flow of plume material. Transform faults may act as barriers to along-axis flow (e.g., *Vogt and Johnson* [1975], *Sleep* [1996]), particularly at large ridge offsets along slow and ultra-slow spreading ridges. We quantify the degree to which transform faults affect axial asthenospheric flow by performing a series of 3D numerical experiments. First, 3D mantle viscosity structure for a ridge-transform-ridge system is determined based on temperature- and pressure-dependent viscosity laws. We consider four half-spreading rates, ranging from ultra-slow (0.75 cm/yr) to fast (7.25 cm/yr), and six transform lengths, spanning 0 to 250 km in increments of 50 km. We then calculate the 3D viscous flow in response to an along-axis pressure gradient corresponding to a ridge-centered hotspot. Modeling results predict that transform faults affect along-axis mantle material flow in two important ways. First, transforms reduce along-axis flux. The longer the transform offset, the more across-transform flux is reduced relative to the zero-offset case. Second, transforms deflect shallow asthenospheric along-axis flow. As transform offset increases and spreading rate decreases, deflection of along-axis flow toward the transform is enhanced. The transform damming effect is most pronounced for viscosity which is strictly pressure- and temperature-dependent. Flux reduction effects could be reduced for viscosity laws which additionally consider dehydration, melting, and change in deformation mechanism. This model predicts that for a given buoyancy of an on-axis plume, the along-axis waist width of the plume is less if it interacts with a highly segmented slow-spreading ridge than with a fast-spreading ridge. This prediction is considerably different from previous fluid dynamical models of a straight ridge interacting with a plume that argue for greater waist width at slower spreading rates.

1. Introduction

A significant portion of the mid-ocean ridge system is influenced by mantle plumes [*Schilling*, 1991]. Near- or on-ridge plumes thicken oceanic crust, alter mid-ocean ridge geochemistry, and impart a strong signal to seafloor bathymetry, gravity, and geoid.

Plumes are linked to ridge geometry reconfiguration, as in the cases of Iceland and Amsterdam-St. Paul, where segments jump to remain in close spatial proximity to the plumes [*Sæmundsson*, 1974; *Jancin et al.*, 1985; *Conder et al.*, 2000a]. Numerous investigations have suggested that transform faults influence the distribution of plume material, including the Charlie Gibbs FZ for the Iceland hotspot [*Vogt and Johnson*, 1976] and the Agulhas FZ for Discovery hotspot [*Douglass et al.*, 1995]. The quantitative influence of ridge offsets on plume dispersal was first explored analytically by *Vogt and Johnson* [1975] and *Vogt* [1976]. However, the interaction between plume-driven flow and transform faults has only recently been addressed by numerical models. While most of the recent plume-ridge numerical experiments generally consider straight ridges, the study of *Yale and Phipps Morgan* [1998] predicts strong focusing of the Kerguelen plume towards a segment of the Southeast Indian Ridge (SEIR) that is displaced towards Kerguelen, suggesting that ridge segmentation is important in plume-ridge interaction.

Segmentation is a first-order feature of mid-ocean ridges. Ridges of all spreading rates are segmented, although segmentation pattern and the associated mantle dynamics vary with spreading rate [e.g., *Macdonald,* 1982; *Schouten et al.,* 1985; *Lin and Phipps Morgan*, 1992]. Figure 1 shows examples of the ultra-slow spreading Southwest Indian Ridge (SWIR) near the Marion hotspot (Figure 1*a*), the slow-spreading Reykjanes Ridge south of Iceland (Figure 1*b*), and the intermediate-spreading Cocos-Nazca Spreading Center (CNSC) near the Galapagos hotspot (Figure 1*c*). Along the SWIR between 25°-45°E, the Andrew Bain and other transform faults cumulatively offset the SWIR by 1520 km (Figure 1*a*), which is roughly three times the cumulative offset (560 km) along the CNSC for similar ridge length (Figure 1*c*). In contrast, ridge offsets south of Iceland along the Reykjanes and Mid-Atlantic ridges are generally small until the 350-km-long

Charlie Gibbs FZ (Figure 1*b*). Thus ridge offset pattern varies considerably among the global ridge systems, creating different conditions for along-axis plume flow.

In this study we use a hybrid finite difference/finite element 3D numerical model to quantify the effects of transform offsets in limiting the along-axis mantle flow driven by an on-axis plume. We examine six transform offset lengths, ranging from 0 to 250 km, and four spreading rates, from ultra-slow to fast, to investigate the global range of ridge geometry. We then examine the sensitivity of the transform effect to mantle viscosity and discuss the implications of model results for plume-ridge interactions.

2. Numerical Method

We model mantle flow along a segmented ridge driven by a plume-related pressure gradient. The model box consists of two segments, each of length L_s, and an intervening transform of length L_t (Figure 2; see Table 1 for definition of model variables). We examine values of L_t ranging from 0 km to 250 km in increments of 50 km, spanning most transform offset lengths observed in the global ridge system. The model box is 750 km in the across-axis, plate-spreading direction (X), 500 km in the along-axis direction (Y), and 660 km in depth (Z) to coincide with the 660 km mantle discontinuity. A range of half-spreading rates, U, were selected to reflect representative cases of plume-ridge systems. A rate of U = 0.75 cm/yr corresponds to the ultra-slow spreading SWIR near the Marion plume; U = 1.25 cm/yr reflects the slow-spreading Mid-Atlantic Ridge (MAR) near the Azores and Iceland plumes; U = 3.0 cm/yr simulates the CNSC near the Galapagos plume and the SEIR near Amsterdam-St. Paul; and 7.25 cm/yr corresponds to the fast-spreading East Pacific Rise (EPR) and the Easter hotspot. All possible combinations of L_t and U are

modeled except L_t = 50 and 100 km for U = 7.25 cm/yr, as calculations showed transform offsets less than 150 km have minimal effect on along-axis flow for fast spreading rates.

Numerical calculations are performed in two steps: (1) We calculate three-dimensional (3D) viscosity structure for a given L_t and U using the approach of *Shen and Forsyth* [1992]; and (2) we use this 3D viscosity structure as input to a fluid dynamical calculation, where a pressure gradient simulating an on-axis plume drives flow along-ridge in the Y-direction. This two-step approach significantly simplifies modeling complexity and enables us to isolate the purely geometrical effects of viscosity structure on along-axis mantle material flow.

Pressure- and temperature-dependent viscosity is calculated using a hybrid, iterative finite element/finite difference approach [*Shen and Forsyth*, 1992]. First, the velocity field for incompressible mantle flow driven by passive plate separation is determined using a finite element code with successive overrelaxation. Then, upwind finite differences are used to solve for the mantle temperature field in the model box, assuming $T_{z=200km}$ = 1350°C and $T_{z=0km}$ = 0°C, and viscosity is calculated at each node according to pressure and temperature. Finally, velocity, temperature, and viscosity calculations are iterated until a stable steady-state solution is reached. The governing equation for viscosity is given by

$$\eta = A\,\sigma^{1-n} \exp\left[(E+PV)/RT \right] \qquad (1)$$

where A is a pre-exponential constant, n is the stress exponent, E is activation energy, P is pressure, V is activation volume, R is the universal gas constant, and T is temperature (Table 1). We set n=1 (Newtonian fluid) for all calculations, yielding a reference minimum viscosity $\eta_{ref} = A\sigma^{1-n} = 10^{19}$ Pa s. Viscosity varies by ~5 orders of magnitude over the model space. For all spreading rates, low viscosity values are predicted for a broad depth range with viscosity minima occurring at a depth of approximately 70-75 km (Figure 3*a*). In plan view, the region of lowest viscosity forms a continuous meandering band along-

axis, with width proportional to spreading rate (Figure 3*b-c*). Further details of the viscosity modeling calculations can be found in *Shen and Forsyth* [1992].

The 3D viscosity field for each combination of U and L_t are then used as input to a finite element fluid dynamical code (ADINA, *Bathe* [1996]) that solves the equation of continuity for an incompressible fluid

$$\nabla \bullet \mathbf{v} = 0 \qquad (2)$$

and the equation of momentum balance

$$\nabla P = \nabla \bullet (\eta \nabla \mathbf{v}) + \rho \mathbf{g} \qquad (3)$$

with no heat transfer and no buoyancy-driven flow, where $\mathbf{v}$ is velocity vector, P is fluid pressure, η is viscosity, ρ is mantle density, and $\mathbf{g}$ is the acceleration of gravity. The driving force for fluid flow is a pressure gradient created by imposing pressure with a Gaussian spatial distribution (Figure 2) at $Y = L_s$ and zero pressure at $Y = -L_s$. The pressure at $Y = L_s$ is assumed to be maximum at the ridge axis with a distribution given by

$$P(x) = P_o \exp [-0.5*(X/x_o)^2] / (2\pi)^{1/2} x_o \qquad (4)$$

where P_o is the maximum pressure and x_o is the Gaussian distribution standard deviation length. P_o is fixed at a constant value of 15 MPa for all calculations; however, we examine the sensitivity of the results to varying both P_o and x_o in a later section. Other boundary conditions are zero shear stress at Z = 0 km and $Z = Z_{max}$, $v_z = 0$ at $Z = Z_{max}$, and zero normal stress at Z = 0 km, $X = X_{max}$, and $X = -X_{max}$. Along-axis flux Q of mantle material is defined as

$$Q(Y) = \int v_y \, dX \, dZ \qquad (5)$$

where v_y is along-axis velocity (Table 1) and the integration is taken over the entire X-Z plane at constant Y.

Viscosity is calculated for a box with dimensions X_{max} x Y_{max} x 200 km, and padded to a depth of 660 km by extrapolation according to pressure-depth relationships. The

computational grid for viscosity structure is 41 x 30 x 19 nodes, yielding resolution of 18.8 x 17.2 x 10.5 km. A slightly different nodal grid of 41 x 25 x 21 nodal grid is used for the flow velocity calculations. This results in spatial resolution of 18.8 x 20.8 km in the X and Y directions, respectively, and variable spacing, from 6 to 60 km, in Z with highest resolution near the surface where vertical gradients in viscosity are greatest. Numerical results for a benchmark isoviscous channel-flow problem differ by <1% from analytical calculations.

3. Results

The presence of a transform offset has two general effects on along-axis material flow, (1) reduction in mantle material flux across the transform, and (2) deflection of shallow mantle flow toward the offset direction. Figure 4 shows both of these effects for the case of L_t = 100 km and U = 1.25 cm/yr. Deflection of the region of high along-axis velocity is evident in Figure 4*b*, where high velocities follow low-viscosity contours; reduction in material flux is evident in tapering of the high-velocity region toward the transform. In across-axis section (Figure 4*c*), the region of high along-axis velocity forms the shape of a flattened triangle, again following viscosity contours. This focused region of high-velocity flow is in great contrast to the much more diffuse cross-sectional pattern of the along-axis velocities calculated for the case of an isoviscous mantle (Figure 5). Along-axis flow decreases both in magnitude and in areal extent as either the transform offset is increased or the spreading rate is decreased (Figure 6). For the prescribed along-axis pressure gradient of 15 MPa over 500 km, the maximum along-axis velocities for L_t = 0 km range from ~10 cm/yr for U = 0.75 cm/yr to ~20 cm/yr for U = 7.25 cm/yr (Figure 7). These high

velocities are achieved at a depth of approximately 75 km, where minima in viscosity-depth profiles are reached (Figure 3*a*).

Due to both material flow in the spreading (X) and vertical (Z) directions and viscous dissipation, the along-axis flux Q decreases as a function of decreasing Y even in the absence of a transform fault (i.e., for L_t = 0 km) (Figure 8). For a spreading rate of 1.25 cm/yr and L_t = 0 km, for example, the calculated flux decreases from Q = 3.5 km^3/yr at Y = L_s to Q = 1 km^3/yr at Y = 0, corresponding to 70% reduction in Q over a distance of L_s. It is also important to note that for the same along-axis pressure gradient, the predicted Q at a given distance Y is smaller for slower spreading ridges than faster spreading ridges. Near the ridge axis, the calculated mantle temperature is lower and thus viscosity is higher for slower spreading ridges, resulting in a volumetrically smaller low-viscosity channel and thus smaller along-axis flux Q. For example, for the same transform length (L_t = 200 km), the calculated flux Q at Y = 0 km for U = 0.75 cm/yr is only 80% that for U = 1.25 cm/yr and 30% that for U = 7.25 cm/yr (Figure 9).

3.1 Reduction in flux across a transform fault

Figure 10 shows the effects of U and L_t on along-axis flux reduction. For each spreading rate, we calculate normalized flux, $Q/Q_{Lt=0}$, to highlight the effect of transform offsets. The presence of a transform fault is predicted to reduce Q along the entire length of the ridge axis both upstream (Y > 0 km) and downstream (Y < 0 km) of the transform fault. For example, in the case of U = 0.75 cm/yr and L_t = 250 km (Figure 10*a*), the calculated $Q/Q_{Lt=0}$ is 0.6 at Y = 0 km, indicating the flux is already reduced substantially upstream of the transform fault. The reduction in flux upstream of the transform reflects widespread increase in mantle viscosity around the transform due to thermal cooling effects. Downstream from the transform fault, the spatial gradient in the reduction of Q is

even greater. As a result, the predicted along-axis material flux Q is essentially zero within 100 km downstream of the transform (Figure 10*a*). In general, the fluxes are predicted to decrease by a greater amount for smaller U and larger L_t.

Gradients in across-transform flux are another measure of the effectiveness of a transform as a barrier to along-axis mantle flow (Figure 11). We define $\Delta Q/\Delta Y$ to be $(Q/Q_{Lt=0|Y=20\ km} - Q/Q_{Lt=0|Y=-20\ km})/\Delta Y$, or the difference between pre-transform and post-transform normalized flux over a fixed distance ΔY of 40 km. For the example of U = 3.0 cm/yr shown in Figure 11, the calculated reduction gradient in across-transform flux $\Delta Q/\Delta Y$ for L_t = 200 km is double that for L_t = 150 km, which in turn is double that of L_t = 100 km. Compared to U = 3.0 cm/yr, $\Delta Q/\Delta Y$ is smaller for all modeled transform offsets for U = 7.25 cm/yr, and the increase in $\Delta Q/\Delta Y$ for successive increases in L_t is less (Figure 11). Therefore, compared to faster spreading rates, transform effects at slower spreading rates are more sensitive to increases in L_t.

3.2 Deflection of asthenospheric flow

Along-axis flow stagnates farther upstream from the transform as L_t increases (Figure 12). At a depth of 72 km, i.e., within the zone of fastest along-axis flow, we define the reference velocity v_{ymax} as the value of v_y at $Y = L_s$. Y_{stag} is the distance at which v_y drops below a threshold value of 18.5% of v_{ymax} as the mantle flows toward the transform. A threshold of 18.5% was selected because it is the characteristic velocity dissipation factor for the L_t = 0 case, i.e., $v_y|_{Y=Ls} = 0.185*v_{ymax}$. Figure 12 suggests that the longer the offset or slower the spreading rate, the farther upstream from the transform fault the high-velocity flow is predicted to stop. For example, for L_t = 150 km, $Y_{stag} = 0.9L_s$ for 3.0 cm/yr, but $Y_{stag} \sim 0.70L_s$ for U = 0.75 cm/yr.

In addition to impeding along-axis flow, transform offsets also deflect it in the direction of the next ridge segment (Figure 13). The deflection is more pronounced for slower spreading rates. Figure 13*a* shows the path that high-velocity along-axis flow follows at a depth of 72 km across a 100-km transform for different spreading rates (U = 0.75, 1.25, and 3.0 cm/yr). ΔD is the distance that this high-velocity flow travels in the X-direction between Y = 250 km and Y = 0 km. Note that ΔD is always smaller than L_t. Figure 13*b* traces the position of high-velocity along-axis flow for different transform offsets at U = 0.75 cm/yr. Again, ΔD is smaller than L_t. In general, the faster the spreading rate, the less sensitive the predicted asthenospheric flow path is to a transform fault (Figure 13*c*). Because a broader low-viscosity zone is predicted for faster-spreading ridges, flow paths are predicted to deviate less from the linear than at slower spreading rates. For example, for L_t = 100 km and U = 3.0 cm/yr, ΔD is only 20 km, but the deflection increases to nearly 100 km for U = 0.75 cm/yr (Figure 13*c*).

4. Sensitivity of Model Results

4.1 Pressure gradients

The effects of different driving pressures on the calculated along-axis flux are evaluated in Figure 14. Since channelized viscous flow velocity scales with dP/dY, it is important to consider how pressure decays with distance away from a plume. For most calculations, we select P_o = 15 MPa, which corresponds to an along-axis pressure gradient dP/dY = P_o/Y_{max} = 15 MPa/500 km = 30 kPa/km. The selection of P_o follows two different arguments, one relating to plume buoyancy and the other to topographic loading. First, following *Conder et al.* [2000b], we assume that plume-induced differential pressure ΔP scales with buoyancy force:

$$\Delta P \sim \rho\alpha\Delta T g \Delta L, \text{ or } \Delta P/\Delta L \sim \rho\alpha\Delta T g \quad (6)$$

where ρ is reference mantle density, ΔT is plume thermal anomaly, ΔL is upwelling length, and α is the coefficient of thermal expansion. If we assume that ρ = 3300 kg/m^3, α = 3x10^{-5} K^{-1}, and g = 9.8 m/s^2,

$$\Delta P/\Delta L \sim \Delta T \quad (7)$$

For the on-axis Iceland plume, models suggest ΔT ~ 50-200 K [*Ito et al.,* 1999], yielding $\Delta P/\Delta L$ ~50-200 kPa/km. This is probably an upper limit for plume-related along-axis pressure gradients. $\Delta P/\Delta L$ will be smaller for off-axis plumes and plumes with smaller ΔT. *Conder et al.* [2000b], for example, model asymmetric flow across the axis of the EPR, assuming that mantle material flow is driven by the Pacific superswell. They assume ΔP = 100 MPa, yielding dP/dY ~30 kPa/km if the pressure gradient is linear and dP/dY ~5 kPa/km if pressure decays radially away from the superswell source.

If mantle material flow is driven by topographic loading of a lithospheric plate by emplacement of a volcanic edifice, ΔP should scale as

$$\Delta P \sim \rho g \Delta h, \text{ or } \Delta P/\Delta L \sim \rho g \Delta h/\Delta L \quad (8)$$

where Δh is elevation of the topographic anomaly relative to the surrounding seafloor, ρ = 2700 kg/m^3, and g = 9.8 m/s^2. Based on the plateau heights of the Galapagos, Azores, and Iceland hotspots, $\Delta h/\Delta L$ is approximately 0.8/500, 4/1300, and 1.8/1100 km/km [*Ito and Lin*, 1995a], respectively, yielding $\Delta P/\Delta L$ ~ 42, 43, and 81 kPa/km. Therefore, these hotspot plateaus, if uncompensated, may drive along-axis mantle material flow. If the plateau is compensated, the predicted pressure gradient is less.

Figure 14 shows the sensitivity of the predicted velocity flow fields to the magnitude of the driving pressure P_o and the pressure standard deviation x_o. Without changing x_o, increasing the magnitude of the driving force to P_o = 25 MPa (dP/dY = 50 kPa/km) changes Q by a constant factor equal to the ratio of 25 MPa/15 MPa. With P_o = 15 MPa,

increasing x_o from 100 km to 150 km increases Q by a factor of 1.2-1.4, as more off-ridge mantle material flows along-axis. Conversely, decreasing x_o to 50 km narrows the conduit of the high-velocity flow and consequently decreases Q by a factor of approximately 0.6.

While our model assumes a depth-independent pressure gradient focused on the ridge, other spatial distributions and types of driving forces associated with a mantle plume may also give rise to along-axis mantle material flow. For example, a pressure that decreases with depth may reflect a hotspot whose origin is a relatively shallow geochemical anomaly with depth extent much less than 660 km. Also, rather than buoyancy-related pressure forces, flow may result from the velocity field of mantle material as it disperses radially away from a plume source.

4.2 Alternative viscosity models

This study considers viscosity as a function of temperature and pressure. However, viscosity is also influenced by other factors including the presence of melt, dehydration during melting, and transitions in creep mechanism [*Hirth and Kohlstedt,* 1995a, 1995b, 1996; *Braun et al.*, 2000]. According to the numerical models of *Braun et al.* [2000], latent heat changes during melting increase mantle viscosity at the depths where dry melting occurs only by less than an order of magnitude compared to strictly temperature- and pressure-dependent viscosity. The retention of a small amount of melt in the mantle matrix also has a relatively small effect, decreasing the shallow mantle viscosity by less than an order of magnitude. In contrast, dehydration during melting is suggested to increase viscosity by approximately two orders of magnitude in the shallow mantle, while transition in creep mechanism results in a viscosity decrease of an order of magnitude. The predicted combined effect of all four of these processes is to cause a maximum increase in viscosity in the dry melting regime (shallow depths) of approximately an order of magnitude, and a

maximum decrease in viscosity in the wet melting regime (greater depths) of approximately an order of magnitude. This effect can be seen in Figure 3*a*, where the *Braun et al.* [2000] viscosity-depth curve for 1.0 cm/yr has higher magnitude than the corresponding *Shen and Forsyth* [1992] solutions for depths in the range of ~25-50 km, but lower viscosities at depths greater than approximately 50 km.

To estimate the potential effects of melting, dehydration, and transition in creep mechanism on along-axis velocity, we computed 3D flow fields using the viscosity structure predicted by *Braun et al.* [2000] for a ridge with U = 3.0 cm/yr (Figure 15). Since *Braun et al.* [2000] only examined a 2D, axis-perpendicular geometry, we stacked their viscosity-depth solution along-axis to generate a 3D viscosity structure with no transform offsets. We adjusted the minimum viscosity used by *Braun et al.* [2000] to match $\eta_{ref} = 10^{19}$ Pa s and refer to this viscosity structure as the "equalized" *Braun et al.* curve (Figure 3*a*). While maximum v_y for the strictly pressure- and temperature-dependent viscosity solution occurs at a depth less than 100 km, the maximum v_y for the equalized *Braun et al.* viscosity structure is found at a depth slightly less than 200 km (Figure 15*a*). Moreover, for the same pressure gradient, the value of the maximum v_y for the equalized *Braun et al.* solution is greater (>30 cm/yr) than that for the strictly pressure- and temperature-dependent viscosity solution (~15 cm/yr) (Figure 15*a*). The calculated Q for the equalized *Braun et al.* viscosity structure is roughly twice that of the strictly pressure- and temperature-dependent solution upstream of the transform (Y > 0 km), but is more than 4 times that of the strictly pressure- and temperature-dependent solution downstream of the transform (at Y ~ -100 km) (Figure 15*b*), suggesting that material is flowing longer distances along-axis for the equalized *Braun et. al.* [2000] viscosity structure. Because more flow can be accommodated at greater depth for the equalized *Braun et al.* [2000] model than the strictly pressure- and temperature-dependent model, the shallow "transform

damming" effect is predicted to be considerably smaller for the equalized *Braun et al.* [2000] viscosity structure.

Clearly, the degree to which transform faults impede along-axis flow is greatly influenced by the choice of 3D viscosity structure. Since the transform cooling effect is greatest at the surface and decreases with depth, transform fault damming is greatest for a viscosity structure in which the depth of minimum viscosity is comparable to lithospheric thickness. Accordingly, the effects of transform damming are predicted to be significant for the *Shen and Forsyth* [1992] curve in Figure 3*a*, where the viscosity minimum occurs at a depth of ~75 km, which is comparable to the thickness of cold lithosphere. In contrast, transforms are unlikely to have a significant effect for the *Ito et al.* [1999] viscosity-depth curve including dehydration, because the entirety of the upper ~110 km of the mantle has high viscosity. In the model of *Ito et al.* [1999], plume material spreads horizontally at depth, and flow is not preferentially channeled along-axis. It is important to note, however, that *Ito et al.* [1999] point out that their calculated dehydration viscosities are somewhat higher than viscosities derived from postglacial rebound and post-seismic deformation studies [*Sigmundsson and Einarsson*, 1992; *Pollitz and Sacks*, 1996]. The comparatively large depth extent of the high-viscosity region in *Ito et al.* [1999] is evident in comparison to the *Braun et al.* [2000] viscosity-depth curve, in which the high-viscosity surface layer is limited to significantly shallower depths (Figure 3*a*).

4.3 Model limitations

Our two-step modeling approach of first calculating 3D viscosity field and second determining mantle material velocity enables us to obtain relatively simple solutions for plume-ridge interactions along a segmented ridge. However, feedback between temperature, viscosity, and velocity fields, which were neglected in the present model, are

expected to change the results quantitatively. For example, flow away from a thermal plume will advect high-temperature material, reducing viscosities and thinning the lithosphere. As the anomalously warm plume material approaches a transform, it is likely that relatively high viscosities near the offset will be reduced, and the transform will experience a form of "thermal erosion" [*Vogt and Johnson*, 1975] that was not considered in the present model. In this way, the transform would present less of a barrier to along-axis flow, and across-transform mantle material flux gradients would decrease. Additional modeling, coupling the temperature, viscosity, and velocity fields, is required to assess the magnitude and importance of these effects.

4.4 Magnitudes of asthenospheric velocities

The results of this study predict that for a pressure gradient $\Delta P/\Delta L$ of 30 kPa/km, the maximum along-axis velocity ranges from ~10 cm/yr (for U = 0.75 cm/yr and L_t = 0 km) to ~20 cm/yr (for U = 7.25 cm/yr and L_t = 0 km). Although such velocities exceed spreading rates, they are consistent with estimations of mantle asthenospheric flow in the vicinity of plumes. South of both Iceland and the Azores, for example, gravity and bathymetry data reveal prominent V-shaped ridges pointing away from the hotspots, which can be inferred to result from hotspot-driven axial mantle flow. *Vogt* [1971a, b] and *White et al.* [1995] estimate along-axis propagation rates for the V-shaped ridges along the Reykjanes Ridge to be 7.5 – 20 cm/yr. Similarly, *Cannat et al.* [1999] infer an along-axis propagation rate of 6 cm/yr for Azores V-shaped ridges. However, a number of factors make it difficult to compare exactly the model-predicted along-axis velocities and the asthenospheric velocity estimated for Iceland and the Azores, including uncertainties in the pressure gradients, more complex ridge geometry than was assumed in the modeling, and the possibility of time-dependent plume flux. Nevertheless, the estimates of along-axis

velocity by *Vogt* [1971a, b], *White et al.* [1995], and *Cannat et al.* [1999] are of the same magnitude as our modeling results. Similarly, *Conder et al.* [2000b] estimated asthenospheric velocities of 17-30 cm/yr from the Pacific superswell to the EPR, a range which overlaps our maximum velocity prediction for U = 7.25 cm/yr.

Further constraints on the magnitude of asthenospheric velocity, albeit not driven by a hotspot plume, may be derived from studies of other tectonic settings including the Australian-Antarctic Discordance (AAD). The AAD is associated with unusually cool mantle, which may give rise to horizontal thermal gradients that drive mantle flow toward the discordance (*West et al.* [1997], and references therein). Investigations of the migration rate of geochemical boundaries [*Pyle et al.,* 1992; 1995], off-axis V-shaped discontinuities [*Marks et al.,* 1990; 1991], and propagating ridges [*Phipps Morgan and Sandwell*, 1994; *Sempéré et al.*, 1997; *West et al.*, 1999], as well as numerical models [*West et al.*, 1997] all suggest that the asthenospheric flow velocities towards the AAD are approximately 1.5–4.5 cm/yr. These velocities are of the same magnitude as the predictions of this study.

5. Discussion: Implications for Plume-Ridge Interactions

5.1 Ultra-slow spreading Southwest Indian Ridge/Marion plume

The results of this modeling may be used to explore how ridge segmentation affects the along-axis length of plume-related geochemical or geophysical anomalies, or waist width W. For example, the ultra-slow spreading SWIR is highly segmented in the vicinity of the Marion hotspot (Figure 1*a*). Based on bathymetric and gravity anomalies, *Georgen et al.* [2001] suggest that the along-axis influence of the Marion hotspot is most prominent between the Andrew Bain and Discovery II FZs (Figure 1*a*). Andrew Bain FZ is among

the world's longest transform offsets, with a length of ~720 km, and Discovery II FZ is a dual fracture zone system with a combined offset of approximately 350 km.

To apply the numerical results obtained in this study to the SWIR, we assume that plume-related material flows in a narrow channel [e.g., *Morgan*, 1978; *Yale and Phipps Morgan*, 1998] between Marion Island and roughly the location of the Eric Simpson FZ system, and then disperses along-axis to both sides of the Eric Simpson FZ [*Vogt*, 1971a, 1976; *Sleep*, 1996]. To the east, the first fracture zone encountered by along-axis flow is Discovery II. According to Figure 10*a*, for an offset of length L_t = 250 km with U = 0.75 cm/yr, the along-axis flux at the Discovery II would be reduced by at least 40% compared to the case with no transform offset. Within a distance of 100 km beyond the transform, Q is predicted to diminish to 0% (Figure 10*a*). Therefore, modeling results predict that the along-axis geophysical expression of the Marion plume would terminate in the vicinity of the Discovery II FZ, consistent with the interpretation of *Georgen et al.* [2001].

5.2 Slow-spreading Reykjanes Ridge/Iceland plume

In contrast to the SWIR, and despite its slow spreading rate, the Mid-Atlantic Ridge south of Iceland has few significant offsets until the Charlie Gibbs FZ more than 1000 km away from the plume center (Figure 1*b*). Results of this study predict that the Bight FZ, with L_t ~ 20 km, should have negligible effect on along-axis material transport away from the Iceland plume. However, the Charlie Gibbs FZ has more significant offset (L_t = 350 km). Critical to determining to what extent the Gibbs FZ diminishes along-axis mantle material flow is knowledge of how far along the Reykjanes Ridge plume-driven flux travels. As noted previously, Icelandic pressure gradients may be on the order of 50-200 kPa/km. Extrapolation of our results to these pressure gradients suggests plume influence in the range of 300 km (for 50 kPa/km) to 1270 km (for 200 kPa/km) along-axis from the

plume center. A pressure gradient of 50 kPa/km, therefore, is not sufficient to drive along-axis flux far enough along the Reykjanes Ridge to reach the Gibbs FZ. In contrast, plume material should reach the vicinity of the Gibbs FZ for pressure gradients in the range of 200 kPa/km. If the Iceland pressure gradient is such that plume material flows to the latitude of the Gibbs FZ, the results of Figure 10*b* suggest that the 350 km offset should be sufficient to block any remaining along-axis mantle material flow.

5.3 Intermediate-spreading Cocos-Nazca Spreading Center/Galapagos plume

Using bathymetric and gravity anomalies, *Ito et al.* [1997] propose that the along-axis influence of the Galapagos plume extends from approximately 86°W to 95°W, centered roughly on the 91°W FZ, an along-axis distance of ~1000 km. Since all offsets of the CNSC in the immediate vicinity of the Galapagos plume are only of 20-30 km length (Figure 1*c*), model results of Figure 10*c* predict it is unlikely that these small ridge discontinuities exert any significant influence on plume-driven axial flow. Similarly, investigations of axial magnetization intensity along the CNSC [*Wilson and Hey*, 1995] suggest that small, 20-30 km offsets do not block along-axis flow. Thus the location of the western end of the Galapagos anomaly may reflect natural plume dissipation, without significant effects of transform damming.

Meanwhile, the eastern end of the Galapagos anomaly at ~86°W may be the combined result of dissipation and the damming effect of two closely spaced transform faults, Inca and Ecuador, with offset lengths of 110 km and 160 km, respectively. Although our modeling results predict little flux reduction for $L_t < 150$ km for U = 3.0 cm/yr, these results were obtained for a transform fault 250 km away from the plume driving force. Since the Inca and Ecuador offsets are located ~500 km away from the Galapagos plume,

close to the plume's natural termination from dissipation effects, perhaps these relatively short offsets are sufficient to block already significantly diminished plume-driven flow.

For a given spreading rate the plan view shape of the high-velocity region changes as spreading rate is increased (Figure 6). For small transform offsets which have relatively little effect on axial flux, the downstream termination of the high-velocity region forms a rather pointed V-shape (Figure 6*d*), reflecting gradual along-axis velocity dissipation. However, for larger offsets, material ponds upstream of the transform, resulting in a smoother, blunter, U-shaped stagnation curve (Figure 6*e*). The relatively U-shaped bathymetric anomaly termination near the Inca FZ, compared to the sharper, more V-shaped termination to the west of the Galapagos plume (Figure 1*c*), may reflect blockage of Galapagos-driven asthenospheric flow by the Inca FZ.

Our extrapolated model results predict that, for U = 3.0 cm/yr, a waist width of ~1000 km requires an along-axis pressure gradient of approximately 75 kPa/km. Translating this pressure gradient into an axial thermal anomaly yields $\Delta T = 75°C$, consistent with the upper bound of an estimate (50±25°C) by *Ito and Lin* [1995b] based on bathymetry and gravity data. However, more recent data for the CNSC, which combines bathymetric, gravity, and seismic constraints, suggest that the present-day Galapagos axial thermal anomaly is closer to 30-40°C [*Canales et al.*, 2000].

5.4 Plume waist width

Results of this study predict that long transform offsets along ultra-slow spreading ridges may strongly localize along-axis plume anomalies and thus decrease the plume width W relative to the case of an unsegmented ridge. Numerical [*Ribe et al.*, 1995; *Ito et al.*, 1996] and laboratory modeling [*Feighner and Richards*, 1995] suggests that steady-state waist width W scales as $W \sim c_o(Q_v/2U)^{1/2}$, where Q_v is plume volume flux and c_o is a

scaling coefficient between 1.77 and 2.12, predicting W increases with decreasing spreading rate U. These studies, however, considered only unsegmented ridges and did not take into account the effects of transform offsets. In contrast, our modeling results suggest the additional relationship that in the presence of a transform offset, W should be reduced more for a slow-spreading than a fast-spreading ridge, predicting W to decrease with U for the same L_t.

The geometric differences between segmented and unsegmented ridges are illustrated in Figure 16. We assume that two plumes, plume 1 and plume 2, have the same flux, and interact with an unsegmented and segmented ridge, respectively. Because along-axis flux is limited by transforms along the segmented ridge, the apparent waist width W_2 for plume 2 will be less than the waist width W_1 for plume 1. Similarly, the flux inferred from waist width for plume 2 will be an underestimate.

6. Conclusions

The results from this study indicate that transform faults affect along-axis mantle material flow in two important ways:

(1) Transform faults reduce along-axis flux. The amount of across-transform flux reduction increases with increasing transform offset and decreasing spreading rate.

(2) Transforms deflect shallow asthenospheric along-axis flow toward the direction of the next ridge segment. This effect is predicted to be enhanced as spreading rate decreases and transform offset increases. This is because the along-axis flow channel defined by low viscosities at the ridge is broader and deviates less from linear for fast-spreading than slow-spreading ridges.

The degree to which transforms affect along-axis asthenospheric flux is sensitive to viscosity structure. The transform damming effect is most pronounced for strictly pressure- and temperature-dependent viscosity, because most flow occurs in a region of low-viscosity at ~75 km depth, approximately the thickness of cold lithosphere. However, transform damming effects could be reduced for viscosity structures which additionally consider the effects of melting, dehydration, and change in deformation mechanism, since such viscosity structures may result in a thick, high-viscosity layer extending to depths greater than lithospheric thickness.

Flows along slower-spreading ridges are predicted to be more sensitive to transform offsets than those along faster-spreading ridges. For a given increase in transform offset, flux across a transform decreases significantly more for ultra-slow spreading rates than fast-spreading ridges. Transform offsets in slow-spreading, highly-segmented ridge environments, therefore, are likely to greatly limit the along-axis dispersion of plume material, resulting in the prediction of an inverse relationship between spreading rate and plume waist width. This prediction is considerably different than those from conventional models based on fluid dynamics of a plume interacting with a straight, unsegmented ridge.

Acknowledgments: We are grateful to Yang Shen for providing computational programs for calculating ridge temperature and viscosity structure and to Mike Braun for providing results of viscosity calculations. This work benefited from discussions with G. Ito, J. Escartin, B. West, Y. Shen, M. Braun, S. Stein, B. Tucholke, M. Behn, and R. Detrick. This work is supported by NSF grants OCE-9811924 and OCE-9907630. Woods Hole Oceanographic Institution contribution number 10487.

References

Bathe, K-J., Finite element procedures, 1037 pp., Prentice Hall, Upper Saddle River, NJ, 1996.

Braun, M.G., G. Hirth, and E.M. Parmentier, The effects of deep damp melting on mantle flow and melt generation beneath mid-ocean ridges, *Earth Planet. Sci. Lett.,* 176, 339-356, 2000.

Canales, J.P., G. Ito, R. Detrick, J. Sinton, T. Blacic, M. Behn, and J. Lin, Origin of the Galapagos swell: Bathymetry, gravity, and seismic constraints along the Galapagos Spreading Center, *EOS Trans. AGU*, 81, F1095, 2000.

Cannat, M., A. Briais, C. Deplus, J. Escartín, J. Georgen, J. Lin, S. Mercouriev, C. Meyzen, M. Muller, G. Pouliquen, A. Rabain, and P. da Silva, Mid-Atlantic Ridge-Azores hotspot interactions: Along-axis migration of a hotspot-derived event of enhanced magmatism 10 to 4 Ma ago, *Earth Planet. Sci. Lett.,* 173, 257-269, 1999.

Conder, J.A., D.S. Scheirer, and D.W. Forsyth, Seafloor spreading on the Amsterdam-St. Paul hotspot plateau, *J .Geophys. Res.,* 105, 8263-8277, 2000a.

Conder, J.A., Tectonics and plate boundary processes along the Southeast Indian Ridge and East Pacific Rise, Ph.D. dissertation, 171 pp., Brown Univ., Providence, 2000b.

Douglass, J., J.-G. Schilling, R.H. Kingsley, and C. Small, Influence of the Discovery and Shona mantle plumes on the southern Mid-Atlantic Ridge: Rare earth evidence, *Geophys. Res. Lett.,* 22, 2893-2896, 1995.

Feighner, M.A. and M.A. Richards, The fluid dynamics of plume-ridge and plume-plate interactions: an experimental investigation, *Earth Planet. Sci. Lett.,* 129, 171-182, 1995.

Georgen, J.E., J. Lin, and H.J.B. Dick, Evidence from gravity anomalies for interactions of the Marion and Bouvet hotspots with the Southwest Indian Ridge: Effects of transform offsets, *Earth Planet. Sci. Lett.*, in press 2001.

Hirth, G. and D.L. Kohlstedt, Experimental constraints on the dynamics of the partially molten upper mantle: Deformation in the diffusion creep regime, *J. Geophys. Res.,* 100, 1981-2001, 1995a.

Hirth, G. and D.L. Kohlstedt, Experimental constraints on the dynamics of the partially molten upper mantle 2. Deformation in the dislocation creep regime, *J. Geophys. Res.*, 100, 15,441-15,449, 1995b.

Hirth, G. and D.L. Kohlstedt, Water in the oceanic upper mantle: implications for rheology, melt extraction and the evolution of the lithosphere, *Earth Planet. Sci. Lett.,* 144, 93-108, 1996.

Ito, G. and J. Lin, Oceanic spreading center-hotspot interactions: Constraints from along-isochron bathymetric and gravity anomalies, *Geology,* 7, 657-660, 1995a.

Ito, G. and J. Lin, Mantle temperature anomalies along the present and paleoaxes of the Galapagos spreading center as inferred from gravity analyses, *J. Geophys. Res.,* 100, 3733-3745, 1995b.

Ito, G., J. Lin, and C.W. Gable, Dynamics of mantle flow and melting at a ridge-centered hotspot: Iceland and the Mid-Atlantic Ridge, *Earth Planet. Sci. Lett.,* 134, 155-168, 1995.

Ito, G., J. Lin, and C.W. Gable, Interaction of mantle plumes and migrating mid-ocean ridges: Implications for the Galapagos plume-ridge system, *J. Geophys. Res.,* 102, 15,403-15,417, 1997.

Ito, G., Y. Shen, G. Hirth, and C.J. Wolfe, Mantle flow, melting, and dehydration of the Iceland mantle plume, *Earth Planet. Sci. Lett.,* 165, 81-96, 1999.

Jancin, M.K., D. Young, B. Voight, J.L. Aronson, and K. Sæmundsson, Stratigraphy and K/Ar ages across the west flank of the northeast Iceland axial rift zone, in relation to the 7 Ma volcano-tectonic reorganization of Iceland, *J. Geophys. Res.,* 90, 9961-9985, 1985.

Lin, J., and J. Phipps Morgan, The spreading rate dependence of three-dimensional mid-ocean ridge gravity structure, *Geophys. Res. Lett.*, 19, 13-16, 1992.

Macdonald, K. C., Mid-ocean ridges: Fine scale tectonic, volcanic, and hydrothermal processes within the plate boundary zone, *Annu. Rev. Earth Planet. Sci.,* 10, 155-190, 1982.

Marks, K.M., P.R. Vogt, and S.A. Hall, Residual depth anomalies and the origin of the Australian-Antarctic Discordance zone, *J. Geophys. Res.,* 95, 17,325-17,338, 1990.

Marks, K.M., D.T. Sandwell, P.R. Vogt, and S.A. Hall, Mantle downwelling beneath the Australian-Antarctic Discordance zone: Evidence from geoid height versus topography, *Earth Planet. Sci. Lett,* 103, 325-338, 1991.

Morgan, W.J., Rodriguez, Darwin, Amsterdam, ..., A second type of hotspot island, *J. Geophys. Res.,* 83, 5355-5360, 1978.

Pollitz, F.F. and I.S. Sacks, Viscosity structure beneath northeast Iceland, *J. Geophys. Res.,* 101, 17,771-17,793, 1996.

Phipps Morgan, J. and D.T. Sandwell, Systematics of ridge propagation south of 30 degrees S, *Earth Planet. Sci. Lett.,* 121, 245-258, 1994.

Pyle, D.G., D.M. Christie, and J.J. Mahoney, Resolving an isotopic boundary within the Australian-Antarctic Discordance, *Earth Planet. Sci. Lett.,* 112, 161-178, 1992.

Pyle, D.G., D.M. Christie, and J.J. Mahoney, Geochemistry and geochronology of ancient southeast Indian and southwest Pacific seafloor, *J. Geophys. Res.,* 100, 22,261-22,282, 1995.

Ribe, N.M., U.R. Christensen, and J. Theißing, The dynamics of plume-ridge interaction, 1: Ridge-centered plumes, *Earth Planet. Sci. Lett.,* 134, 155-168, 1995.

Sæmundsson, K., Evolution of the axial rifting zone in northern Iceland and the Tjörnes fracture zone, *Geol. Soc. Am. Bull.,* 85, 495-504, 1974.

Sigmundsson, F. and P. Einarsson, Glacio-isostatic crustal movements caused by historical volume changes of the Vatnajokull ice cap, Iceland, *Geophys. Res. Lett.,* 19, 2123-2126, 1992.

Sempéré, J.-C., J.R. Cochran, and the SEIR scientific team, The Southeast Indian Ridge between 88°E and 118°E: Variations in crustal accretion at constant spreading rate, *J. Geophys. Res.,* 102, 15,489-15,505, 1997.

Schilling, J.-G., Fluxes and excess temperatures of mantle plumes inferred from their interaction with migrating mid-ocean ridges, *Nature,* 352, 397-403, 1991.

Schouten, H, K.D. Klitgord, and J.A. Whitehead, Segmentation of mid-ocean ridges, *Nature,* 317, 225-229, 1985.

Shen, Y. and D.W. Forsyth, The effects of temperature- and pressure-dependent viscosity on three-dimensional passive flow of the mantle beneath a ridge-transform system, *J. Geophys. Res.,* 97, 19,717-19,728, 1992.

Sleep, N.H., Lateral flow of hot plume material ponded at sublithospheric depths, *J. Geophys. Res.*, 101, 28,065-28,083, 1996.

Vogt, P.R., Asthenosphere motion recorded by the ocean floor south of Iceland, *Earth Planet. Sci. Lett.,* 13, 153-160, 1971a.

Vogt, P.R., Asthenosphere motions recorded by the ocean floor south of Iceland, *EOS, Trans. AGU,* 52, 352, 1971b.

Vogt , P.R. and G. L. Johnson, Transform faults and longitudinal flow below the midoceanic ridge, *J. Geophys. Res.,* 80, 1399-1428, 1975.

Vogt, P.R., Plumes, subaxial pipe flow, and topography along the mid-oceanic ridge, *Earth Planet. Sci. Lett.,* 29, 309-325, 1976.

West, B.P., W.S.D. Wilcock, J.-C. Sempéré, and L. Géli, Three-dimensional structure of asthenospheric flow beneath the Southeast Indian Ridge, *J. Geophys. Res.,* 102, 7783-7802, 1997.

West, B.P., J. Lin, and D.M. Christie, Forces driving ridge propagation, *J. Geophys. Res.,* 104, 22,845-22,858, 1999.

White, R.S., J.W. Bown, and J.R. Smallwood, The temperature of the Iceland plume and origin of outward propagating V-shaped ridges, *J. Geol. Soc. London.,* 152, 1039-1045, 1995.

Wilson, D.S. and R.N. Hey, History of rift propagation and magnetization intensity for the Cocos-Nazca spreading center, *J. Geophys. Res.,* 100, 10,041-10,056, 1995.

Yale, M.M. and J. Phipps Morgan, Asthenosphere flow model of hotspot-ridge interactions: a comparison of Iceland and Kerguelen, *Earth Planet. Sci. Lett.,* 161, 45-56, 1998.

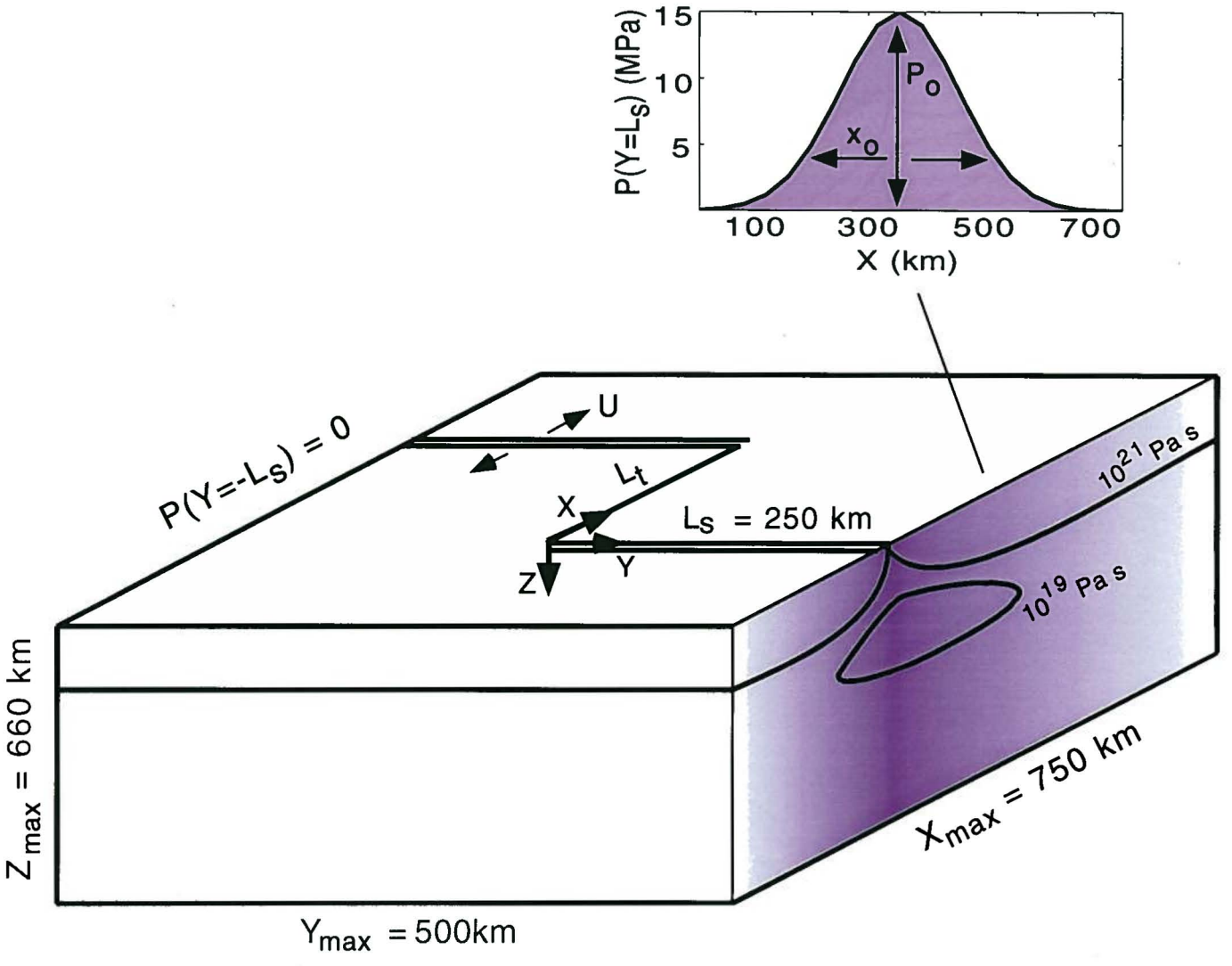
P(Y=Ls) (MPa)
15
10
5
Po
xo
100
300
500
700
X (km)
P(Y=-Ls) = 0
U
Lt
X
Ls = 250 km
Z
Y
10^21 Pa s
10^19 Pa s
Zmax = 660 km
Xmax = 750 km
Ymax = 500km

Figure 2

Table 1: Model Parameters

Variable	Meaning	Value	Units
E	Activation energy	520	kJ/mol
V	Activation volume	10×10^{-6}	m^3/mol
n	Stress exponent	1	
η_{min}	Minimum viscosity	10^{19}	Pa s
ρ	Mantle density	3300	kg/m^3
g	Gravitational acceleration	9.8	m/s^2
$\mathbf{g}$	Gravity vector		
R	Universal gas constant	8.3144	J/mol·K
$T_{z=0}$	Surface temperature	0	℃
$T_{z=200\ km}$	Mantle temperature	1350	℃
α	Thermal diffusivity	10^{-6}	m^2/s
X	Distance in spreading direction		km
X_{max}	Box length, spreading direction	750	km
Y	Along-axis distance		km
Y_{max}	Box length, along-axis direction	500	km
Z	Depth below surface		km
Z_{max}	Box depth	660	km
L_s	Segment length	250	km
L_t	Transform length	0, 50, 100, 150, 200, 250	km
U	Half-spreading rate	0.75, 1.25, 3.0, 7.25	cm/yr
$\mathbf{v}$	Velocity vector		cm/yr
v_x	Velocity in spreading direction		cm/yr
v_y	Along-axis velocity		cm/yr
v_z	Vertical velocity		cm/yr
Q	Along-axis volumetric flux		km^3/yr
P	Pressure		Pa
P_o	Maximum pressure at $Y=L_s$	15	MPa
x_o	Pressure Gaussian length	100	km

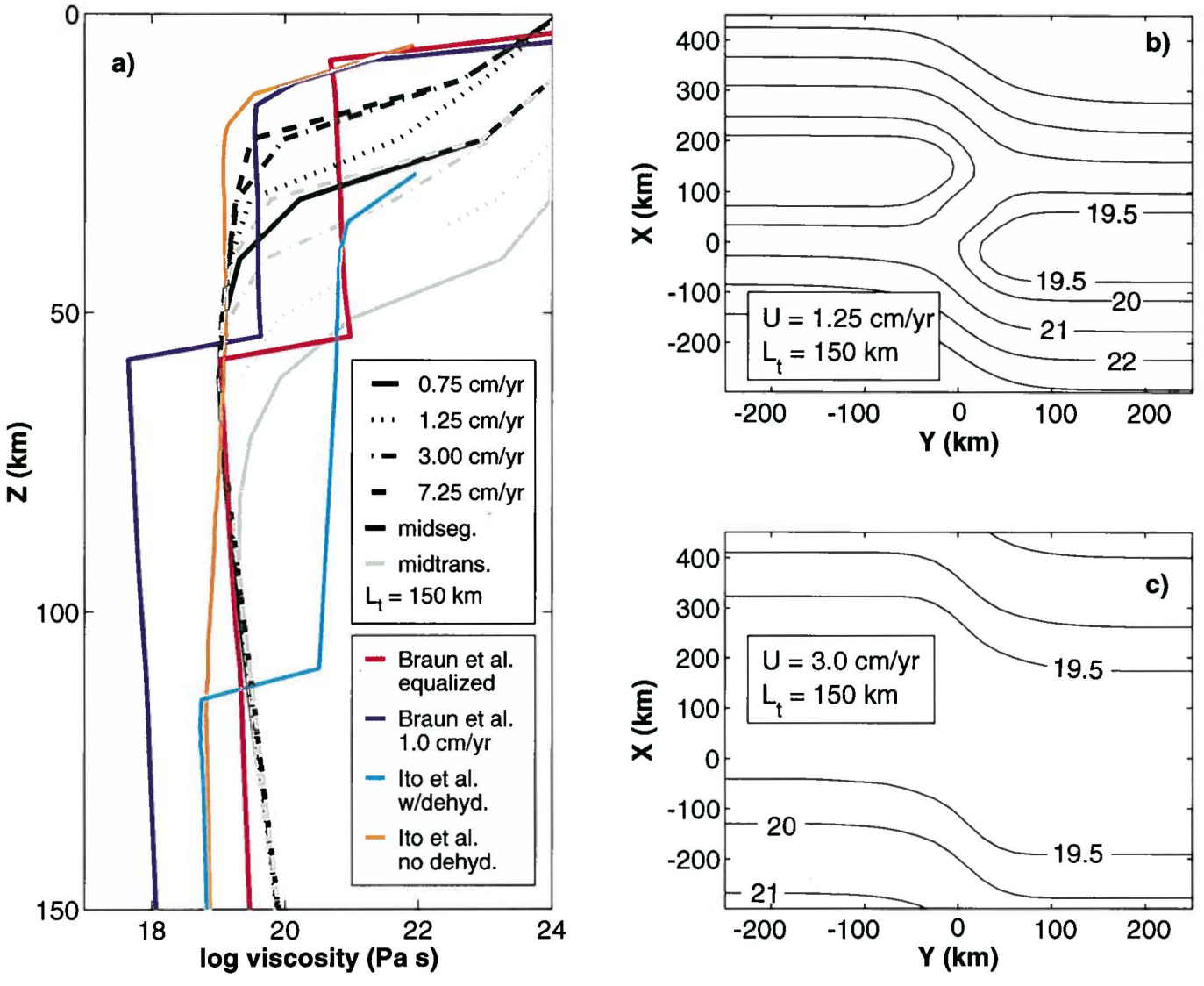
a)
b)
c)
Z (km)
log viscosity (Pa s)
0
50
100
150
18
20
22
24
0.75 cm/yr
1.25 cm/yr
3.00 cm/yr
7.25 cm/yr
midseg.
midtrans.
L_t = 150 km
Braun et al. equalized
Braun et al. 1.0 cm/yr
Ito et al. w/dehyd.
Ito et al. no dehyd.
X (km)
Y (km)
400
300
200
100
0
-100
-200
-200
-100
0
100
200
U = 1.25 cm/yr
L_t = 150 km
19.5
19.5
20
21
22
U = 3.0 cm/yr
L_t = 150 km
19.5
20
19.5
21

Figure 3

Figure 1: a) Bathymetric map of the Southwest Indian Ridge in the vicinity of the Marion plume, with depths less than 3 km shaded. Fracture zones abbreviations are AB = Andrew Bain FZ, M = Marion FZ, PE = Prince Edward FZ, ES = Eric Simpson FZ, and DII = Discovery II FZ. Transform offset lengths are indicated in km, rounded to the nearest 10 km. Contours are drawn at 1.5, 3.0, and 4.5 km depth, and a half-spreading rate of 0.8 cm/yr is indicated. b) Bathymetry of the Reykjanes Ridge in the northern Atlantic Ocean, south of Iceland. CG = Charlie Gibbs FZ and B = Bight FZ. Half-spreading rate is 1.0 cm/yr. Contours are drawn at 1, 2.5, and 4 km depth, and regions with depths shallower than 2.5 km are shaded. c) Bathymetry of the Cocos-Nazca spreading center near the Galapagos plume. Contours mark 1.8, 2.8, and 3.8 km depth, and seafloor shallower than 2.8 km is shaded. IN = Inca FZ and EC = Ecuador FZ. Insets show blow-ups of the inferred eastern and western termination of the Galapagos plume axial bathymetric anomaly.

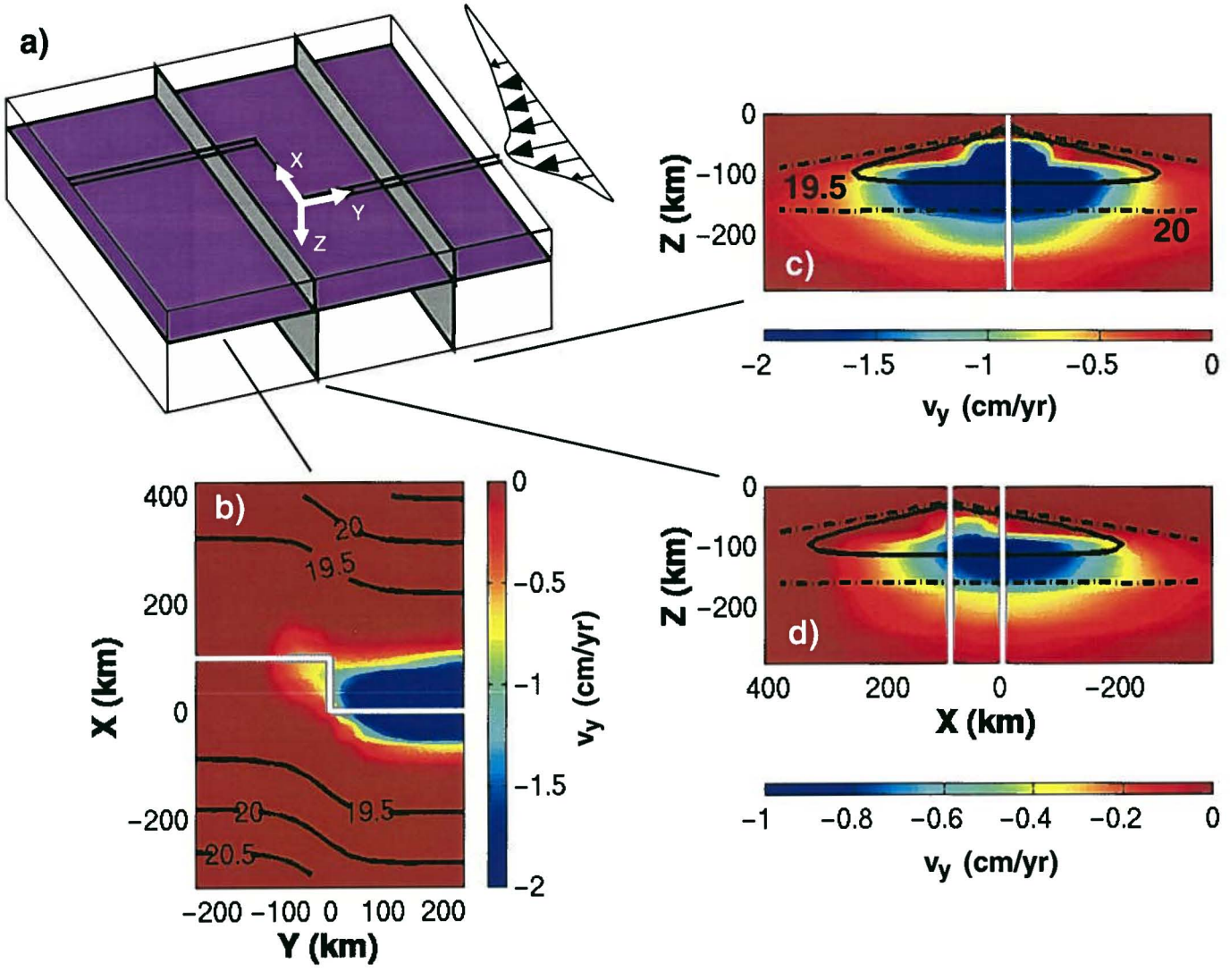
a)
X
Y
Z
b)
20
19.5
20
19.5
20.5
400
200
0
−200
X (km)
−200 −100 0 100 200
Y (km)
0
−0.5
−1
−1.5
−2
v_y (cm/yr)
c)
19.5
20
0
−100
−200
Z (km)
−2 −1.5 −1 −0.5 0
v_y (cm/yr)
d)
0
−100
−200
Z (km)
400 200 0 −200
X (km)
−1 −0.8 −0.6 −0.4 −0.2 0
v_y (cm/yr)

Figure 4

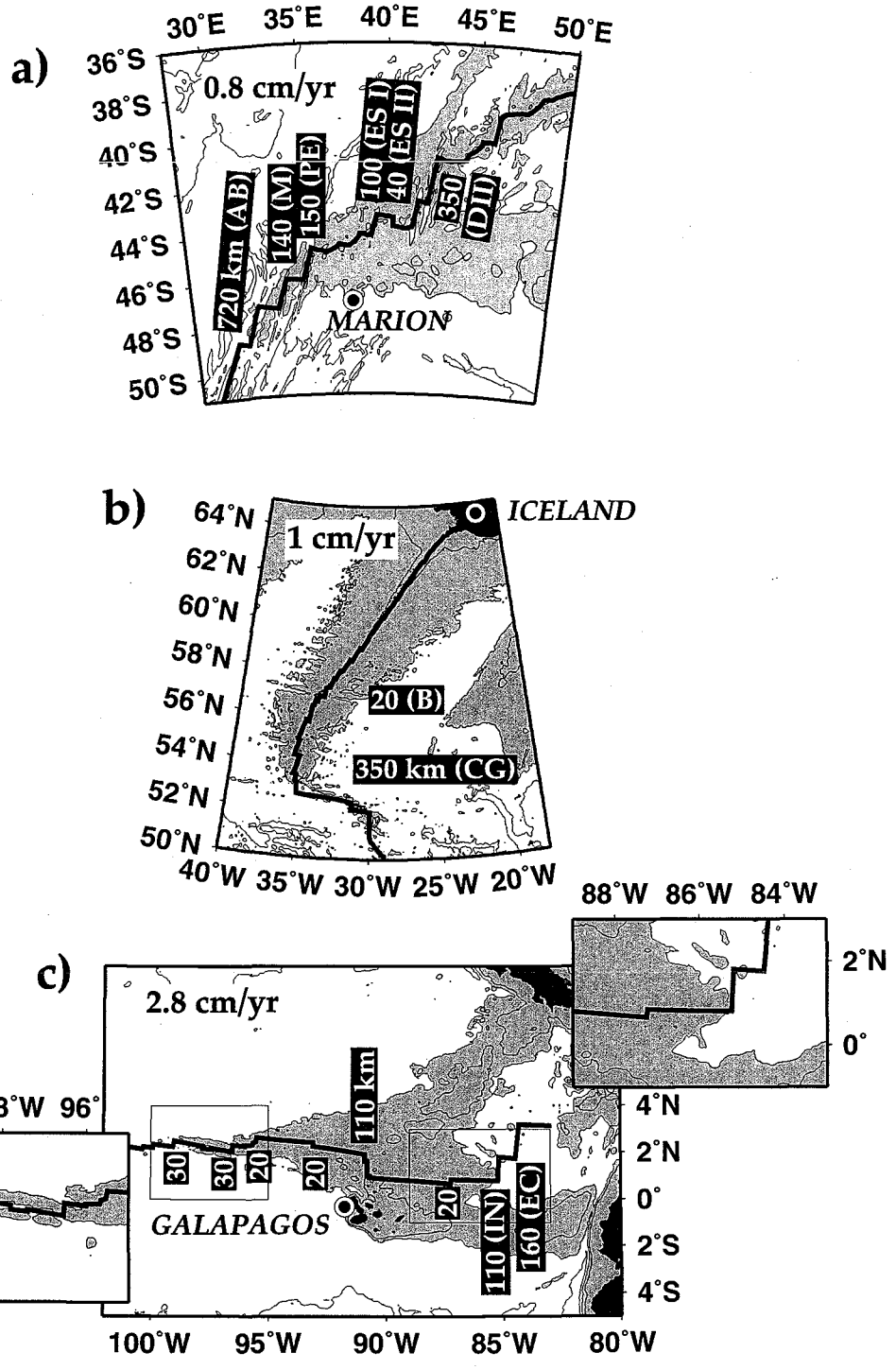
a)
30°E 35°E 40°E 45°E 50°E
36°S
38°S
40°S
42°S
44°S
46°S
48°S
50°S
0.8 cm/yr
720 km (AB)
140 (M)
150 (PE)
100 (ES I)
40 (ES II)
350
(DII)
MARION
b)
64°N
62°N
60°N
58°N
56°N
54°N
52°N
50°N
40°W 35°W 30°W 25°W 20°W
1 cm/yr
ICELAND
20 (B)
350 km (CG)
c)
88°W 86°W 84°W
2°N
0°
2.8 cm/yr
110 km
100° 98°W 96°
4°N
2°N
0°
30
30
20
20
20
110 (IN)
160 (EC)
GALAPAGOS
4°N
2°N
0°
2°S
4°S
100°W 95°W 90°W 85°W 80°W

Figure 1

Figure 2: Set-up of the model domain. Two ridge segments, indicated by double lines and each of length L_s = 250 km, are offset by a transform fault of length L_t. Our experiments examine L_t ranging from 0 km to 250 km in increments of 50 km. For a given L_t, half-spreading rate, U, is set equal to 0.75, 1.25, 3.0, or 7.25 cm/yr in the numerical experiments. The model box is X_{max} = 750 km in the spreading direction, Y_{max} = 500 km in the along-axis direction, and Z_{max} = 660 km in depth. A pressure gradient is imposed by applying $P(x) = P_o \exp(-0.5* (X/x_o)^2) / (2\pi)^{1/2}x_o$ at $Y = L_s$ and $P = 0$ at $Y = -L_s$. This pressure gradient drives viscous flow. As shown by shading, the spatial distribution of pressure follows a Gaussian distribution, with maximum amplitude P_o = 15 MPa at the ridge and standard deviation width x_o = 100 km. The locations of the 10^{19} Pa s and 10^{21} Pa s viscosity contours are schematically indicated. Other boundary conditions are zero shear stress at Z = 0 km and $Z = Z_{max}$, $v_z = 0$ at $Z = Z_{max}$, and zero normal stress at Z = 0 km. In calculating viscosity structure, temperature is set to be 0°C at Z = 0 km and 1350°C at Z = 200 km.

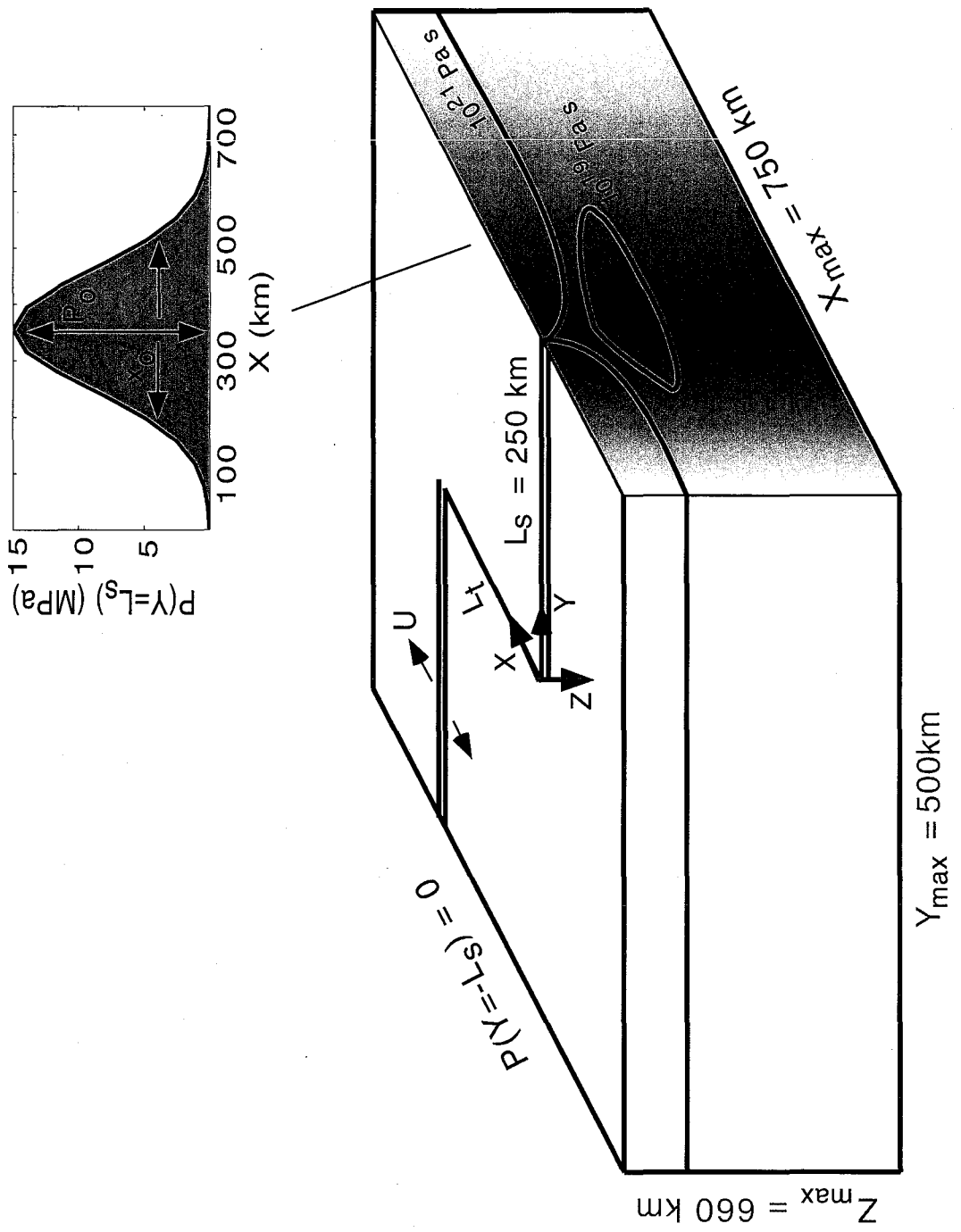
P(Y=Ls) (MPa)
15
10
5
100
300
500
700
X (km)
Xmax = 750 km
Ls = 250 km
Lt
U
X
Y
Z
P(Y=-Ls) = 0
Zmax = 660 km
Ymax = 500km

Figure 2

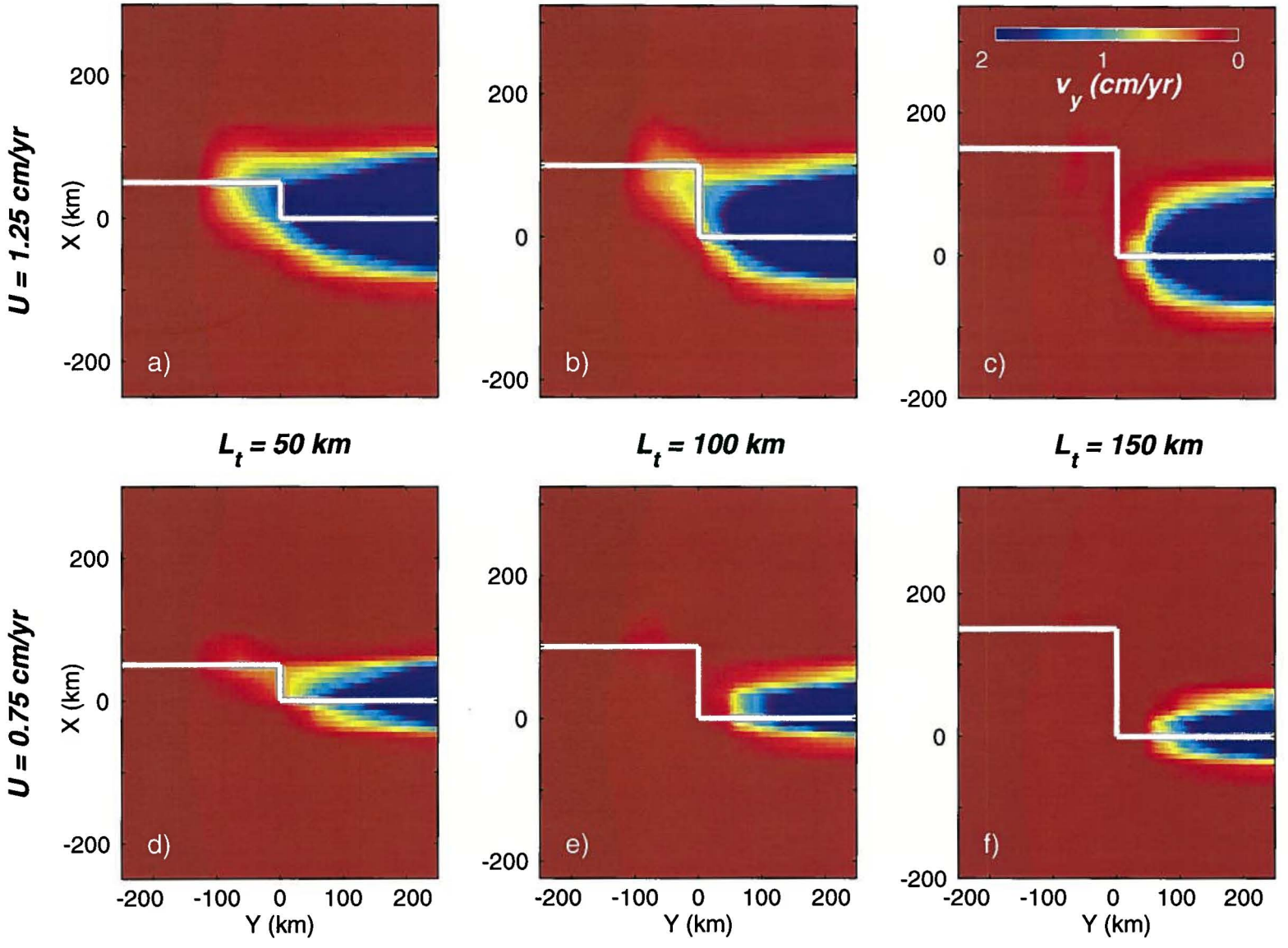
U = 1.25 cm/yr
U = 0.75 cm/yr
L_t = 50 km
L_t = 100 km
L_t = 150 km
v_y (cm/yr)
2
1
0
X (km)
Y (km)
200
0
-200
-100
100
a)
b)
c)
d)
e)
f)

Figure 6

Figure 3: a) Viscosity-depth profiles, using pressure- and temperature-dependent viscosity [*Shen and Forsyth*, 1992], for the top 150 km of the model space (black and gray lines). Profiles for L_t = 150 km are given for each of the four spreading rates (U = 0.75, 1.25, 3.0, and 7.25 cm/yr) at mid-segment and mid-transform. Additional profiles (colored lines) show viscosity-depth profiles from other modeling studies. The profile labeled "Braun et al. equalized" (red line) shows a mid-segment profile for U = 3.0 cm/yr when the effects of not only pressure and temperature but also dehydration, melting, and deformation mechanism are considered [*Braun et al.*, 2000]. *Braun et al.* [2000] assume a mantle potential temperature of 1350°C at 660 km and a reference viscosity of $5x10^{18}$ Pa s at a depth of approximately 115 km. Note that the *Braun et al.* [2000] solution predicts a high-viscosity lid extending to depths of ~70 km, the transition from dry to damp melting. In contrast, *Ito et al.* [1999], who also consider the effects of dehydration on viscosity, place the boundary of wet and dry melting at approximately 110 km (blue curve). The *Ito et al.* [1999] viscosity-depth profile is taken through the center of a ridge-centered plume. Mantle potential temperature was assumed to be 1530°C for Z > 240 km, half-spreading rate was 0.95 cm/yr, and viscosity was $3.5x10^{19}$ Pa s at 200 km depth. For comparison, the *Ito et al.* [1999] viscosity-depth profile without dehydration is plotted in orange. b) Viscosity slice at Z = 43 km for U= 1.25 cm/yr and L_t = 150 km. Viscosity contours are in Pa s. c) Same as in panel b), but for U = 3.0 cm/yr.

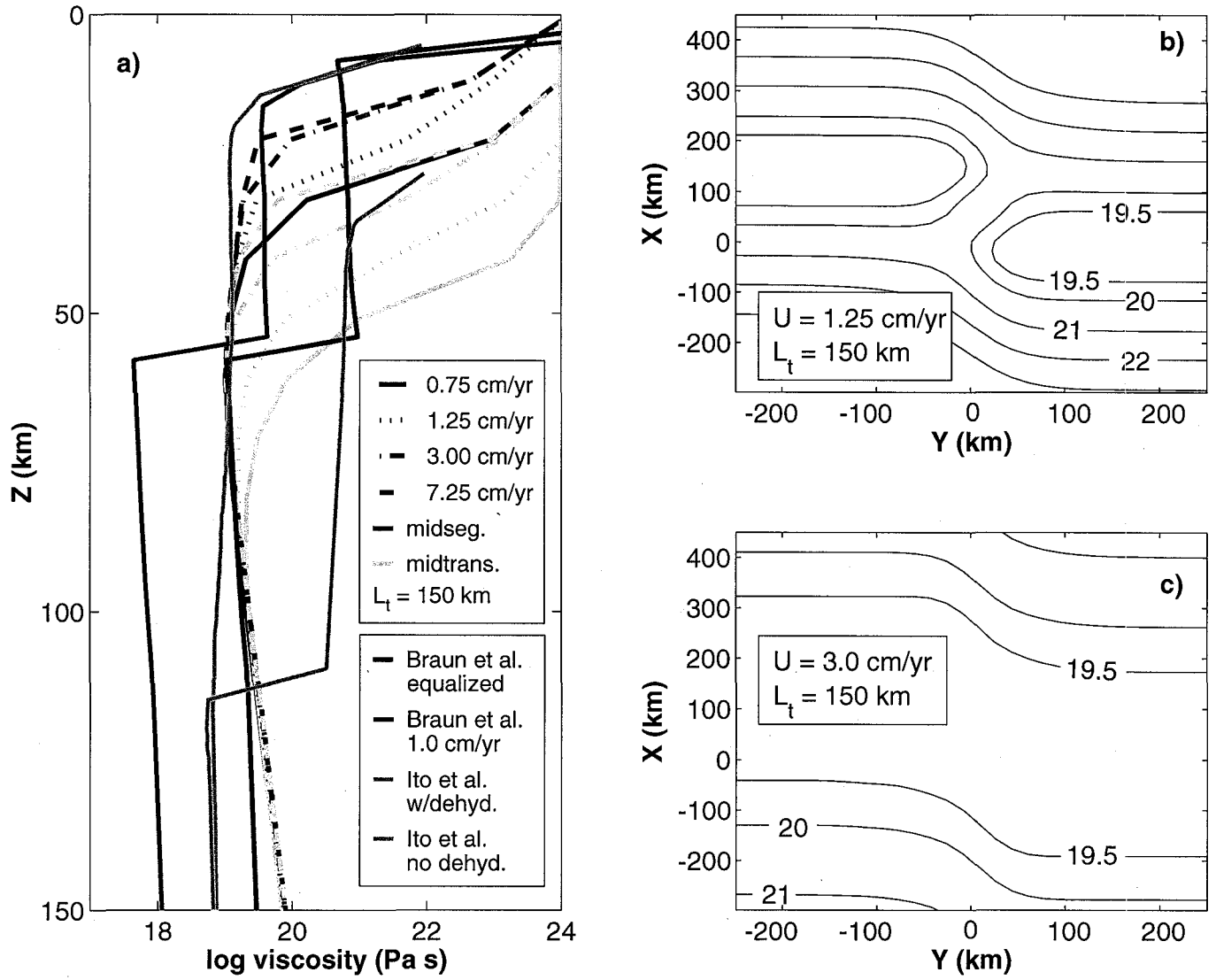
a)
Z (km)
log viscosity (Pa s)
0.75 cm/yr
1.25 cm/yr
3.00 cm/yr
7.25 cm/yr
midseg.
midtrans.
L_t = 150 km
Braun et al. equalized
Braun et al. 1.0 cm/yr
Ito et al. w/dehyd.
Ito et al. no dehyd.
b)
X (km)
Y (km)
U = 1.25 cm/yr
L_t = 150 km
19.5
20
21
22
c)
U = 3.0 cm/yr
L_t = 150 km

Figure 3

Figure 4: a) Sketch of the model domain, with ridges indicated as double lines and the positions of slices in panels b, c, and d shown as purple and gray-shaded planes. The magnitude of the plume driving pressure is schematically shown with arrows of varying lengths. Calculations are for U = 1.25 cm/yr and L_t = 100 km. b) Slice of v_y at Z = 72 km. Contours show viscosity of $10^{19.5}$, 10^{20}, and $10^{20.5}$ Pa s. Note that the high-velocity region (blue color) curves as it encounters the transform fault. c) Across-axis slice of v_y at Y = 125 km. Black dot-dash contour delineates $\eta = 10^{20}$ Pa s and solid black contour shows the position of $\eta = 10^{19.5}$ Pa s. The position of the ridge axis for Y > 0 km is marked by a thick white and gray vertical line at X = 0 km. Note that the high-velocity region is centered about the ridge axis. d) Across-axis slice of v_y at Y = -50 km. Viscosity contours are as in b. The vertical white and gray lines at X = 100 km and 0 km indicate the position of the ridge axis for Y < 0 km and Y > 0 km, respectively. Note that color scale is different from that used in panel b. Also note that the shallowest high-velocity region does not coincide with the location of either ridge axis, but instead falls in between them.

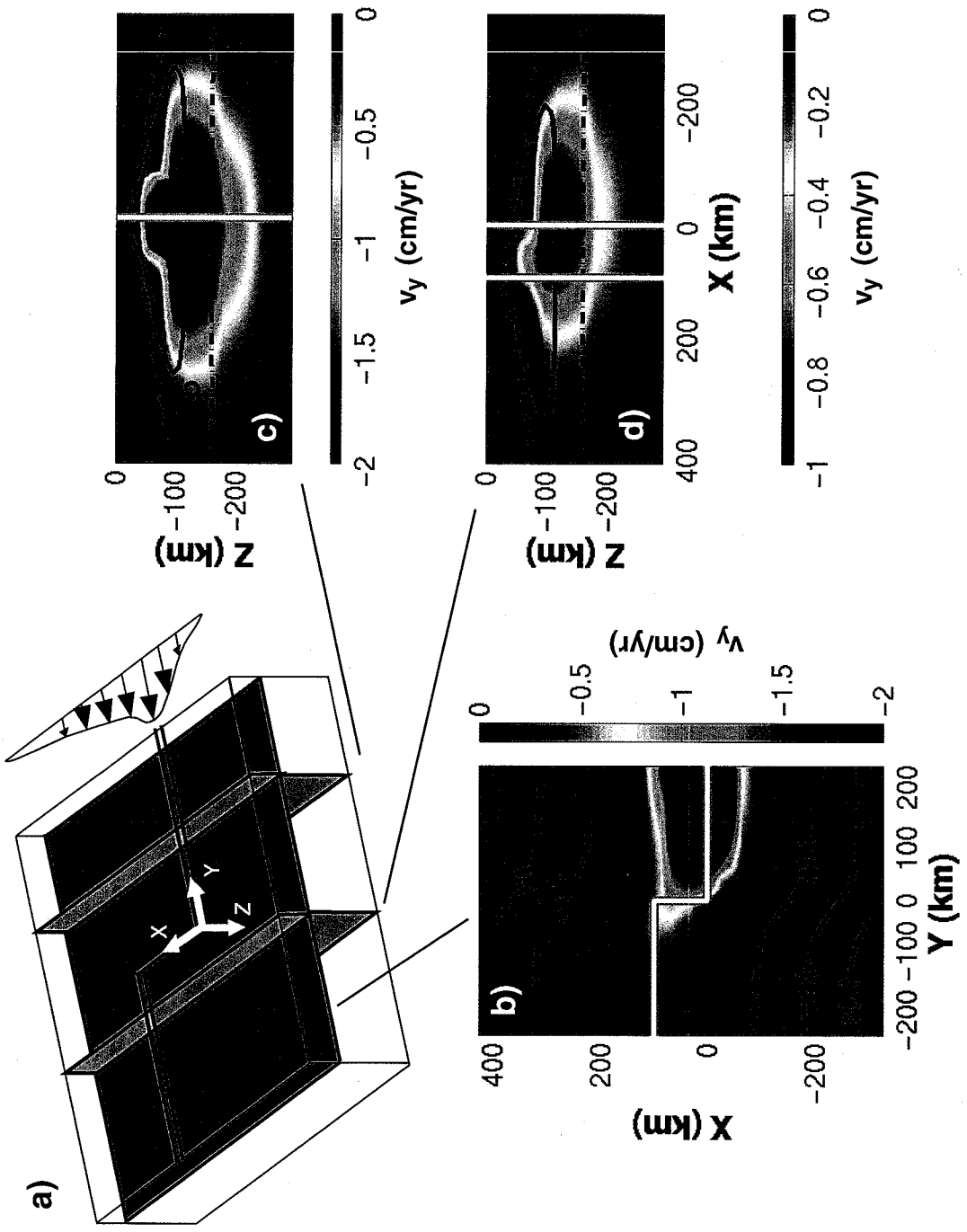
a)
X
Y
Z
b)
X (km)
Y (km)
400
200
0
−200
−200 −100 0 100 200
v_y (cm/yr)
0
−0.5
−1
−1.5
−2
c)
Z (km)
0
−100
−200
v_y (cm/yr)
−2
−1.5
−1
−0.5
0
d)
Z (km)
0
−100
−200
X (km)
400
200
0
−200
v_y (cm/yr)
−1
−0.8
−0.6
−0.4
−0.2
0

Figure 4

Figure 5: a) Across-axis cross-section of v_y at Y = 125 km. Viscosity is pressure- and temperature-dependent and ranges from approximately 10^{19} Pa s to 10^{24} Pa s in this slice. U = 1.25 cm/yr and L_t = 0 km. b) Across-axis slice of v_y also at Y = 125 km, but for an isoviscous (10^{21} Pa s) model calculation. Note that the high-velocity region is much more focused for the variable viscosity case (panel a) than for the isoviscous case (panel b).

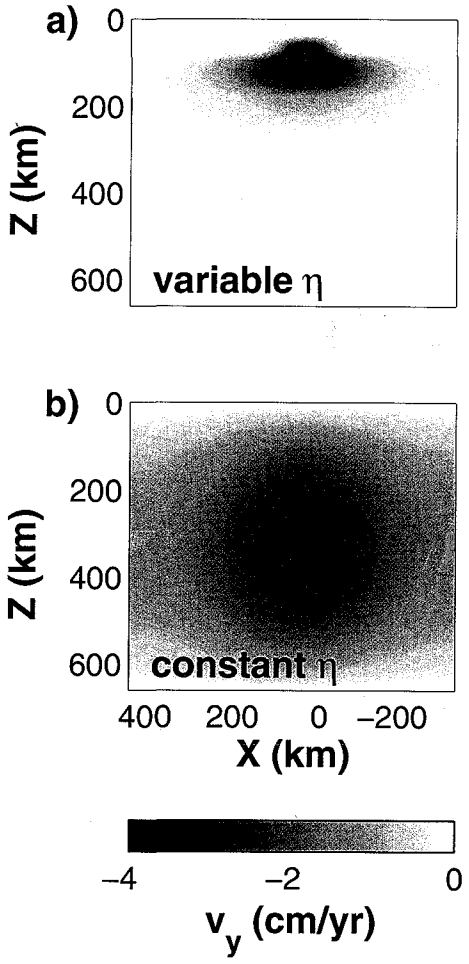
a)
0
200
400
600
Z (km)
variable η
b)
0
200
400
600
Z (km)
constant η
400
200
0
−200
X (km)
−4
−2
0
v_y (cm/yr)

Figure 5

Figure 6: Plan view slices of along-axis velocity at Z = 72 km. Panels a-c are for U = 1.25 cm/yr, and panels d-f are for U = 0.75 cm/yr. Offsets vary from 50 km (panels a and d) to 100 km (panels b and e) to 150 km (panels c and f).

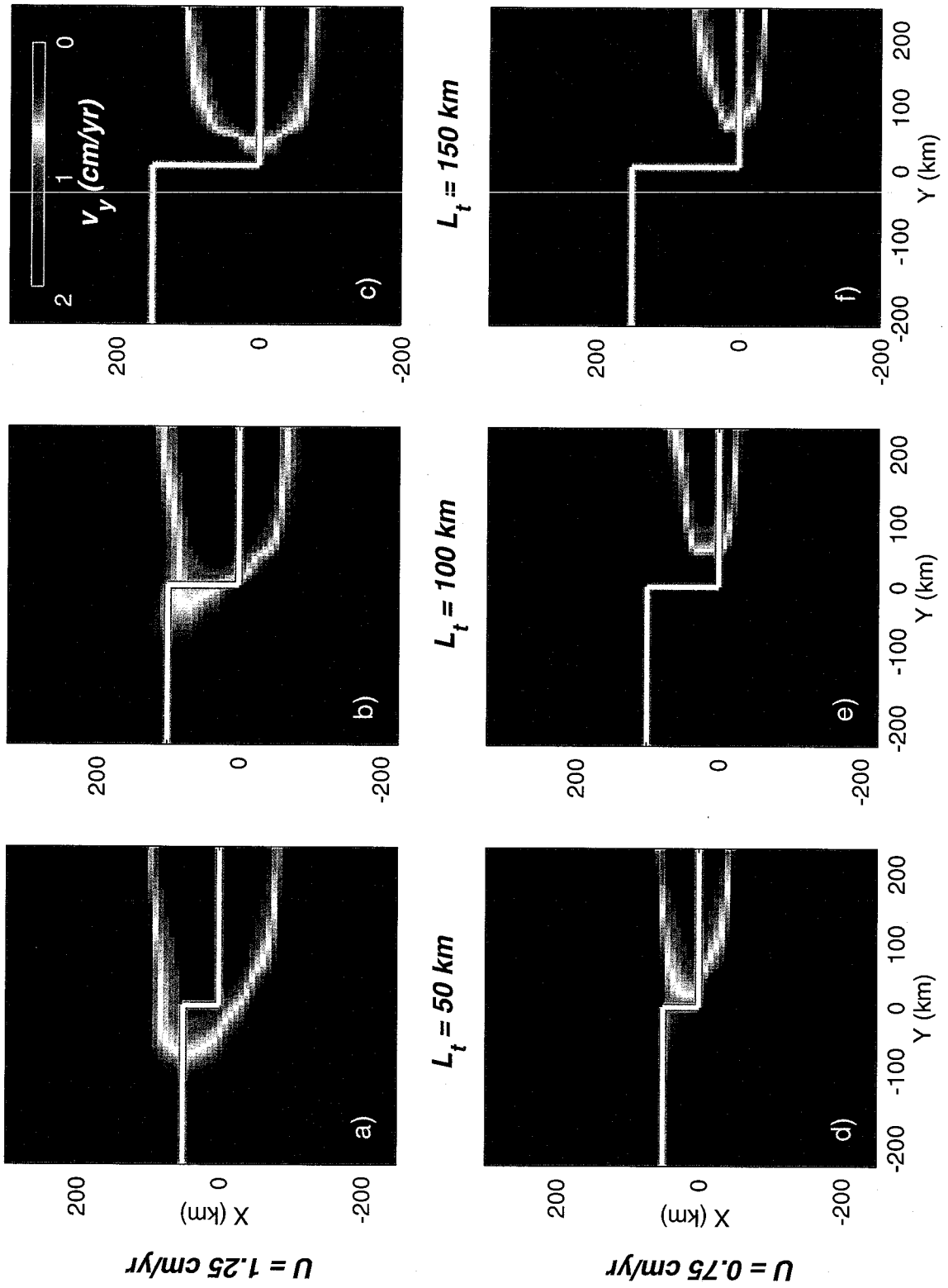
U = 1.25 cm/yr
U = 0.75 cm/yr
L_t = 50 km
L_t = 100 km
L_t = 150 km
v_y (cm/yr)
2
1
0
a)
b)
c)
d)
e)
f)
X (km)
Y (km)
200
0
-200
-100
100

Figure 6

Figure 7: Maximum v_y within the model domain for all spreading rates and L_t = 0 km under the prescribed along-axis pressure gradient of 15 MPa over 500 km. Note that maximum v_y for the isoviscous case (diamond, $\eta = 10^{21}$ Pa s) is substantially smaller than that for the case of variable viscosity with pressure- and temperature-dependence (circle) for U = 1.25 cm/yr. This is because the sloping base of the lithosphere in the variable viscosity case channelizes flow along-axis.

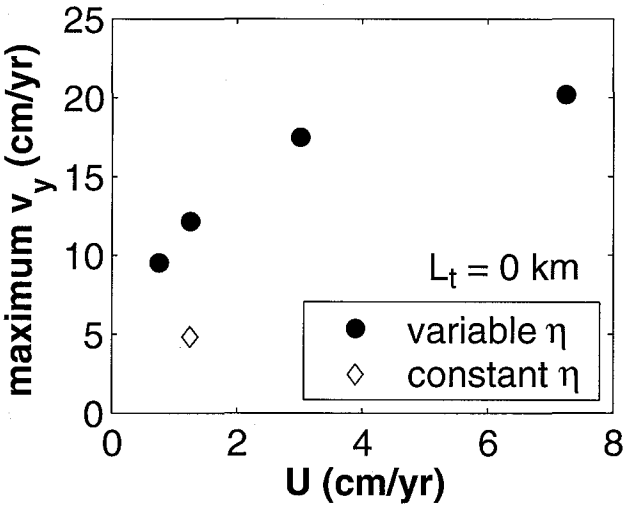
maximum v_y (cm/yr)
25
20
15
10
5
0
0
2
4
6
8
U (cm/yr)
L_t = 0 km
variable η
constant η

Figure 7

Figure 8: Along-axis volumetric material flux Q through vertical planes perpendicular to the spreading axis, for the case of $L_t = 0$ km and U = 1.25 cm/yr. Note that flux decreases in the along-axis direction away from the plume pressure center at Y = 250 km, even without a transform offset.

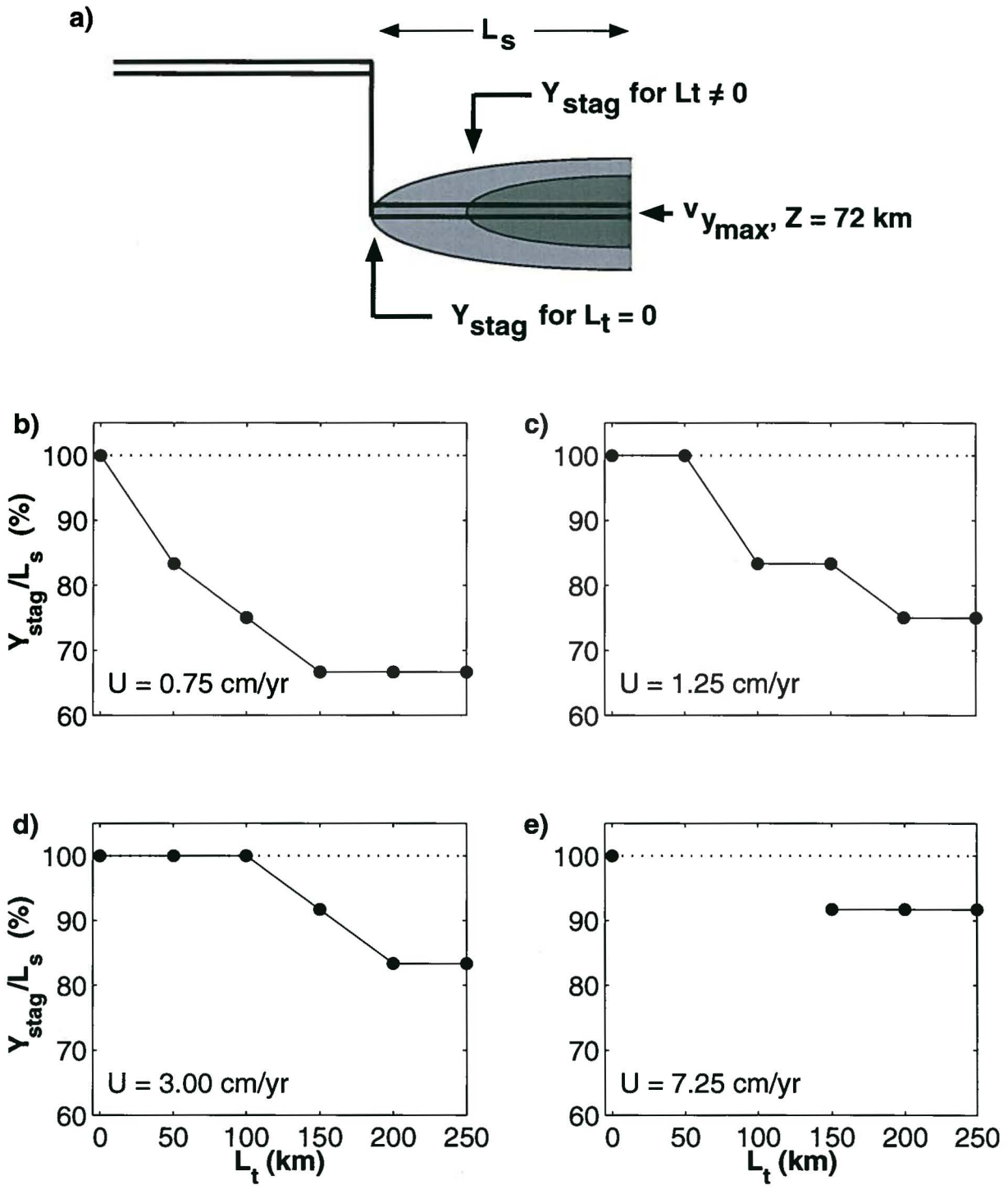
a)
L_s
Y_{stag} for Lt ≠ 0
$v_{y_{max}}$, Z = 72 km
Y_{stag} for L_t = 0
b)
c)
d)
e)
Y_{stag}/L_s (%)
100
90
80
70
60
U = 0.75 cm/yr
U = 1.25 cm/yr
U = 3.00 cm/yr
U = 7.25 cm/yr
0
50
100
150
200
250
L_t (km)

Figure 12

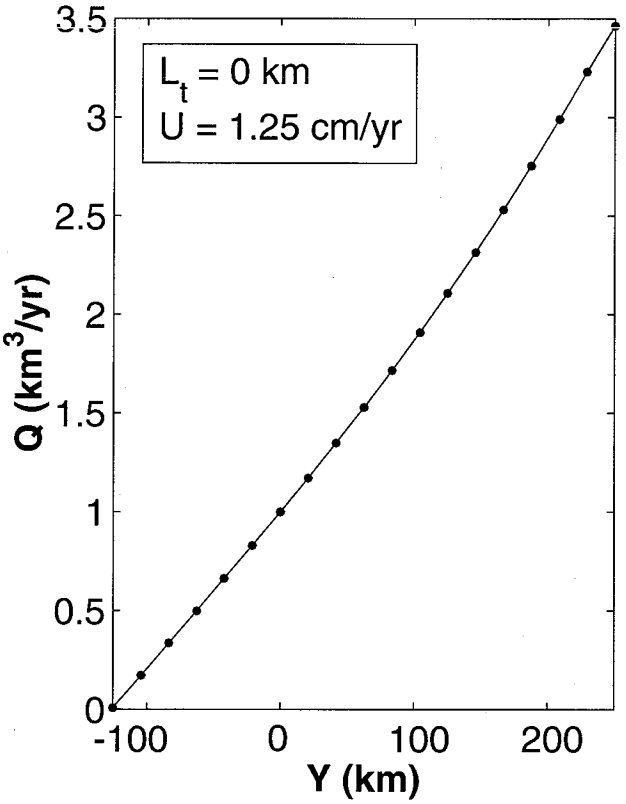

Figure 8

Figure 9: Flux Q across a transform offset of 200 km for U = 0.75, 1.25, and 3.0 cm/yr, normalized to the flux across the transform for U = 7.25 cm/yr.

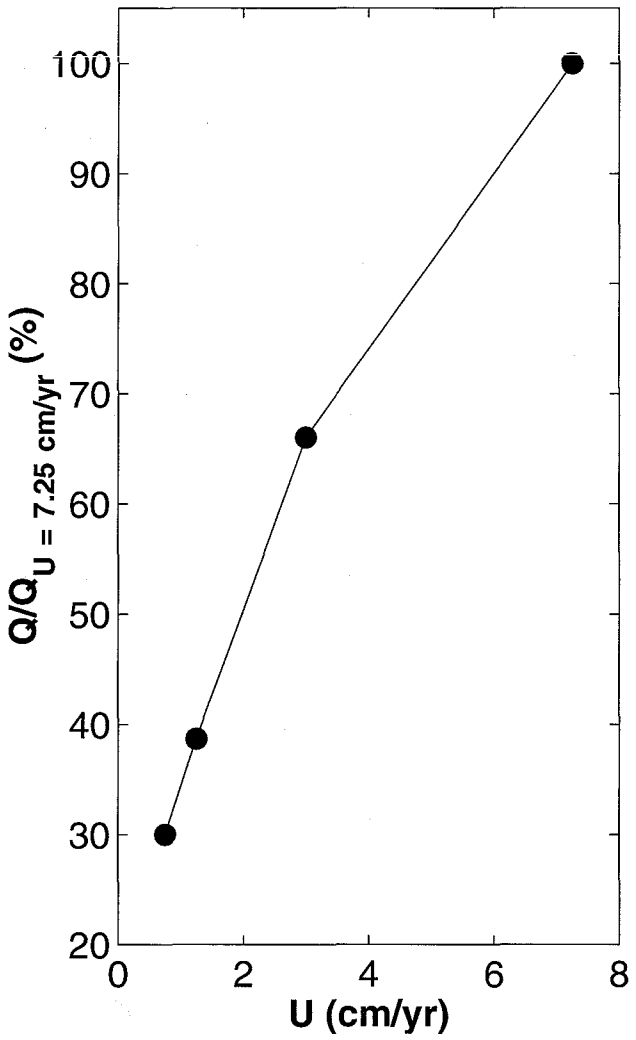

Figure 9

Figure 10: a) Normalized flux $Q/Q_{Lt=0}$ as a function of along-axis distance for U = 0.75 cm/yr. Normalized flux curves are given for all six L_t, ranging from 0 km to 250 km. The transform offset is located at Y = 0 km. Note that flux decreases with increasing transform length L_t. b-d) Same as for a, but for U = 1.25, 3.0, and 7.25 cm/yr, respectively.

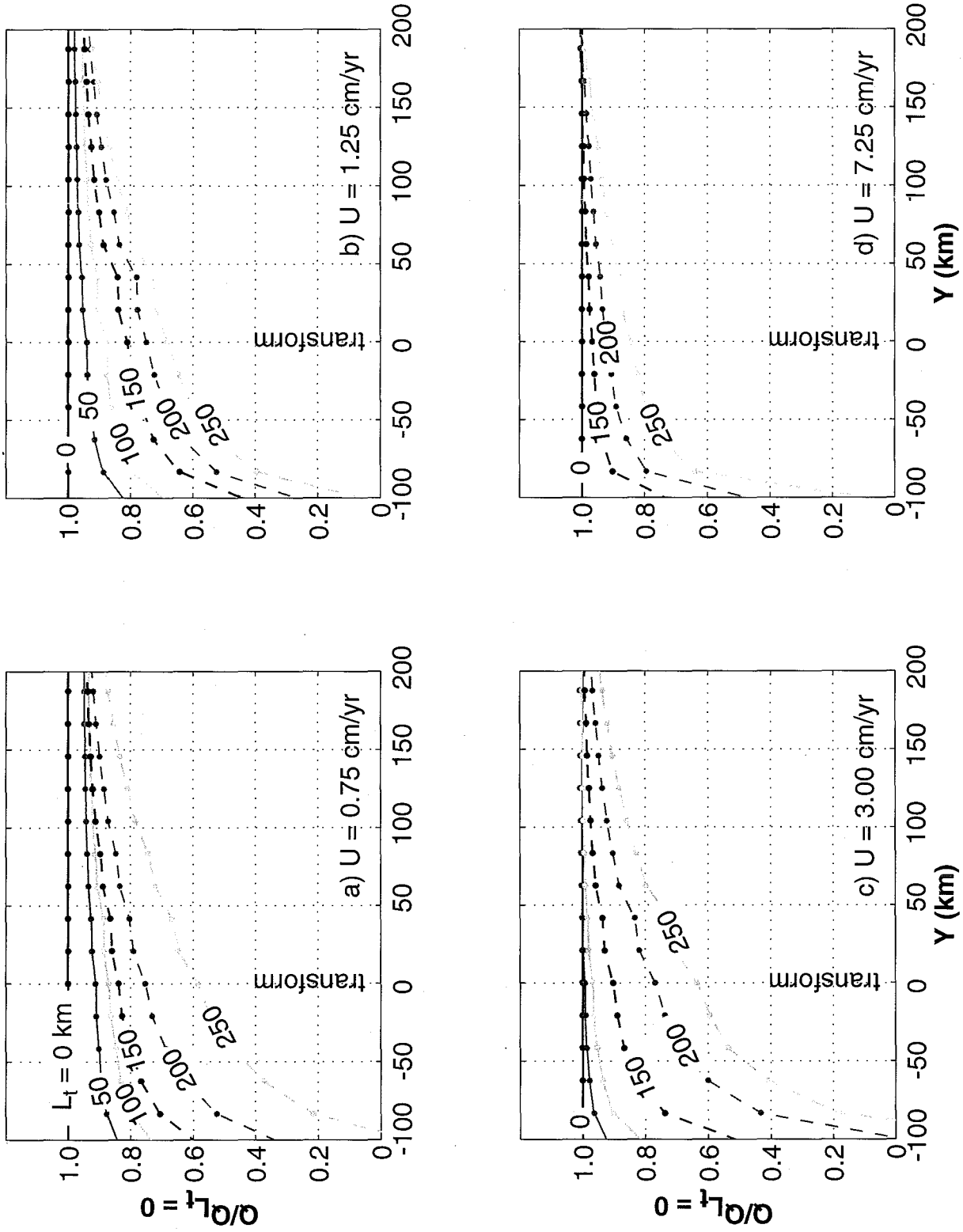
a) U = 0.75 cm/yr
b) U = 1.25 cm/yr
c) U = 3.00 cm/yr
d) U = 7.25 cm/yr
transform
Q/QL_t = 0
L_t = 0 km
0
50
100
150
200
250
Y (km)
1.0
0.8
0.6
0.4
0.2
0
-100
-50
0
50
100
150
200

Figure 10

Figure 11: Gradients in across-transform flux for U = 3.0 and 7.25 cm/yr. $\Delta Q/\Delta Y$ is defined to be $(Q/Q_{Lt=0}|_{Y=20\ km} - Q/Q_{Lt=0}|_{Y=-20\ km})/\ \Delta Y$, or the difference between pre-transform and post-transform normalized flux over a fixed distance ΔY of 40 km (inset). Large $\Delta Q/\Delta Y$ indicate significant drops in along-axis flux across the transform. Note that the effect of increasing transform length on $\Delta Q/\Delta Y$ is greater for U = 3.0 cm/yr than for u = 7.25 cm/yr.

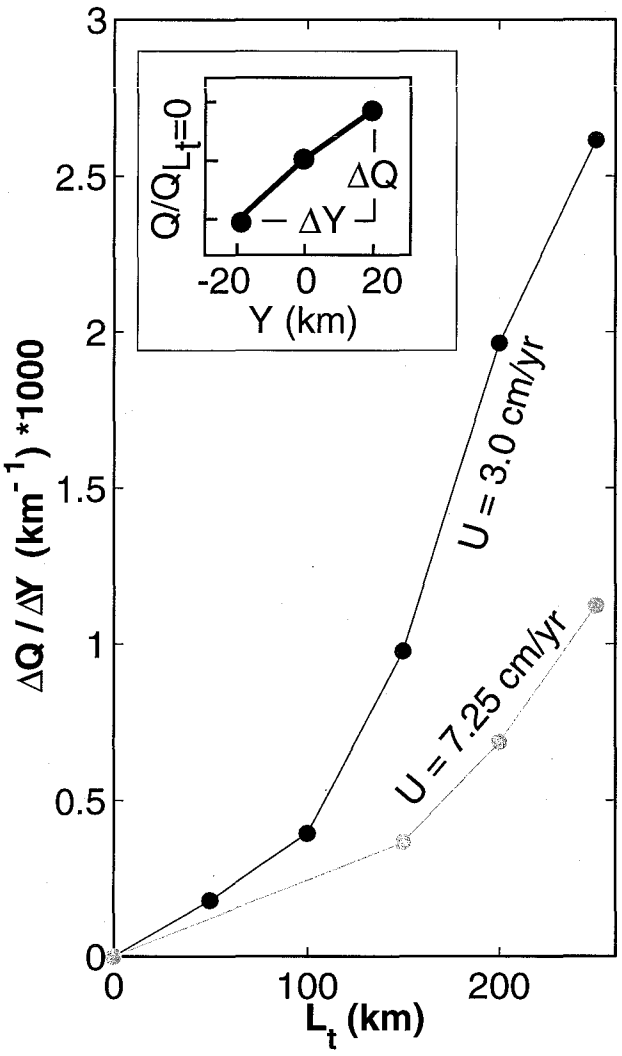
3
2.5
2
1.5
1
0.5
0
0
100
200
L_t (km)
$\Delta Q / \Delta Y$ (km^{-1}) *1000
U = 3.0 cm/yr
U = 7.25 cm/yr
$Q/Q_{L_t=0}$
ΔQ
ΔY
-20
0
20
Y (km)

Figure 11

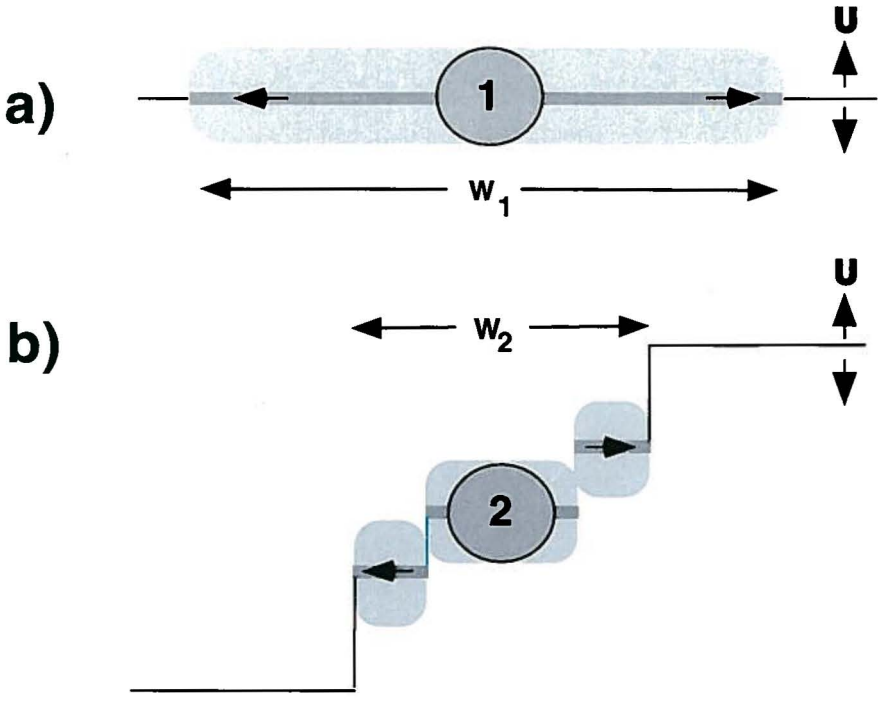

Figure 16

Figure 12: The effects of spreading rate and transform offset length on the along-axis dispersal distance of high-velocity flow. a) We define v_{ymax} as the maximum along-axis velocity within the model box at Z = 72 km, within the zone of fastest along-axis flow. Y_{stag} is defined as the distance at which $v_{y|Z=72\ km}$ first drops below 18.5% of v_{ymax}. A threshold of 18.5% was selected because it is the characteristic velocity dissipation factor for the $L_t = 0$ case. That is, $v_{y|Y=0\ km} = 0.185 * v_{y|Y=Ls}$ for U = 0.75 cm/yr and L_t = 0 km. b) Y_{stag}/L_s for U = 0.75 cm/yr . Note that the longer the transform offset, the shorter the distance of the stagnation point from the plume center. c-e) Same as in a, but for U = 1.25, 3.0, and 7.25 cm/yr, respectively.

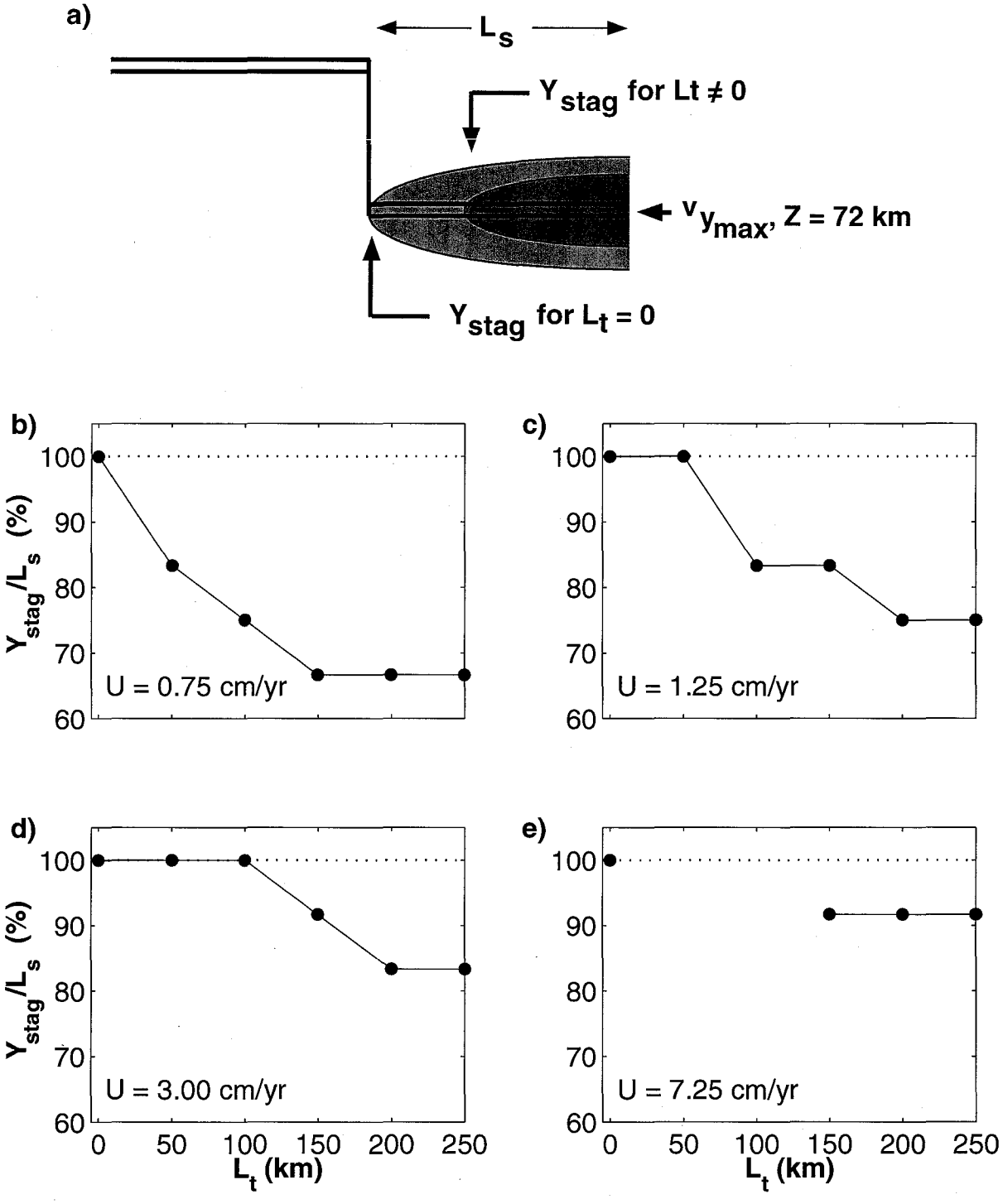
a)
L_s
Y_{stag} for Lt ≠ 0
$v_{y_{max}}$, Z = 72 km
Y_{stag} for L_t = 0
b)
c)
d)
e)
Y_{stag}/L_s (%)
100
90
80
70
60
U = 0.75 cm/yr
U = 1.25 cm/yr
U = 3.00 cm/yr
U = 7.25 cm/yr
0
50
100
150
200
250
L_t (km)

Figure 12

Figure 13: a) The path of the highest-velocity flow at Z = 72 km for L_t = 100 km and U = 0.75, 1.25, and 3.0 cm/yr. Light gray lines indicate ridge axis, with a single gray line marking the transform fault at Y = 0 km. ΔD is defined as the distance between X = 0 km and the position of the high-velocity flow at the transform fault at Y = 0 km. b) The path of the highest-velocity flow at Z = 72 km for U = 0.75 cm/yr and L_t = 0, 50, and 100 km. The locations of grid nodes are indicated with light gray dots. c) ΔD as a function of L_t for U = 0.75, 1.25, and 3.0 cm/yr. Note that ΔD is always less than L_t, although ΔD is closer to L_t for slower spreading rates than faster spreading rates.

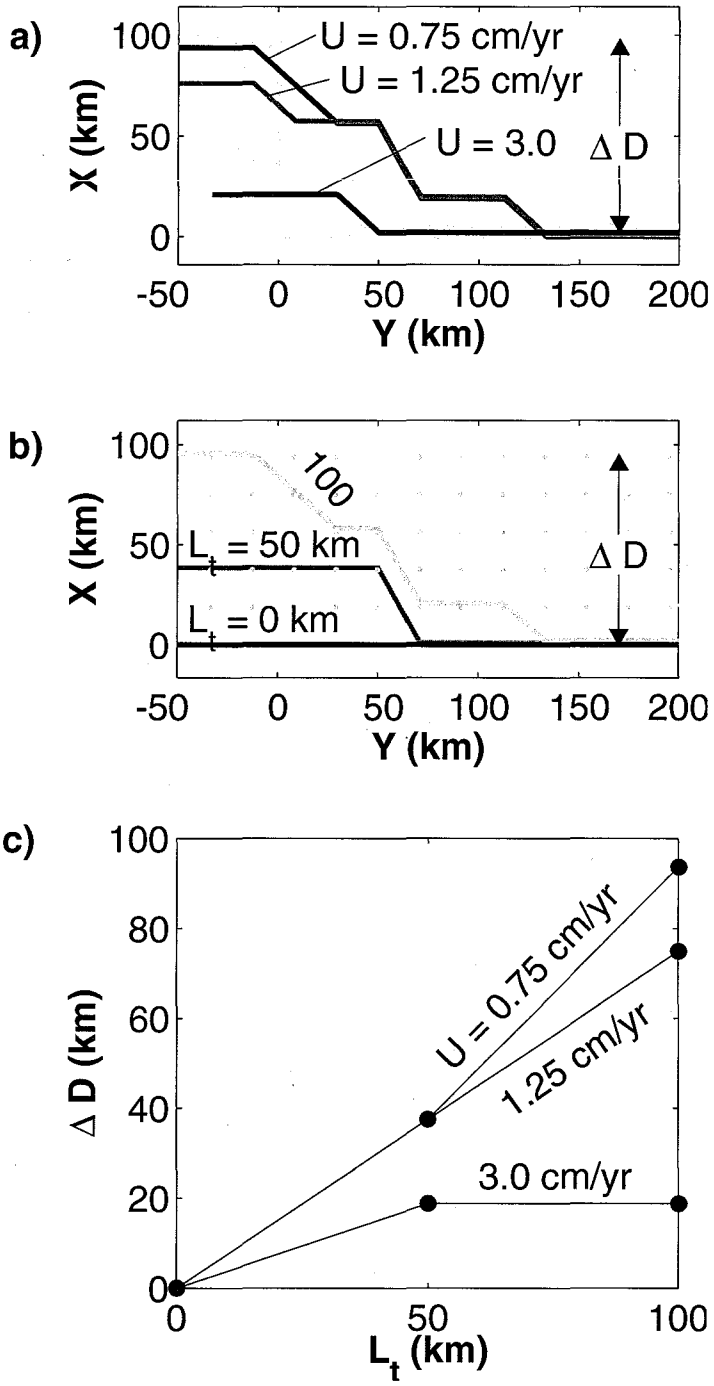
a)
100
50
0
X (km)
U = 0.75 cm/yr
U = 1.25 cm/yr
U = 3.0
Δ D
-50
0
50
100
150
200
Y (km)
b)
100
50
0
X (km)
100
L_t = 50 km
L_t = 0 km
Δ D
-50
0
50
100
150
200
Y (km)
c)
100
80
60
40
20
0
Δ D (km)
U = 0.75 cm/yr
1.25 cm/yr
3.0 cm/yr
0
50
100
L_t (km)

Figure 13

Figure 14: Sensitivity of normalized flux $Q/Q_{(Po=15\ MPa,\ xo=100\ km)}$ to different driving pressure P_o and pressure standard deviation length x_o. For all of the model runs shown, L_t = 100 km and U= 1.25 cm/yr.

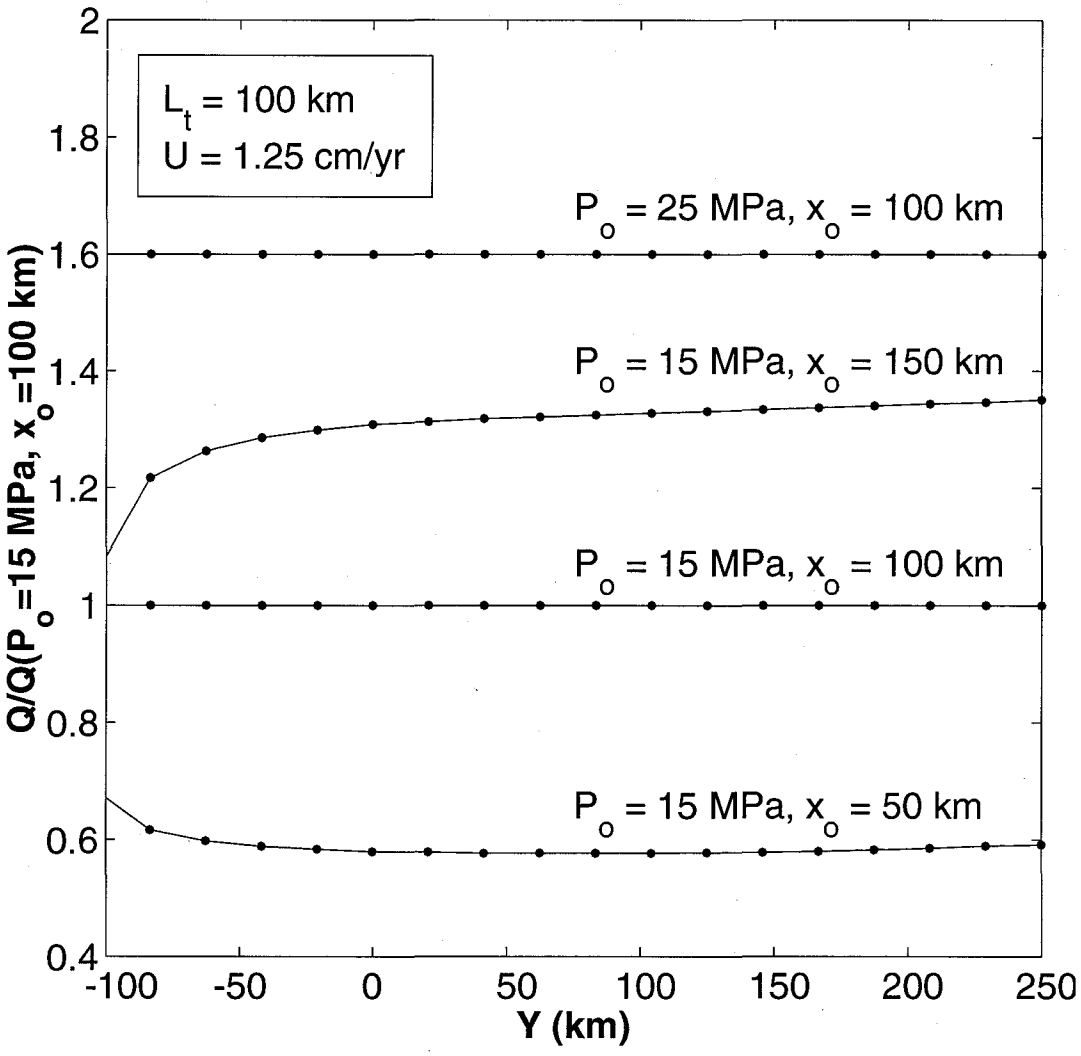
L_t = 100 km
U = 1.25 cm/yr
P_o = 25 MPa, x_o = 100 km
P_o = 15 MPa, x_o = 150 km
P_o = 15 MPa, x_o = 100 km
P_o = 15 MPa, x_o = 50 km
Q/Q(P_o=15 MPa, x_o=100 km)
Y (km)
2
1.8
1.6
1.4
1.2
1
0.8
0.6
0.4
-100
-50
0
50
100
150
200
250

Figure 14

Figure 15: a) A comparison of axial velocity-depth profiles calculated using pressure- and temperature-dependent viscosities (this study, black line) based on *Shen and Forsyth* [1992] and the viscosity solution of *Braun et al.* [2000] (gray line), which considers the additional effects of melting, dehydration, and change in deformation mechanism. Velocity profiles were taken at X = 0 km and Y = 250 km, for L_t = 0 km and U = 3.0 cm/yr. b) A comparison of along-axis flux calculated using the viscosity solutions of this study (based on *Shen and Forsyth* [1992]) and *Braun et al.* [2000].

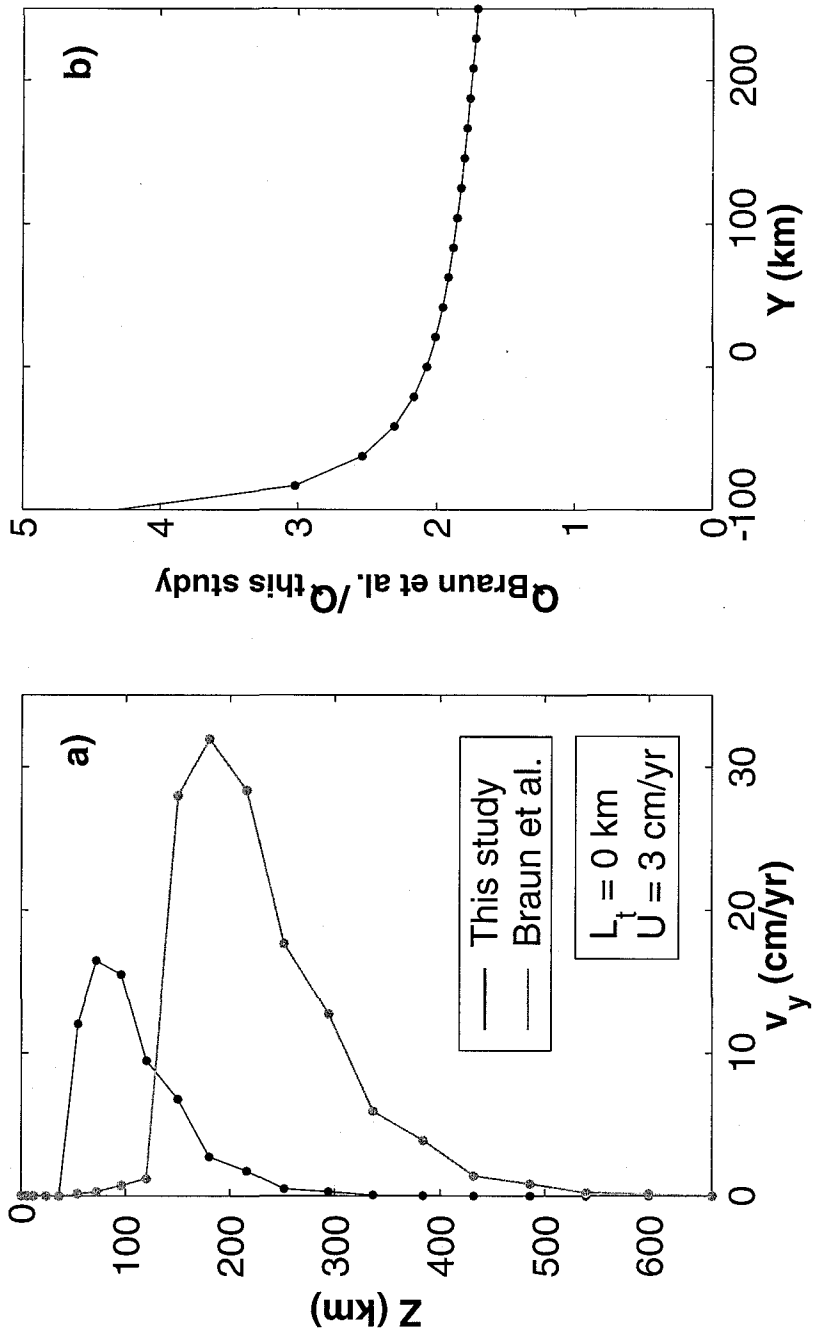
b)
$Q_{Braun\ et\ al.}/Q_{this\ study}$
Y (km)
a)
This study
Braun et al.
L_t = 0 km
U = 3 cm/yr
Z (km)
v_y (cm/yr)

Figure 15

Figure 16: Schematic cartoons of plume-ridge interaction for an unsegmented ridge (a) and a ridge with significant transform offsets (b). Dark gray circles show plan view of a hypothesized vertical plume conduit. The conduit size and flux of plume 1 are assumed to equal to those of plume 2. Light gray shading depicts along-axis dispersal of plume material along a low-viscosity channel, and the ridge axes with a plume signature are emphasized with dark gray lines. The lengths of the ridges affected by the plumes, or waist width, are W_1 and W_2. Because along-axis flux in b is limited by transform faults, $W_2 < W_1$. Thus, flux inferred from waist width will be an underestimate for plume 2 compared to the case of an unsegmented ridge.

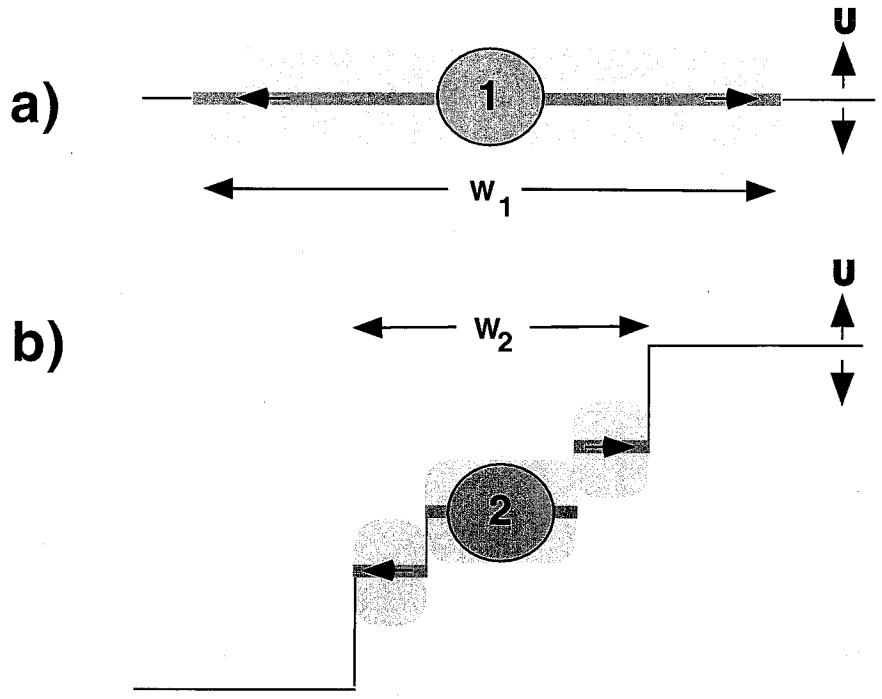

Figure 16

Chapter 4

Helium isotope systematics of the western Southwest Indian Ridge: Effects of plume influence, spreading rate, and source heterogeneity

Jennifer E. Georgen, Mark D. Kurz, Henry J.B. Dick, and J. Lin

Abstract

$^3He/^4He$ ratios have been measured for a suite of basalt glass samples from the ultra-slow spreading (0.8 cm/yr half-rate) western Southwest Indian Ridge. The study area is divided into two subregions, a supersegment between 9° and 16°W where poorly-defined ridge segments lie at a highly oblique angle to the regional spreading direction, and a supersegment between 16° and 24°W where ridge segments are nearly orthogonal to the spreading direction. Although earlier geochemical studies suggested that the western oblique supersegment may be affected by the high $^3He/^4He$ Bouvet plume more than 700 km away, there is no evidence for elevated $^3He/^4He$ in the region. In fact, $^3He/^4He$ throughout the entire study area ranges from 6.3 – 7.3 R_a, values that are significantly below normal mid-ocean ridge basalt helium isotopic ratios of 8 ± 1 R_a. The preferred explanation for low $^3He/^4He$ ratios is mantle heterogeneity from recycled crustal or lithospheric material. Other possible explanations for such consistently low $^3He/^4He$ ratios include prior mantle melting and vertical mantle stratification. In addition to low ratios, $^3He/^4He$ measurements for the western Southwest Indian Ridge are characterized by low variability, despite earlier studies' predictions of an inverse relationship between spreading rate and helium isotope standard deviation.

To better understand the systematics of $^3He/^4He$ variation around hotspots such as Bouvet, helium isotopic ratios are compared to geophysical descriptors of plume geodynamics such as mantle Bouguer anomaly, waist width, and plume flux. Unlike Iceland, where a clear trend of increasing $^3He/^4He$ ratios toward the hotspot is observed along the relatively unsegmented Reykjanes Ridge, $^3He/^4He$ systematics near Bouvet are influenced by segment-scale processes and the geodynamical effects of long transform offsets. Correlations between $^3He/^4He$ and mantle Bouguer anomaly amplitude, plume waist width, and plume flux for a global array of hotspots may suggest that relatively high-flux plumes originate in the comparatively undegassed deep mantle.

1. Introduction

Along the global mid-ocean ridge system, areas affected by hotspots often have distinct geochemistry from "normal" mid-ocean ridge basalt (MORB). Analyses of major element,

rare earth element, and isotopic data for axial dredge samples can be merged with geophysical data such as bathymetry and gravity to delineate portions of ridge influenced by a nearby mantle plume [*Hart et al.*, 1973; *Schilling*, 1975; *Mahoney et al.*, 1989; *Schilling*, 1991; *Ito and Lin*, 1995a, b]. Helium isotopic data are often a sensitive indicator of plume influence [*Kurz et al.*, 1982a, b; *Poreda et al.*, 1985; *Moreira et al.*, 1995; *Graham et al.*, 1999]. One assumption commonly made in interpreting noble gas geochemical data is that the hotspot source is relatively undegassed lower mantle. Under this assumption, high $^3He/^4He$ indicates plume-like upwelling, since the deep earth is believed to be a source of primordial ^3He with a relatively low time-integrated (U+Th)/He ratio. The overall goal of this investigation is to explore the relationship between $^3He/^4He$ ratios and mid-ocean ridge geophysics, particularly in plume-affected areas.

Values of $^3He/^4He$ for normal MORB generally fall in the range of 8±1, normalized to the atmospheric ratio of 1.384×10^{-6} (R_a) [*Kurz and Jenkins*, 1981]. The assumption of a normal MORB value of 8±1 R_a has been calculated using along-axis studies [e.g., *Kurz et al.*, 1982b; *Graham et al.*, 1993a; *Poreda et al.*, 1993], and omitting significant $^3He/^4He$ variations near hotspots. More recent studies, incorporating data from a variety of geologic settings including ridges, back-arc basins, hotspot-influenced sections of ridge, and near-ridge seamounts, have questioned this value and suggest that the global mean $^3He/^4He$ ratio is 9.1±3.5 R_a [*Anderson*, 2000]. This estimate, however, suffers from numerous statistical effects, including the assumption that $^3He/^4He$ ratios are Gaussian-distributed and artifacts from spatial averaging of unevenly distributed data. For the purpose of this study, we will assume that normal MORB helium ratios are 8±1 R_a, because it serves as a useful reference. However, this study has implications for the definition of global "normal" MORB values, particularly for the Southwest Indian Ridge (SWIR).

Helium ratios around hotspots are often significantly different from those for normal MORB. For example, Hawaii has elevated $^3He/^4He$, in the range of 8-32 R_a [e.g., *Kurz et al.*, 1982a; 1983; 1991; 1996]. In the vicinity of Iceland, $^3He/^4He$ increases from <8 R_a to the south of the Gibbs Fracture Zone to ~15 R_a on the southern submarine portion of the Iceland plateau, to a high of 37 R_a on the island itself [*Hilton et al.*, 2000]. Furthermore, Galapagos helium ratios fall between 8.6 and 27 R_a [e.g., *Graham et al.*, 1993a; *Kurz and Geist*, 1999]. Moreover, Reunion Island helium measurements range from 11-14 R_a [*Graham et al.*, 1990; *Staudacher et al.*, 1990], and isotopic ratios around the Bouvet plume in the southern Atlantic Ocean reach 14.2 R_a [*Kurz et al.*, 1998].

There are also ocean islands and ridge segments with $^3He/^4He$ ratios lower than 8 R_a. Notably, most $^3He/^4He$ ratios along the Mid-Atlantic Ridge (MAR) near the Azores range from approximately 7 to 10 R_a [*Kurz et al.*, 1982b]. *Kurz et al.* [1982a] and *Graham et al.* [1992a,b] found ratios for Tristan da Cunha, Gough, and St. Helena to be uniformly less than 7 R_a. Similarly, Marion Island, near the central SWIR, has $^3He/^4He$ of 6.7-7.7 R_a [*Kurz et al.*, 1982a; *Mahoney et al.*, 1989]. Possible explanations for low $^3He/^4He$ ratios include the addition of low He/(U+Th) material into the mantle source by recycling of subducted oceanic crust or delaminated continental lithosphere, and magma chamber or post-eruptive degassing followed by radiogenic ingrowth [*Kurz et al.*, 1982b; *Hart and Zindler*, 1986; *Sarda et al.*, 2000].

The overall goal of this investigation is to explore the relationship between $^3He/^4He$ ratios and mid-ocean ridge geophysics, particularly in plume-affected areas. This investigation also explores helium isotope systematics for the western SWIR, between 10.67° and 23.12° E. This study area includes the slowest spreading rates for which $^3He/^4He$ ratios have yet been measured, as well as a section of ridge postulated to be affected by the Bouvet plume [*le Roex et al.*, 1992]. Surprisingly, for this ~800-km-long

portion of the SWIR, we report $^{3}He/^{4}He$ ratios that are both remarkably uniform and consistently below normal MORB values.

2. Geological and geochemical setting

2.1 Ridge geometry

The SWIR extends ~8000 km, from the Bouvet Triple Junction (BTJ) in the west to the Rodrigues Triple Junction in the east (Figure 1). Spreading rates along the SWIR are ultra-slow and relatively uniform, with half-rates ranging from 0.7-0.9 cm/yr over much of the ridge's length. Two near-ridge hotspots, Bouvet and Marion, affect accretionary processes along the SWIR [*Georgen et al.*, 2001]. The Bouvet hotspot is located approximately 300 km east of the BTJ and roughly 50 km from the nearest spreading segment of the SWIR. Marion is approximately 250 km south of the ridge axis in the central portion of the SWIR, to the east of the Andrew Bain FZ.

The western SWIR can be divided into three sections based on spreading geometry (Figure 1). Between the BTJ and the Shaka FZ, well-defined short ridge segments, orthogonal to the regional spreading direction, are offset by relatively long-lived transform faults. In contrast, segmentation is poorly defined along the 400-km-long section of ridge between 9°E and 16°E. This portion of the SWIR lies at a high angle to the regional spreading direction, and consequently is referred to here as the oblique supersegment. Because of its obliquity, this SWIR section has an effective spreading rate, or spreading rate measured orthogonal to the local ridge trend, of only 0.5 cm/yr. This is the slowest rate along the accessible portion of the global ridge system (only the Arctic ridges are slower). Between 16°E and 25°E, the SWIR is composed of a series of short (~42 km) segments separated by non-transform offsets [*Grindlay et al.*, 1998]. Since ridge segments

are locally perpendicular to the regional spreading direction in this area, this portion of the SWIR will be referred to as the orthogonal supersegment. The orthogonal supersegment was the focus of a detailed geophysical survey by *Grindlay et al.* [1998], while the recent R/V Knorr cruise KN162 (Austral summer 2000-2001) surveyed bathymetry, magnetics, and gravity of the oblique supersegment and dredged >50 locations on both the oblique and orthogonal supersegments [*Dick et al.,* 2001a].

The BTJ is the intersection of the SWIR, American-Antarctic Ridge (AAR), and southern MAR. Over the past few million years, half-spreading rates for the AAR and MAR have been 0.9 and 1.4 cm/yr, respectively [*Mitchell and Livermore*, 1998]. Spiess Seamount, a large volcanic edifice on the first SWIR segment to the east of the BTJ, may reflect recent reorganization of the triple junction and/or the present-day location of the Bouvet plume [*Ligi et al.*, 1997; *Mitchell and Livermore*, 1998].

2.2 Geochemistry: Bouvet Triple Junction vicinity and western SWIR

Values of $^{3}He/^{4}He$ in the immediate vicinity of the BTJ range from 6.5 to 14.2 R_a [*Kurz et al.*, 1998]. Along the SWIR, relatively high (9.98 – 12.9 R_a) values were obtained for four samples on the ridge segment closest to the Bouvet plume; a single measurement for Bouvet Island itself is 12.4 R_a. Ratios for the segments flanking the Bouvet Ridge segment are low (7.12 - 7.45 R_a). Surprisingly, however, the highest measurements were obtained for the ridge segment between the Islas Orcadas and Shaka FZs, where a single dredge haul included rocks with ratios ranging from 7.41 - 14.9 R_a. Along the eastern AAR, $^{3}He/^{4}He$ ratios are systematically higher near the BTJ (8.95 - 9.71 R_a), compared to lower values between 15°W and 18°W (6.68 - 8.1 R_a).

Four hotspots are located within 750 km of the southern MAR, Tristan, Gough, Discovery, and Shona (Figure 1). As noted previously, Tristan and Gough are both low

$^3He/^4He$ hotspots, with ratios <7 R_a [*Kurz et al.*, 1982a; *Graham et al.*, 1992a,b]. However, both Shona and Discovery are characterized by well-defined axial $^3He/^4He$ highs, with maximum $^3He/^4He$ ratios of 14.7 and 14.2 R_a, respectively [*Moreira et al.*, 1995; *Kurz et al.*, 1998; *Sarda et al.*, 2000]. To the south of Shona, in the immediate vicinity of the BTJ, MAR $^3He/^4He$ ratios return to lower values of 7.11 to 7.66 R_a [*Kurz et al.*, 1998]. Note that these values are slightly lower than 8 R_a, the typical value for N-MORB.

Between the BTJ and 11°E along the SWIR, normal, transitional, and enriched MORB are juxtaposed with no clear gradient away from the Bouvet plume [*le Roex et al.*, 1983]. This geochemical variability is attributed to the ultra-slow spreading rate, which allows the persistence of small, localized plume-related heterogeneities without magma mixing or homogenization [*le Roex et al.*, 1983; 1992]. To the east, few published geochemical data exist for the orthogonal supersegment. However, for the oblique supersegment, isotopic, major element, and trace element data are available for six dredge hauls [*le Roex et al.*, 1992]. Dredged lavas are highly K-enriched, nepheline-normative alkali basalts and hawaiites with highly fractionated incompatible element ratios. *Le Roex et al.* [1992] explain these basalts as the products of extremely low percentage melting (<5%) of a veined mantle source. They postulate that the isotopically- and trace-element-enriched veins result from lateral dispersion of the Bouvet plume more than 700 km away.

2.3 Study motivation

This study documents variations in $^3He/^4He$ ratios along the western SWIR. Since these $^3He/^4He$ measurements correspond to the slowest spreading rates for which helium data are currently available, we first determine how $^3He/^4He$ values from the oblique and orthogonal supersegments compare to measurements at faster spreading ridges. Second,

we evaluate whether $^3He/^4He$ measurements differ systematically between the orthogonal and oblique supersegments, as a function of both proximity to the Bouvet hotspot and change in effective spreading rate. Third, we place the variability of $^3He/^4He$ along the western SWIR in a global context. In particular, we evaluate the hypothesis that $^3He/^4He$ variability for this ultra-slow spreading ridge should be high, given the linear relationship between reciprocal spreading rate and $^3He/^4He$ variance proposed by *Allegre et al.* [1995]. Finally, we relate $^3He/^4He$ ratios to magmatic robustness by comparing $^3He/^4He$ to mantle Bouguer anomaly (MBA) calculations, both for the hotspots around the BTJ as well as for Iceland and Azores in the north Atlantic.

3. Samples and analytical procedures

The samples used in this study primarily came from dredge sampling of the SWIR between 10°E and 23°E during Legs 162-7 and 162-9 of R/V Knorr (Austral summer 2000-2001) [*Dick et al.*, 2001b]. Samples from Leg ANT IV/4 of the F.S. Polarstern (1986) and the 1981 Agulhas Leg 22 cruise supplemented Knorr dredges. Although KN162 included over 60 dredges along the SWIR axis, the recovered rocks varied in lithology and degree of alteration. The samples used in this investigation were selected for the availability of fresh basaltic glass. Vesicularities of the measured glasses range from <1% to 5%. In general, glasses from the oblique supersegment were more altered than those from the orthogonal supersegment. The locations of the analyzed basalts are indicated in Figure 1 and Tables 1 and 2.

Fresh glasses in the 0.5 – 2 mm size fraction were handpicked under magnification and cleaned ultrasonically in ethanol and acetone. Helium measurements were generally performed by crushing in vacuum, although a few samples were analyzed by melting in a

high vacuum furnace. Crushing *in vacuo* selectively releases helium contained by vesicles, and is the preferred method here for two reasons. First, it minimizes post-eruptive radiogenic contributions from decay of Th and U, which reside in the solid matrix. Second, based on glass-vesicle equilibrium studies, 1-5% vesicularity corresponds to vesicle/glass helium concentration ratios of 1 to 100 [*Kurz and Jenkins*, 1981]. Therefore, glass matrix $^3He/^4He$ ratios are more susceptible to change by radiogenic ingrowth not only because of higher (U+Th), but also because overall gas concentrations are lower. Concentrations for selected samples were determined by both crushing and melting of the remaining powder. All measurements were performed at Woods Hole Oceanographic Institution on a 90° sector mass spectrometer. Extraction lines for crushing and melting, mass spectrometry, and blank values are described elsewhere [*Kurz et al.*, 1987; 1996]. ^4He blanks during the course of these measurements were ~6 x 10^{-11} ccSTP, and uncertainties in the concentrations are ~1%.

Associated major element, rare earth element, and isotopic data are not yet available for the KN162 samples. Petrographic descriptions, as well as whole rock and glass analyses for the Polarstern samples, can be found in *le Roex et al.* [1992]. Isotopic, major element, and trace element data for AG22-9-2 are described in *Mahoney et al.* [1992].

4. Results

The ^4He concentrations and $^3He/^4He$ ratios (R/R_a) are reported in Tables 1 (oblique supersegment) and 2 (orthogonal supersegment). Errors for the isotopic ratios are 1σ. Concentrations of ^4He vary widely, from 0.006447 μccSTP/g (KN162-9-64-1) to 38.06 μccSTP/g (KN162-7-11-25), although it should be noted that this range includes measurements by both melting and crushing (Figure 2). Figure 3 suggests that ^4He

concentrations for samples from the oblique supersegment are more variable and may generally be lower than those from the orthogonal supersegment, although there are certainly exceptions to this generalization (e.g., AG22-5-14). Lower concentrations for the oblique supersegment may reflect disorganized spreading, allowing for more extensive surface degassing. There may be some indication that shallower samples might have lower ^{4}He concentrations (Figure 4). However, these comparisons are preliminary because most of the data were obtained by crushing *in vacuo*, and therefore represent a minimum concentration bound.

Isotopic compositions of samples with extremely low gas contents may have been affected by degassing followed by post-eruptive radiogenic ingrowth or seawater interaction. To guard against overinterpretation of such data, this discussion focuses on samples with ^{4}He concentrations greater than 0.4 μccSTP/g. Over time scales of < 1 Myr, it is unlikely that post-eruptive radiogenic ingrowth of ^{4}He by U+Th decay would affect the ^{3}He/^{4}He ratios of samples with concentrations higher than this. After 1 Myr of radiogenic ingrowth in a closed system, a sample with a ^{4}He concentration of 0.4 μccSTP/g and an initial ^{3}He/^{4}He ratio of 8 R_a would decrease by only 10% (Figure 5), assuming a uranium concentration [U] of 0.6 ppm [*Kurz et al.*, 1998] and a Th/U ratio of 3 [*Jochum et al.*, 1983]. Moreover, ~10 Myr would be required for the ^{3}He/^{4}He ratio for a sample with ^{4}He = 4 μccSTP/g to decrease by 10%. For ^{4}He = 40 μccSTP/g, approximately the highest concentration measured in this suite of basalts, this time scale is on the order of 100 Myr. In 1 Myr, the decrease in ^{3}He/^{4}He for ^{4}He = 40 μccSTP/g is smaller than analytical error. Therefore, a concentration cutoff of 0.4 μccSTP/g is very conservative both because the samples were dredged at the ridge axis and are most likely < 300 kyr in age, and also because these calculations assume fairly high Th+U concentrations.

Two samples (PS86-6-2 and KN162-7-6-2) were analyzed by both crushing and melting. For sample KN162-7-6-2, the $^3He/^4He$ ratio obtained by crushing (6.80 ± 0.04 R_a) is statistically indistinguishable from that obtained by melting (6.74 ± 0.05 R_a). In contrast, for sample PS86-6-2, the melting-derived ratio of 3.21 ± 0.07 R_a is significantly lower than the crushing-derived ratio of 5.98 ± 0.40 R_a, which is consistent with radiogenic ^4He in the glass. *Graham et al.* [1987] determined eruption ages for Pacific seamounts using helium disequilibrium suggested by discrepant crushing and melting measurements for a given sample. Assuming that the $^3He/^4He$ ratio obtained by crushing is representative of the initial isotopic value, [U] = 0.6 ppm [*Kurz et al.*, 1998], Th/U = 3 [*Jochum et al.*, 1983], helium was in equilibrium at eruption, and the only source of low $^3He/^4He$ ratio is radiogenic ingrowth, the eruption age for PS86-6-2 is approximately 106 ka. If instead the initial isotopic value was equal to the highest $^3He/^4He$ ratio along the oblique supersegment, 6.94 R_a, the corresponding eruption age is approximately 123 ka. These calculations indicate that $^3He/^4He$ ratios for low-^4He samples can be significantly altered by post-eruptive radiogenic ingrowth on ~100 kyr time scales, and reinforce the necessity of making measurements by crushing *in vacuo* and using a cutoff concentration. It should be noted, however, that uncertainties in parameters such as [U] may contribute significantly (~30%) to error in these age calculations. Also, in the absence of other rare gas isotopic data, it is difficult to rule out contributions by atmospheric contamination, as is suggested by near-atmospheric $^3He/^4He$ ratios in samples such as KN162-9-33-51 (1.25 R_a) and KN162-9-61-71 (1.18 R_a).

For samples with ^4He concentrations above 0.4 μccSTP/g, $^3He/^4He$ ratios vary between 6.3 and 7.3 R_a. These values are assumed to represent the mantle and are uniformly below the global average of 8 R_a for normal MORB. $^3He/^4He$ ratios for the oblique supersegment show no systematic trend with longitude (Figure 1). In contrast, for

the eastern portion of the study area, there is a trend of increasing $^3He/^4He$ ratios toward the Du Toit FZ (Figure 6). Isotopic ratios for the samples east of 16°E are well described by a linear relationship between $^3He/^4He$ and longitude, with $r^2 = 0.85$. Over this region, $^3He/^4He$ ratios increase by approximately 0.7 R_a, or approximately 20 times the average 1σ measurement error.

Interestingly, both long-wavelength MBA (Figure 6) and the geoid also increase from 16° to 24°E. As described in detail in a later section, lower values of MBA indicate thickened crust, lower mantle temperatures, and/or lower crustal density. A trend of eastward increasing MBA along the orthogonal supersegment is generally consistent with the supersegment's position between the thermally warm Bouvet Triple Junction region and the cool, long-offset Du Toit and Andrew Bain fracture zones. However, a positive correlation between MBA and $^3He/^4He$ ratio is unusual in both hotspot-affected (e.g., Iceland) and non-hotspot-affected (e.g., Australian-Antarctic Discordance [*Graham et al.*, 2001]) settings, where the $^3He/^4He$-MBA correlation is often negative. A prominent, roughly circular global geoid high, with a diameter of a few thousand kilometers, is centered at approximately the location of the Marion plume [*Lemoine et al.*, 1998]. This geoid high indicates a deep-seated and spatially extensive planetary density anomaly which could contribute to the gravity gradient observed for the orthogonal supersegment.

5. Discussion

5.1 Influence of the Bouvet plume on the oblique supersegment

Despite evidence from major element, trace element, and other isotopic data for influence of the Bouvet plume on the oblique supersegment [*le Roex et al.*, 1992], helium isotopes do not indicate that a deep-seated, relatively undegassed mantle plume is presently

affecting accretionary processes along this portion of the SWIR. Over the oblique supersegment, $^3He/^4He$ ratios range from 6.26 to 6.94 R_a, significantly below values for normal MORB. Since Bouvet is a "high $^3He/^4He$" hotspot, these values do not suggest mixing between normal MORB and a Bouvet plume end-member.

We suggest three possible explanations for the discrepancy between $^3He/^4He$ ratios and other geochemical indicators of plume influence along the oblique supersegment. The first explanation posits that lateral dispersion of the Bouvet plume away from its vertically upwelling plume conduit at Bouvet Island (3°E) is broad. Absolute plate motion of the African and Antarctic plates would shear upwelling plume material to the east [*Richards and Griffiths*, 1989], similar to the case of the Galapagos plume [*Kurz and Geist*, 1999]. For Galapagos, *Kurz and Geist* [1999] postulate that helium is preferentially extracted from the vertically upwelling plume, resulting in $^3He/^4He$ values that are high at Fernandina, inferred to be directly over the plume conduit, and that decrease rapidly away. In contrast, plume-like isotopic ratios of Sr, Nd, and Pb, which are assumed to be less incompatible than He, remain in the advected plume mantle farther away from the center of focused upwelling. Therefore, samples dredged far from the Bouvet conduit, but still within the range of Bouvet influence, could have low $^3He/^4He$ ratios but enrichments in other isotopic systems. In this way, the oblique supersegment could be influenced by Bouvet but lack high $^3He/^4He$ ratios. However, other data suggest that the broad Bouvet plume hypothesis is unlikely. For example, integrated analysis of gravity and bathymetry data indicate that the Bouvet plume along-axis anomaly is strongly localized between the Bouvet and Islas Orcadas fracture zones, ~300 km from the oblique supersegment [*Georgen et al.*, 2001]. Although a broad thermal plume should be associated with thickened crust [e.g., *Ito and Lin*, 1995a; *Allen et al.*, 1997], crustal thickness for the oblique segment inferred from gravity data is at most that of normal oceanic crust [*Georgen and Lin*, 1996]. For these

reasons, we discount invoking broad plume dispersal to explain the low $^3He/^4He$ values for the oblique supersegment.

A second explanation for the discrepancy between $^3He/^4He$ ratios and other geochemical indicators of plume influence relates to degassing of a vein assemblage emplaced by the Bouvet plume in the oblique supersegment mantle source region >30 Ma. Reconstructions suggest that interaction between the Bouvet plume and the SWIR began in the vicinity of the Shaka FZ at approximately 30 Ma, although the precise time is poorly constrained and could easily vary by as much as ±20 Ma [*Hartnady and le Roex*, 1985; *Georgen et al.*, 2001]. As the SWIR moved eastward over the plume, ridge segments to the west of the Shaka FZ progressively acquired a Bouvet plume signature. Assuming that basalts along the oblique supersegment are produced solely by preferential melting of the enriched vein assemblage, that the vein assemblage represents a closed system, and that the initial $^3He/^4He$ ratio of these veins at the time of emplacement was equal to that observed at Bouvet Island today (12.4 R_a) [*Kurz et al.*, 1998], it is possible that pre-eruptive radiogenic ingrowth of ^4He since the time of emplacement has been sufficient to lower $^3He/^4He$ ratios to the observed value of ~7 R_a.

The simplest explanation for the low $^3He/^4He$ ratios along the oblique supersegment, however, is that the isotopic, major element, and trace element variability observed by *le Roex et al.* [1992] is characteristic of melting of a heterogeneous ambient mantle at ultra-slow spreading rates, and does not require a Bouvet plume end member. This suggestion is corroborated by similar observations of juxtaposed plume, transitional, and normal MORB along the AAR, far from the Bouvet plume source [*le Roex et al.*, 1985]. Furthermore, since the mean $^3He/^4He$ ratio (6.6 R_a) for the non-plume-influenced orthogonal supersegment is very similar to that of the oblique supersegment (6.9 R_a), this explanation does not require fortuitous evolution of oblique $^3He/^4He$ ratios to match

orthogonal $^3He/^4He$ ratios. However, thorough geochemical analysis of the dredge samples from both supersegments is required to evaluate this hypothesis.

5.2 $^3He/^4He$ variability and spreading rate

Because the SWIR samples were dredged from a portion of ridge with extremely slow spreading rate, it is important to compare their $^3He/^4He$ ratios to those obtained for samples from faster-spreading ridges. Figure 7 shows the locations of all $^3He/^4He$ measurements on mid-ocean ridge glasses in the RIDGE PETDB database [*Langmuir et al.*, 2001], supplemented by analyses for the Easter microplate by *Poreda et al.* [1993] and for the Southeast Indian Ridge (SEIR) by *Graham et al.* [2001]. Analyses are available for 11 ridge systems, AAR, SWIR, MAR, SEIR, East Pacific Rise, Galapagos Spreading Center, Juan de Fuca, Kolbeinsey, Red Sea, Reykjanes Ridge, and Central Indian Ridge. This database covers both hotspot- and non-hotspot-affected portions of ridge, but does not include data from oceanic islands.

Comparison of samples from the ultra-slow SWIR to those from the slow-spreading MAR and intermediate-spreading SEIR illustrates the effects of spreading rate on $^3He/^4He$ ratios. Since it is unlikely that the oblique and orthogonal supersegments are hotspot-influenced, we cull from the RIDGE PETDB database all samples that occur within a plume-affected region. We define plume-affected regions as areas with seafloor > ~20% shallower or deeper than a local baseline depth, following the methods of *Ito and Lin* [1995b] and using ridge topography profiles from *Graham et al.* [1992b], *Ito and Lin* [1995b], *Smith and Sandwell* [1997], *Minshull et al.* [1998], *Douglass et al.* [1999], *Graham et al.* [1999], and *Georgen et al.* [2001]. We also eliminate measurements from the Australian-Antarctic Discordance (AAD) along the SEIR, an area with unusually cool

mantle temperatures. Note that both the MAR and SEIR have a large database of non-plume-affected samples, unlike other ridge systems such as the East Pacific Rise.

Examining similarly filtered data sets from the MAR, SWIR, Central Indian Ridge, Juan de Fuca Ridge, and East Pacific Rise, *Allegre et al.* [1995] suggested a linear correlation between $^{3}He/^{4}He$ standard deviation and reciprocal spreading rate. Figure 8, which includes the correlation suggested by *Allegre et al.* [1995], indicates that this relationship may no longer hold true for the larger MAR, SEIR, and SWIR databases that have accumulated over the past half-decade. However, it is clear from Figure 8 that the samples from 10°-25°E on the SWIR have significantly *lower* standard deviation than the MAR, SEIR, or full SWIR data sets. This relative helium isotopic uniformity is in strong contrast to the variability between the BTJ and 7°E, where ratios range from 7.12 to 14.9 R_a, as well as to the heterogeneity of other isotopic systems, such as $^{87}Sr/^{86}Sr$ ratios. Even though Sr, Nd, and Pb isotopic data are not yet available for the Knorr samples, six $^{87}Sr/^{86}Sr$ values for the oblique supersegment range from 0.70290 to 0.70368 [*le Roex et al.,* 1992], ranging from MORB-like to hotspot values [*Hart and Zindler*, 1989].

5.3 Low $^{3}He/^{4}He$ values

In addition to low isotopic variability, another salient characteristic of the oblique and orthogonal supersegments are $^{3}He/^{4}He$ ratios that are uniformly below "normal" MORB. Figure 9 shows $^{3}He/^{4}He$ frequency histograms for each of the ridges in Figure 8. Compared to the MAR and SEIR, a large fraction of all non-plume-affected SWIR measurements are <7.5 (Figure 9b). Moreover, between 10°E and 25°E, *all* existing measurements are <7.5 R_a. Several potential causes of these low $^{3}He/^{4}He$ ratios are now evaluated.

Degassing. As discussed in an earlier section, degassing followed by post-eruptive radiogenic ingrowth of ^{4}He by decay of U+Th can lower time-integrated ^{3}He/^{4}He ratios. However, the use of a threshold ^{4}He concentration makes it unlikely that radiogenic ingrowth is sufficient to decrease SWIR ^{3}He/^{4}He ratios by approximately 1-2 R_a, from 8 R_a to 6-7 R_a. Therefore, degassing alone does not seem to explain the low ^{3}He/^{4}He ratios.

Preferential melting of clinopyroxene. In a study of Juan de Fuca Ridge basalts, *Lupton et al.* [1993] explain correlations between ^{3}He/^{4}He ratios, $Na_{8.0}$, and $Fe_{8.0}$ by invoking preferential melting of clinopyroxene. They point out that most U and Th in peridotite is located in clinopyroxene, and that clinopyroxene melting contributes relatively larger proportions to melts formed at lower temperatures. Therefore, they suggest that cooler, slower-spreading ridges should systematically have lower ^{3}He/^{4}He ratios than warmer, faster-spreading ridges. Although this explanation is consistent with low ^{3}He/^{4}He ratios at the ultra-slow spreading SWIR, rapid He diffusion makes it unlikely that mineral-scale isotopic heterogeneity can persist for characteristic time scales of > 100 years [*Trull and Kurz*, 1993]. Thus, preferential melting of clinopyroxene at low mantle temperatures cannot explain low ^{3}He/^{4}He ratios.

Effects of prior melting. The oblique and orthogonal supersegments occupy a relatively unique location in the global ridge system, near the three-ridge intersection of the Bouvet Triple Junction. Because both the African and Antarctic plates have a significant component of eastward motion [*Gripp and Gordon*, 1990], it is possible that the western SWIR directly inherits mantle previously melted by the MAR and AAR. As mantle material travels eastward from the MAR and AAR, pre-eruptive radiogenic ingrowth of ^{4}He could lower ^{3}He/^{4}He ratios.

A series of calculations quantitatively illustrates the effects of mantle aging on ^{3}He/^{4}He ratios. Assuming (1) closed system evolution of the mantle, (2) ^{4}He concentrations in

MORB of 0.04, 0.4, 4, and 40 μccSTP/g (spanning most of the range observed in the SWIR sample suite), (3) 10% melting, (4) perfectly incompatible partitioning behavior of helium, (5) mantle uranium concentration [U] of 0.006 ppm [*Jochum et al.*, 1983], and (6) Th/U = 3 [*Jochum et al.*, 1983], the minimum time required to lower a mantle $^3He/^4He$ ratio of 8 R_a by 10% is approximately 100 Myr (Figure 10). For samples with ^4He above the cutoff threshold of 0.4 μccSTP/g, this time is roughly 1 Gyr. This time scale becomes greater than the age of the Earth for higher ^4He concentrations, such as 4 and 40 μccSTP. Therefore, prior melting is not a feasible mechanism for lowering $^3He/^4He$ ratios from 8 to ~6-7 R_a on reasonable time scales.

Mantle heterogeneity. $^3He/^4He$ ratios as low as 6.2 R_a have been observed for basalts from the AAD [*Graham et al.*, 2001]. Analysis of basalts [*Klein et al.*, 1991] and numerical modeling work [*West et al.*, 1997] suggest that mantle temperatures may be as much as 150°C lower in the AAD than along surrounding sections of the SEIR. *Graham et al.* [2001] note a correlation between $^3He/^4He$ ratios and $Fe_{8.0}$, implying that lower $^3He/^4He$ ratios are associated with shallower depths of melting. Two possible explanations for this correlation include a vertically stratified mantle and melting of discrete heterogeneities [*Graham et al.*, 2001]. The first explanation assumes that the upper mantle is vertically stratified, with relatively more degassed material with lower $^3He/^4He$ ratios overlying less degassed material. Since melting occurs at shallower depths for thermally cool ridges such as the western SWIR and eastern SEIR than for faster-spreading or warmer ridges, melts produced at cool ridges should have lower $^3He/^4He$ ratios. A good test of this hypothesis for the SWIR will come from $Fe_{8.0}$ variation along the orthogonal and oblique supersegments, data which are not yet available. Interestingly, the portion of the SWIR between the Melville FZ at 61°E and the Rodrigues Triple Junction at 70°E has the greatest axial depth along the entirety of the SWIR, suggesting anomalously cool mantle

temperatures [*Rommevaux-Jestin et al.*, 1997; *Cannat et al.*, 1999]. However, limited investigation of $^3He/^4He$ ratios from the eastern SWIR near the Rodrigues Triple Junction has yielded values of 7.68, 8.11, and 8.09 R_a [*Mahoney et al.*, 1989], higher than values observed along the orthogonal and oblique supersegments and counter to the predictions of the vertically stratified mantle model. Furthermore, three-dimensional thermal modeling calculations for passive plate separation predict that for depths within the melting region, axial temperature for the oblique supersegment is approximately 50-100°C lower than the orthogonal supersegment [*Georgen et al.*, 1998]. Therefore, if the vertically stratified mantle model applies, there should be a systematic difference between relatively low $^3He/^4He$ ratios along the oblique supersegment and relatively high $^3He/^4He$ ratios for the orthogonal supersegment. Although the predicted difference between oblique and orthogonal supersegment $^3He/^4He$ ratios may not be as great as the AAD $^3He/^4He$ anomaly because of the overall colder thermal regime of the SWIR, no such difference was observed.

Preferential melting of discrete mantle heterogeneities with lower solidus temperature than surrounding material may also result in low $^3He/^4He$ ratios [*Graham et al.*, 2001]. For example, if crustal recycling veined the AAD MORB source with low-$^3He/^4He$ garnet pyroxenite, then such veins would form a relatively large proportion of melt generated at cool ridges because they melt preferentially to mantle peridotite [*Graham et al.*, 2001]. With increasing mantle temperature and depth of melting, mantle peridotite with high $^3He/^4He$ would dilute garnet pyroxenite melts, resulting in MORB with $^3He/^4He$ ratios closer to 8 R_a. In general, the most likely explanation for low $^3He/^4He$ ratios appears to be introduction of recycled crustal or oceanic lithospheric material [e.g., *Kurz et al.*, 1982b; *Graham et al.*, 1993b; *Sarda et al.*, 2000; *Moreira and Kurz*, 2001], with relatively high (U+Th)/He ratios, into the source region for orthogonal and oblique supersegment MORB.

It is important to note, however, that evaluation of this hypothesis requires geochemical data from the oblique and orthogonal supersegments that are not yet available.

Overall, the existence of low $^3He/^4He$ ratios over a long portion of the SWIR suggests that the average value of 8±1 R/R_a for normal MORB may need to be referenced judiciously. It is possible that average MORB $^3He/^4He$ ratios vary between ridge systems. Currently, well-sampled ridges such as the slow-spreading MAR are over-represented in the global $^3He/^4He$ ratio database. However, the results of this study suggest that at least the ultra-slow spreading SWIR has systematically lower values than 8±1 R/R_a.

5.4 Helium isotope ratios and hotspot flux

Although $^3He/^4He$ ratios for this new SWIR data do not appear to reflect contamination by the Bouvet plume, the global $^3He/^4He$ data set described above permits comparison between $^3He/^4He$ ratios and geophysical indicators of plume influence. Such comparisons place further constraints on potential causes for $^3He/^4He$ variability and comprise an independent test of the hypothesis that high $^3He/^4He$ ratios come from the deep mantle. Here we evaluate the possibility that $^3He/^4He$ ratios are correlated with hotspot crustal production or flux. Qualitatively, larger-flux hotspots, such as Hawaii and Galapagos, appear to have higher $^3He/^4He$ ratios than smaller hotspots, such as Shona and Bouvet. As a proxy for hotspot flux, we first examine the covariation of mantle Bouguer anomaly and $^3He/^4He$ ratios for the north Atlantic (Iceland and Azores) and the south Atlantic (Bouvet and Shona).

Gravity calculations. Calculation of MBA requires well-constrained seafloor bathymetry and gravity. The primary bathymetric data source for this study was the shiptrack soundings used by *Smith and Sandwell* [1997] to calculate predicted seafloor topography from combined ship surveys and satellite-altimetry-derived gravity.

Advantages of this database include its global coverage and prior editing by *Smith and Sandwell* [1997] to retain only high-quality, well-navigated seafloor depths. Using the predicted topography grids to calculate MBA is circular since predicted topography calculations include satellite altimetry; this problem was avoided by using only shiptrack soundings. Survey data from a number of individual cruises relevant to the areas of interest, including *Douglass et al.* [1995], *Detrick et al.* [1995], *Searle et al.* [1998], *Grindlay et al.* [1998], and *Ligi et al.* [1999], were also added to this database. Shiptrack coverage is relatively dense along long portions of the ridge axis. To guard against overinterpretation of somewhat sparser bathymetry data off-axis, maps of gravity anomalies calculated using shiptrack soundings are masked with white where grid nodes lack shiptrack control within a 5' radius.

We extracted free-air anomaly (FAA) gravity data from the 2' grid spacing global database calculated by *Sandwell and Smith* [1997] from declassified Geosat and ERS-1 altimetry. *Neumann et al.* [1993] showed that the 3' grid that preceded the current 2' database is coherent with bathymetry to wavelengths as short as 27.5 km for the MAR between 31° and 36°S. Similarly, *Rommevaux-Jestin et al.* [1997] found reasonably good correspondence between shipboard and satellite free-air anomaly for wavelengths greater than 30-50 km for the eastern SWIR. Further, *Georgen et al.* [2001] suggest that intermediate- to long-wavelength features, such as hotspot swells, are well-resolved in gravity calculations based on the satellite altimetry database.

The free-air gravity data contains signals from seafloor topography as well as crust and mantle density anomalies. To reveal the more subtle crust and mantle anomalies, we used well-established algorithms for calculating MBA [*Kuo and Forsyth,* 1988; *Lin et al.*, 1990] and subtracted from FAA the theoretical gravity effects of the water-crust and crust-mantle interfaces assuming a constant density, 5-km-thick model crust. The densities for

seawater, crust, and mantle were assumed to be 1030, 2800, and 3300 kg/m^3, respectively. The resulting mantle Bouguer anomaly maps are shown in Figures 11 and 12 for the south and north Atlantic, respectively. Although MBA contains signals from variations in both crustal thickness and mantle temperature, *Ito and Lin* [1995a] suggest that crustal thickness may account for as much as 70% of along-axis MBA. We therefore assume that MBA reflects, to first order, hotspot magmatic production or flux, although it may also contain information about crustal density variations.

Correlation between ^{3}He/^{4}He and MBA for the north and south Atlantic. Prominent MBA lows exist in the vicinity of Iceland, Azores, Bouvet, and Shona (Figures 11-13). Around Bouvet, a ~75-100 mGal low between the Bouvet and Islas Orcadas FZs is well-correlated with high ^{3}He/^{4}He ratios (Figure 11). However, high ^{3}He/^{4}He values also exist in areas which lack pronounced MBA lows, including the ridge segment between the Islas Orcadas and Shaka fracture zones. In contrast, long-wavelength MBA lows and bathymetric highs correspond well to elevated ^{3}He/^{4}He ratios around Iceland (Figure 13). Although the MAR axis around the Azores has both shallow depth and low MBA, there does not appear to be a systematic correlation with ^{3}He/^{4}He (Figure 13).

Figure 14 quantifies the relationship between ^{3}He/^{4}He ratios and MBA for these four hotspots. The correlation is strongest for Iceland, with an r^2 of 0.69. For a relatively limited range in MBA compared to Bouvet, Iceland, and Azores, Shona also has a reasonably good correlation between ^{3}He/^{4}He and MBA, with an r^2 of 0.56. However, correlations are weak for both Azores ($r^2 = 0.13$) and Bouvet ($r^2 = 0.11$).

The lack of significant correlation between MBA and ^{3}He/^{4}He ratio around the Azores and Bouvet may be due to several factors, including ridge geometry and source geochemistry. Along the Reykjanes Ridge, ridge offsets are generally small; only one transform offset occurs between the Charlie Gibbs FZ and Iceland. This ridge geometry is

significantly different from that along the western SWIR, where long transform offsets separate relatively short ridge segments. It is possible that much of the variability in MBA around Bouvet reflects segment-scale processes, such as magmatic focusing toward the center of segments [*Magde and Sparks*, 1997] and thermal effects of transform cooling [*Phipps Morgan and Forsyth*, 1988]. In the case of the Azores, the lack of correlation between MBA and $^3He/^4He$ ratios may reflect the absence of a $^3He/^4He$ anomaly rather than the fidelity of the MBA signal. As noted earlier, low $^3He/^4He$ values around the Azores may be explained by the addition of (U+Th) into the plume source region by recycled subducted oceanic crust [*Kurz et al.*, 1982b].

Hotspot flux and $^3He/^4He$ ratios. In order to perform a more global comparison between $^3He/^4He$ ratios and geophysical indicators of plume robustness, we explore the relationship between geophysical anomaly amplitudes and maximum $^3He/^4He$ values for various hotspots (Figure 15). To describe a given hotspot, we select $^3He/^4He_{max}$ rather than some statistical average of $^3He/^4He$ ratios to avoid ambiguity associated with unequal sample numbers and spatial coverage. Where available, $^3He/^4He_{max}$ is the maximum $^3He/^4He$ ratio measured on an oceanic island. However, for hotspots such as Easter where such measurements do not exist, $^3He/^4He_{max}$ is defined as the highest $^3He/^4He$ ratio observed along a nearby ridge system. ΔRB, ΔMBA, and W are employed as described in *Ito and Lin* [1995b] to describe plume residual bathymetry anomaly amplitude, MBA anomaly amplitude, and waist width, respectively. W is defined as the length of ridge affected by an on- or near-axis plume [*Schilling*, 1991]. To first order, W reflects a balance between vertical plume flux and horizontal plume dispersion. W is well described by the scaling relationship

$$Q = W^2U/c^2 \qquad (1)$$

where Q is vertical plume flux, U is full-spreading rate, and c is a scaling constant equal to approximately 3 [*Ribe et al.*, 1995; *Feighner and Richards*, 1995; *Ito et al.*, 1996].

The correlation between ΔRB and $^3He/^4He_{max}$ is relatively weak ($r^2 = 0.39$) (Figure 15a), possibly because ΔRB is affected by processes such as isostatic compensation. In contrast, ΔMBA, which reflects integrated crustal and mantle density anomalies over a large depth range, correlates more strongly with $^3He/^4He_{max}$ ($r^2 = 0.74$). The correlation between W and $^3He/^4He_{max}$ is even closer ($r^2 = 0.91$), while r^2 for Q vs $^3He/^4He_{max}$ is 0.97.

Note that only "high-$^3He/^4He$" hotspots (i.e., hotspots for which most available $^3He/^4He$ ratios are greater than normal MORB) are included in the calculation of regression lines for ΔMBA, W, and Q. Because of the possibility of contamination by subducted crustal or lithospheric material, the "low-$^3He/^4He$" Azores and Tristan hotsptos are not used in the regression calculation. Although it is possible that the "high-$^3He/^4He$" hotspots have experienced similar contamination, it is difficult to quantify the extent to which this may have occurred. For reference, Figure 15d also shows a point representing Hawaii. However, since Hawaiian flux was estimated by multiplying the scaling-law-derived flux for Iceland by the ratio of the Hawaii and Iceland fluxes derived by *Sleep* [1990], use of Hawaii in calculating the correlation between $^3He/^4He_{max}$ and Q is tenuous and was avoided.

The particularly strong correlation between $^3He/^4He_{max}$ and Q may reflect a combination of effects. The simplest interpretation of this correlation is that high-flux plumes originate at relatively greater mantle depths, where they tap less-degassed mantle material. A deep source region for the Iceland plume inferred from $^3He/^4He$ data is qualitatively consistent with seismic evidence for an Icelandic plume conduit which extends to at least a depth of 400 km, if not greater [*Wolfe et al.*, 1997; *Shen et al.*, 1998]. However, since similar

seismic constraints are lacking for other plumes, such as Galapagos, Reunion, and Bouvet, it is difficult to conclusively extend this argument to lower-$^3He/^4He$ plumes.

6. Conclusions

The main results of this study of $^3He/^4He$ isotope systematics along the western SWIR include the following:

(1) $^3He/^4He$ isotopic ratios are uniformly low along both the oblique supersegment (9°E-16°E) and the orthogonal supersegment (16°E-24°E) of the SWIR. Ratios range from 6.3 to 7.3 R_a, significantly lower than the global MORB average of 8 ± 1 R_a. These low ratios show that average values of $^3He/^4He$ for "normal" MORB ratios must be used carefully, and may suggest that average $^3He/^4He$ ratios vary from ridge to ridge. The low ratios are not the result of post-eruptive radiogenic ingrowth processes. Possible, although unlikely, explanations for low $^3He/^4He$ ratios include a vertically stratified mantle or melting of mantle which has experienced a prior melting event. The preferred explanation is introduction of U+Th into the SWIR mantle source by recycling of crustal or lithospheric material, although detailed evaluation of this explanation awaits further geochemical data from the oblique and orthogonal supersegments.

(2) Despite prediction by earlier studies of an inverse relationship between $^3He/^4He$ variability and spreading rate, $^3He/^4He$ ratios between 9°E and 24°E are relatively constant, with a standard deviation from the mean of approximately 0.3 R_a.

(3) Despite a significant difference in ridge orientation between the orthogonal and oblique supersegments, there does not appear to be any systematic isotopic difference between the two ridge sections. Moreover, there is no evidence from high $^3He/^4He$ ratios for influence of the high-$^3He/^4He$ Bouvet plume on either supersegment. Along the

orthogonal supersegment, $^3He/^4He$ ratios increase eastward. Although the overall change in $^3He/^4He$ along this trend is small, $^3He/^4He$ ratios are significantly correlated with longitude and MBA.

(4) Global correlations between $^3He/^4He$ ratios and mantle Bouguer anomaly, plume waist width, and plume flux suggest that high-flux plumes originate at relatively deep mantle depths, where they tap comparatively undegassed mantle.

Acknowledgments: We are grateful to the scientific party and crew of Knorr leg 162, whose unparalleled dedication, perseverance, and resourcefulness made possible a very successful dredging program despite the most difficult of circumstances. We also acknowledge the tremendous assistance provided by Josh Curtice, whose efforts and expertise in the laboratory made it possible to amass the SWIR data set in a remarkably short period of time. JG thanks the members of the WHOI Tectonics and Geodynamics discussion group, as well as Bob Detrick and Maria Zuber for their input and suggestions. Manuel Moreira graciously provided an unpublished $^3He/^4He$ measurement for the Azores.

References

Allegre, C.J., M. Moreira, and T. Staudacher, $^{4}He/^{3}He$ dispersion and mantle convection, *Geophys. Res. Lett.*, 22, 2325-2328, 1995.

Allen, R.M., G. Nolet, W.J. Morgan, K. Vogfjord, B.H. Bergsson, P. Erlendsson, G.R. Foulger, S. Jakobsdottir, B.R. Julian, M. Pritchard, S. Ragnarsson, and R. Stefansson, Crustal thickness across Iceland, *EOS, Trans. AGU*, 78, F500, 1997.

Anderson, D.L., The statistics of helium isotopes along the global spreading ridge system and the central limit theorem, *Geophys. Res. Lett.*, 27, 2401-2404, 2000.

Cannat, M., C. Rommevaux-Jestin, D. Sauter, C. Deplus, and V. Mendel, Formation of the axial relief at the very slow spreading Southwest Indian Ridge (49 degrees to 69 degrees E), *J. Geophys. Res.*, 104, 22825-22843, 1999.

DeMets, C., R.G. Gordon, D. Argus, and S. Stein, Current plate motions, *Geophys. J. Int.*, 101, 425-478, 1990.

DeMets, C., R.G. Gordon, D.F. Argus, and S. Stein, Effect of recent revisions to the geomagnetic reversal time scale on estimates of current plate motions, *Geophys. Res. Lett.*, 21, 2191-2194, 1994.

Detrick, R.S., H.D. Needham, and V. Renard, Gravity anomalies and crustal thickness variations along the Mid-Atlantic Ridge between 33°N and 40°N, *J. Geophys. Res.*, 100, 3767-3787, 1995.

Dick, H.J.B., H. Schouten, and J. Lin, Crustal (?) accretion during extreme oblique spreading at an ultra-slow mid-ocean ridge, *EOS, Trans. AGU*, spring 2001a.

Dick, H.J.B., J. Lin, and H. Schouten, An investigation of the effects of ridge geometry on crustal accretion at ultra-slow spreading rates: The SW Indian Ridge from 9°-23.5°E, cruise report, R/V Knorr cruise 162, legs VII to IX (Dec. 9, 2000 – Jan. 30, 2001), 2001b.

Douglass, J., J.G. Schilling, R.H. Kingsley, and C. Small, Influence of the Discovery and Shona mantle plumes on the southern Mid-Atlantic Ridge: Rare Earth evidence, *Geophys. Res. Lett.*, 22, 2893-2986, 1995.

Douglass, J., J.G. Schilling, and D. Fontignie, Plume-ridge interactions of the Discovery and Shona mantle plumes with the southern Mid-Atlantic Ridge (40°-55°S), *J. Geophys. Res.*, 104, 2941-2962, 1999.

Feighner, M.A. and M.A. Richards, The fluid dynamics of plume-ridge and plume-plate interactions: An experimental investigation, *Earth Planet. Sci. Lett.*, 129, 171-182, 1995.

Georgen, J. and J. Lin, Constraints from bathymetric and gravity anomalies of the effects of the Marion and Bouvet hotspots on the Southwest Indian Ridge, *EOS, Trans. AGU*, 77, F671, 1996.

Georgen, J., J. Lin, and H.J.B. Dick, Models of mantle upwelling beneath the Southwest Indian Ridge: The effects of ridge-transform geometry on magma supply at an ultra-slow spreading ridge, *EOS, Trans. AGU*, 79, F854, 1998.

Georgen, J., J. Lin, and H.J.B. Dick, Evidence from gravity anomalies for interactions of the Marion and Bouvet hotspots with the Southwest Indian Ridge: Effects of transform offsets, *Earth Planet. Sci. Lett.,* 187, 283-300, 2001.

Graham, D.W., W.J. Jenkins, M.D. Kurz, and R. Batiza, Helium isotope disequilibrium and geochronology of glassy submarine basalts, *Nature*, 326, 284-286, 1987.

Graham, D., J. Lupton, F. Albarede, and M. Condomines, Extreme temporal homogeneity of helium isotopes at Piton la Fournaise, Reunion Island, *Nature*, 347, 545-548, 1990.

Graham, D.W., S.E. Humphris, W.J. Jenkins, and M.D. Kurz, Helium isotope geochemistry of some volcanic rocks from Saint Helena, *Earth Planet. Sci. Lett.*, 110, 121-131, 1992a.

Graham, D.W., W.J. Jenkins, J.-G. Schilling, G. Thompson, M.D. Kurz, and S.E. Humphris, Helium isotope geochemistry of mid-ocean ridge basalts from the South Atlantic, *Earth Planet. Sci. Lett.*, 110, 133-147, 1992b.

Graham, D.W., D.M. Christie, K.S. Harpp, and J.E. Lupton, Mantle plume helium in submarine basalts from the Galapagos platform, *Science*, 262, 2023-2026, 1993a.

Graham, D.W., S.E. Humphris, W.J. Jenkins, and M.D. Kurz, Helium isotope geochemistry of some volcanic rocks from Saint Helena, *Earth Planet. Sci. Lett.*, 81, 127-150, 1993b.

Graham, D.W., K.T.M. Johnson, L.D. Prieve, and J.E. Lupton, Hotspot-ridge interaction along the Southeast Indian Ridge near Amsterdam and St. Paul islands: helium isotope evidence, *Earth Planet. Sci. Lett.*, 167, 297-310, 1999.

Graham, D.W. J.E. Lupton, F.J. Spera, and D.M. Christie, Upper-mantle dynamics revealed by helium isotope variations along the Southeast Indian Ridge, *Nature*, 409, 701-703, 2001.

Grindlay, N.R., J. Madsen, C. Rommevaux-Jestin, and J. Sclater, A different pattern of ridge segmentation and mantle Bouguer gravity anomalies along the ultra-slow spreading Southwest Indian Ridge (15°30'E to 25°E), *Earth Planet. Sci. Lett.,* 161, 243-253, 1998.

Gripp, A.E. and R.G. Gordon, Current plate velocities relative to the hotspots incorporating the NUVEL-1 global plate motion model, *Geophys. Res. Lett.*, 17, 1109-1112, 1990.

Hart, S.R., J.G. Schilling, and J.L. Powell, Basalts from Iceland and along the Reykjanes Ridge: Strontium isotope geochemistry, *Nature*, 246, 104-107, 1973.

Hart, S.R. and A. Zindler, In search of a bulk-Earth composition, *Chem. Geol.*, 57, 247-267, 1986.

Hart, S.R. and A. Zindler, Constraints on the nature and development of chemical heterogeneities in the mantle, in *Mantle convection: plate tectonics and global dynamics*, W. R. Peltier (ed.), *The Fluid Mechanics of Astrophysics and Geophysics*, 4, 261-387, 1989.

Hartnady, C.J.H. and A.P. le Roex, Southern Ocean hotspot tracks and the Cenozoic absolute motion of the African, Antarctic, and South American plates, *Earth Planet. Sci. Lett., 75*, 245-257, 1985.

Hilton, D.R., M.F. Thirwall, R.N. Taylor, B.J. Murton, and A. Nichols, Controls on magmatic degassing along the Reykjanes Ridge with implications for the helium paradox, *Earth Planet. Sci. Lett.*, 183, 43-50, 2000.

Ito, G. and J. Lin. Mantle temperature anomalies along the present and paleoaxes of the Galapagos spreading center as inferred from gravity analysis, *J. Geophys. Res.*, 100, 3733-3745, 1995a.

Ito, G. and J. Lin, Oceanic spreading center-hotspot interactions: Constraints from along-isochron bathymetric and gravity anomalies, *Geology*, 23, 657-660, 1995b.

Ito, G., J. Lin, and C.W. Gable, Dynamics of mantle flow and melting at a ridge-centered hotspot: Iceland and the Mid-Atlantic Ridge, *Earth Planet. Sci. Lett.*, 144, 53-74, 1996.

Ito. G., J. Lin, and C.W. Gable, Interaction of mantle plumes and migrating mid-ocean ridges: Implications for the Galapagos plume-ridge system, *J. Geophys. Res.,* 102, 15403-15417, 1997.

Jochum, K.L., A.W. Hoffmann, E. Ito, H.M. Seufert, and W.M. White, Potassium, uranium, and thorium in mid-ocean ridge basalt glasses and heat production, K/U, and K/Rb in the mantle, *Nature,* 306, 431, 1983.

Klein, E.M., C.H. Langmuir, and H. Staudigal, Geochemistry of basalts from the South East Indian Ridge, 115°E-138°E, *J. Geophys. Res.*, 96, 2089-2107, 1991.

Kuo, B.Y and D.W. Forsyth, Gravity anomalies of the ridge-transform system in the South Atlantic between 31 and 34.5°S: Upwelling centers and variations in crustal thickness, *Mar. Geophys. Res.,* 10, 205-232, 1988.

Kurz, M.D. and D. Geist, Dynamics of the Galapagos hotspot from helium isotope geochemistry, *Geochim. Cosmochim. Acta*, 63, 4139-4156, 1999.

Kurz, M.D. and W.J. Jenkins, The distribution of helium in oceanic basalt glasses, *Earth Planet. Sci. Lett.*, 53, 41-54, 1981.

Kurz, M.D., and D.P. Kammer, Isotopic evolution of Mauna Loa volcano, *Earth Planet. Sci. Lett.,* 103, 257-269, 1991.

Kurz, M.D., W.J. Jenkins, and S.R. Hart, Helium isotope systematics of oceanic islands and mantle heterogeneity, *Nature*, 297, 43-47, 1982a.

Kurz, M.D., W.J. Jenkins, J.G. Schilling, and S.R. Hart, Helium isotopic variations in the mantle beneath the central North Atlantic Ocean, *Earth Planet. Sci. Lett.*, 58, 1-14, 1982b.

Kurz, M.D., W.J. Jenkins, S.R. Hart, and D.A. Clague, Helium isotopic variations in volcanic rocks from Loihi Seamount and the Island of Hawaii, *Earth Planet. Sci. Lett.,* 66, 388-406, 1983.

Kurz, M.D., P.S. Meyer, and H. Sigurdsson, Helium isotope systematics within the neovolcanic zones of Iceland, *Earth Planet. Sci. Lett.,* 74, 291-305, 1985.

Kurz, M.D., J.J. Gurney, W.J. Jenkins, and D.E. Lott, Helium isotopic variability from the Orapa Kimberlite, *Earth Planet. Sci. Lett.*, 86, 57-68, 1987.

Kurz, M.D., T.C. Kenna, J.C. Lassiter, and D.J. DePaolo, Helium isotopic evolution of Mauna Kea volcano: first results from the 1-km drill core, *J. Geophys. Res.*, 101, 11781-11791, 1996.

Kurz, M.D., A.P. le Roex, and H.J.B. Dick, Isotope geochemistry of the oceanic mantle near the Bouvet triple junction, *Geochim. Cosmochim. Acta.*, 62, 841-852, 1998.

Lemoine, F.G., S.C. Kenyon, J.K. Factor, R.G. Trimmer, N.K. Pavlis, D.S. Chinn, C.M. Cox, S.M. Klosko, S.B. Lutchke, M.H. Torrence, Y.M. Wang, R.G. Willianson, E.C. Pavlis, R.H. Rapp, and T.R. Olson, The development of the Joint NASA GSFC and NIMI Geopotential Model EGM96, NASA Goddard Space Flight Center, Greenbelt, Maryland, 1998.

le Roex, A.P., H.J.B. Dick, A.J. Erlank, A.M. Reid, F.A. Frey, and S.R. Hart, Geochemistry, mineralogy and petrogenesis of lavas erupted along the Southwest Indian Ridge between the Bouvet Triple Junction and 11 degrees east, *J. Petrol.,* 24, 267-318, 1983.

le Roex, A.P., H.J.B. Dick, A.M. Reid, F.A. Frey, A.J. Erlank, and S.R. Hart, Petrology and geochemistry of basalts from the American-Antarctic Ridge, Southern Ocean: Implications for the westward influence of the Bouvet mantle plume, *Contrib. Mineral. Petrol.*, 90, 367-380, 1985.

le Roex, A.P., H.J.B. Dick, and R.T. Watkins, Petrogenesis of anomalous K-enriched MORB from the Southwest Indian Ridge: 11°53'E to 14°38'E, *Contrib. Mineral. Petrol.*, 110, 253-268, 1992.

Ligi, M., E. Bonatti, G. Bortoluzzi, G. Carrara, P. Fabretti, D. Penitenti, D. Gilod, A.A. Peyve, S. Skolotnev, and N. Turko, Death and transfiguration of a triple junction in the south Atlantic, *Science*, 276, 243-245, 1997.

Ligi, M. E. Bonatti, G. Bortoluzzi, G. Carrara, P. Fabretti, D. Gilod, A.A. Peyve, S. Skolotnev, and N. Turko, Bouvet Triple Junction in the South Atlantic: Geology and evolution, *J. Geophys. Res.*, 104, 29365-29385, 1999.

Lin, J., G.M. Purdy, H. Schouten, J.-C. Sempere, and C. Zervas, Evidence from gravity data for focused magmatic accretion along the Mid-Atlantic Ridge, *Nature*, 344, 627-632, 1990.

Lupton, J.E., D.W. Graham, J.R. Delaney, and H.P. Johnson, Helium isotope variations in Juan de Fuca Ridge basalts, *Geophys. Res. Lett.*, 20, 1851-1854, 1993.

Magde, L.S. and D.W. Sparks, Three-dimensional mantle upwelling, melt generation, and melt migration beneath segment slow spreading ridges, *J. Geophys. Res.*, 102, 20571-20583, 1997.

Mahoney, J.J., J.H. Natland, W.M. White, R. Poreda, S.H. Bloomer, R.L. Fisher, and A.N. Baxter, Isotopic and geochemical provinces of the western Indian Ocean spreading centers, *J. Geophys. Res.*, 94, 4033-4052, 1989.

Mahoney, J., A.P. le Roex, Z. Peng, R.L. Fisher, and J.H. Natland, Southwestern limits of Indian Ocean ridge mantle and the origin of low $^{206}Pb/^{204}Pb$ mid-ocean ridge basalt: Isotope systematics of the central Southwest Indian Ridge (17°-50°E), *J. Geophys. Res.*, 97, 19771-19790, 1992.

Minshull, T.A., N.J. Bruguier, and J.M. Brozena, Ridge-plume interactions or mantle heterogeneity near Ascension Island?, *Geology*, 26, 115-118, 1998.

Mitchell, N.C. and R.A. Livermore, Spiess Ridge: An axial high on the slow spreading Southwest Indian Ridge, *J. Geophys. Res.*, 103, 15457-15471, 1998.

Moreira, M., T. Staudacher, P. Sarda, J.G. Schilling, and C.J. Allegre, A primitive plume neon component in MORB: The Shona Ridge anomaly, South Atlantic (51-52 S), *Earth Planet. Sci. Lett.*, 133, 367-377, 1995.

Moreira, M. and M.D. Kurz, Subducted oceanic lithosphere and the origin of the 'himu' basalt helium isotopic signature, *Earth Planet. Sci. Lett.*, 189, 49-57, 2001.

Neumann, G.A., D.W. Forsyth, and D. Sandwell, Comparison of marine gravity from shipboard and high-density satellite altimetry along the Mid-Atlantic Ridge, 30.5°-35.5°S, *Geophys. Res. Lett.*, 20, 1639-1642, 1993.

Poreda, R.J. and J.G. Schilling, Helium isotope ratios in Easter Microplate basalts, *Earth Planet. Sci. Lett.*, 119, 319-329, 1993.

Poreda, R., J.G. Schilling, and H. Craig, Helium and hydrogen isotopes in ocean ridge basalts north and south of Iceland, *Earth Planet. Sci. Lett.*, 78, 1-17, 1985.

Phipps Morgan, J. and D.W. Forsyth, 3-D flow and temperature perturbations due to transform offset: effects on oceanic crustal and upper mantle structure, *J. Geophys. Res.*, 93, 2955-2966, 1988.

Ribe, N.M., U.R. Christensen, and J. Theissing, The dynamics of plume-ridge interaction, 1: ridge-centered plumes, *Earth Planet. Sci. Lett.*, 134, 155-168, 1995.

Richards, M.A. and R.W. Griffiths, Thermal entrainment by deflected mantle plumes, *Nature*, 342, 1989.

Rommevaux-Jestin, C., C. Deplus, and P. Patriat, Mantle Bouguer anomaly along an ultra-slow spreading ridge: Implications for accretionary processes and comparison with results from central Mid-Atlantic Ridge, *Mar. Geophys. Res.*, 19, 481-503, 1997.

Langmuir, C.H., Ryan, W.B.F., K. Lehnert, Y.J. Su, and W. Jin, Petrological database of the ocean floor, http://petdb.ldeo.columbia.edu/petdb.

Sandwell, D.T. and W.H.F. Smith, Marine gravity anomaly from Geosat and ERS 1 satellite altimetry, *J. Geophys. Res.*, 102, 10039-10054, 1997.

Sarda, P., M. Moreira, T. Staudacher, J.G. Schilling, and C.J. Allegre, Rare gas systematics on the southernmost Mid-Atlantic Ridge: Constraints on the lower mantle and Dupal source, *J. Geophys. Res.*, 105, 5973-5996, 2000.

Schilling, J.-G., Azores mantle blob: Rare earth evidence, *Earth Planet. Sci. Lett.*, 25, 103-115, 1975.

Schilling, J.-G., Fluxes and excess temperatures of mantle plumes inferred from their interaction with migrating mid-ocean ridges, *Nature*, *352*, 397-403, 1991.

Searle, R.C., J. A. Keeton, R. B. Owens, R.S. White, R. Mecklenburgh, B. Parsons, and S.M. Lee, The Reykjanes Ridge: structure and tectonics of a hot-spot-influenced slow-spreading ridge, from multibeam bathymetry, gravity, and magnetic investigations, *Earth Planet. Sci. Lett.*, 160, 463-478, 1998.

Shen, Y., S.C. Solomon, I.Th. Bjarnason, and C.J. Wolfe, Seismic evidence for a lower mantle origin of the Iceland mantle plume, *Nature*, 395, 62-65, 1998.

Sleep, N.H., Hotspots and mantle plumes: Some phenomenology, *J. Geophys. Res.*, 95, 6715-6736, 1990.

Smith, W.H.F. and D. Sandwell, Global sea floor topography from satellite altimetry and ship depth soundings, *Science,* 277, 1956-1962, 1997.

Staudacher, T., Ph. Sarda, and C.J. Allegre, Noble gas systematics of Reunion Island, Indian Ocean, *Chem. Geol.*, 89, 1-17, 1990.

Trull, T.W. and M.D. Kurz, Experimental measurements of ^{3}He and ^{4}He mobility in olivine and clinopyroxene at magmatic temperatures, *Geochim. Cosmochim. Acta*, 57, 1313-1324, 1993.

West, B.P., W.S.D. Wilcock, J.-C. Sempéré, and L. Géli, Three-dimensional structure of asthenospheric flow beneath the Southeast Indian Ridge, *J. Geophys. Res.,* 102, 7783-7802, 1997.

Wolfe, C.J., I.Th. Bjarnason, J.C. VanDecar, and S.C. Solomon, Seismic structure of the Iceland mantle plume, *Nature*, 385, 245-247, 1997.

Table 1. Helium data for the western SWIR, oblique supersegment (10°-16°E)

Sample	Lat. (°S)	Long. (°E)	Depth (m)	^{4}He conc. (μccSTP/g)	^{3}He/^{4}He (R/R_a)	+/	Crush/ melt
KN162-9-28-32	-52.90	10.67	3803	0.0184	5.81	0.26	crush
KN162-9-31-1	-52.81	11.08	3074	2.02	6.61	0.05	crush
KN162-9-28-32	-52.90	10.67	3803	0.0184	5.81	0.26	crush
KN162-9-30-12	-52.99	11.16	3587	2.97	6.49	0.04	crush
KN162-9-32-11	-52.75	11.22	2720	0.00383	4.71	1.15	crush
KN162-9-33-51	-52.82	11.39	1462	0.0299	1.25	0.14	crush
KN162-9-34-39	-52.86	11.43	2126	2.05	6.52	0.04	crush
KN162-9-36-27	-52.75	11.71	4017	13.8	6.94	0.05	crush
KN162-9-49-13	-52.48	12.86	4193	1.55	6.80	0.04	crush
PS86-6-1	-52.35	13.13	~4000	0.0171	3.43	0.16	melt
PS86-6-2	-52.35	13.3	~4000	0.02819	3.21	0.07	melt
PS86-6-2-12996				0.00242	5.98	0.40	crush
KN162-9-61-71	-52.10	14.60	2282	0.01391	1.18	0.08	crush
PS86-2-14	-52.22	14.63	~3200	15.92	6.26	0.03	melt
KN162-9-64-1	-52.29	15.64	2947	0.006447	6.31	0.34	crush

Table 2. Helium data for the western SWIR, orthogonal supersegment (16°-23°E)

Sample	Lat. (°S)	Long. (°E)	Depth (m)	^{4}He conc. (μccSTP/g)	^{3}He/^{4}He (R/R_a)	+/	Crush/ melt
KN162-7-2-1	-52.33	16.23	3855	0.6343	6.77	0.04	crush
KN162-7-3-27	-52.30	16.51	3481	0.5479	6.57	0.03	crush
KN162-7-4-31	-52.36	17.11	3928	2.972	6.67	0.03	crush
KN162-7-5-1	-52.42	17.43	3090	1.106	6.64	0.04	crush
KN162-7-6-2	-52.52	17.70	3582	15.1	6.80	0.04	crush
				10.58	6.74	0.05	melt
KN162-7-8-5	-52.61	18.34	3702	2.882	6.88	0.03	crush
AG22-5-2	-52.76	19.10	~3700	0.7269	6.97	0.03	melt
AG22-5-7	-52.76	19.10	~3700	3.541	7.03	0.06	melt
AG22-5-18	-52.76	19.10	~3700	0.717	6.87	0.03	melt
AG22-5-14	-52.76	19.10	~3700	0.03521	6.67	0.10	melt
KN162-7-11-25	-52.80	19.20	3886	38.06	6.89	0.03	crush
KN162-7-10-21	-52.75	19.27	3165	3.309	6.90	0.04	crush
KN162-7-13-29	-52.86	19.91	4071	22.49	6.91	0.04	crush
KN162-7-14-7	-52.92	20.38	3450	18.33	6.94	0.04	crush
KN162-7-18-17	-52.99	21.41	4507	2.822	7.03	0.02	crush
KN162-7-23-107	-53.17	22.57	3658	20.47	7.28	0.04	crush
AG22-9-2	-53.13	22.88	~3800	25.53	7.23	0.04	melt
KN162-7-25-3	-53.17	23.12	3995	1.478	7.09	0.03	crush
KN162-7-26-3	-53.21	23.36	3325	2.351	7.25	0.06	crush

Figure 1: a) Locations of the dredged samples analyzed in this study. Most samples are from Knorr cruise 162, legs 7 and 9 (KN162- designation, squares); samples with PS86- and AG22- prefixes (triangles) were obtained during leg ANT IV/4 of the F.S. Polarstern (1986) and Agulhas Leg 22 (1981), respectively. Filled symbols indicate measurement by crushing *in vacuo*, while open symbols were analyzed by melting. Arrows indicate plate spreading direction [*De Mets et al.*, 1990; 1994]. The ridge axis between 9°E and 16°E is referred to as the oblique supersegment because the ridge lies at a high angle to the regional spreading direction. In contrast, spreading is nearly perpendicular to the strike of the ridge between 16°E and 25°E, referred to as the orthogonal supersegment. Ridge coordinates for the orthogonal supersegment are from *Grindlay et al.* [1998]. Bathymetry data are extracted from the global predicted seafloor topography database [*Smith and Sandwell*, 1997]. The shallowest seafloor (shaded white) is < 3 km deep; the contour interval is 1 km. DT FZ and AB FZ are the Du Toit and Andrew Bain fracture zones, respectively. Inset shows the regional setting of the study area, just to the east of the Bouvet Triple Junction at ~0°E. The Bouvet Triple Junction joins the Southwest Indian Ridge (SWIR), American-Antarctic Ridge (AAR), and southern Mid-Atlantic Ridge (MAR). The locations of hotspots in the vicinity of the Bouvet Triple Junction are indicated with gray filled circles. b) $^{3}He/^{4}He$ ratios along the SWIR between 10°E and 24°E. Horizontal line at 8 R_a indicates average $^{3}He/^{4}He$ for normal mid-ocean ridge basalt (N-MORB). Gray line shows axial topography, extracted from the predicted topography database [*Smith and Sandwell*, 1997].

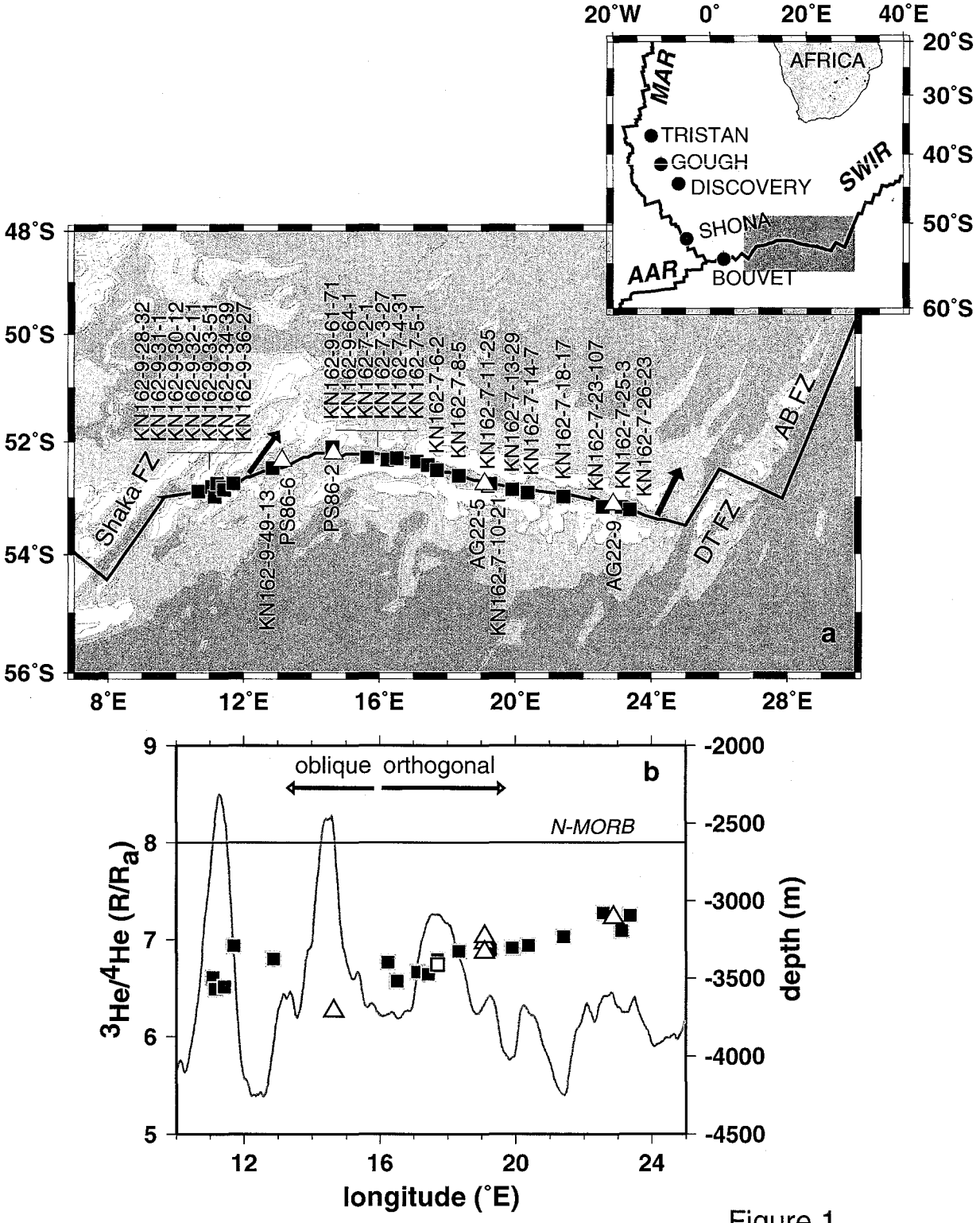
20°W
0°
20°E
40°E
20°S
30°S
40°S
50°S
60°S
AFRICA
MAR
TRISTAN
GOUGH
DISCOVERY
SWIR
SHONA
AAR
BOUVET
48°S
50°S
52°S
54°S
56°S
8°E
12°E
16°E
20°E
24°E
28°E
KN162-9-28-32
KN162-9-31-1
KN162-9-30-12
KN162-9-32-11
KN162-9-33-51
KN162-9-34-39
KN162-9-36-27
KN162-9-49-13
PS86-6
KN162-9-61-71
KN162-9-64-1
KN162-7-2-1
KN162-7-3-27
KN162-7-4-31
KN162-7-5-1
PS86-2
KN162-7-6-2
KN162-7-8-5
KN162-7-10-21
AG22-5
KN162-7-11-25
KN162-7-13-29
KN162-7-14-7
KN162-7-18-17
KN162-7-23-107
AG22-9
KN162-7-25-3
KN162-7-26-23
Shaka FZ
DTFZ
AB FZ
a
9
8
7
6
5
-2000
-2500
-3000
-3500
-4000
-4500
oblique
orthogonal
b
N-MORB
3He/4He (R/Ra)
depth (m)
12
16
20
24
longitude (°E)

Figure 1

Figure 2: Variation of ^{4}He concentration as a function of ^{3}He/^{4}He ratio. Only ^{3}He/^{4}He ratios for samples with ^{4}He concentrations above a cutoff of 0.4 μccSTP/g were considered representative of the mantle magmatic ratio, since low-^{4}He samples may have been affected by degassing and post-eruptive radiogenic ingrowth. For the remaining, high-^{4}He samples, ^{3}He/^{4}He ratios fall in the range of 6.3 to 7.3 R_a. Symbols are described in the caption to Figure 1. The concentration threshold cutoff represented by a horizontal line at 0.4 μccSTP/g is explained in Figure 5.

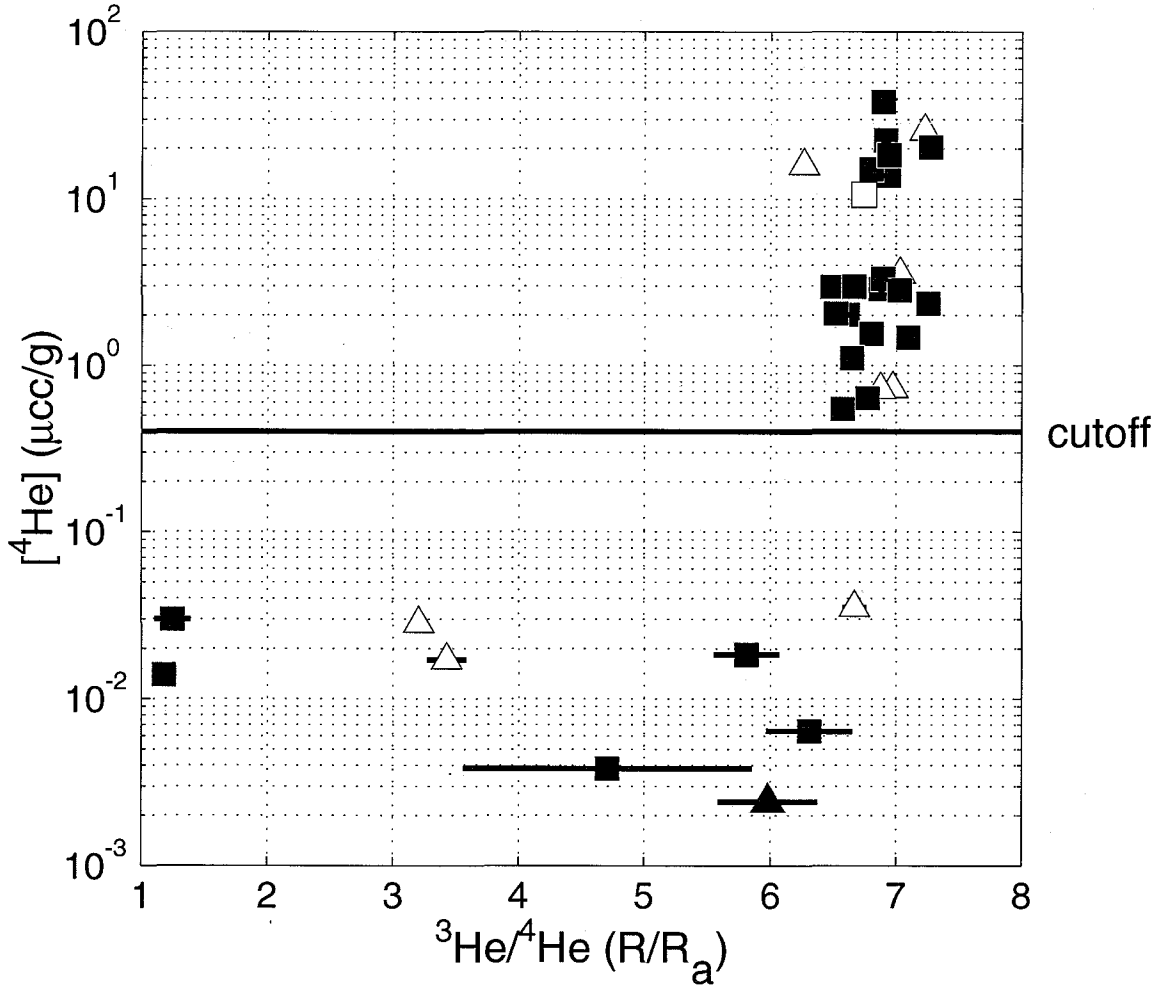

Figure 2

Figure 3: Variation of ^{4}He concentration as a function of longitude. In general, low-^{4}He samples appear to occur more frequently along the oblique supersegment than the orthogonal supersegment, possibly reflecting the confused segmentation pattern of the oblique supersegment. Symbols are described in the caption to Figure 1. The concentration threshold cutoff represented by a horizontal line at 0.4 μccSTP/g is explained in Figure 5.

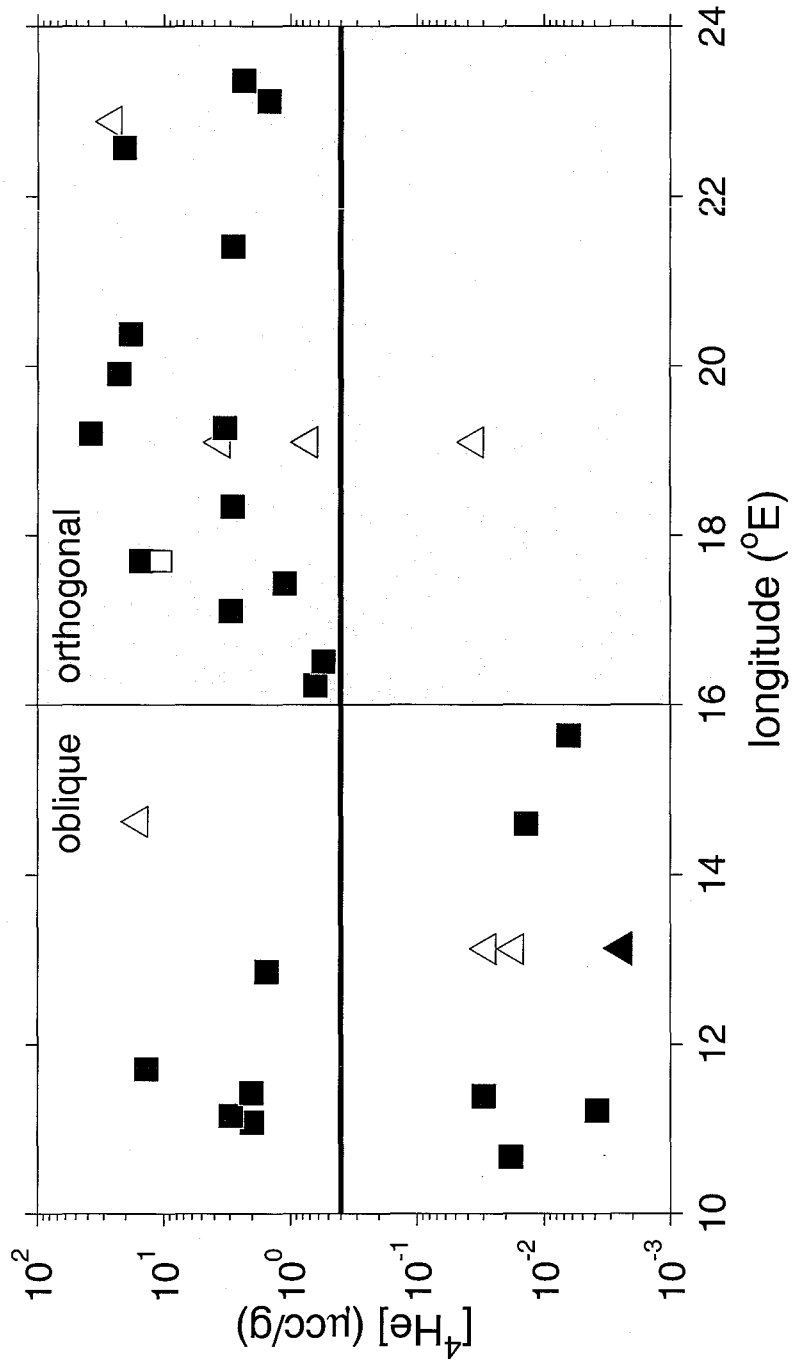
oblique
orthogonal
[4He] (μcc/g)
longitude (°E)
10^2
10^1
10^0
10^-1
10^-2
10^-3
10
12
14
16
18
20
22
24

Figure 3

Figure 4: Concentration of ^{4}He as a function of seafloor depth for the Knorr samples. ^{4}He concentrations for the Polarstern and Agulhas samples were not plotted because depths for these samples are poorly constrained. Line indicates a least squares fit to the data, which have a correlation coefficient r^2 of 0.3. There is the possibility of a trend toward higher ^{4}He concentrations at greater depths, although several samples dredged from ~3000 m or greater have low ^{4}He. The measurement for the unfilled square was determined by melting; all other measurements were obtained by crushing *in vacuo*.

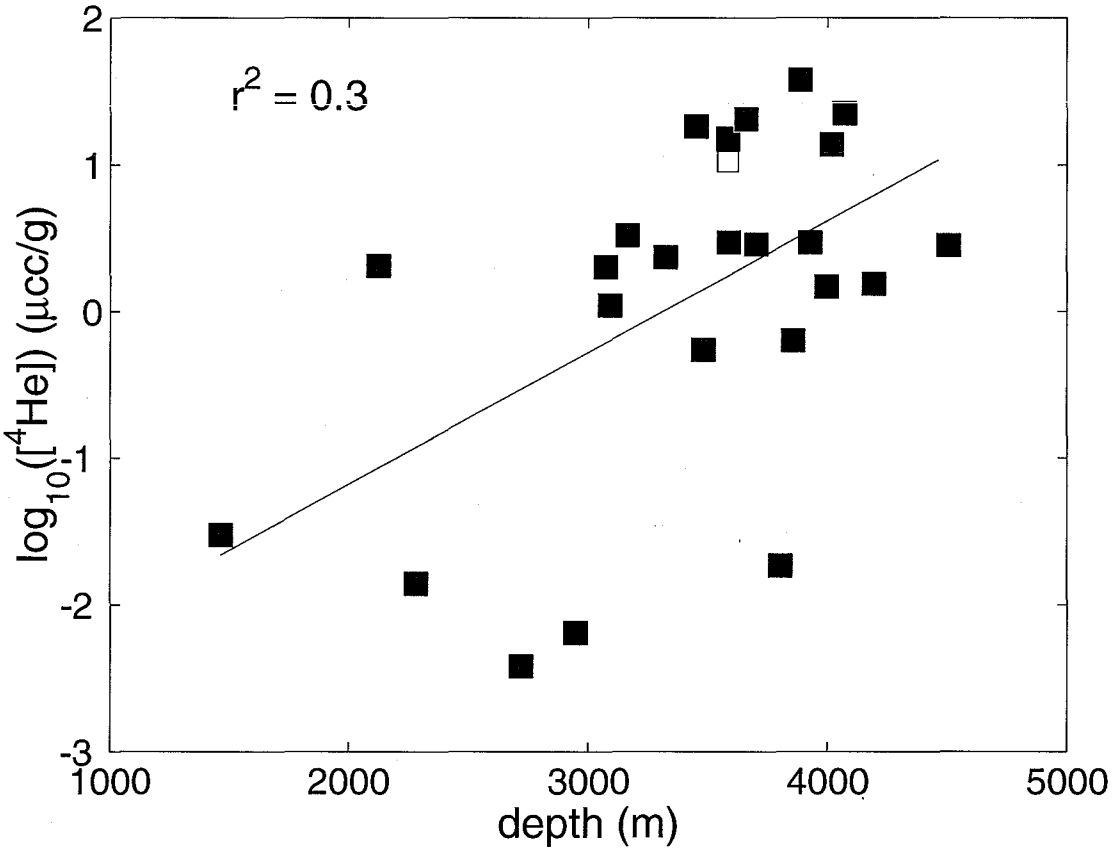

Figure 4

Figure 5: Time-dependent evolution of $^3He/^4He$ ratios resulting from post-eruptive radiogenic ingrowth of ^4He by decay of U+Th. Curves were calculated for four initial ^4He concentrations, 0.04, 0.4, 4, and 40 μccSTP/g, overlapping the concentration range observed in the SWIR sample suite. Assumptions include an initial $^3He/^4He$ ratio of 8 R_a, [U] of 0.6 ppm [*Kurz et al.*, 1998], and a Th/U ratio of 3 [*Jochum et al.*, 1983]. Dashed line indicates 10% reduction in initial $^3He/^4He$ ratio. This study interprets only samples with concentrations sufficiently high that post-eruptive radiogenic ingrowth does not lower their $^3He/^4He$ ratio below the 10% threshold for time scales < 1 Myr. This concentration threshold corresponds to 0.4 μccSTP/g, and is indicated on Figures 2 and 3.

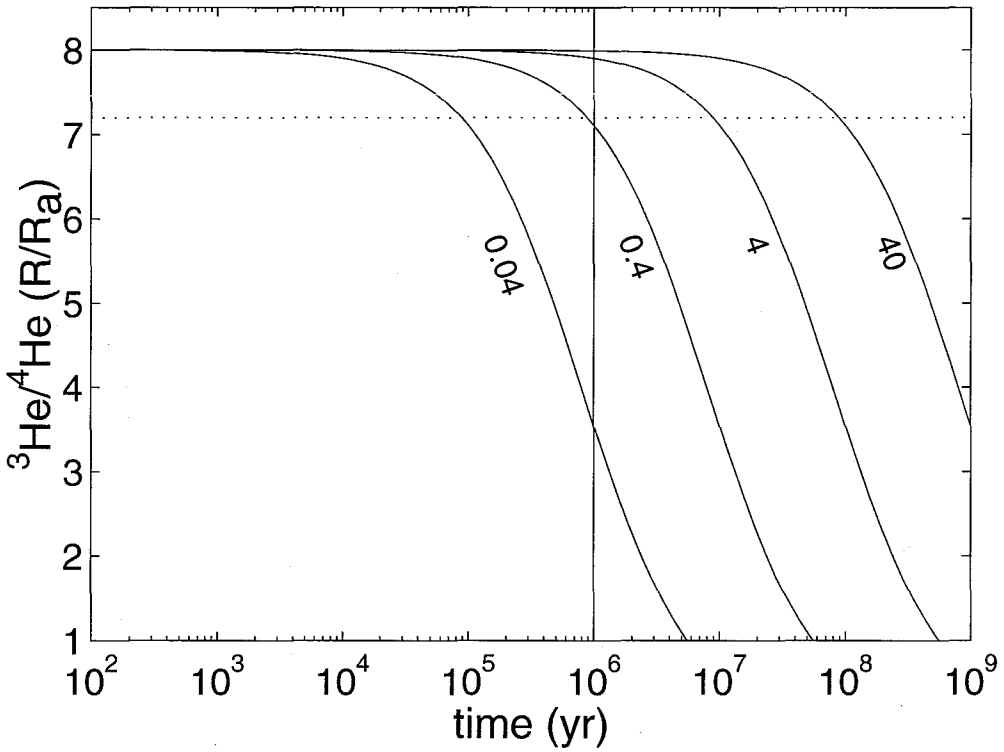
8
7
6
5
4
3
2
1
$^3He/^4He$ (R/R_a)
0.04
0.4
4
40
10^2
10^3
10^4
10^5
10^6
10^7
10^8
10^9
time (yr)

Figure 5

Figure 6: $^{3}He/^{4}He$ ratios increase eastward along the orthogonal supersegment. Least-squares regression (black line) indicates that $^{3}He/^{4}He$ and longitude are correlated with r^2 = 0.85. There is also a correlation between long-wavelength mantle Bouguer anomaly (MBA, gray line) and $^{3}He/^{4}He$ ratios. The MBA profile was calculated by applying a 150-km cutoff lowpass filter to the MBA data in *Grindlay et al.* [1998], sampled every 10 km.

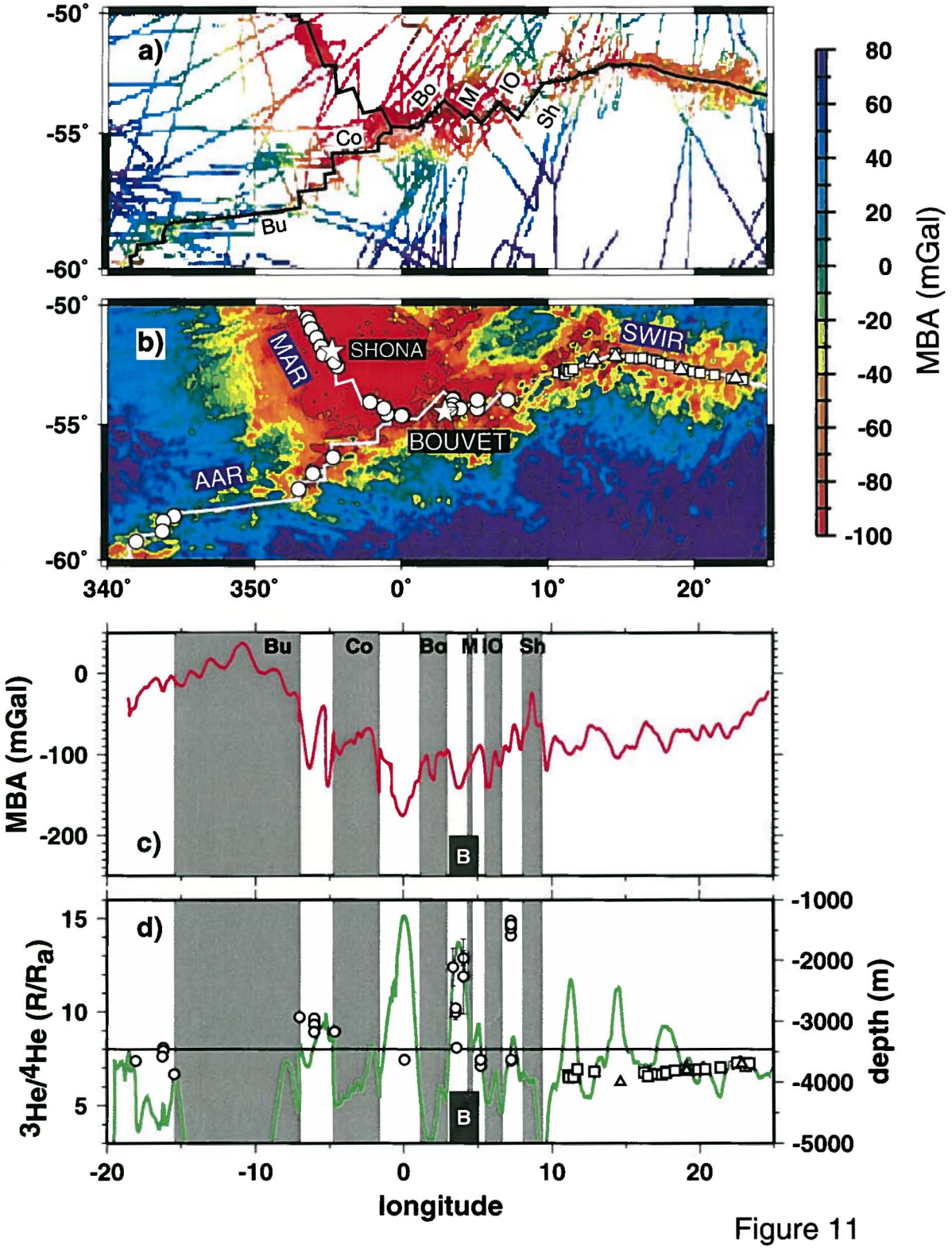
a)
b)
c)
d)
Bu
Co
Bo
M
IO
Sh
MAR
SHONA
BOUVET
SWIR
AAR
-50°
-55°
-60°
340°
350°
0°
10°
20°
80
60
40
20
0
-20
-40
-60
-80
-100
MBA (mGal)
0
-100
-200
B
15
10
5
$^3He/^4He$ (R/R_a)
-1000
-2000
-3000
-4000
-5000
depth (m)
-20
-10
0
10
20
longitude

Figure 11

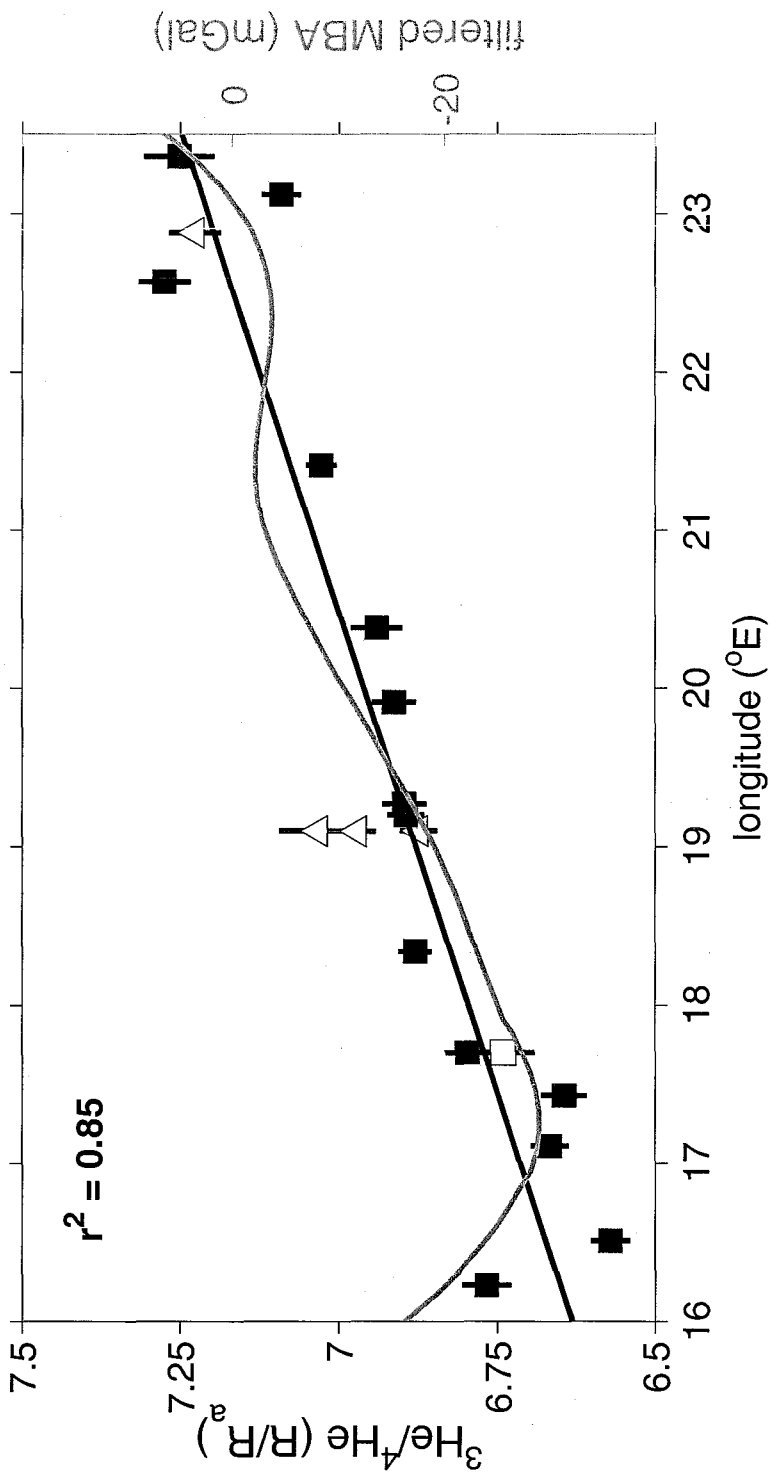
filtered MBA (mGal)
0
-20
$^3He/^4He$ (R/R_a)
7.5
7.25
7
6.75
6.5
$r^2 = 0.85$
16
17
18
19
20
21
22
23
longitude (^oE)

Figure 6

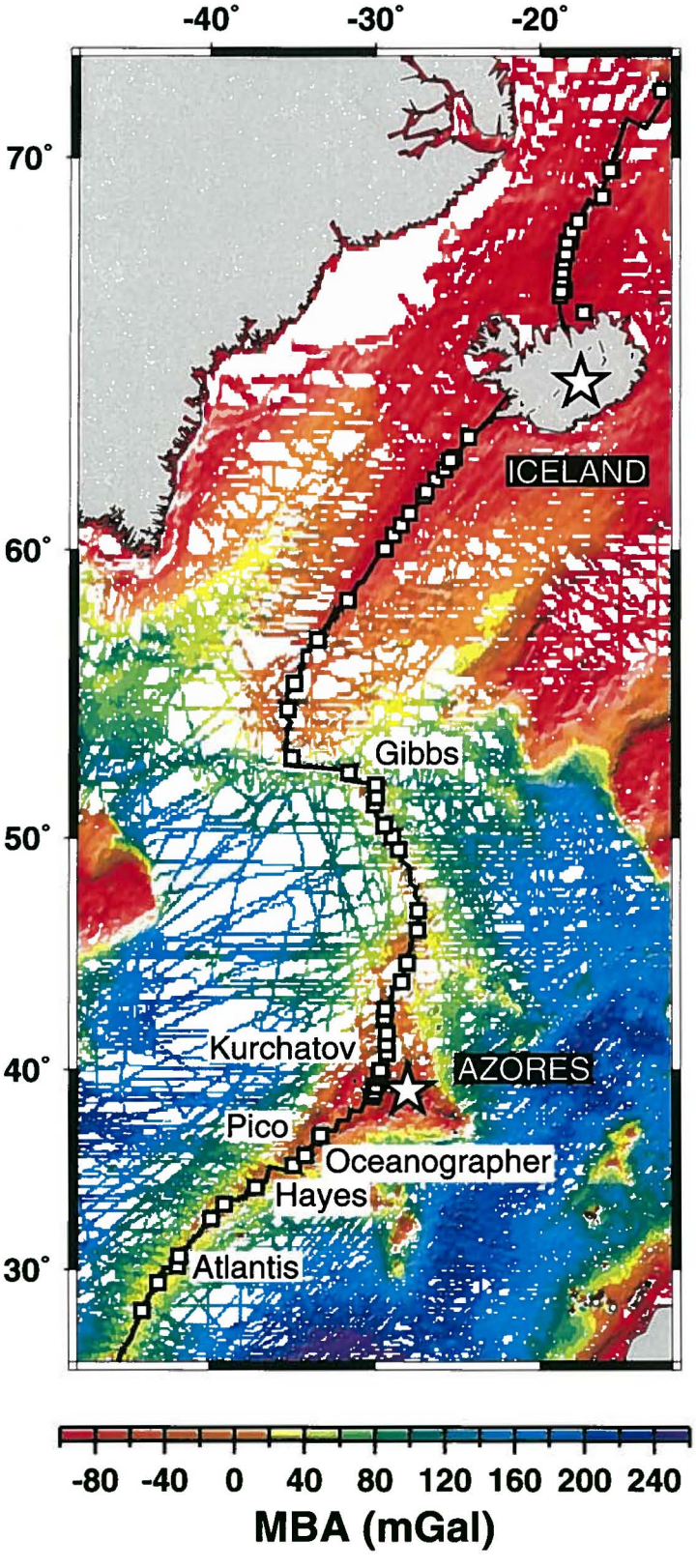
-40°
-30°
-20°
70°
60°
50°
40°
30°
ICELAND
Gibbs
Kurchatov
AZORES
Pico
Oceanographer
Hayes
Atlantis
-80 -40 0 40 80 120 160 200 240
MBA (mGal)

Figure 12

Figure 7: Locations of $^{3}He/^{4}He$ measurements on mid-ocean ridge basalt glasses in the RIDGE PETDB database [*Langmuir et al.*, 2001]. Additional samples between the Amsterdam-St. Paul Plateau and 120°W along the Southeast Indian Ridge are from *Graham* [2001], and Easter microplate data are from *Poreda et al.* [1993]. The locations of selected plumes are indicated with unfilled circles.

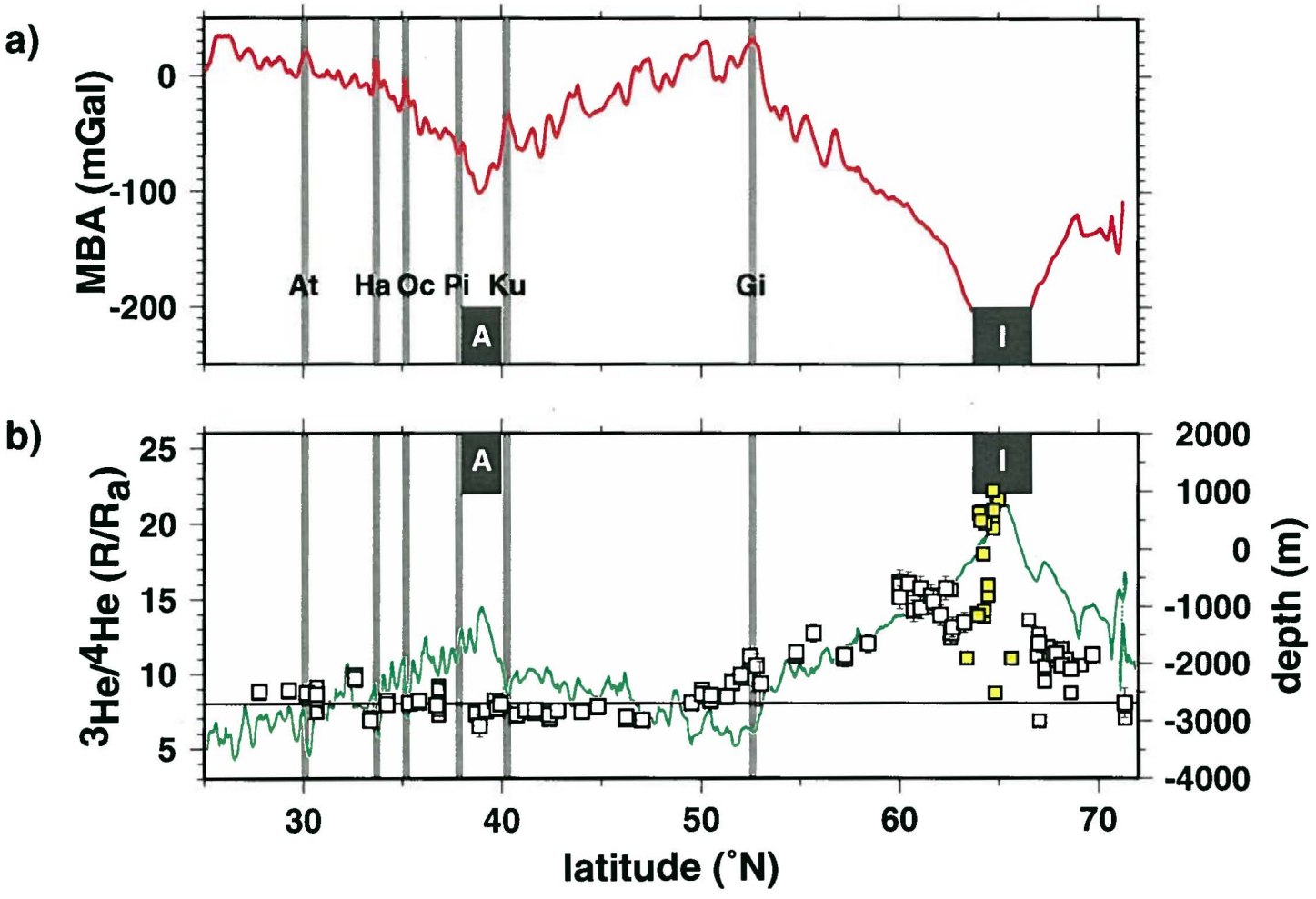
a)
MBA (mGal)
0
-100
-200
At
Ha
Oc
Pi
Ku
Gi
A
I
b)
$^3He/^4He$ (R/R_a)
25
20
15
10
5
2000
1000
0
-1000
-2000
-3000
-4000
depth (m)
30
40
50
60
70
latitude (°N)

Figure 13

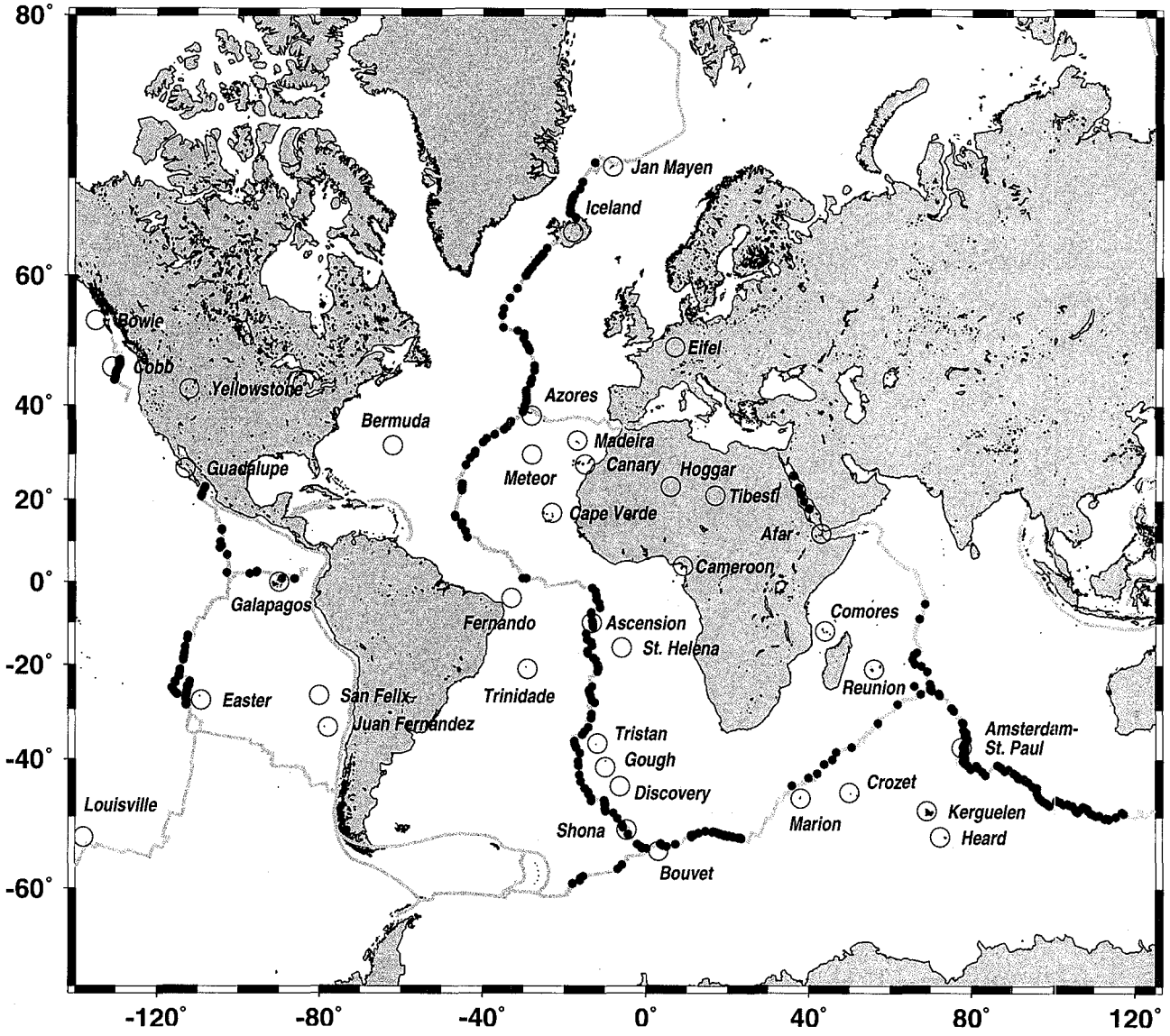
80°
60°
40°
20°
0°
-20°
-40°
-60°
-120°
-80°
-40°
0°
40°
80°
120°
Jan Mayen
Iceland
Eifel
Bowie
Cobb
Yellowstone
Azores
Bermuda
Madeira
Canary
Meteor
Hoggar
Tibesti
Guadalupe
Cape Verde
Afar
Cameroon
Galapagos
Fernando
Ascension
St. Helena
Comores
Reunion
Easter
San Felix
Juan Fernandez
Trinidade
Tristan
Gough
Amsterdam-
St. Paul
Discovery
Crozet
Louisville
Shona
Marion
Kerguelen
Heard
Bouvet

Figure 7

Figure 8: Standard deviation of $^{3}He/^{4}He$ ratios measured on MORB glasses as a function of inverse spreading rate for the Mid-Atlantic Ridge (MAR), Southeast Indian Ridge (SEIR), and Southwest Indian Ridge (SWIR). To calculate $^{3}He/^{4}He$ variability, we first culled all samples lying within a plume-influenced region from the data set shown in Figure 7. Plume-influenced regions were defined by axial depth anomalies following *Ito and Lin* [1995]. Data from the Australian-Antarctic Discordance along the SEIR, a region with unusually cool mantle temperatures [*Klein et al.*, 1991; *West et al.*, 1997], were also eliminated. For each ridge, standard deviation was then calculated using all of the remaining samples. The relationship suggested by *Allegre et al.* [1995], correlating high $^{3}He/^{4}He$ ratio standard deviation with slow spreading rate, is shown with a black line. The points for the SEIR (n=85), MAR (n=96), and SWIR (all, n=34) calculated in this study do not strongly support such a correlation, which may reflect the improved global data set since 1995. Notably, the standard deviation for samples from 10°E-25°E along the SWIR is considerably lower than that for the MAR, SEIR, or total SWIR data sets.

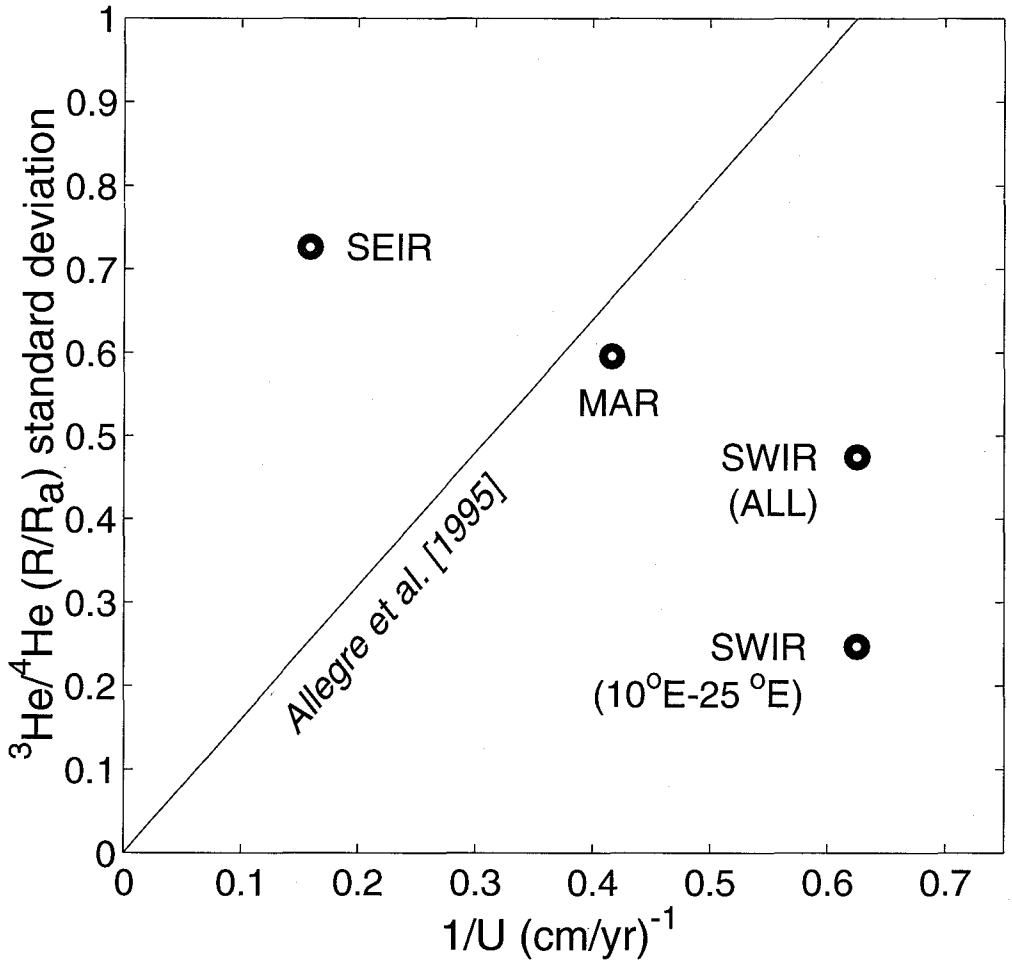
SEIR
MAR
SWIR
(ALL)
SWIR
(10°E-25 °E)
Allegre et al. [1995]
$^3He/^4He$ (R/R_a) standard deviation
1/U (cm/yr)$^{-1}$
0
0.1
0.2
0.3
0.4
0.5
0.6
0.7
0.8
0.9
1

Figure 8

Figure 9: Frequency histograms of $^{3}He/^{4}He$ ratios for non-plume-influenced MORB glasses from (a) the Southwest Indian Ridge between 10°E and 25°E, (b) the entire Southwest Indian Ridge, (c) the Mid-Atlantic Ridge, and (d) the Southeast Indian Ridge, excluding data from the Australian-Antarctic Discordance. Note that all samples available for 10°E-25°E SWIR have $^{3}He/^{4}He$ ratios below 7.5 R_a. As spreading rate increases, the peak in $^{3}He/^{4}He$ ratios appears to become less pronounced and may shift to higher values.

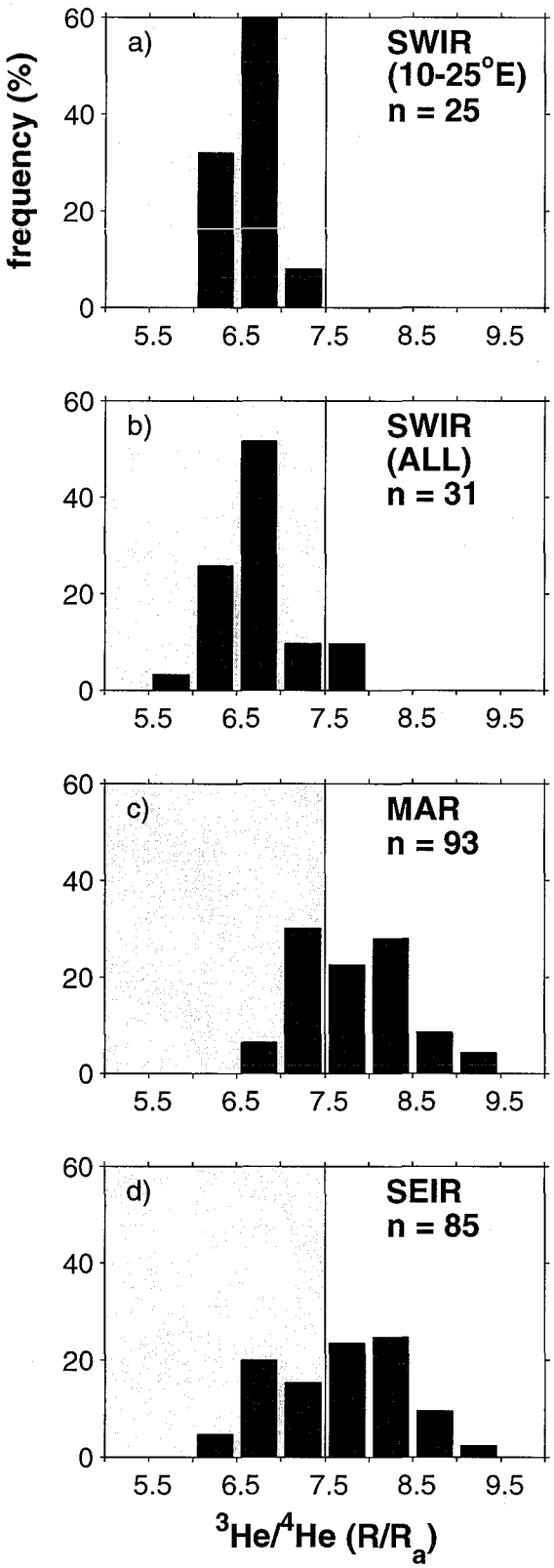
frequency (%)
a)
SWIR
(10-25°E)
n = 25
b)
SWIR
(ALL)
n = 31
c)
MAR
n = 93
d)
SEIR
n = 85
0
20
40
60
5.5
6.5
7.5
8.5
9.5
$^3He/^4He$ (R/R_a)

Figure 9

Figure 10: Time-dependent evolution of mantle $^3He/^4He$ ratios resulting from pre-eruptive radiogenic decay of U+Th. Curves are shown for four MORB ^4He concentrations, 0.04, 0.4, 4, and 40 μccSTP/g. MORB is assumed to result from 10% melting of mantle source. Other assumptions include a mantle [U] of 0.006 ppm and Th/U of 3 [*Jochum et al.*, 1983], perfect incompatibility of helium during melting, and an initial $^3He/^4He$ ratio of 8 R_a. The dashed line at 7.2 R_a indicates a 10% decrease in $^3He/^4He$ ratio. Note that for MORB ^4He concentrations of 4 and 40 μccSTP/g, $^3He/^4He$ ratios do not decrease below this 10% threshold on time scales less than the age of the Earth (vertical line).

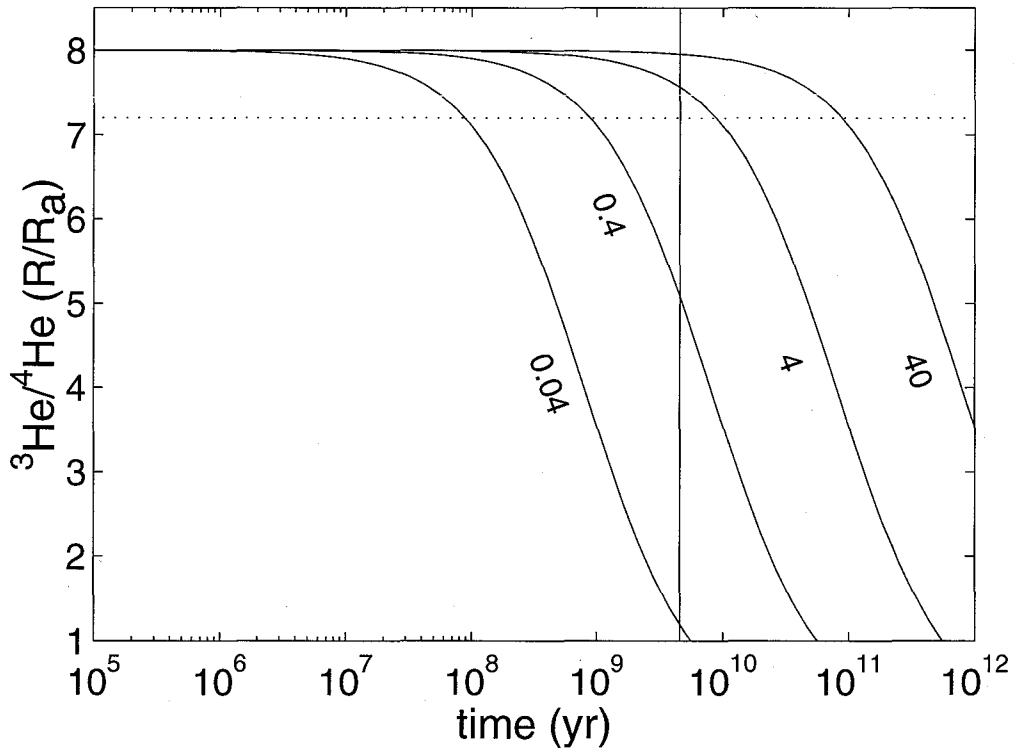
8
7
6
5
4
3
2
1
$^3He/^4He$ (R/Ra)
0.4
0.04
4
40
10^5
10^6
10^7
10^8
10^9
10^{10}
10^{11}
10^{12}
time (yr)

Figure 10

Figure 11: a) Map of mantle Bouguer anomaly (MBA), calculated by subtracting from free-air anomaly the gravitational effects of the water-crust and crust-mantle interfaces assuming a constant 5-km-thick reference crust. The densities for seawater, crust, and mantle are assumed to be 1030, 2800, and 3300 kg/m^3, respectively. Grid nodes without shiptrack control within a 5' radius are masked with white. Grid spacing is 5' and contour interval is 100 mGal. An artificial illumination is imposed from the NW. Free-air anomaly data are from *Sandwell and Smith* [1997], and bathymetry data are from *Smith and Sandwell* [1997], *Douglass et al.* [1995], *Grindlay et al.* [1998], and *Ligi et al.* [1999]. The names of selected fracture zones are labeled as Bu = Bullard FZ, Co = Conrad FZ, Bo = Bouvet FZ, M = Moshesh FZ, IO = Islas Orcadas FZ, and Sh = Shaka FZ. b) MBA, as in panel a), but without shiptrack masking. Locations of ^{3}He/^{4}He data are indicated with squares (Knorr samples), triangles (Polarstern and Agulhas samples), and circles (*Kurz et al.* [1998] and *Moreira et al.* [1995]). White stars give the positions of the Bouvet and Shona hotspots. c) Axial profile of MBA. Vertical lines indicate the locations of fracture zones. B = Bouvet plume. d) Profiles of ^{3}He/^{4}He ratios (symbols) and axial topography (green line, data from *Smith and Sandwell* [1997]).

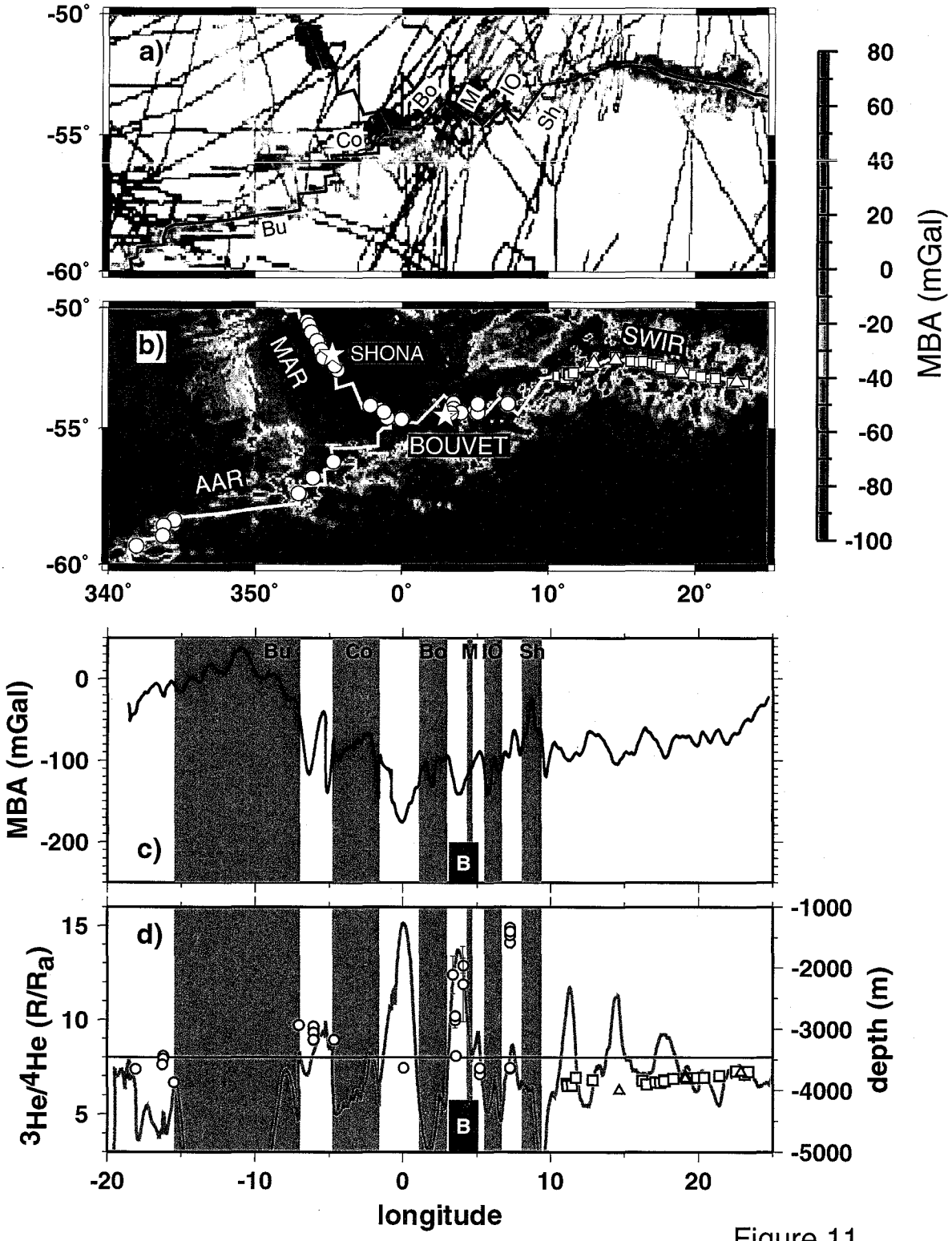
a)
b)
c)
d)
Bu
Co
Bo
MIO
Sh
MAR
SHONA
SWIR
BOUVET
AAR
B
-50°
-55°
-60°
340°
350°
0°
10°
20°
80
60
40
20
0
-20
-40
-60
-80
-100
MBA (mGal)
0
-100
-200
15
10
5
-1000
-2000
-3000
-4000
-5000
depth (m)
-20
-10
0
10
20
longitude

Figure 11

Figure 12: MBA for the north Atlantic Ocean. MBA is calculated as described in the text and caption to Figure 11a. Bathymetry data sources are *Smith and Sandwell* [1997], *Detrick et al.* [1995], and *Searle et al.* [1998]. Free-air anomaly are from *Sandwell and Smith* [1997]. Squares mark the locations of $^{3}He/^{4}He$ data from *Kurz et al.* [1982], *Schilling et al.,* [1999], *Poreda et al.* [1986], and the RIDGE PETDB database [*Langmuir et al.*, 2001]. The Azores and Iceland hotspots are indicated with white stars. As in Figure 11a, areas lacking shiptrack control within a 5' radius are masked with white.

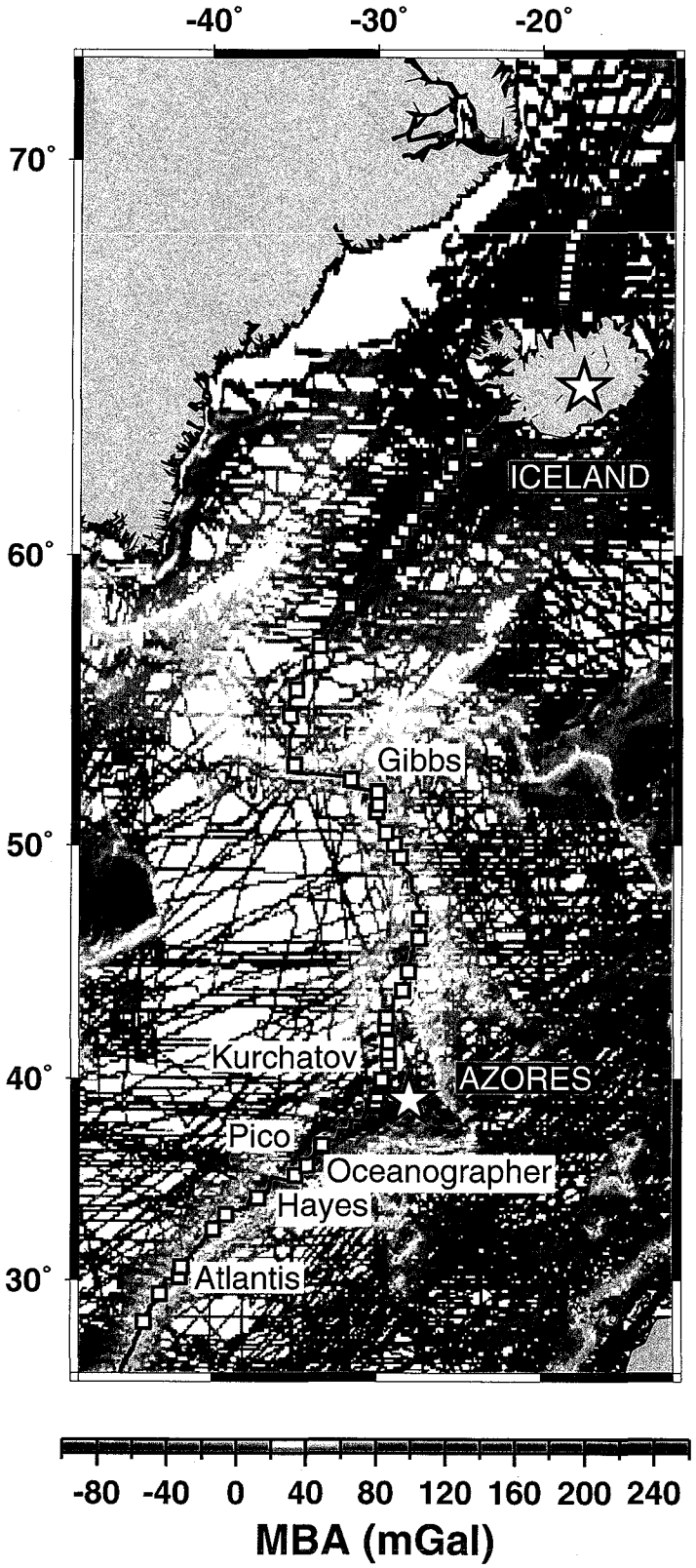
-40°
-30°
-20°
70°
60°
50°
40°
30°
ICELAND
Gibbs
Kurchatov
AZORES
Pico
Oceanographer
Hayes
Atlantis
-80 -40 0 40 80 120 160 200 240
MBA (mGal)

Figure 12

Figure 13: a) Along-axis profile of MBA. A = Azores and I = Iceland. Prominent fracture zones are indicated with vertical gray lines and are labeled as At (Atlantis FZ), Ha (Hayes FZ), Oc (Oceanographer FZ), Pi (Pico FZ), Ku (Kurchatov FZ), and Gi (Gibbs FZ). b) $^{3}He/^{4}He$ ratios along the Mid-Atlantic and Reykjanes ridges. Data sources are provided in the caption to Figure 12. Yellow squares are subaerial samples from *Kurz et al.* [1985]; they were not included in comparison of $^{3}He/^{4}He$ to MBA (Figure 14b). Green line indicates ridge axial depth, extracted from *Sandwell and Smith* [1997].

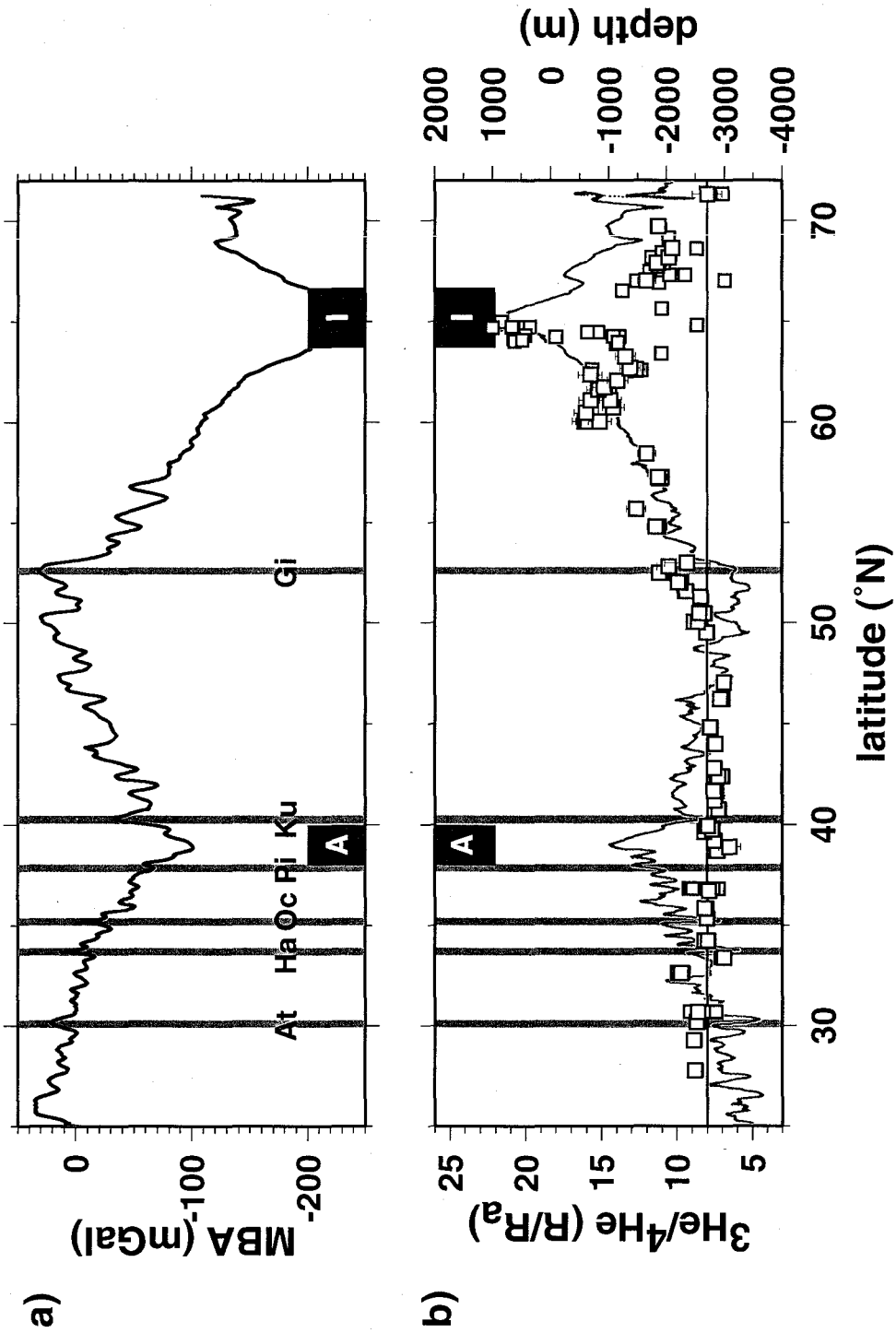
a)
b)
MBA (mGal)
0
-100
-200
At
Ha
Oc
Ri
Ku
Gi
A
I
3He/4He (R/Ra)
25
20
15
10
5
depth (m)
2000
1000
0
-1000
-2000
-3000
-4000
latitude (°N)
30
40
50
60
70

Figure 13

Figure 14: a) Comparison of $^{3}He/^{4}He$ ratios to MBA for the ridge segments around the Bouvet (black symbols) and Shona (light gray symbols) plumes. For Bouvet, symbols are described in the caption to Figure 11b. Note that the correlation between $^{3}He/^{4}He$ ratios and MBA is weak for Bouvet, but stronger for Shona, albeit over a limited range of values of MBA. b) As in a), but for the Iceland (black symbols) and Azores (light symbols) plumes. Data sources are provided in the captions to Figures 11 and 12.

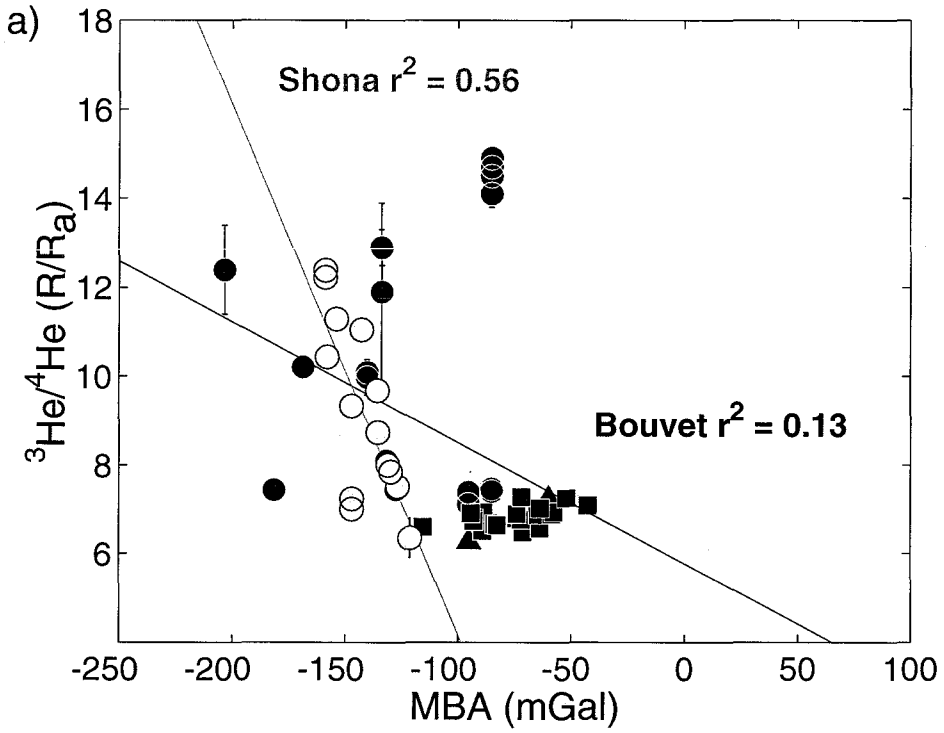
a)
Shona r^2 = 0.56
Bouvet r^2 = 0.13
$^3He/^4He$ (R/R_a)
MBA (mGal)
18
16
14
12
10
8
6
-250
-200
-150
-100
-50
0
50
100

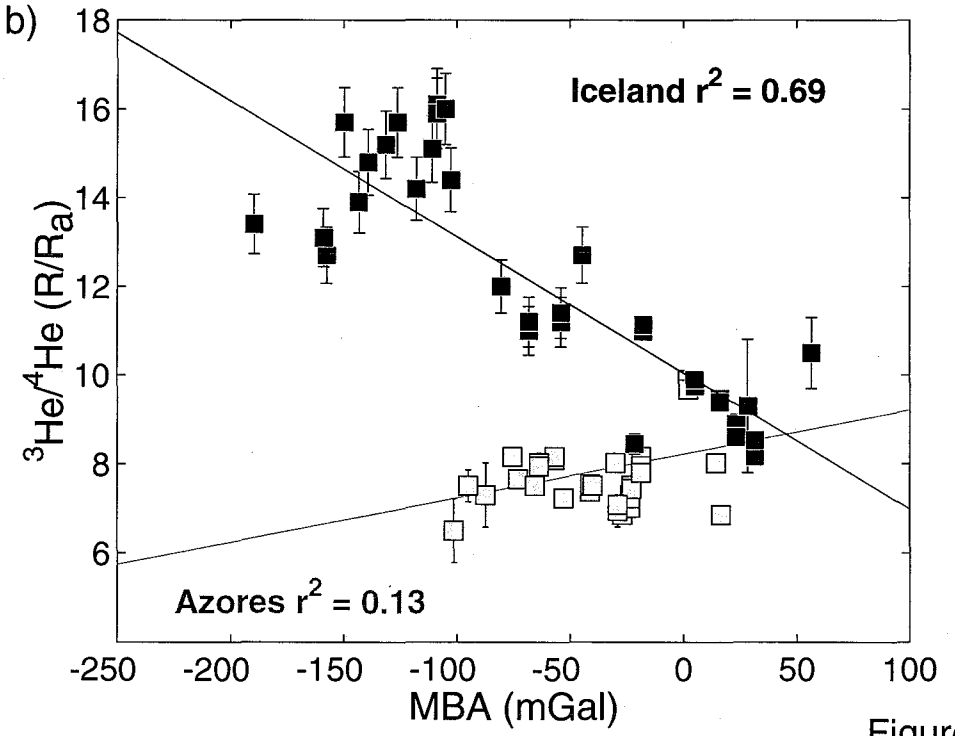
b)
Iceland r^2 = 0.69
Azores r^2 = 0.13
$^3He/^4He$ (R/R_a)
MBA (mGal)
18
16
14
12
10
8
6
-250
-200
-150
-100
-50
0
50
100

Figure 14

Figure 15: a-d) ΔRB (residual bathymetry anomaly), ΔMBA (MBA anomaly), W (waist width), and Q (vertical plume flux) vs $^3He^4He_{max}$, respectively. $^3He/^4He_{max}$, is the maximum $^3He/^4He$ measurement for the ocean island associated with a given plume, where available. Because $^3He/^4He$ ratios are not available for the islands in the Easter/Salas y Gomez chain, $^3He/^4He_{max}$ is defined to be the maximum $^3He/^4He$ ratio along the adjacent section of the East Pacific Rise. ΔRB, ΔMBA, and W are described in the text and used as defined in *Ito and Lin* [1995b]. A = Azores, AS = Amsterdam-St. Paul, B = Bouvet, E = Easter, G = Galapagos, H = Hawaii, I = Iceland, R = Reunion, and T = Tristan da Cunha. In b)-c), regression lines were calculated omitting the Azores and Tristan. In d), U = full spreading rate, and regression line was calculated omitting the Azores, Tristan, and Hawaii. Flux is estimated for Hawaii by multiplying the scaling-law-derived flux for Iceland by the ratio of the Hawaii and Iceland fluxes calculated by *Sleep* [1990].

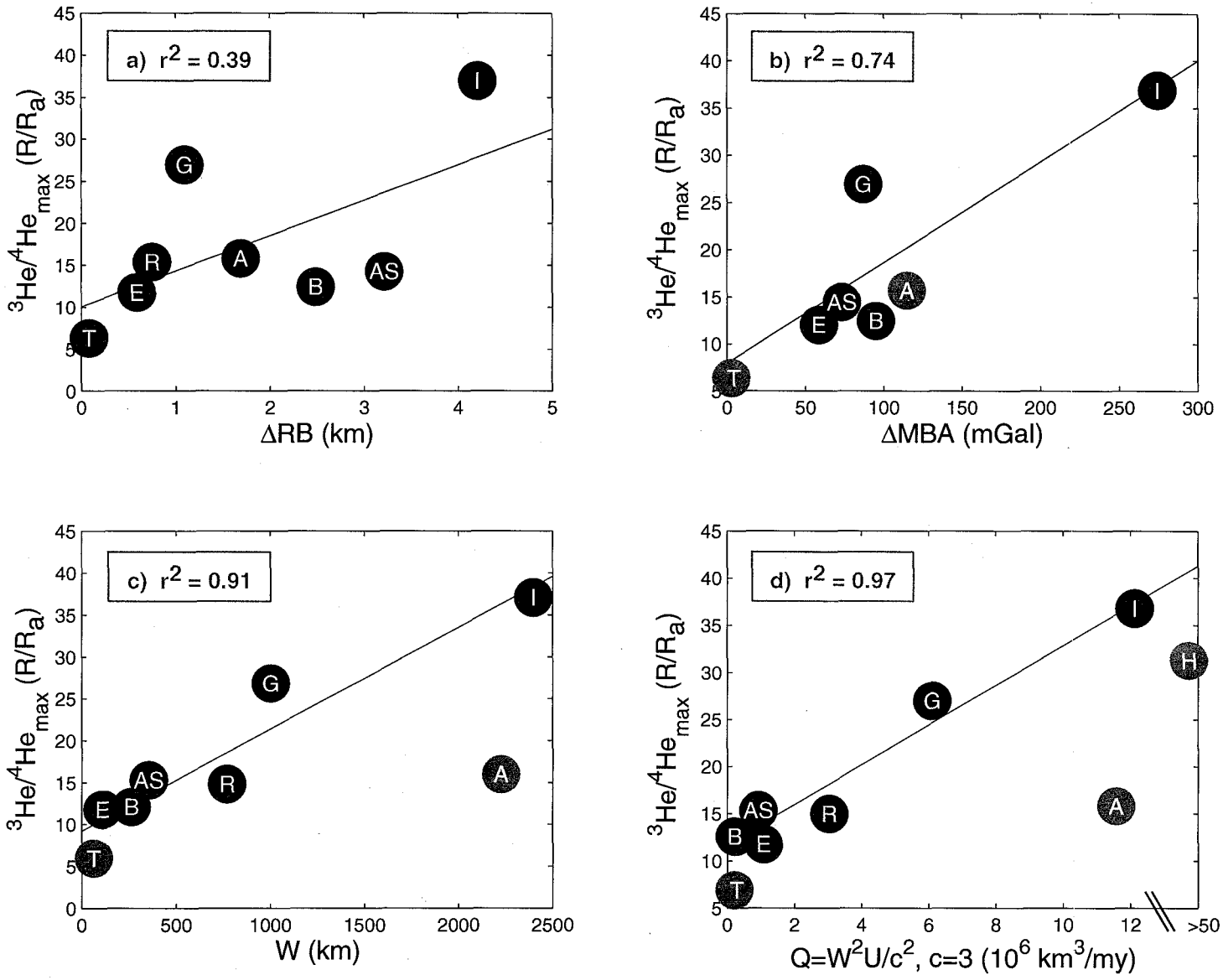
a) r2 = 0.39
b) r2 = 0.74
c) r2 = 0.91
d) r2 = 0.97
3He/4Hemax (R/Ra)
ΔRB (km)
ΔMBA (mGal)
W (km)
Q=W2U/c2, c=3 (10^6 km^3/my)
>50
I
G
R
A
E
AS
B
T
H

Figure 15

Chapter 5

Three-dimensional passive flow and temperature structure beneath oceanic ridge-ridge-ridge triple junctions

Jennifer E. Georgen and Jian Lin

Abstract

Oceanic triple junctions in ridge-ridge-ridge (RRR) configuration reflect unusual regions of crustal and lithospheric creation in comparison to normal spreading systems where only two plates diverge. This study investigates the characteristics of mantle flow and thermal structure in the vicinity of prominent RRR triple junctions, including Rodrigues, Azores, and Galapagos. In each of these three triple junctions, the slowest-spreading ridge branch intersects the near-collinear faster-spreading branches quasi-orthogonally. We first study a triple junction free of influence from a nearby hotspot, similar to the Rodrigues Triple Junction. A finite element model was used to calculate the steady-state three-dimensional (3D) velocity flow field and temperature patterns resulting from the passive divergence of three plates away from the triple junction. Model results predict a strong component of along-axis velocity directed away from the triple junction for the slowest-spreading branch. Both upwelling velocity and temperature are calculated to increase along the slowest-spreading ridge toward the triple junction, approaching the upwelling rate and temperature of the fastest-spreading branch. Within 300 km of the triple junction, upwelling velocity is predicted to increase more than threefold along the slowest-spreading ridge. In contrast, calculated upwelling velocity and temperature for the fastest-spreading branch are not significantly different from the case of a single spreading ridge. We next investigate how the predicted strong along-axis flow along the slowest-spreading branch can advect the thermal anomaly from a plume source originating below the depth of partial melting, such as near the Azores Triple Junction. We consider two end-member plume geometries, a narrow, hot plume source (radius 100 km and ΔT = 200°C), and a broad, cooler plume source (radius 300 km and ΔT = 70°C). We locate each of these plume sources either at the triple junction or at a fixed distance (200 km) away from the triple junction along the slowest-spreading branch. Because of the strong component of along-axis flow along the slowest-spreading ridge, model results predict much greater hotspot-induced increases in mantle temperature for the slowest-spreading ridge than for the faster spreading branches, regardless of plume source position and size.

1. Introduction

Triple junctions, defined as the location where three plate boundaries meet, mark a unique and important geological setting along the global mid-ocean ridge system. Triple

junctions are geometrically required features of a planet with more than two tectonic plates. Because of their unusual configuration, triple junctions provide tectonic windows for studying mantle and lithospheric dynamics. For example, at an oceanic ridge-ridge-ridge (RRR) triple junction, the upwelling patterns of three spreading centers interact, revealing information about mantle dynamics beyond what can be learned from the case of a single ridge.

Several studies have addressed the plate kinematics, geophysics, and seafloor morphology of triple junctions. For example, using constraints from GLORIA sidescan sonar data, *Mitchell and Parson* [1993] investigated the long-term evolution of ridge segmentation at the Rodrigues Triple Junction (RTJ, Figure 1a) in the central Indian Ocean. *Searle* [1980] and *Searle and Francheteau* [1986] used multibeam bathymetry and sidescan sonar to investigate the seafloor fabric and history of rift propagation at the Azores Triple Junction (ATJ, Figure 1b) and Galapagos Triple Junction (GTJ, Figure 1c), respectively. *Sclater et al.* [1976] interpreted magnetic data to show that the Bouvet Triple Junction (BTJ, Figure 1d) in the southern Atlantic Ocean has alternated between RRR and ridge-fault-fault (RFF) configuration.

Numerical geodynamical models of 3D mantle flow for a single ridge system have greatly aided our understanding of ridge crustal and mantle geodynamics (e.g., *Phipps Morgan and Forsyth* [1988]; *Shen and Forsyth* [1992]; *Sparks and Parmentier* [1993]; *Rabinowicz et al.* [1993]). However, no numerical models of 3D triple junction mantle flow have been developed to date. The purpose of this study is to explore long-wavelength patterns of mantle flow and temperature beneath oceanic RRR triple junctions. We first investigate a generic triple junction geometry, resembling Rodrigues, Azores and Galapagos, to determine the essential features of 3D mantle velocity and temperature structure beneath an RRR spreading system. We quantify how the triple junction

configuration can induce along-axis flow and cause thermal perturbations. Using the same generic geometry, we then investigate how the triple junction flow can advect the thermal anomaly of a hotspot plume source located below the depths of partial melting, and discuss the implications of this flow for the Azores Triple Junction.

2. Triple junction geometry

Each branch of a triple junction may be a ridge, trench, or transform fault. Theoretically, sixteen possible triple junction configurations exist, although not all are stable. The velocity vector method used to assess triple junction stability [*McKenzie and Morgan*, 1969] shows that only the RRR configuration is stable for all spreading rates and boundary orientations. Because the RRR configuration represents the simplest flow geometry of any triple junction, it is appropriate as the topic for this first attempt at 3D numerical modeling. This investigation explores long-wavelength flow and thermal patterns around a generic RRR triple junction which captures the salient geometrical characteristics of three prominent triple junctions, Rodrigues, Azores, and Galapagos. The kinematics of each of these three triple junctions is described below.

2.1 RRR triple junctions

The RTJ, also referred to as the Indian Ocean Triple Junction, is composed of the Southeast Indian Ridge (SEIR), Central Indian Ridge (CIR), and Southwest Indian Ridge (SWIR), with half-spreading rates of 2.9, 2.4, and 0.7 cm/yr, respectively [*Tapscott et al.*, 1980; *Patriat and Parson*, 1989] (Figure 1a). The SEIR and CIR are nearly collinear, and are intersected quasi-orthogonally by the SWIR [*Tapscott et al.*, 1980]. The RTJ has been stable for at least the last 5-10 myr, and perhaps for as much as 40 myr [*Tapscott et al.*,

1980; *Sclater et al.*, 1981]. For the last ~80 myr, the RTJ has been propagating eastward [*Patriat et al.*, 1997]; since 10 Ma, the SWIR and CIR have lengthened by an average of 2.7 and 1.3 cm/yr, respectively [*Tapscott et al.*, 1980]. The nearest hotspot, Reunion, is at present more than 1000 km from the RTJ, and therefore is presumed not to directly affect the mantle geodynamics of the RTJ.

The GTJ marks the intersection of a northern branch of the East Pacific Rise (N. EPR), a southern branch of the East Pacific Rise (S. EPR), and the Galapagos Spreading Center (GSC) (Figure 1c). The GSC opens at a rate of 2.1 cm/yr, while half-rates for the N. EPR and S. EPR are 6.9 cm/yr and 6.8 cm/yr, respectively [*Hey et al.*, 1977]. Locally, the Galapagos Microplate complicates the tectonics of the GTJ. The Galapagos Microplate has an area of 13,000 km^2 and rotates clockwise at 6°/myr [*Lonsdale*, 1988]. Although the Galapagos plume imparts significant bathymetric, seismic, gravity, and geochemical anomalies to the GSC [*Schilling et al.*, 1982; *Verma et al.*, 1983; *Ito and Lin*, 1995a; *Canales et al.*, 1997; 2000], it is located more than 1000 km away from the GTJ, making it unlikely that it directly influences GTJ geodynamics.

In contrast to the RTJ and GTJ, both the ATJ and the BTJ are affected by the presence of a nearby hotspot. The ATJ (Figure 1b) is composed of a northern branch of the Mid-Atlantic Ridge (N. MAR, half-rate 1.2 cm/yr), a southern branch of the Mid-Atlantic Ridge (S. MAR, half-rate 1.1 cm/yr), and the slow-opening Terceira Rift (Ter. R., half-rate 0.3 cm/yr). It has evolved from RFF to its present RRR configuration since its formation 45 Ma [*Krause and Watkins*, 1970; *Searle*, 1980]. *Searle* [1980] pointed out that detailed understanding of the evolution of the ATJ is complicated by extremely slow spreading rates along the Ter. R. and the resultant lack of identifiable magnetic anomalies. The Azores hotspot affects crustal accretion processes at the ATJ. Consistent with the general position of a broad S-wave seismic velocity anomaly [*Zhang and Tanimoto*, 1992], the locations of

recent volcanism in the Azores Archipelago suggest that the center of excess hotspot magma flux is approximately 100-200 km to the east of the MAR, at approximately the location of Faial Island [*Schilling et al.*, 1991]. The Azores hotspot imparts long-wavelength bathymetric, geochemical, and gravity gradients over distances ~1500-2000 km along the MAR, from the Kane FZ to approximately 44°N (e.g., *Dosso et al.*, 1993; *Ito and Lin,* 1995b; *Detrick et al.*, 1995; *Goslin et al.,* 1999; *Cannat et al.*, 1999a). Creation of the Azores Plateau north of the Azores may have begun as early as 36 Ma [*Campan et al.*, 1993]. A significant episode of excess crustal production south of the Azores occurred approximately 10 to 4 Ma [*Cannat et al.,* 1999a; *Escartin et al.*, in press].

The SWIR, American-Antarctic Ridge (AAR), and MAR join at the BTJ (Figure 1d). These ridges have half-spreading rates of 0.8, 0.9, and 1.6 cm/yr, respectively, [*Sclater et al.*, 1976] and are spaced at nearly equal angles from one another. *Sclater et al.* [1976] suggested that over the past 20 myr, the BTJ has spent 15 myr in an RFF configuration and 5 myr in the RRR mode, which is the current geometry. *Ligi et al.* [1997] confirmed that the BTJ is locally RRR using high-resolution bathymetric, gravity, and magnetics data. The BTJ is associated with three hotspot-like melting anomalies within a 500 km radius, the Bouvet and Shona hotspots and Spiess Seamount [*Hartnady and le Roex*, 1985; *Douglass et al.*, 1995; *Small et al.*, 1995; *Moreira et al.*, 1995; *Ligi et al.*, 1997; *Mitchell and Livermore*, 1998; *Georgen et al.*, 2001]. However, the volcanic constructional features of all three anomalies are volumetrically small compared to islands such as Hawaii, Iceland, and Reunion [e.g., *Sleep*, 1990]

Three of the four triple junctions described above have similar geometry. In the RTJ, ATJ, and GTJ, the two fastest-spreading ridges have nearly equal spreading rate and are roughly collinear, forming a trend which the slowest-spreading ridge intersects quasi-orthogonally. This geometric similarity is shown quantitatively in Figure 2, where U_1, U_2,

and U_3 are the spreading rates of the fastest, intermediate, and slowest-spreading ridges, respectively. For all of the RTJ, ATJ, and GTJ, U_1/U_2 is roughly 1, while U_1/U_3 is approximately 3-4.5. In contrast, the BTJ has considerably different geometry as well as significantly different spreading velocity ratios. In this study, we focus only on a generic triple junction with geometric characteristics similar to the RTJ, ATJ, and GTJ.

2.2 Simplified triple junction kinematics

The primary purpose of this investigation is to examine how the long-wavelength mantle dynamics beneath a triple junction differ from that of a single ridge, and thus a simplified geometry is used to characterize triple junction plate kinematics. Rather than explicitly incorporating local, detailed ridge and transform segmentation patterns, we approximate the overall geometry of a given spreading center using a single, straight ridge aligned according to its regional, average strike. Diagrams of the simplified RTJ, ATJ, and GTJ are shown in Figure 3. This simplification is desirable for illustrating the essential features of mantle upwelling patterns beneath a triple junction, and is justified because the spatial scale of the long-wavelength mantle flow and temperature structure beneath a triple junction is much greater than that of individual segments. This approximation, therefore, also ignores features such as microplates, as in the case of the GTJ. Furthermore, for a number of triple junctions including the RTJ [*Mendel et al.*, 2000], the three ridge branches fail to meet at a strict "triple point," instead being joined by a zone of diffuse deformation near the "virtual" triple junction. The gap distance between the termination of well-defined spreading along any given ridge axis and the virtual triple point is less than 100 km for all of the triple junctions considered here [*Ligi et al.*, 1997; *Searle*, 1980; *Mitchell*, 1991], again considerably shorter than the much longer wavelength patterns that are the subject of this investigation.

Because the RTJ is not affected by a nearby hotspot, we selected it as the basis for our numerical model. In the first model explored (Model 1), the half-spreading rates of the three ridge branches are set equal to the spreading rates of the SEIR, CIR, and SWIR. For discussion purposes, we refer to the ridge with the relatively fastest spreading rate U_1 as R_1. Similarly, the ridge with intermediate spreading rate is R_2, and the slowest-spreading ridge is R_3.

3. Numerical model set-up

We use a finite element numerical model to solve for the steady-state 3D mantle velocity and temperature fields resulting from the surface divergence of three plates. The top surface of Model 1 is divided into the African, Antarctic, and Australian plates (Figure 4). Figure 1a shows clear lines of seafloor fabric discontinuities expanding in a V-shape away from the RTJ along the SWIR. These seafloor fabric discontinuities bound crust created at the SWIR during the eastward propagation of the RTJ. A similar triple junction trace exists on the Australian Plate (Figure 4a), but it is not as distinct as the African and Antarctic traces because of the similarity in spreading rate and near collinearity of the SEIR and CIR.

We fix the location of the triple junction in the center of Model 1, and prescribe the motions of the three plates with respect to the triple junction according to the RTJ velocity triangle calculated by *Tapscott et al.* [1980]. The component of the plate motion vector perpendicular to each ridge is equal to that ridge's spreading direction and velocity. For the top model surface, $\sigma_{zz} = 0$. For velocity boundary conditions on the vertical sides and the bottom of the model box, we prescribe the analytical solution for upwelling and horizontal velocity for each grid node as a function of depth and perpendicular distance from the appropriate ridge axis, using the 2D formulations of *Reid and Jackson* [1981].

Temperature is assigned to be 0° and 1350°C on the top and bottom boundaries of the model, respectively, and the horizontal temperature gradients are set to zero on the vertical sides of the model domain.

The model box is 2000 km x 2000 km x 200 km (Figure 4b), enabling us to investigate mantle flow and thermal fields along at least 1000 km of each ridge. The model box is discretized into 41 x 41 x 15 grid nodes, with highest horizontal resolution near the triple junction and greatest vertical resolution near the top surface of the box where velocity and temperature gradients are greatest. In the horizontal direction, grid spacing ranges from 20 to 99 km, while vertical grid spacing increases from 5 to 29 km with depth.

To solve for mantle velocity and temperature, we use a 3D fluid dynamical code (ADINA, *Bathe* [1996]) that solves the equation of continuity for an incompressible fluid

$$\nabla \cdot \mathbf{v} = 0 \qquad (1)$$

and the equation of momentum balance with constant viscosity and no buoyancy-driven flow

$$\nabla P = \eta \nabla^2 \mathbf{v} + \rho \mathbf{g} \qquad (2)$$

where $\mathbf{v}$ is velocity vector, P is fluid pressure, η is viscosity, ρ is mantle density, and $\mathbf{g}$ is the acceleration of gravity. In these calculations, mantle viscosity is set to a constant 10^{21} Pa s. The steady-state temperature field is solved using

$$\nabla^2 T + \mathbf{v} \nabla T = 0 \qquad (3)$$

where velocity vector $\mathbf{v}$ is derived from solution of Equation (2) and T is mantle temperature.

4. Model results

4.1 Triple junction velocity and temperature fields

In Model 1, the divergence of three surface plates away from the triple junction induces a component of flow along each of R_1, R_2, and R_3 (Figure 5). This calculated along-axis flow is strongest for the slowest-spreading ridge R_3 (SWIR), where it is directed away from the triple junction. At a representative location within the partial melting zone at 50 km depth and 300 km away from the triple junction, the magnitude of along-axis velocity is predicted to be 90% of upwelling velocity for R_3. A moderate component of along-axis velocity is present for R_2 (CIR) as well. For R_2, along-axis velocity is 70% of upwelling velocity. In contrast, the calculated mantle flow is nearly vertical along R_1 (SEIR). R_1 along-axis velocity magnitude is only 2% that of upwelling velocity at a depth of 50 km, 300 km away from the triple junction.

The calculated upwelling velocity increases significantly along R_3 towards the triple junction (Figure 6). At a far-field distance of 500 km from the triple junction, R_3 upwelling velocity is approximately equal to the upwelling velocity generated in the simpler case when two plates diverge with a half-rate of 0.7 cm/yr. However, within 200 km of the triple junction, R_3 upwelling velocity increases more than threefold, approaching the upwelling velocity along R_1. A similar, though less pronounced, increase is also predicted along R_2.

Figure 7a shows the calculated triple junction temperature field at a depth of 32 km, within the depths of partial melting. The strong thermal signatures of the faster-spreading R_1 and R_2 are clearly apparent. On the other hand, R_3 has lower overall axial temperatures, consistent with its ultra-slow spreading rate. However, beneath the axis of R_3, mantle temperature at 32 km depth is calculated to increase by 70-100°C towards the triple junction as a result of enhanced triple junction upwelling (Figure 8a). In fact, for all depths, the

along-ridge temperature increase relative to the case of a single ridge is profoundly greater for R_3 (Figure 9).

In general, far from the RTJ (> 500 km), the calculated upwelling velocity and thermal fields of R_3 and R_2 are similar to the case of the simple divergence of two plates with corresponding half-spreading rates. However, both upwelling velocity and temperature for these two slower-spreading ridges are predicted to increase toward the triple junction to approach those of the fastest-spreading ridge. In contrast, upwelling velocity and temperature for R_3 is little affected by the presence of the other two ridges, maintaining upwelling velocity and temperatures fields similar to the simpler two-plate case. Note that these model calculations predict little material transfer from the fastest-spreading ridge to the two slower-spreading ridges.

4.2 Effects of absolute magnitude of spreading rates

To determine the effects of increasing or decreasing the absolute magnitude of spreading velocity for the three ridges while keeping their relative ratios unchanged, we calculate velocity field and temperature for the same model geometry described in Section 3, scaling the surface divergence velocities by a factor of either 1/2.4 (Model 2) or 2.4 (Model 3). Application of these scaling factors roughly yields the spreading rates for the ridges of the ATJ and GTJ, respectively. The results of the thermal calculations are shown in Figures 7b-c and 8b-c. Because of the overall slower spreading rates for Model 2 as compared to Model 1, temperature magnitudes are correspondingly lower at a given depth (Figure 7). The calculated temperature increase along the ultra-slow spreading R_3 (Ter. R.) for Model 2 is dramatic. Within 500 km of the triple junction, temperature within the partial melting region is predicted to increase by more than 250°C, approaching the value for R_1 (N. MAR) (Figure 8b). Axial temperature is also predicted to increase for R_2 (S.

MAR), although the magnitude of the increase is considerably less than that of R_3 because of the similarity in spreading rate between R_1 and R_2.

Model 3 (Figure 7c) represents two fast-spreading ridge branches (N. EPR and S. EPR) intersected by an intermediate-spreading ridge (GSC). Since all three ridges spread at relatively rapid rates, the thermal contrast between them is not as pronounced as for Model 1 or Model 2. Correspondingly, no significant along-axis temperature increase is predicted for R_3 (Figure 8c). Instead, at depths within the partial melting zone (30-80 km), all three ridges maintain temperatures close to their temperature far away from the triple junction.

4.3 RTJ thermal topography

To evaluate how model predictions compare to observed bathymetric trends, we examine in detail the thermal structure for R_3 in Model 1 and compare it to the SWIR near the RTJ. East of the Melville Fracture Zone at 61°E, the SWIR achieves its greatest axial depth (Figure 10a). *Cannat et al.* [1999b] suggest that this extreme depth can be explained by mantle temperatures that are significantly cooler than normal, with a concomitant decrease in magmatic production. In the immediate vicinity of the RTJ, however, the maximum depth of the SWIR axis shallows significantly (Figure 10b). To determine if our model predictions are consistent with the observed shallowing, we calculate the topography resulting from mantle density variations due to thermal structure, assuming that vertical columns of mantle are in isostatic equilibrium at 200 km depth. The topographic variation Δh can be calculated as:

$$\Delta h = \int \alpha \rho_m (T-T_o)/ (\rho_c-\rho_w) \quad dy, \qquad (4)$$

where the coefficient of thermal expansion $\alpha = 3 \times 10^{-5}$ °C^{-1}, reference mantle density ρ_m = 3300 kg/m^3, reference crustal density ρ_c = 2700 kg/m^3, water density ρ_w = 1030 kg/m^3, T

is mantle temperature, and reference mantle temperature T_o = 1350°C. Gravity studies along the GSC in the vicinity of the Galapagos plume [*Ito and Lin*, 1995a] and along the Reykjanes Ridge near Iceland [*Ito et al.*, 1996] suggest that mantle thermal variations contribute approximately 25-30% to the topography and mantle Bouguer gravity signal, with the rest attributable to crustal thickness variations. Accordingly, we calculate an isostatic topography profile assuming that thermal variations account for 30% the overall ridge topography.

Figure 10b suggests that that the general long-wavelength shallowing of the SWIR axis toward the RTJ is consistent with the isostatic topography predicted by the triple junction thermal model. We note that high-resolution studies around the RTJ [*Mitchell*, 1991; *West et al.*, 1995] indicate that the detailed local geology is suggestive of a propagator feature which terminates ~50-100 km west of the triple junction, with a rift tip that is locally depressed and supported by dynamic stresses [*Phipps Morgan and Parmentier*, 1985]. Between this anomalously deep rift tip and the triple junction, seafloor depth recovers to more average values. These complications prevent more definitive interpretation of the SWIR bathymetry near the RTJ.

Further test of the model prediction of increased axial temperature along the slowest-spreading branch of a triple junction could come from regional geochemical studies. For example, Model 1 predicts progressively greater extents of melting along the SWIR towards the RTJ. Such variations could be detected from $Na_{8.0}$ and other geochemical systematics [*Dick et al.*, 1984; *Klein and Langmuir*, 1987]. Currently, however, major element data for the SWIR in the immediate vicinity of the RTJ are sparse, and the spatial coverage necessary to discern trends on the order of several hundreds of kilometers is lacking.

4.4 Advection of plume anomaly by along-axis flow

A major predicted feature of velocity structure beneath a triple junction with the geometry of Model 1 is that mantle material flows away from the triple junction along the slowest and intermediate spreading branches (Figure 5). To further investigate the implications of such along-axis flow for ridge dynamics, we add a hotspot thermal anomaly source to the base of the numerical box for Model 2 (ATJ) and examine how this thermal anomaly is advected both horizontally and vertically. We follow *Ito and Lin* [1995b] and *Cannat et al.* [1999a] in ascribing the Azores volcanism to elevated mantle temperatures. If the Azores plume is of chemical origin [*Bonatti*, 1990], the detailed melting mechanism would differ from that of a thermal plume, but the effects of triple junction flow on advecting the plume anomaly would be similar.

We test two temperature distributions to explore how the anomaly is advected by triple junction flow, and how sensitive the advection is to the location and source characteristics of the anomaly. In both distributions, a circular thermal anomaly is imposed on the bottom of the model box. The anomaly decreases linearly from a maximum of ΔT at the plume center to zero at the radius of the plume source. In the narrow plume source model, ΔT = 200°C, and the radius of the anomaly is 100 km. In the broad plume source model, ΔT = 70°C, and the anomaly radius is 300 km. *Cannat et al.* [1999a] estimated that the thermal anomaly required to produce the observed bathymetry and gravity anomalies south of the Azores Plateau is on the order of 70°C, providing a lower bound for our Azores plume anomaly. We place each of the narrow and broad plume sources in two different locations, one centered on the triple junction and the other at a fixed distance (200 km) to the east of the triple junction along R_3 (Ter. R.) (Figure 11). The latter location is consistent with the observed focus of Azores volcanism [*Schilling et al.*, 1991] and the center of an upper

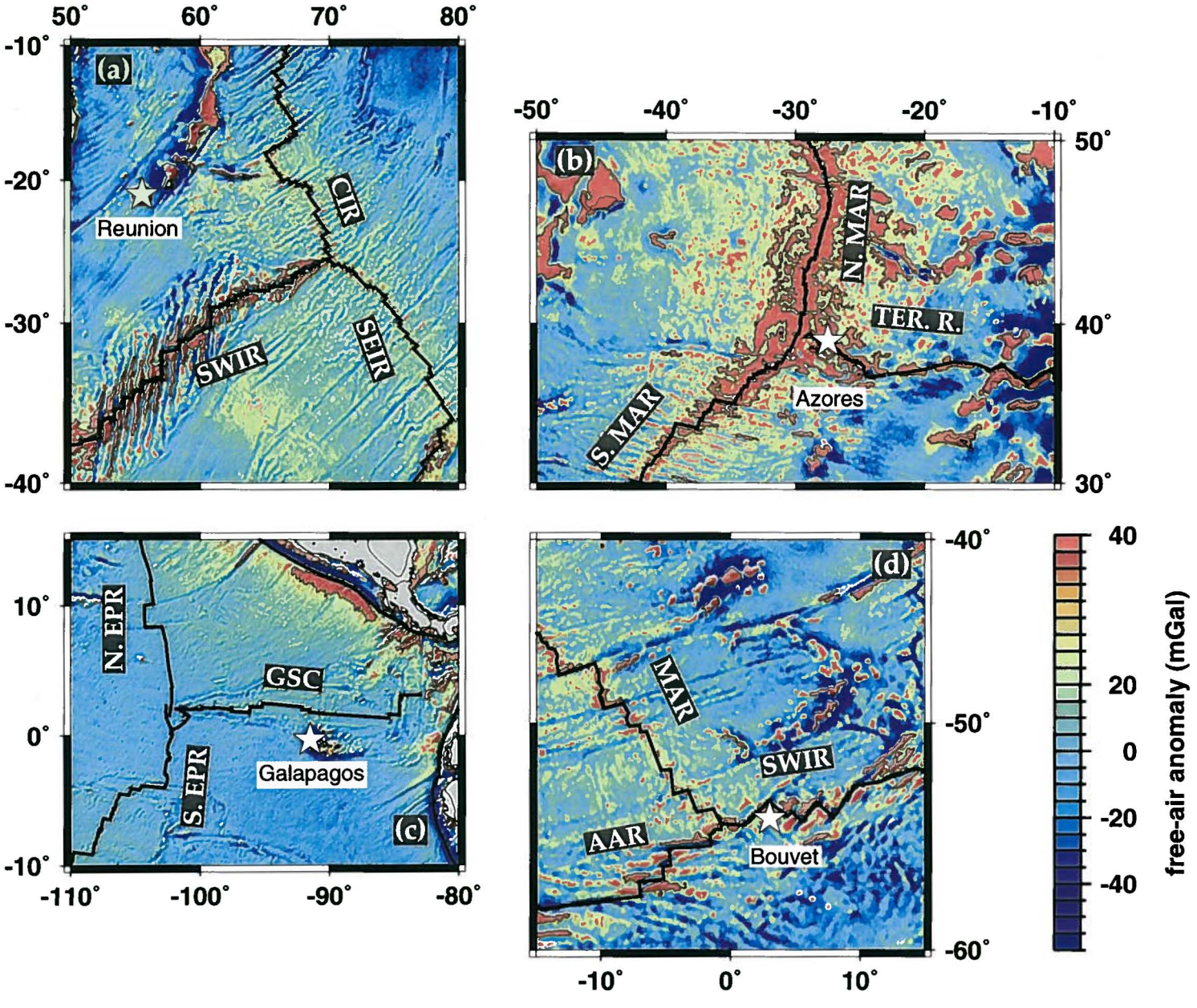
(a)
Reunion
CIR
SEIR
SWIR
(b)
N. MAR
TER. R.
Azores
S. MAR
(c)
N. EPR
GSC
Galapagos
S. EPR
(d)
MAR
SWIR
AAR
Bouvet
50°
60°
70°
80°
-10°
-20°
-30°
-40°
-50°
-40°
-30°
-20°
-10°
50°
40°
30°
10°
0°
-10°
-110°
-100°
-90°
-80°
-40°
-50°
-60°
-10°
0°
10°
40
20
0
-20
-40
free-air anomaly (mGal)

Figure 1

mantle velocity anomaly imaged by seismic tomography studies [*Zhang and Tanimoto*, 1992].

A narrow, hot plume source centered on the triple junction (Figure 11b) is calculated to impart a high-amplitude thermal anomaly which remains relatively confined to the immediate vicinity of the triple junction. Flow along R_3 distributes the shallow thermal anomaly only a short distance (<100 km) along-axis (Figure 12b). In contrast, when the narrow plume source is located 200 km off-axis (Figure 11c), along-axis flow advects the shallow thermal anomaly for more than 200 km of additional distance along-axis (Figure 12c), carrying the plume signal to a total distance of more than 400 km away from the triple junction. At a depth within the partial melting zone of 53 km, the thermal profile for the narrow, TJ-centered plume source has a single high which decreases monotonically with distance away from the triple junction, while the profile for the narrow, R_3-centered plume source has an additional high at a distance of approximately 300 km away from the ATJ, downstream from the plume source (Figure 13a, d).

Compared to the narrow plume source case, the thermal anomaly created by the TJ-centered broad plume disperses to greater distances along R_3 (Figures 12d, 13a, 13d). The magnitude of the thermal anomaly at a depth of 53 km imparted by the broad plume source is less than that resulting from the narrow plume to distances of approximately 100-150 km away from the triple junction, but for greater along-axis distances, the broad plume thermal anomaly persists (Figure 13d).

In general, the plume-imparted thermal anomalies are of smaller magnitude and shorter wavelength for R_1 and R_2 than for R_3 (Figures 13b-c). For the narrow, TJ-centered plume source, the root-mean-square (RMS) increase in along-R_3 temperature at a depth of 53 km relative to the no-plume case is 29°C, compared to 24°C for both R_1 and R_2. For the broad, TJ-centered plume source, the RMS temperature increases are 27°C, 21°C, and 20°C for

R_3, R_2, and R_1, respectively. The thermal anomaly created by the narrow, TJ-centered plume source along R_1 and R_2 remains confined to only a few hundred kilometers from the triple junction. In contrast, the broad, TJ-centered plume is calculated to increase temperatures along R_1 and R_2 over a much longer distance of ~300-400 km. Neither the broad nor the narrow R_3-centered plume significantly affects temperatures for R_1 or R_2.

4.5 ATJ thermal topography

We investigate how model plume sources in various locations with respect to the triple junction are able to reproduce long-wavelength bathymetric trends around the ATJ. Figure 14 shows a map of filtered bathymetry for the ATJ. Salient characteristics of ATJ bathymetry include high topography along R_3 (Ter. R.) to approximately 200 km away from the ATJ, and relatively shallower seafloor along R_2 (S. MAR) than R_1 (N. MAR) for a given distance away from the triple junction. Filtered bathymetry profiles along the N. MAR, S. MAR, and Ter. R., with transform offsets omitted, are plotted in Figure 15a. Figures 15b-e show the isostatic topography resulting from a plume with a radius of 190 km and a thermal anomaly of 190°C, calculated using the methods described in Section 4.3. The plume source was placed at a fixed distance of 200 km away from the triple junction, and at angular distances ranging from on R_3 to 1/15, 1/10, or 1/5 of the angle from R_3 to R_2. As the plume source increases its angular distance away from R_3 toward R_2, the predicted length of the plume bathymetric anomaly increases along R_2 while slightly decreasing along R_3. For nearly all of the plume locations, the predicted topography along R_3 reaches its shallowest depths a few hundred kilometers away from the triple junction, and then increases rapidly for greater distances, roughly in agreement with the observed long-wavelength bathymetric trends. Furthermore, to distances within a couple of hundred kilometers away from the triple junction, the predicted isostatic topography for R_2 is

shallower than that for R_1 for plumes located off of R_3. Again, this is in qualitative agreement with observations from gravity and seismic tomography which suggest that Azores plume influence is stronger along the Mid-Atlantic Ridge to the south of the ATJ than to the north [*Goslin et al.*, 1999].

5. Discussion

The primary goal of this investigation is to quantify the long-wavelength patterns of passive mantle upwelling and temperature beneath an RRR triple junction and to contrast them with the simpler case of a single ridge. We purposefully select to first focus on purely passive upwelling because this approach isolates the simplest physics inherent to the triple junction problem. Similar to the incremental approach used in developing single ridge models [e.g., *Phipps Morgan and Forsyth*, 1988; *Shen and Forsyth*, 1991; *Sparks and Parmentier*, 1993; *Barnouin-Jha et al.*, 1997; *Braun et al.*, 2001], subsequent triple junction models may progressively investigate the effects of adding variable viscosity, thermal buoyancy, melt retention buoyancy, melting, and the like. Future studies may further explore the essential predicted triple junction flow features suggested by this investigation, such as the predicted strong along-axis flow and increased upwelling rate and temperature along the slowest-spreading ridge. In the following paragraphs we qualitatively discuss the potential effects of a few factors not incorporated in the present models.

Melting and crustal thickness variations. An important test of the mantle flow and thermal fields predicted in this modeling study will come from calculations of the resultant patterns of melting and magmatic crustal thickness. However, such calculations are complicated because of the highly 3D nature of melt transportation paths expected for

the triple junction geometry. For example, predictions of crustal thickness along a single, linear ridge have been made by integrating all melt generated in a plane perpendicular to the spreading axis [e.g., *Phipps Morgan and Forsyth*, 1988; *Ito and Lin*, 1995a]. However, for the model geometry considered here, careful account must be made of the partitioning of melt between the three spreading branches. Furthermore, because of the inherent migration of the triple junction, melt calculations must incorporate the fact that ridge systems will tap mantle that has been previously melted.

Variable viscosity and buoyancy. Earlier modeling studies [e.g., *Shen and Forsyth*, 1992] predict that upwelling for the case of a temperature- and pressure-dependent mantle viscosity is both stronger and more localized to the region immediately below the ridge axis compared to the case of constant mantle viscosity. For example, the across-axis width of the axial high-velocity upwelling zone for temperature- and pressure-dependent viscosity is approximately 70-80% that for the constant viscosity case. Thus use of a pressure- and temperature-dependent mantle viscosity is likely to more closely confine along-axis increases in upwelling velocity and temperature to the immediate vicinity of the triple junction. One implication of this localization is that the region over which axial melt production is predicted to increase along R_3 may be shorter than in the case of constant viscosity by ~20-30%.

Use of variable viscosity may also change the constrast in upwelling velocity magnitude between R_1 and R_3. The increase in upwelling velocity magnitude due to use of a pressure- and temperature-dependent viscosity as opposed to constant viscosity is predicted to be spreading-rate dependent [*Shen and Forsyth*, 1992]. For half-spreading rates comparable to the SWIR, axial upwelling velocity is predicted to be ~85% faster for variable viscosity. However, this increase is <40% for SEIR and CIR half-rates. Therefore, the relative difference in axial upwelling rates between the SWIR and SEIR may be decreased by the

use of variable viscosity, resulting in a smaller predicted along-R_3 increase in vertical velocity.

Similarly, buoyancy forces due to thermal, melt retention, and melt depletion effects are anticipated to increase upwelling rates and narrow the width of the upwelling *zone [Su and Buck*, 1993; *Barnouin-Jha et al.*, 1997]. Thus it is possible that addition of buoyancy forces may decrease the length along R_3 over which upwelling velocity and temperature are increased due to the triple junction effect. The combined effects of variable viscosity and buoyancy in enhancing upwelling in the immediate proximity of the triple junction, however, may be counteracted by the effects of diffuse spreading and ridge reorganizations described next.

"Virtual" vs actual triple point. Several high-resolution studies of RRR triple junctions have suggested that, rather than meeting at a strict geometrical point, the three spreading branches often fail to connect. Evidence for ridge non-connectivity is seen at the BTJ [*Ligi et al.*, 1997], ATJ [*Searle,* 1980], and RTJ [*Mitchell,* 1991; *Mendel et al.*, 2000], among others. Commonly, the slowest-spreading branch is separated from a triple junction by a zone of diffuse deformation, leading to the suggestion that at a local scale (<100 km away from the triple point), spreading at an RRR triple junction may occur in an areal fashion rather than linearly along three well-defined ridges [*Zonenshain et al.,* 1980]. Observations further suggest that the width of the diffuse spreading zone may vary with time. In this case, periods when the triple junction migrates away from the locus of spreading termination along one or more ridges alternate with periods of rapid ridge propagation, when the ridges extend to reconnect at a point [*Searle and Francheteau*, 1986; *Mendel et al.*, 2000]. Such localized ridge kinematics, which result in less organized spreading, are anticipated to reduce upwelling beneath the triple junction.

Detailed ridge segment geometry. The models described in this investigation purposefully make use of a simplified ridge geometry to isolate the first-order mantle dynamics arising from the conjunction of three divergent plates. More detailed ridge geometry incorporating segmentation will add local complexity to the 3D flow fields. However, we anticipate these effects to be limited only to ridge segment scales.

6. Conclusions

The main conclusions of this study of mantle flow and temperature patterns generated by passive plate separation at an oceanic RRR triple junction are:

(1) When the slowest-spreading ridge intersects two nearly-collinear faster-spreading ridges quasi-orthogonally, such as at the Rodrigues, Azores, and Galapagos triple junctions, the upwelling velocity and temperature along the slowest-spreading branch is calculated to increase toward the triple junction, approaching the greater upwelling rate and higher temperature of the fastest-spreading branch. For a model geometry resembling the SWIR branch of the RTJ, upwelling velocity is predicted to increase more than threefold within 300 km of the triple junction. In contrast, the velocity and thermal fields for the fastest-spreading ridge are not significantly different from the case where the two slower-spreading ridges are not present.

(2) When a basal thermal anomaly representing a plume source is added to the triple junction model, thermal patterns for all three ridge branches are altered. Relative to the case with no plume, addition of a plume source anomaly changes the thermal structure of the slowest-spreading ridge more than that of the intermediate- or faster-spreading branches. The divergence of the surface plates away from the triple junction results in a flow field which advects the plume thermal anomaly along the slowest-spreading ridge away from the

triple junction. As a result, the location of the maximum along-axis thermal anomaly at a given depth is predicted to be farther away from the triple junction than the original plume source beneath the depths of partial melting.

Acknowledgments: We wish to thank the members of the Geodynamics and Tectonics Group at WHOI for many useful suggestions and insightful comments. We also thank Henry Dick for many interesting conversations about triple junctions, Bob Detrick and Maria Zuber for helpful guidance, and Mark Behn and Allegra Hosford for discussion on numerical models. This work was supported by NSF grant OCE-990630.

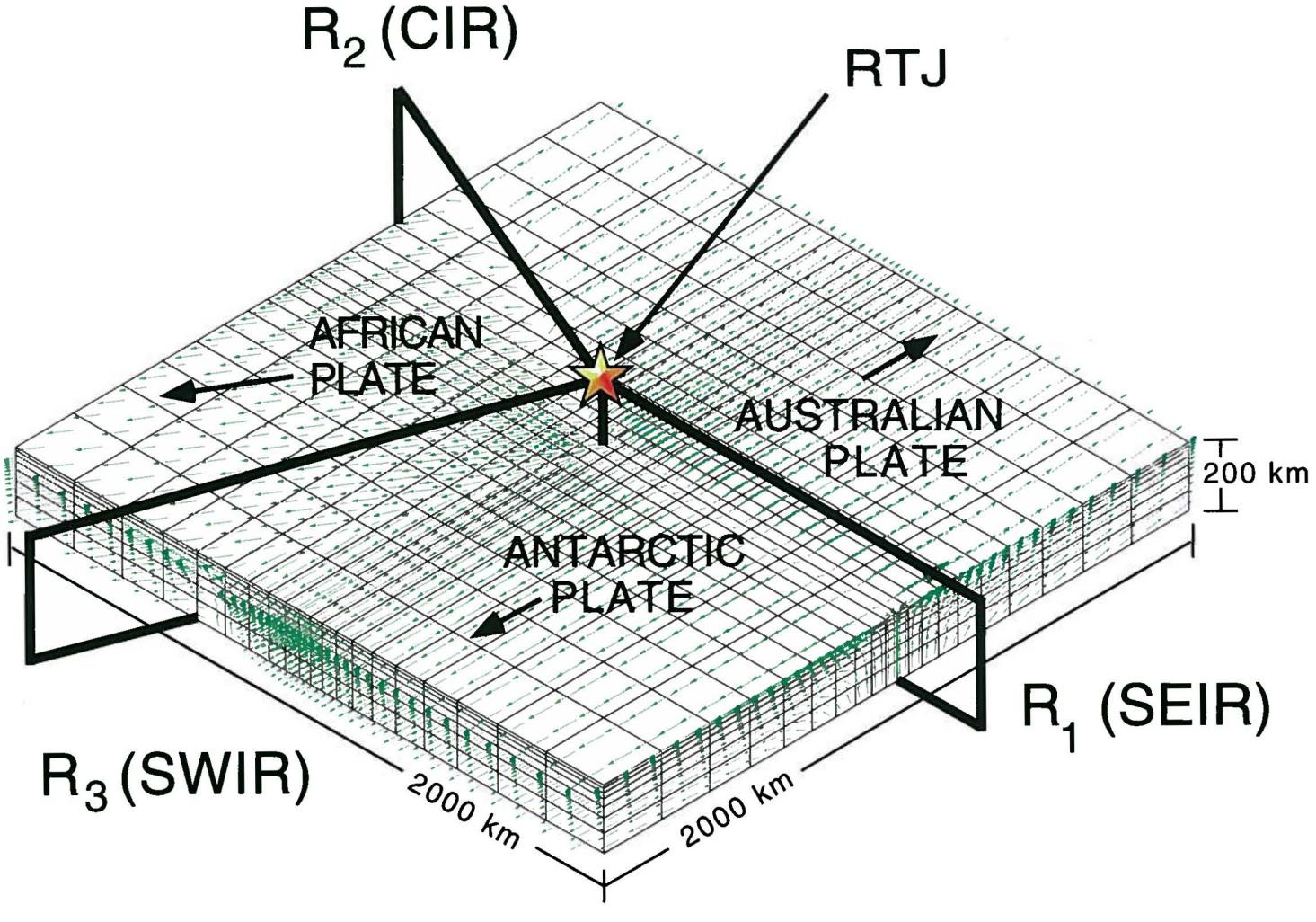
R2 (CIR)
RTJ
AFRICAN PLATE
AUSTRALIAN PLATE
ANTARCTIC PLATE
200 km
R1 (SEIR)
R3 (SWIR)
2000 km
2000 km

Figure 4b

References

Barnouin-Jha, K., E.M. Parmentier, and D.W. Sparks, Buoyant mantle upwelling and crustal production at oceanic spreading centers: On-axis segmentation and off-axis melting, *J. Geophys. Res.*, 102, 11979-11989, 1997.

Bathe, K-J., Finite element procedures, 1037 pp., Prentice Hall, Upper Saddle River, NJ, 1996.

Bonatti, E., Not so hot 'hot spots' in the oceanic mantle, *Science*, 250, 107-111, 1990.

Braun, M.G., G. Hirth, and E.M. Parmentier, The effects of deep damp melting on mantle flow and melt generation beneath mid-ocean ridges, *Earth Planet. Sci. Lett.*, 176, 339-356, 2000.

Campan, A., J.-Y. Royer, P. Gente, J.-L. Olivet, and R.D. Muller, Evolution of the Azores-Gibraltar plate boundary for the last 36 Ma, *EOS, Trans. AGU*, 75, F586, 1993.

Canales, J.P., J.J. Danobeitia, R.S. Detrick, E.E.E. Hooft, R. Bartolome, and D.F. Naar, Variations in axial morphology along the Galapagos spreading center and the influence of the Galapagos hotspot, *J. Geophys. Res.*, 102, 27341-27354, 1997.

Canales, J.P., G. Ito, R. Detrick, J. Sinton, T. Blacic, M. Behn, and J. Lin, Origin of the Galapagos swell: Bathymetry, gravity, and seismic constraints along the Galapagos Spreading Center, *EOS, Trans. AGU*, 81, F1095, 2000.

Cannat, M., A. Briais, C. Deplus, J. Escartin, J. Georgen, J. Lin, S. Mercouriev, C. Meyzen, M. Muller, G. Pouliquen, A. Rabain, and P. da Silva, Mid-Atlantic Ridge-Azores hotspot interactions: along-axis migration of a hotspot-derived event of enhanced magmatism 10 to 4 Ma ago, *Earth Planet. Sci. Lett.*, 173, 257-269, 1999a.

Cannat, M., C. Rommevaux-Jestin, D. Sauter, C. Deplus, and V. Mendel, Formation of the axial relief at the very slow spreading Southwest Indian Ridge (49 degrees to 69 degrees E), *J. Geophys. Res.*, 104, 22825-22843, 1999b.

Detrick, R.S., H.D. Needham, and V. Renard, Gravity anomalies and crustal thickness variations along the Mid-Atlantic Ridge between 33°N and 40°N, *J. Geophys. Res.*, 100, 3767-3787, 1995.

Dick, H.J.B., R.L. Fisher, and W.B. Bryan, Mineralogic variability of the uppermost mantle along mid-ocean ridges, *Earth Planet. Sci. Lett.*, 69, 88-106, 1984.

Dosso, L., H. Bougault, and J.-L. Joron, Geochemical morphology of the North Mid-Atlantic Ridge, 10 degrees – 24 degrees N: Trace element-isotope complementarity, *Earth Planet. Sci. Lett.*, 120, 443-462, 1993.

Douglass, J., J.G. Schilling, R.H. Kingsley, and C. Small, Influence of the Discovery and Shona mantle plumes on the southern Mid-Atlantic Ridge: Rare Earth evidence, *Geophys. Res. Lett.*, 22, 2893-2986, 1995.

Escartin, J., M. Cannat, G. Pouliquen, A. Rabain, and J. Lin, Crustal thickness of the V-shaped ridges south of the Azores hotspot (36°-39°N): Constraints on ridge-hotspot interactions, *J. Geophys. Res.*, in press, 2001.

Georgen, J., J. Lin, and H.J.B. Dick, Evidence from gravity anomalies for interactions of the Marion and Bouvet hotspots with the Southwest Indian Ridge: Effects of transform offsets, *Earth Planet. Sci. Lett.*, 187, 283-300, 2001.

Goslin, J. and the Triatnord Scientific Party, Extent of Azores plume influence on the Mid-Atlantic Ridge north of the hotspot, *Geology*, 27, 991-944, 1999.

Hartnady, C.J.H. and A.P. le Roex, Southern Ocean hotspot tracks and the Cenozoic absolute motion of the African, Antarctic, and South American plates, *Earth Planet. Sci. Lett.*, 75, 245-257, 1985.

Hey, R.N., G.L. Johnson, and A. Lowrie, Recent plate motions in the Galapagos area, *Geol. Soc. Am. Bull.*, 88, 1385-1403, 1977.

Ito, G. and J. Lin. Mantle temperature anomalies along the present and paleoaxes of the Galapagos spreading center as inferred from gravity analysis, *J. Geophys. Res.*, 100, 3733-3745, 1995a.

Ito, G. and J. Lin, Oceanic spreading center-hotspot interactions: Constraints from along-isochron bathymetric and gravity anomalies, *Geology*, 23, 657-660, 1995b.

Ito, G., J. Lin, and C.W. Gable, Dynamics of mantle flow and melting at a ridge-centered hotspot: Iceland and the Mid-Atlantic Ridge, *Earth Planet. Sci. Lett.*, 144, 53-74, 1996.

Klein, E.M. and C.H. Langmuir, Global correlations of ocean ridge basalt chemistry with axial depth and crustal thickness, *J. Geophys. Res.*, 92, 8089-8115, 1987.

Krause, D.C. and N.D. Watkins, North Atlantic crustal genesis in the vicinity of the Azores, Geophys. *J. R. astr. Soc.*, 19, 261-283, 1970.

Ligi, M., E. Bonatti, G. Bortoluzzi, G. Carrara, P. Fabretti, D. Penitenti, D. Gilod, A.A. Peyve, S. Skolotnev, and N. Turko, Death and transfiguration of a triple junction in the south Atlantic, *Science*, 276, 243-245, 1997.

Lonsdale, P., Structural pattern of the Galapagos Microplate and evolution of the Galapagos triple junctions, *J. Geophys. Res.*, 93, 13551-13574, 1988.

McKenzie, D.P. and W.J. Morgan, Evolution of triple junctions, *Nature*, 224, 125-133, 1969.

Mendel, V., D. Sauter, Ph. Patriat, and M. Munschy, Relationship of the Central Indian Ridge segmentation with the evolution of the Rodrigues Triple Junction for the past 8 Myr, *J. Geophys. Res.*, 105, 16563-16575, 2000.

Mitchell, N.C., Distributed extension at the Indian Ocean triple junction, *J. Geophys. Res.*, 96, 8019-8043, 1991.

Mitchell, N.C. and L.M. Parson, The tectonic evolution of the Indian Ocean triple junction, Anomaly 6 to present, *J. Geophys. Res.*, 98, 1793-1812, 1993.

Mitchell, N.C. and R.A. Livermore, Spiess Ridge: An axial high on the slow spreading Southwest Indian Ridge, *J. Geophys. Res.*, 103, 15457-15471, 1998.

Moreira, M., T. Staudacher, P. Sarda, J.G. Schilling, and C.J. Allegre, A primitive plume neon component in MORB: The Shona Ridge anomaly, South Atlantic (51-52 S), *Earth Planet. Sci. Lett.*, 133, 367-377, 1995.

Mueller, R.D, W.R. Roest, J.-Y Royer, L.M. Gahagan, and J.G. Sclater, Digital isochrons of the world's ocean floor, *J. Geophys. Res.*, 102, 3211-3214, 1997.

Patriat, P., D. Sauter, M. Munschy, L. Parson, A survey of the Southwest Indian Ridge axis between Atlantis II Fracture Zone and the Indian Ocean Triple Junction: Regional setting and large scale segmentation, *Mar. Geophys. Res.*, 19, 457-480, 1997.

Patriat, P. and L. Parson, A survey of the Indian Ocean Triple Junction trace within the Antarctic Plate: Implications for the junction evolution since 15 Ma, *Mar. Geophys. Res.*, 11, 89-100, 1989.

Phipps Morgan, J. and D.W. Forsyth, 3-D flow and temperature perturbations due to transform offset: effects on oceanic crustal and upper mantle structure, *J. Geophys. Res.*, 93, 2955-2966, 1988.

Phipps Morgan, J. and E.M. Parmentier, Causes and rate-limiting mechanisms of ridge propagation: a fracture mechanics model, *J. Geophys. Res.*, 90, 8603-8612, 1985.

Rabinowicz, M., S. Rouzo, J.C. Sempere, and C. Rosemberg, Three-dimensional mantle flow beneath mid-ocean ridges, *J. Geophys. Res.*, 98, 7851-7869, 1993.

Reid, I. and H.R. Jackson, Oceanic spreading rate and crustal thickness, *Mar. Geophys. Res.*, 5, 165-171, 1981.

Sandwell, D.T. and W.H.F. Smith, Marine gravity anomaly from Geosat and ERS 1 satellite altimetry, *J. Geophys. Res.*, 102, 10039-10054, 1997.

Schilling, J.-G., R.H. Kingsley, and J.D. Devine, Galapagos hot spot-spreading center system 1. Spatial petrological and geochemical variations (83°W-101°E), *J. Geophys. Res.*, 87, 5593-5610, 1982.

Schilling, J.-G., Fluxes and excess temperatures of mantle plumes inferred from their interaction with migrating mid-ocean ridges, *Nature*, 352, 397-403, 1991.

Sclater, J.G., C. Bowin, R. Hey, H. Hoskins, J. Peirce, J. Phillips, and C. Tapscott, The Bouvet Triple Junction, *J. Geophys. Res.*, 81, 1857-1869, 1976.

Sclater, J.G., R.L. Fisher, Ph. Patriat, C. Tapscott, and B. Parsons, Eocene to recent development of the Southwest Indian Ridge, a consequence of the evolution of the Indian Ocean triple junction, *Geophys. J. R. astr. Soc.*, 64, 587-604, 1981.

Searle, R.C., Tectonic pattern of the Azores spreading center and triple junction, *Earth Planet. Sci. Lett.*, 51, 415-434, 1980.

Searle, R.C. and J. Francheteau, Morphology and tectonics of the Galapagos triple junction, *Mar. Geophys. Res.*, 8, 95-129, 1986.

Shen, Y. and D.W. Forsyth, The effects of temperature- and pressure-dependent viscosity on three-dimensional passive flow of the mantle beneath a ridge-transform system, *J. Geophys. Res.*, 97, 19727-19728, 1992.

Sleep, N.H., Hotspots and mantle plumes: Some phenomenology, *J. Geophys. Res.*, 95, 6715-6736, 1990.

Small, C., Observations of ridge-hotspot interactions in the Southern Ocean, *J. Geophys. Res.*, 100, 17931-17946, 1995.

Smith, W.H.F. and D. Sandwell, Global sea floor topography from satellite altimetry and ship depth soundings, *Science*, 277, 1956-1962, 1997.

Sparks, D.W. and E.M. Parmentier, The structure of three-dimensional convection beneath oceanic spreading centers, *Geophys. J. Int.*, 112, 81-91, 1993.

Su, W. and W.R. Buck, Buoyancy effects on mantle flow under mid-ocean ridges, *J. Geophys. Res.*, 98, 12191-12205, 1993.

Tapscott, C., Ph. Patriat, R.L. Sclater, J.G., Hoskins, H. and B. Parsons, The Indian Ocean Triple Junction, *J. Geophys. Res.*, 85, 3969-4723, 1980.

Verma, S.P., J.-G. Schilling, and D.G. Waggoner, Neodymium isotopic evidence for Galapagos hotspot-spreading centre system evolution, *Nature*, 306, 654-657, 1983.

West, B.P., H. Fujimoto, C. Honsho, K. Tamaki, and J.C. Sempere, A three-dimensional gravity study of the Rodrigues triple junction and Southeast Indian Ridge, *Earth Planet. Sci. Lett.*, 133, 175-184, 1995.

Zhang, Y. and T. Tanimoto, Ridges, hotspots, and their interactions as observed in seismic velocity maps, *Nature*, 355, 45-49, 1992.

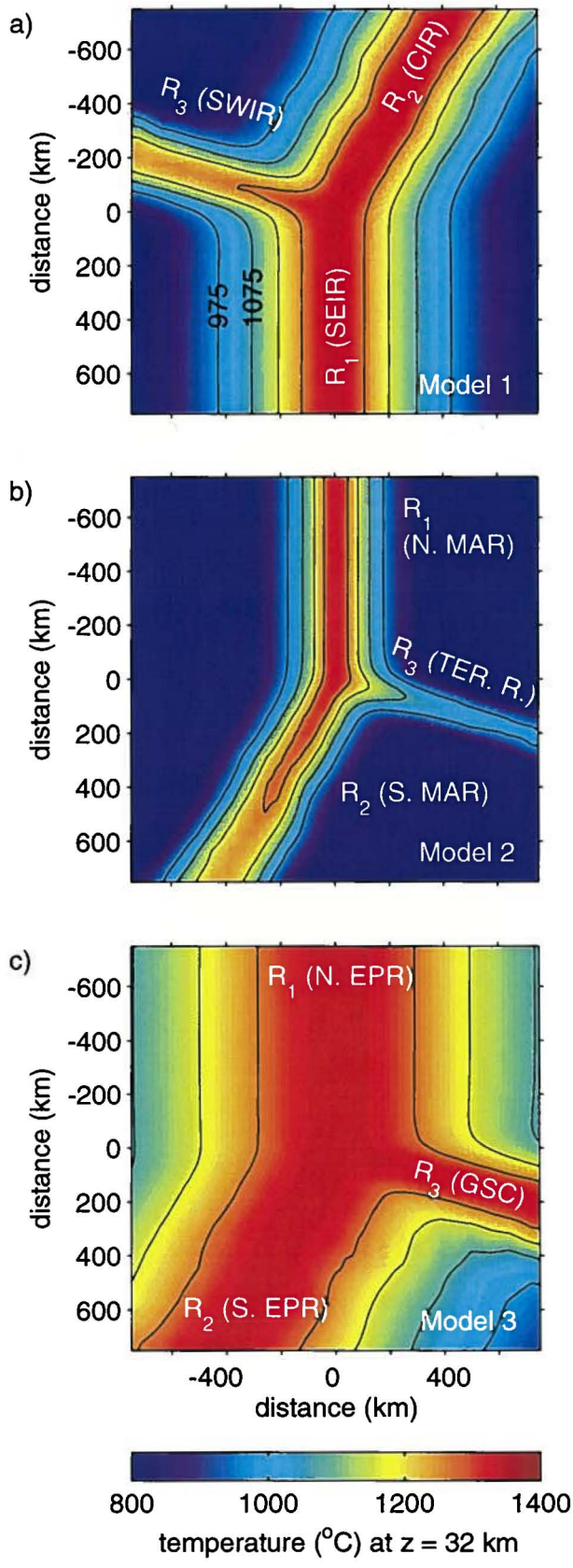
a)
-600
-400
-200
0
200
400
600
distance (km)
R3 (SWIR)
R2 (CIR)
975
1075
R1 (SEIR)
Model 1
b)
R1
(N. MAR)
R3 (TER. R.)
R2 (S. MAR)
Model 2
c)
R1 (N. EPR)
R3 (GSC)
R2 (S. EPR)
Model 3
-400
0
400
distance (km)
800
1000
1200
1400
temperature (°C) at z = 32 km

Figure 7

Figure 1: Location maps for four ridge-ridge-ridge triple junctions, a) Rodrigues, b) Azores, c) Galapagos, and d) Bouvet. Ridge coordinates are from *Mueller et al.* [1997], and free-air gravity data were extracted from the global database of *Sandwell and Smith* [1997]. For each triple junction, the location of the 35 mGal contour is indicated, and an artificial illumination is applied from the NNW. The position of the nearest hotspot to each triple junction is indicated with a white star. Ridge abbreviations are as follows: SWIR = Southwest Indian Ridge, CIR = Central Indian Ridge, SEIR = Southeast Indian Ridge, N. MAR = Mid-Atlantic Ridge to the north of the Azores Triple Junction, S. MAR = Mid-Atlantic Ridge to the south of the Azores Triple Junction, TER. R. = Terceira Rift, N. EPR = East Pacific Rise to the north of the Galapagos Triple Junction, S. EPR = East Pacific Rise to the south of the Galapagos Triple Junction, GSC = Galapagos Spreading Center, and AAR = American-Antarctic Ridge.

(a)
Reunion
CIR
SEIR
SWIR
50°
60°
70°
80°
-10°
-20°
-30°
-40°
(b)
N. MAR
TER. R.
Azores
S. MAR
-50°
-40°
-30°
-20°
-10°
50°
40°
30°
(c)
GSC
Galapagos
S. EPR
N. EPR
10°
0°
-10°
-80°
-90°
-100°
-110°
(d)
MAR
SWIR
Bouvet
AAR
-40°
-50°
-60°
10°
0°
-10°
40
20
0
-20
-40
free-air anomaly (mGal)

Figure 1

Figure 2: The geometric similarity of the Rodrigues (RTJ), Azores (ATJ), and Galapagos (GTJ) triple junctions is shown by plotting half-spreading rate ratios. For each triple junction, half-rates for the three ridges are U_1, U_2, and U_3, with $U_1 > U_2 > U_3$. In all three of the RTJ, ATJ, and GTJ, the two fastest-spreading ridges are nearly collinear, and are intersected nearly perpendicularly by the slowest-spreading ridge. The ridge configuration is different, however, for the Bouvet Triple Junction (BTJ), where the three ridges have nearly equal separation angles from each other.

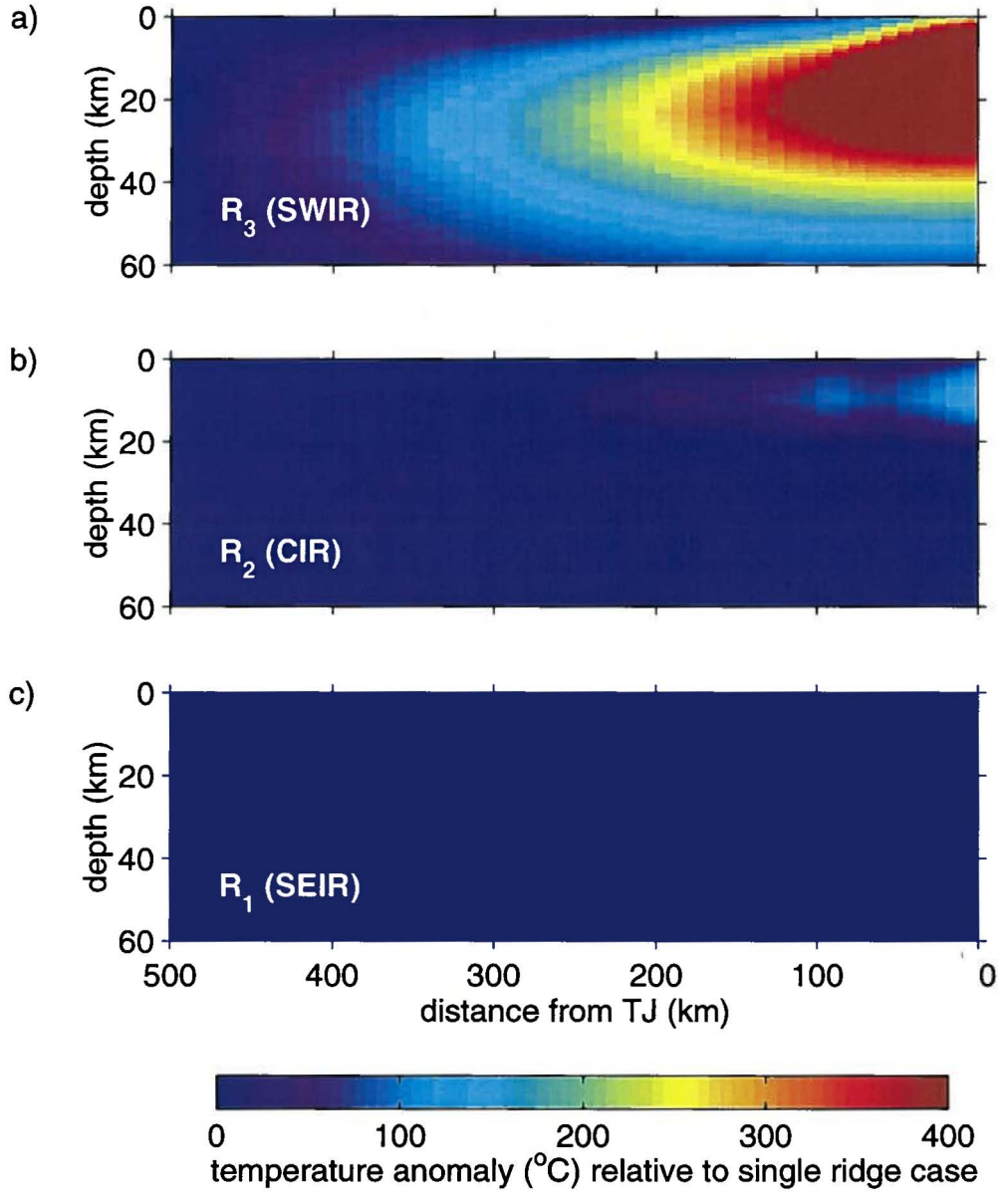
a)
b)
c)
depth (km)
0
20
40
60
R3 (SWIR)
R2 (CIR)
R1 (SEIR)
500
400
300
200
100
0
distance from TJ (km)
0
100
200
300
400
temperature anomaly (°C) relative to single ridge case

Figure 9

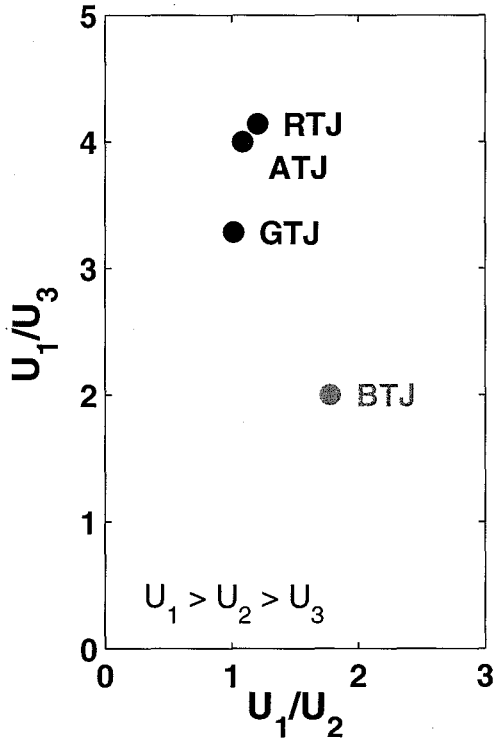

Figure 2

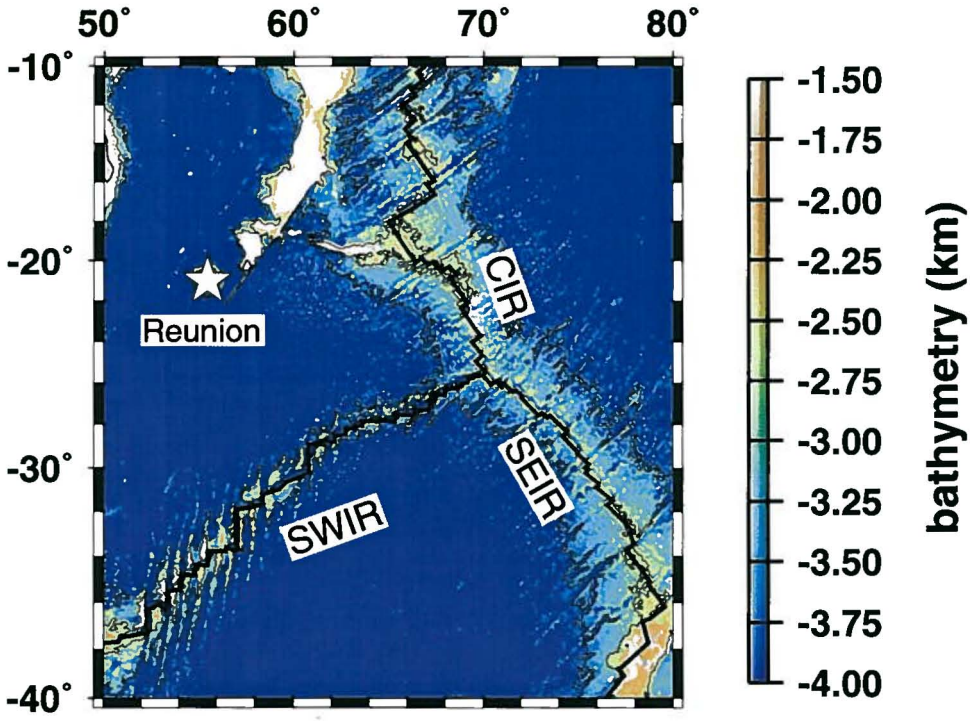
50°
60°
70°
80°
-10°
-20°
-30°
-40°
Reunion
CIR
SEIR
SWIR
-1.50
-1.75
-2.00
-2.25
-2.50
-2.75
-3.00
-3.25
-3.50
-3.75
-4.00
bathymetry (km)

Figure 10a

Figure 3: Simplified geometry of the a) Rodrigues, b) Azores, and c) Galapagos triple junctions. Simplified geometry reflects the regional trend of each of the spreading branches comprising a given triple junction, omitting transform offsets, microplates, and small zones of disconnectivity between the three ridges and the triple junction point. The half-spreading rate for each of the ridges is indicated, and ridge abbreviations are given in Figure 1. Arrows show plate motion with respect to the triple junction, modified from *Tapscott et al.* [1980], *Searle* [1980], and *Searle and Francheteau* [1986]. R_1 designates the ridge with the fastest half-spreading rate, R_2 the ridge with intermediate spreading rate, and R_3 the ridge with the slowest spreading rate.

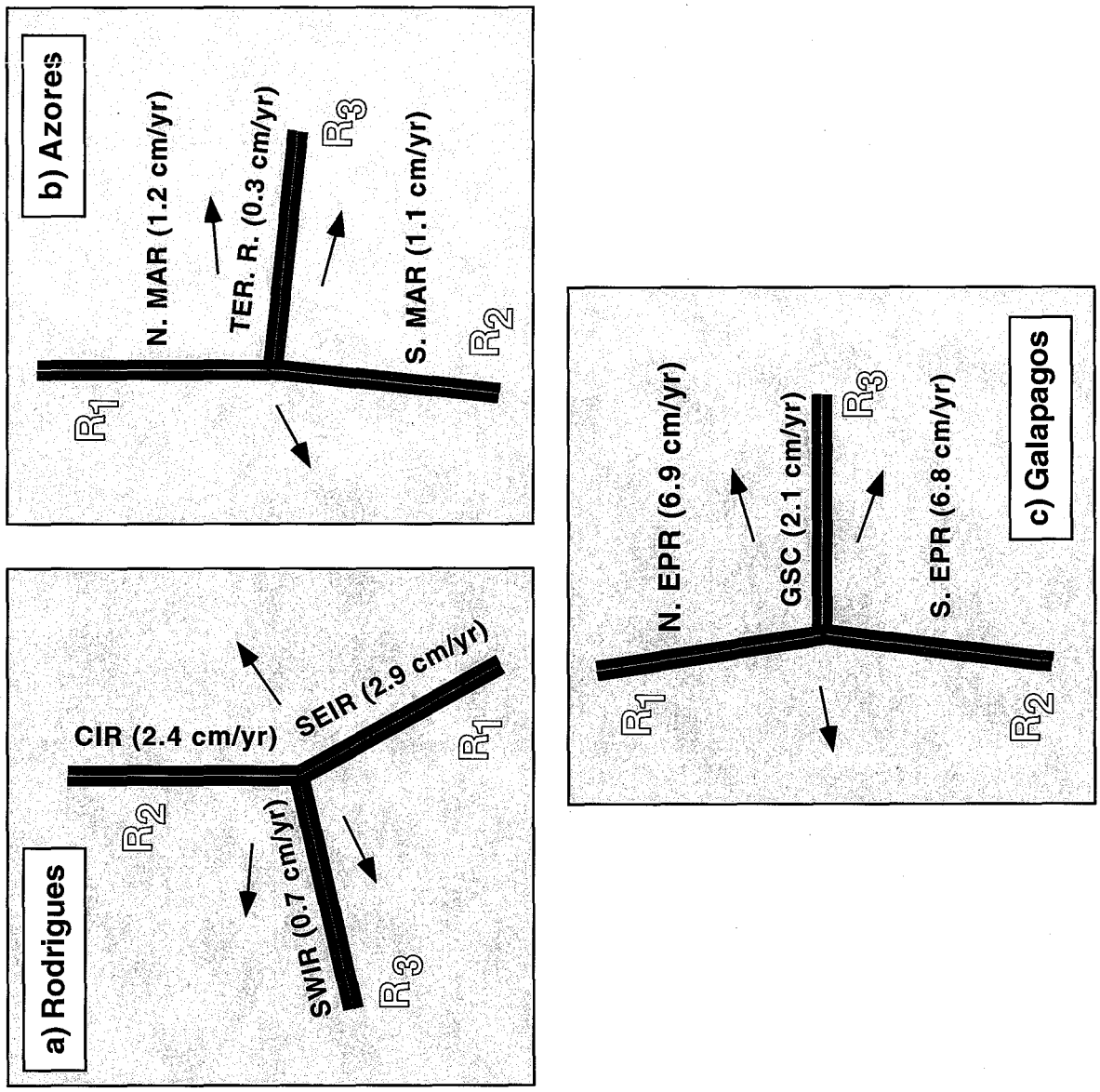
b) Azores
N. MAR (1.2 cm/yr)
TER. R. (0.3 cm/yr)
S. MAR (1.1 cm/yr)
R1
R2
R3
a) Rodrigues
CIR (2.4 cm/yr)
SEIR (2.9 cm/yr)
SWIR (0.7 cm/yr)
R1
R2
R3
c) Galapagos
N. EPR (6.9 cm/yr)
GSC (2.1 cm/yr)
S. EPR (6.8 cm/yr)
R1
R2
R3

Figure 3

Figure 4: a) The top surface of the set-up for Model 1. Flow within the model box is driven by the divergence of the African (AFR), Antarctic (ANT), and Australian (AUS) plates. The position of the triple junction is fixed in the model reference frame, and the motions of the three plates with respect to the triple junction are indicated by thick black arrows. The component of the plate motion vectors perpendicular to R_3 (SWIR), R_2 (CIR), or R_1 (SEIR) is equal to the ridge's half-spreading rate and direction. RTJ traces represent accretionary boundaries dividing the crust created at two adjacent ridges. Light gray orthogonal lines represent the numerical grid.

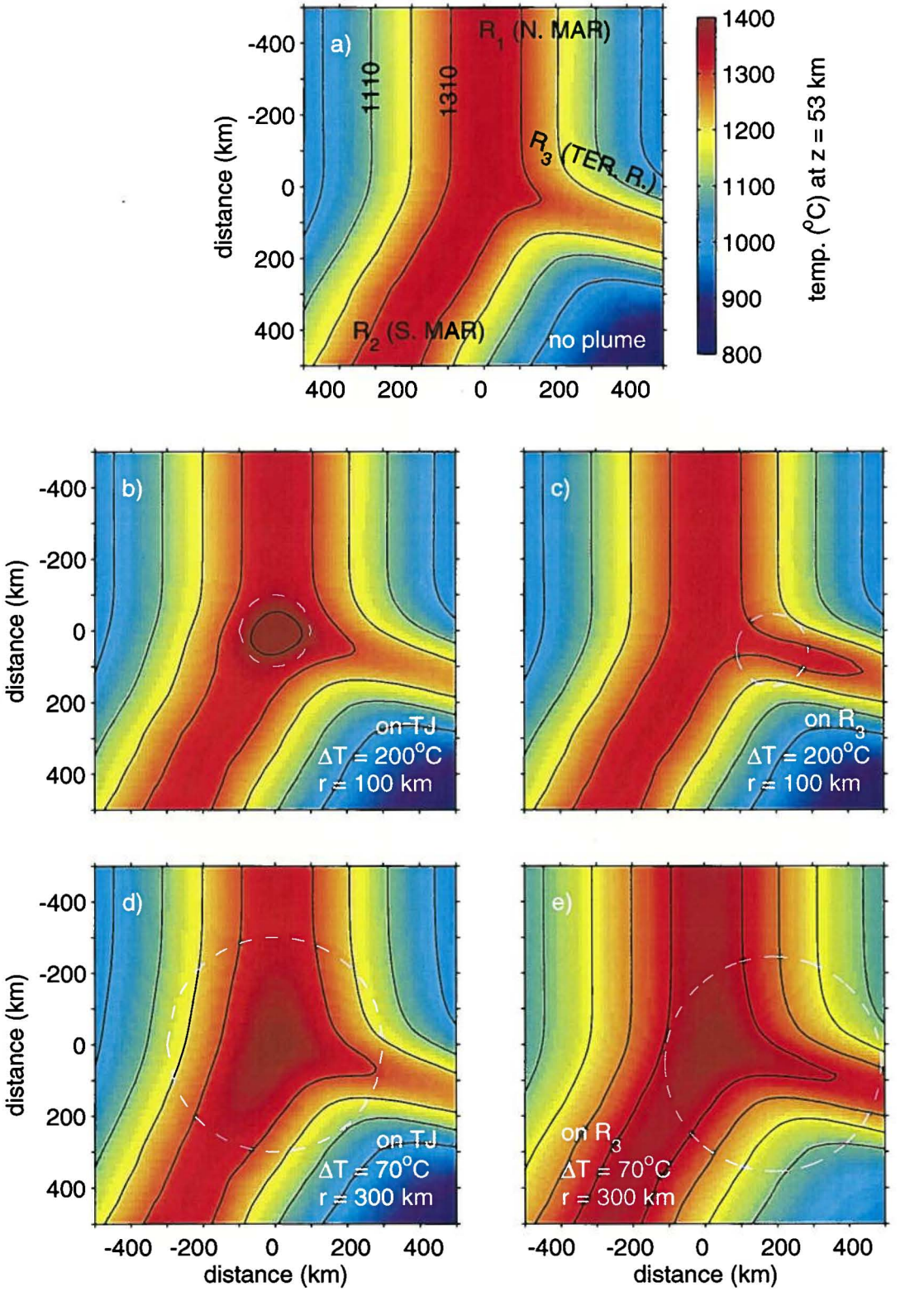
a)
R1 (N. MAR)
1110
1310
R3 (TER. R.)
R2 (S. MAR)
no plume
distance (km)
-400
-200
0
200
400
400 200 0 200 400
1400
1300
1200
1100
1000
900
800
temp. (°C) at z = 53 km
b)
on TJ
ΔT = 200°C
r = 100 km
c)
on R3
ΔT = 200°C
r = 100 km
d)
on TJ
ΔT = 70°C
r = 300 km
e)
on R3
ΔT = 70°C
r = 300 km
distance (km)
-400 -200 0 200 400
distance (km)

Figure 11

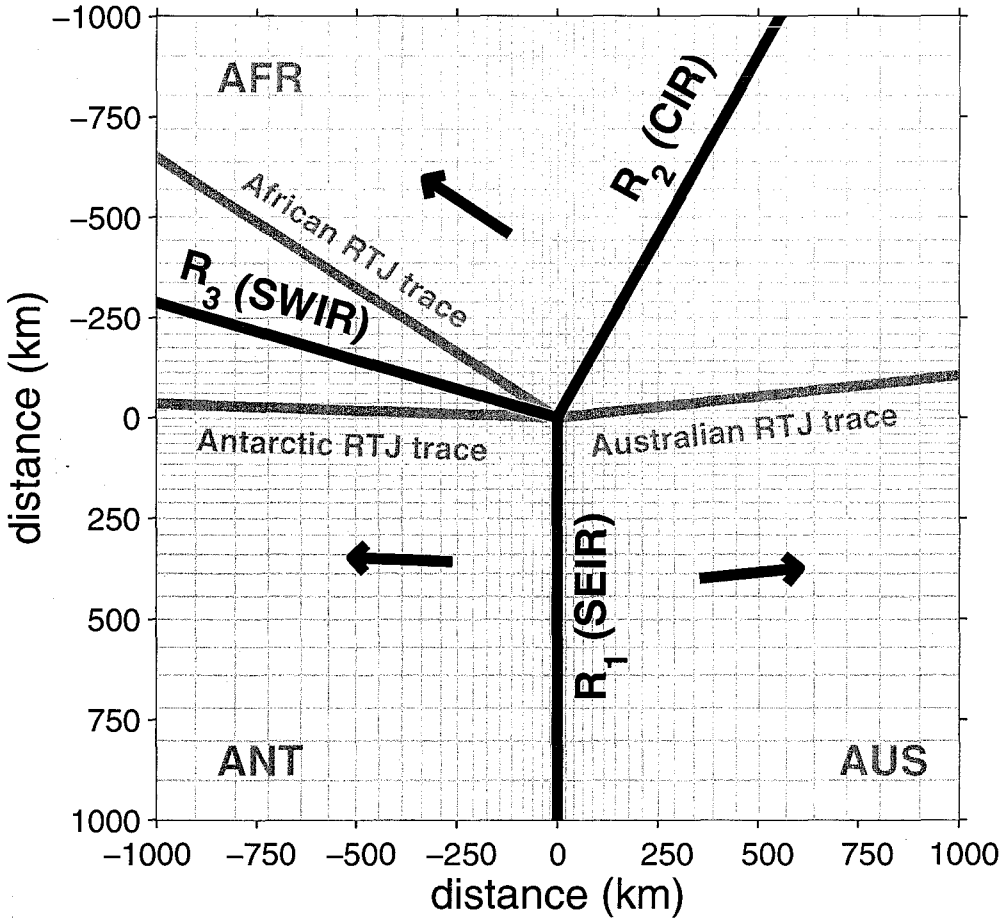
AFR
African RTJ trace
R_2 (CIR)
R_3 (SWIR)
Antarctic RTJ trace
Australian RTJ trace
R_1 (SEIR)
ANT
AUS
distance (km)
distance (km)
−1000
−750
−500
−250
0
250
500
750
1000

Figure 4a

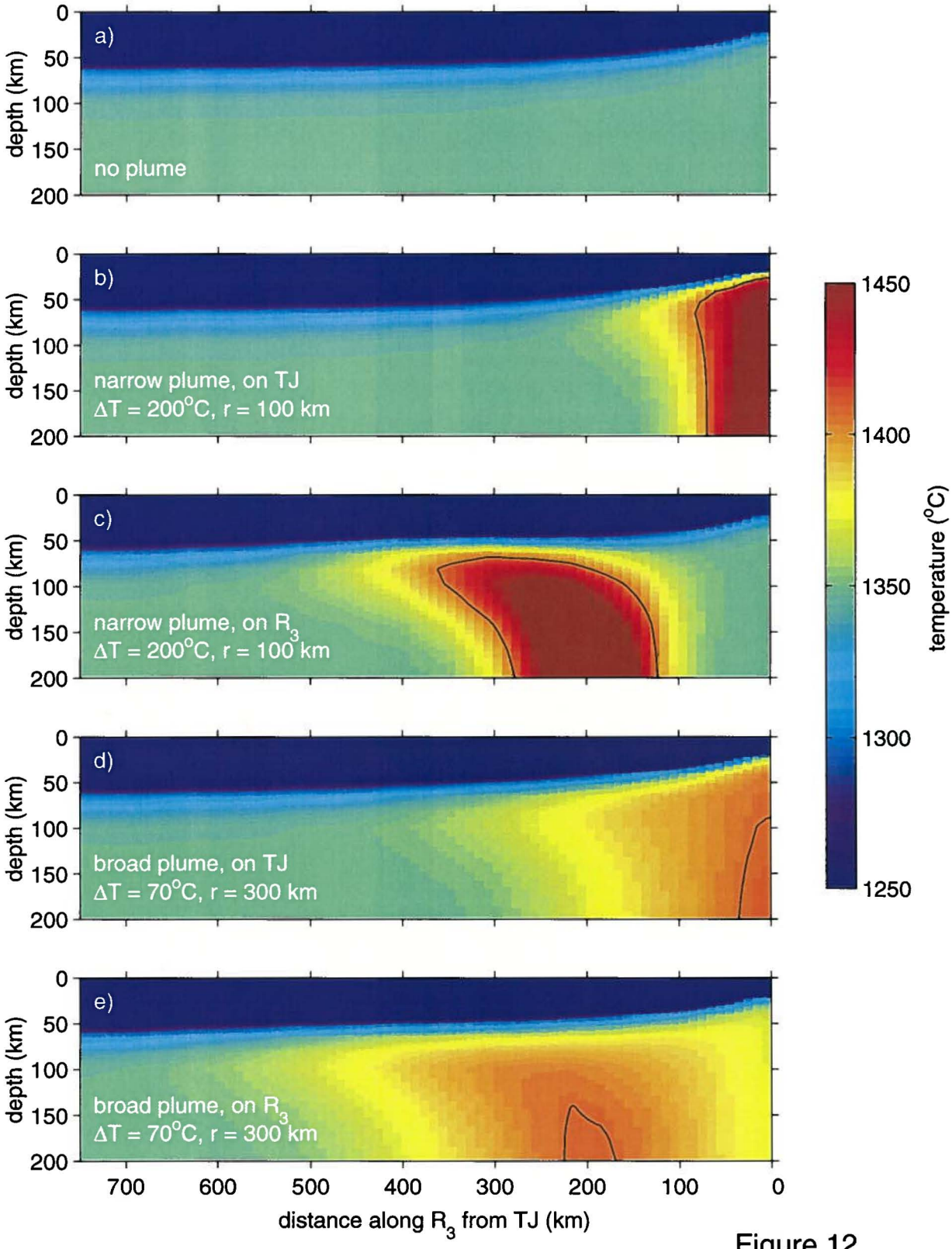
a)
no plume
b)
narrow plume, on TJ
ΔT = 200°C, r = 100 km
c)
narrow plume, on R3
ΔT = 200°C, r = 100 km
d)
broad plume, on TJ
ΔT = 70°C, r = 300 km
e)
broad plume, on R3
ΔT = 70°C, r = 300 km
depth (km)
0
50
100
150
200
700
600
500
400
300
200
100
0
distance along R3 from TJ (km)
1450
1400
1350
1300
1250
temperature (°C)

Figure 12

Figure 4: b) Three-dimensional schematic representation of the model domain. The positions of the SEIR, CIR, and SWIR are indicated with lines on the top of the model domain, and the divergence of the Australian, Antarctic, and African plates about the Rodrigues Triple Junction (star) is indicated by black arrows. The calculated 3D velocity field is shown by small green arrows. The model box is 2000 x 2000 km in the horizontal direction, and 200 km in depth.

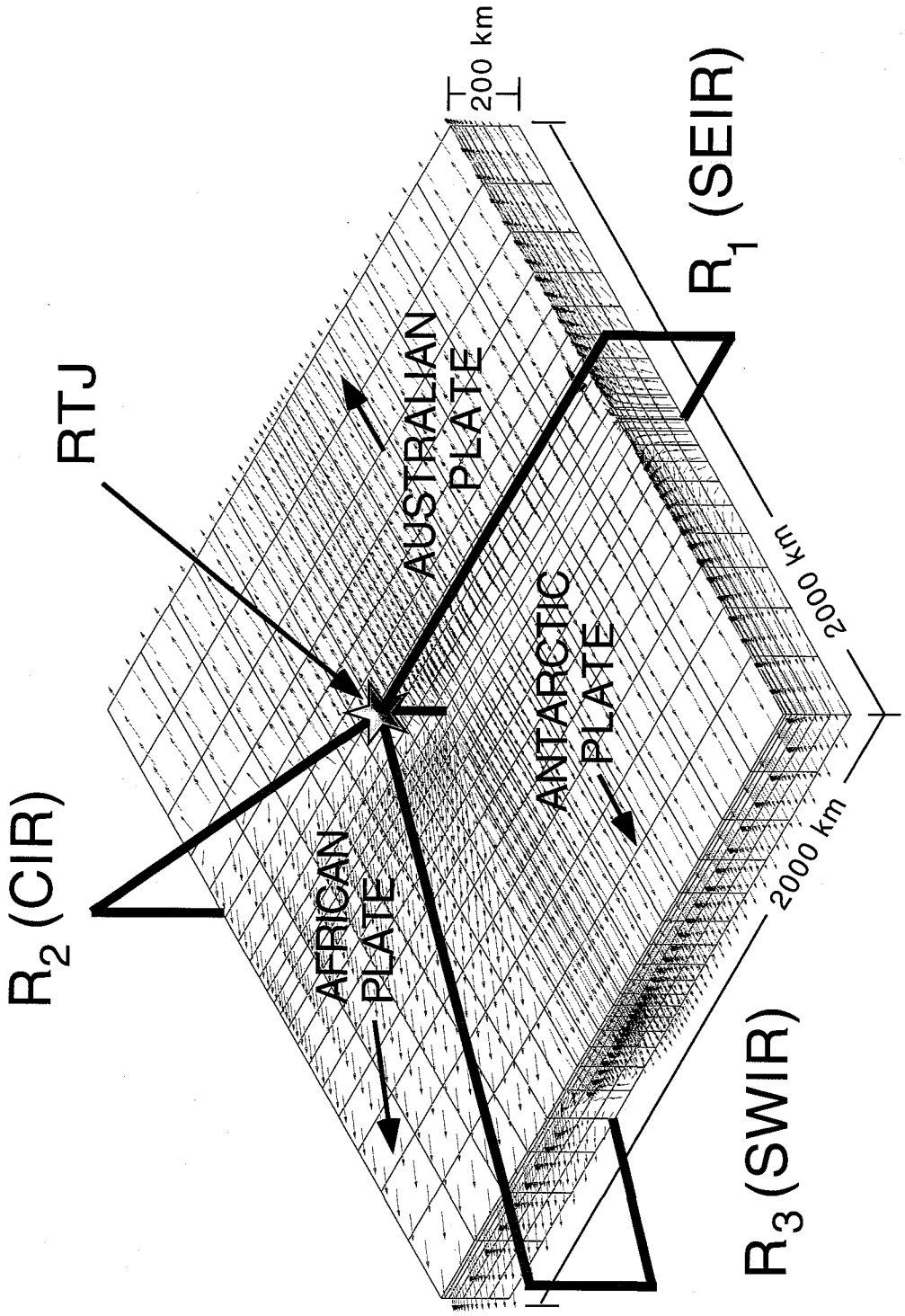
200 km
RTJ
AUSTRALIAN PLATE
ANTARCTIC PLATE
AFRICAN PLATE
2000 km
2000 km
R1 (SEIR)
R2 (CIR)
R3 (SWIR)

Figure 4b

Figure 5: Model-predicted mantle velocity, projected onto the planes of the a) R_3, b) R_2, and c) R_1 spreading branches. Note the strong component of along-axis velocity for R_3 (SWIR). In contrast, mantle motion is almost completely dominated by vertical upwelling for R_1 (SEIR). Gray shading indicates mantle temperature, with shading changes every 100°C.

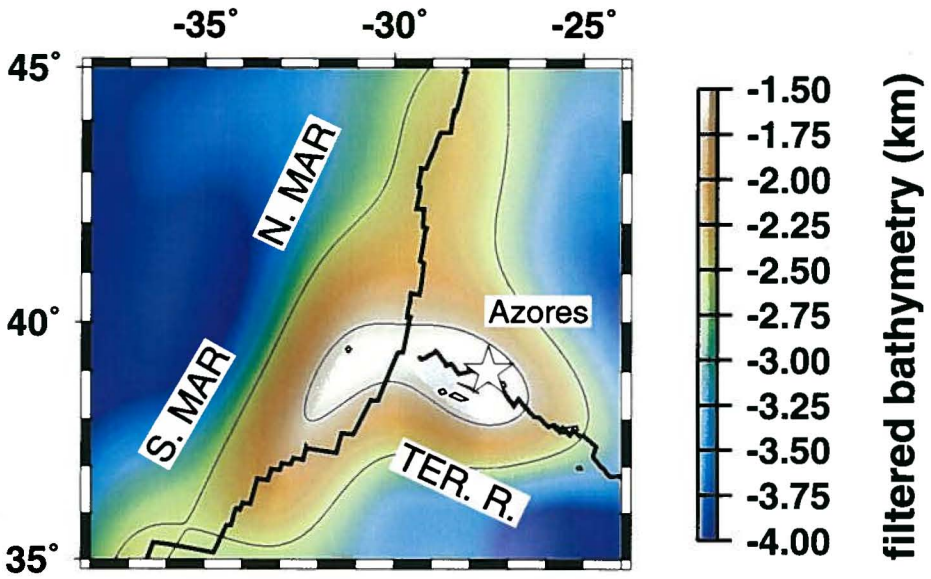
-35°
-30°
-25°
45°
40°
35°
N. MAR
S. MAR
Azores
TER. R.
-1.50
-1.75
-2.00
-2.25
-2.50
-2.75
-3.00
-3.25
-3.50
-3.75
-4.00
filtered bathymetry (km)

Figure 14

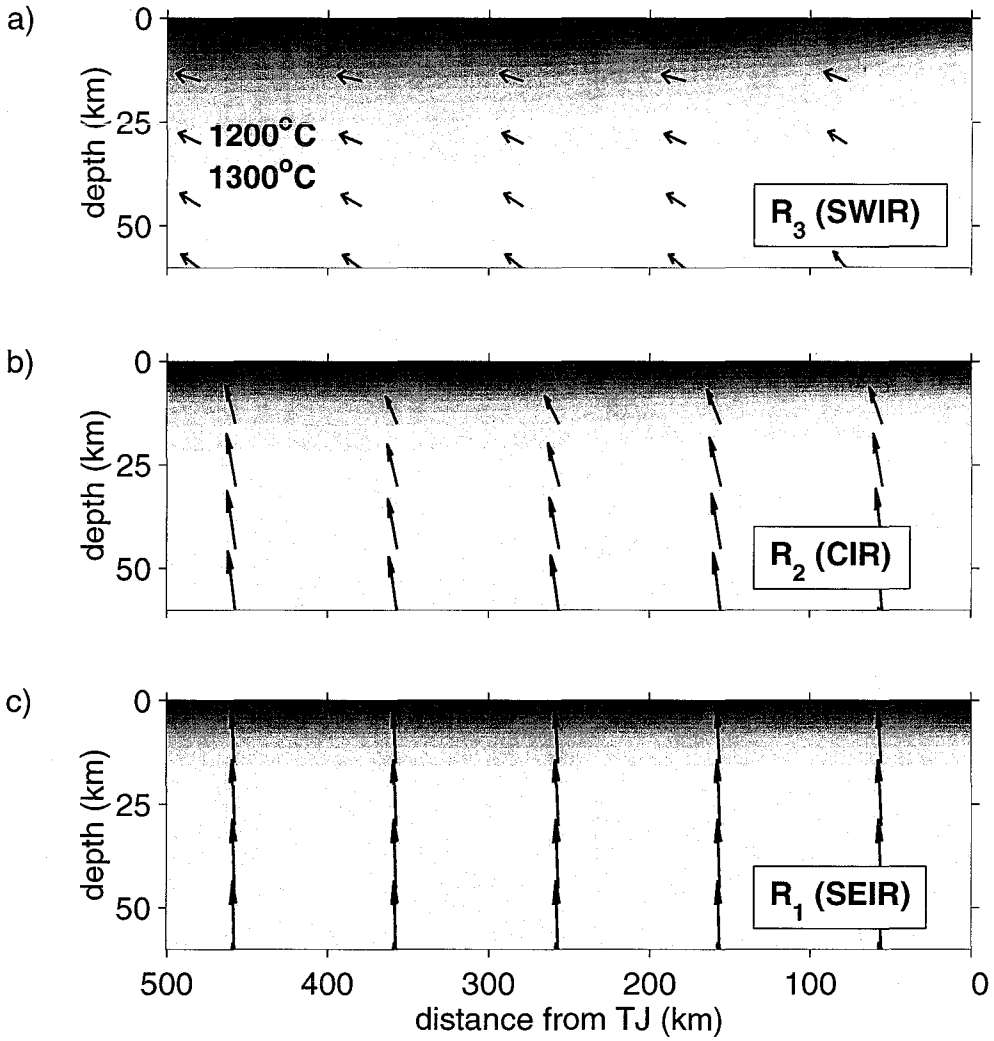
a)
b)
c)
depth (km)
0
25
50
1200°C
1300°C
R3 (SWIR)
R2 (CIR)
R1 (SEIR)
500
400
300
200
100
0
distance from TJ (km)

Figure 5

Figure 6: The calculated upwelling velocity magnitude along R_1 (SEIR, solid line), R_2 (CIR, dashed line), and R_3 (SWIR, dash-dot line), at a depth of 75 km. For comparison, the magnitude of upwelling velocity driven by passive two-plate separation at the appropriate half-spreading rate is indicated by a light gray box. Note that the magnitude of the upwelling velocity for R_3, and to a lesser extent R_2, increases toward the triple junction to approach R_1 upwelling velocity. Note also that R_1 upwelling velocity does not appear to be significantly changed by the presence of the other two ridges.

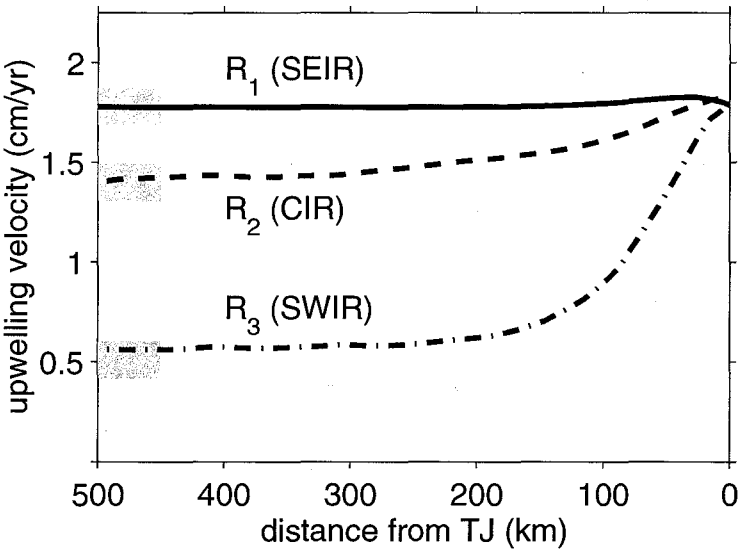
upwelling velocity (cm/yr)
2
1.5
1
0.5
R1 (SEIR)
R2 (CIR)
R3 (SWIR)
500
400
300
200
100
0
distance from TJ (km)

Figure 6

Figure 7: Plan view of predicted temperature patterns for a) Model 1, b) Model 2, and c) Model 3 at a depth of 32 km. Note that for all three triple junctions, the two fastest-spreading ridges dominate the thermal structure of the region, while the temperature of the slowest-spreading ridge increases toward the triple junction.

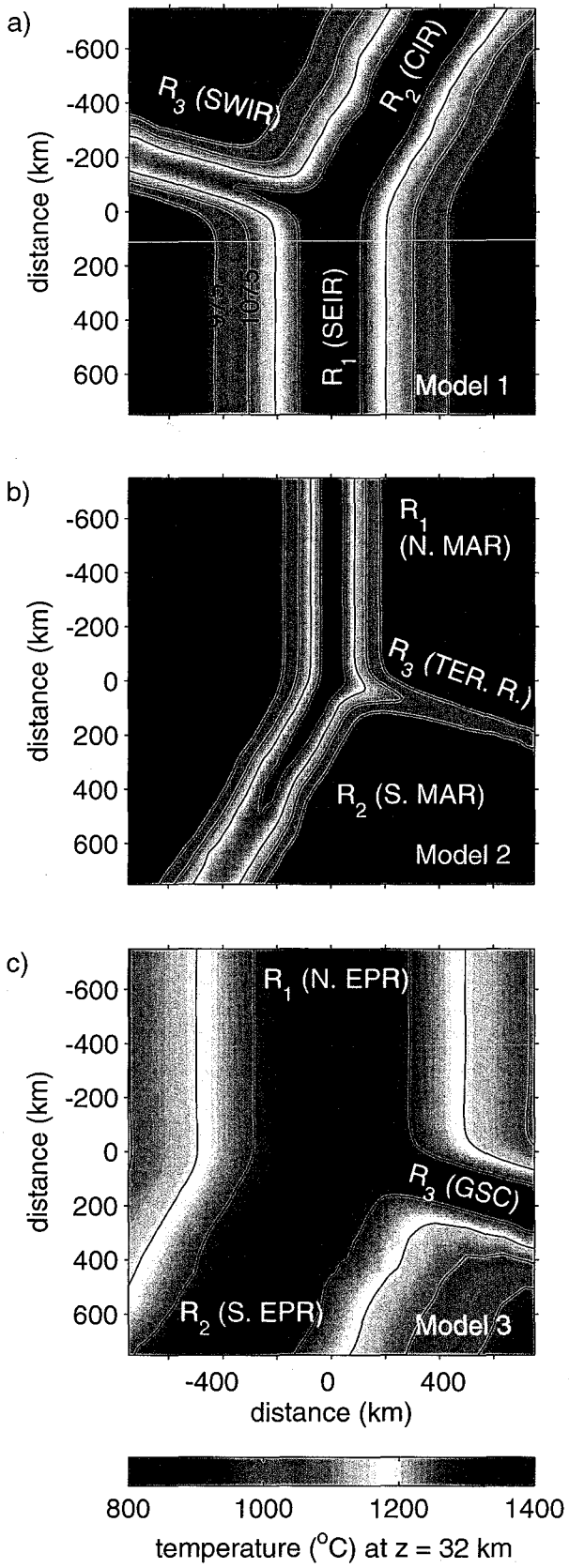
a)
-600
-400
-200
0
200
400
600
distance (km)
R3 (SWIR)
R2 (CIR)
R1 (SEIR)
Model 1
b)
R1
(N. MAR)
R3 (TER. R.)
R2 (S. MAR)
Model 2
c)
R1 (N. EPR)
R3 (GSC)
R2 (S. EPR)
Model 3
-400
0
400
distance (km)
800
1000
1200
1400
temperature (°C) at z = 32 km

Figure 7

Figure 8: Along-axis profiles of temperature at a depth of 32 km for a) Model 1, b) Model 2, and c) Model 3. Note that in all three panels, the predicted temperature increase toward the triple junction is most pronounced for the slowest-spreading branch (dash-dot line).

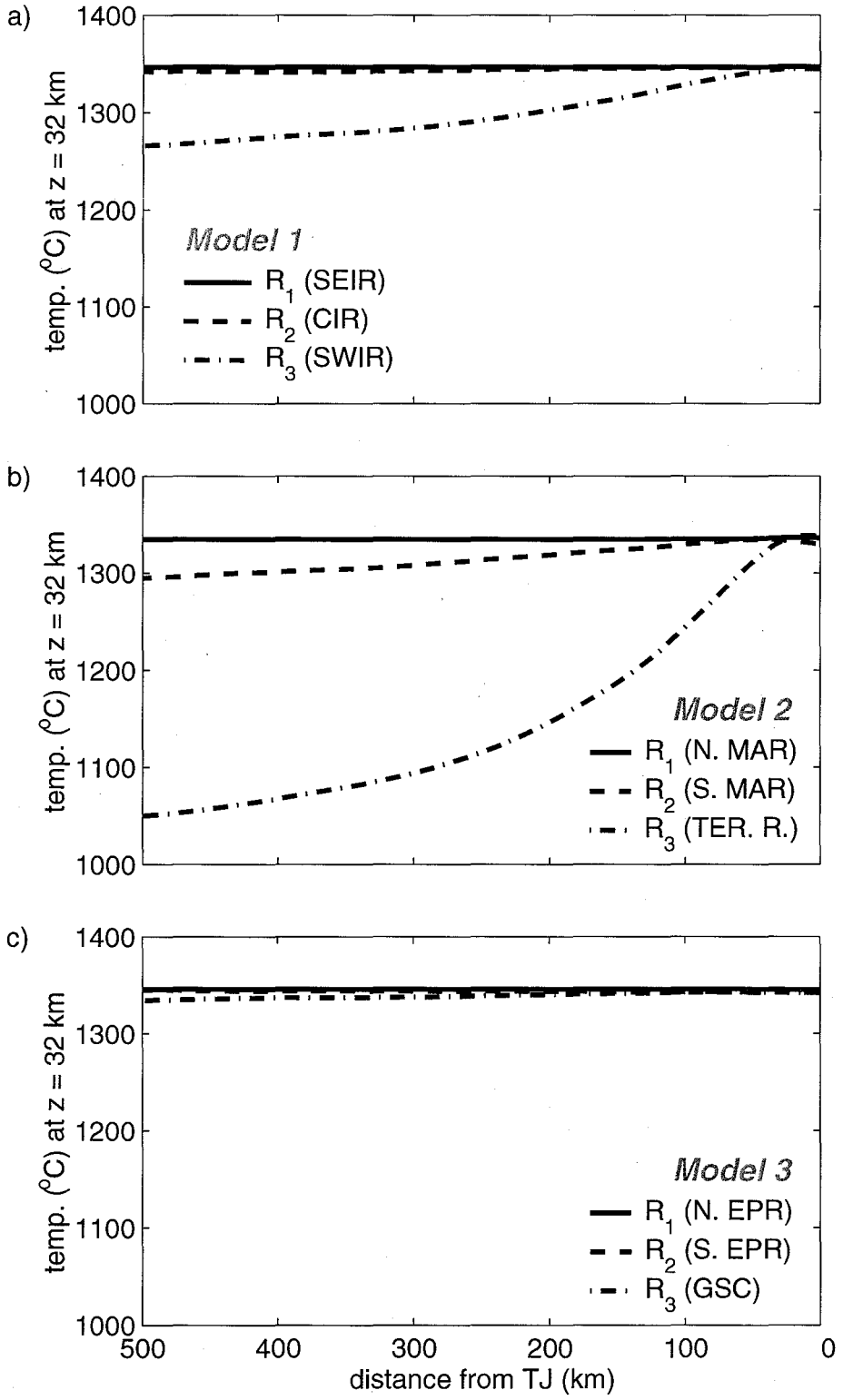
a)
b)
c)
1400
1300
1200
1100
1000
temp. (°C) at z = 32 km
Model 1
R1 (SEIR)
R2 (CIR)
R3 (SWIR)
Model 2
R1 (N. MAR)
R2 (S. MAR)
R3 (TER. R.)
Model 3
R1 (N. EPR)
R2 (S. EPR)
R3 (GSC)
500
400
300
200
100
0
distance from TJ (km)

Figure 8

Figure 9: The calculated temperature anomaly caused by triple junction flow for a) R_3 (SWIR) b) R_2 (CIR) and c) R_1 (SEIR). Temperature anomaly was calculated by subtracting the temperature-depth section calculated for a single ridge case with the spreading rate of R_1, R_2, or R_3 from the temperature-depth section calculated for the ridge as shown in Figure 5. Note that the slowest-spreading ridge R_3 has the most pronounced thermal anomaly with respect to the single ridge case, while the predicted thermal increase for R_2 is small and confined to the immediate vicinity of the triple junction. In contrast, the temperature field for R_3 in the triple junction configuration is very similar to the single ridge case.

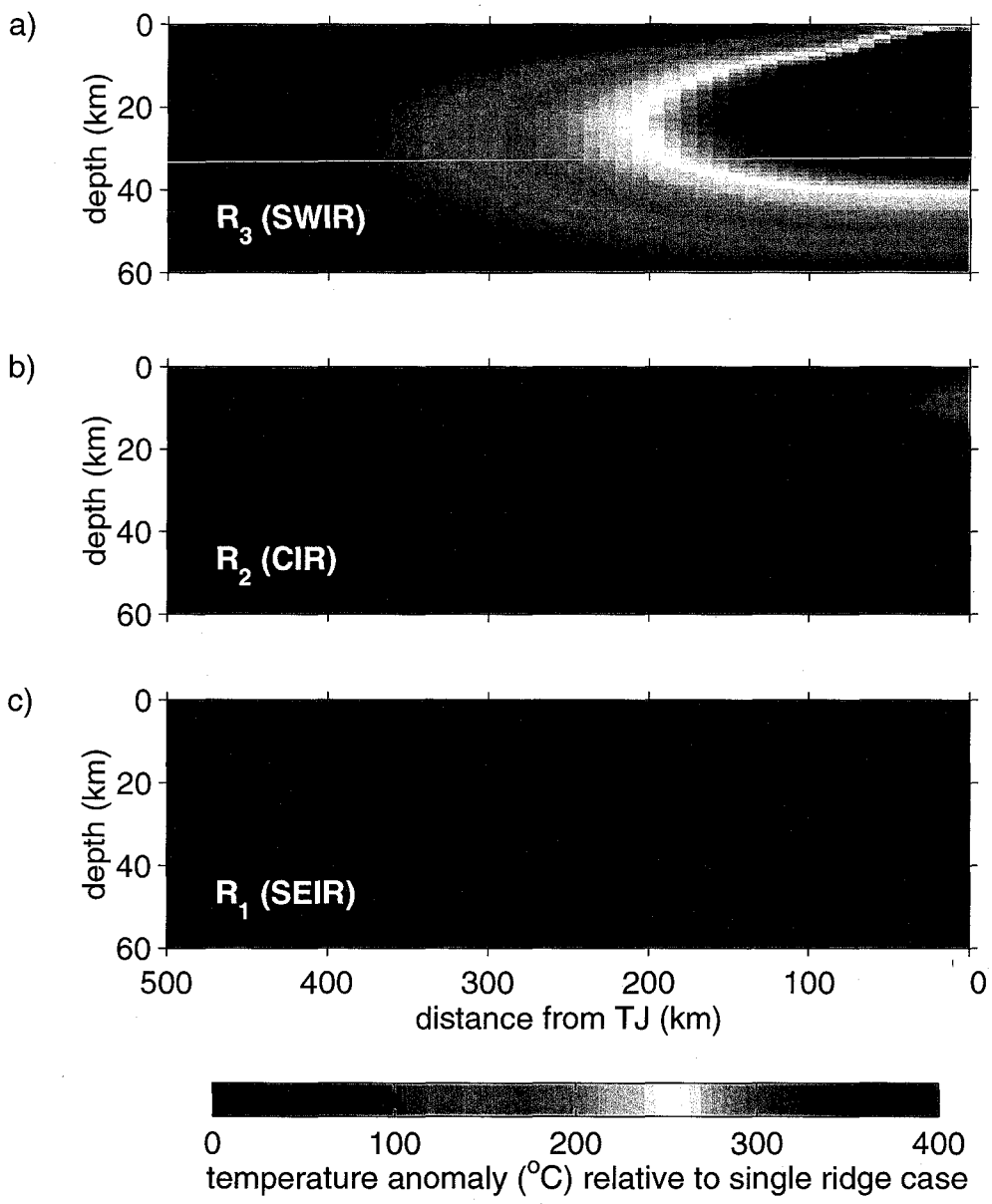
a)
b)
c)
depth (km)
0
20
40
60
R3 (SWIR)
R2 (CIR)
R1 (SEIR)
500
400
300
200
100
0
distance from TJ (km)
0
100
200
300
400
temperature anomaly (°C) relative to single ridge case

Figure 9

Figure 10: a) Bathymetry map for the Rodrigues Triple Junction region. Bathymetry data were extracted from the *Smith and Sandwell* [1997] database, and contours delineate 2.75 and 3.75 km depth.

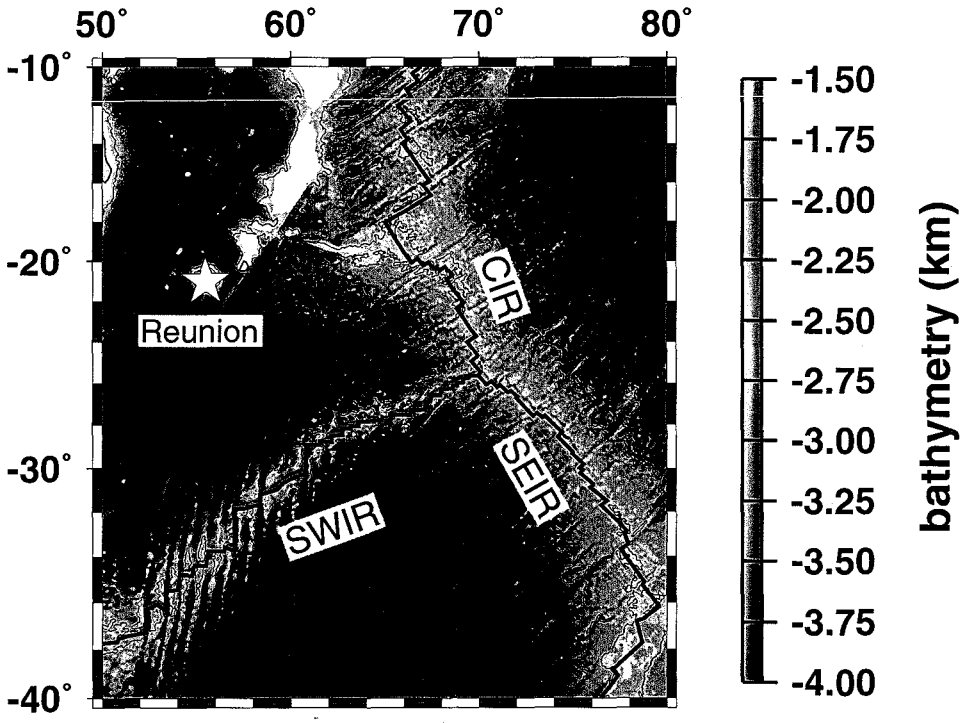
50°
60°
70°
80°
-10°
-20°
-30°
-40°
Reunion
CIR
SEIR
SWIR
-1.50
-1.75
-2.00
-2.25
-2.50
-2.75
-3.00
-3.25
-3.50
-3.75
-4.00
bathymetry (km)

Figure 10a

Figure 10: b) Along-axis profile of ridge axis depth for the SWIR compiled from *West et al.* [1995] and *Cannat et al.* [1995b]. Data gap at a distance of ~100 km results from non-overlap of the surveys in these two sources. The deepest portion of the SWIR is located to the east of the Melville Fracture Zone at 61°E. However, the ridge axis appears to shallow within a distance of ~150 km from the Rodrigues Triple Junction. Gray curve indicates the model-predicted isostatic topography due to mantle thermal variations. Following the studies of *Ito and Lin* [1995a] and *Ito et al.* [1996] which suggest that ~70-75% of along-axis mantle Bouguer gravity and bathymetry signals are attributable to crustal thickness variation, we calculate isostatic bathymetry assuming that mantle thermal variations contribute 30% to total topographic relief.

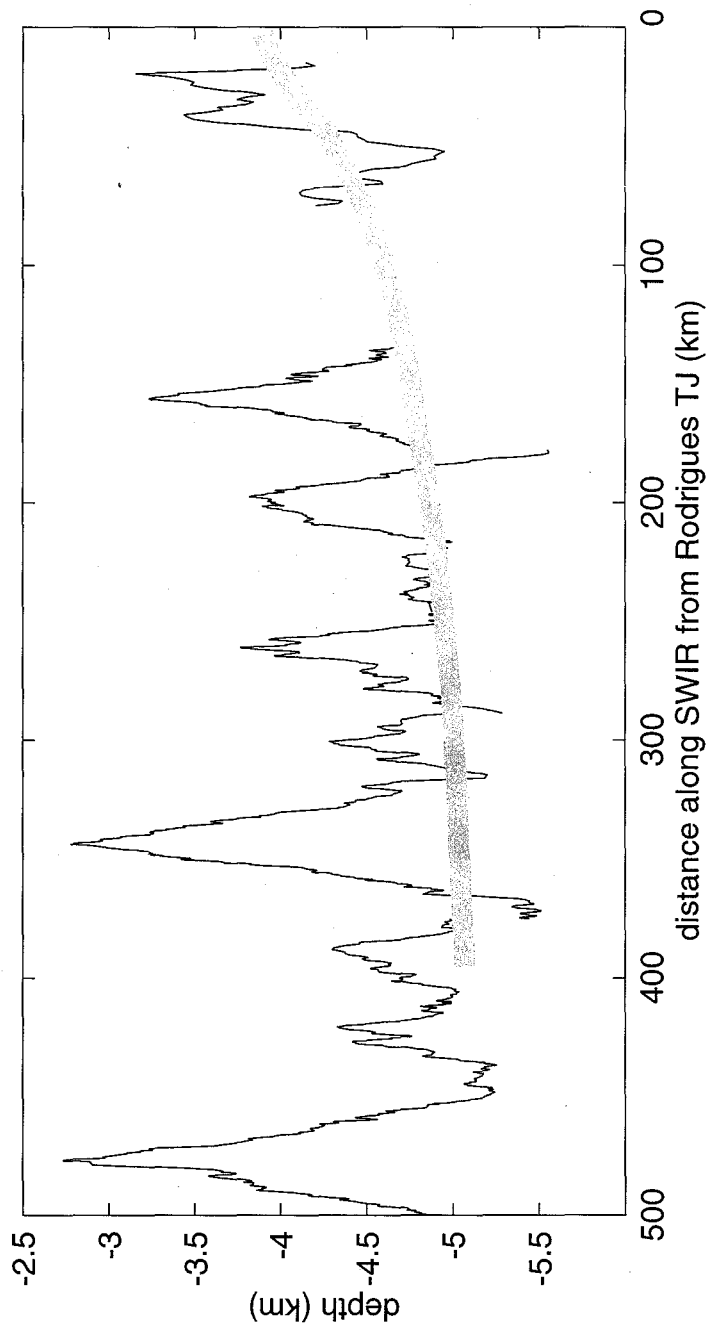
depth (km)
-2.5
-3
-3.5
-4
-4.5
-5
-5.5
distance along SWIR from Rodrigues TJ (km)
0
100
200
300
400
500

Figure 10b

Figure 11: Plan-view slices of predicted temperature for Model 2. a) No plume is present in panel a). b) The white dashed circle indicates a plume with radius 100 km and thermal anomaly ΔT of 200°C that is centered on the triple junction. ΔT, the maximum thermal anomaly with respect to the ambient mantle temperature of 1350°C, is greatest at the center of the plume and decreases linearly away. This plume is referred to in the text as a narrow, hot plume. c) A narrow, hot plume is located 200 km to the east of the triple junction along R_3. d) and e) The results of adding a broad (r = 300 km), cool (ΔT = 70°C) plume to the triple junction model. In panel d), the plume is triple-junction-centered, while in panel e), the plume center is 200 km to the east of the triple junction along R_3, similar to the geometry of panel c). For all panels, temperature contours of 100°C are indicated in black.

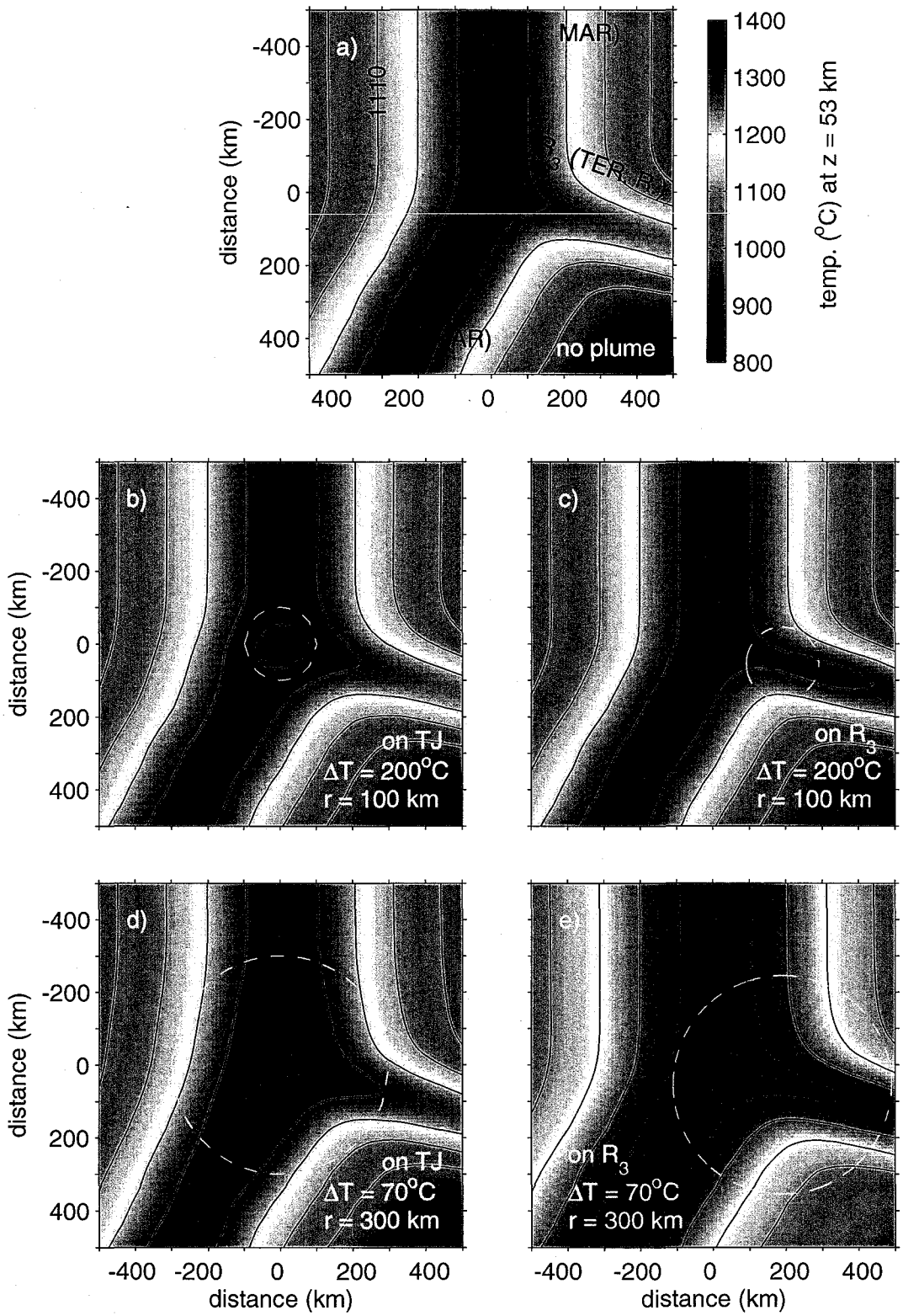
a)
MAR
1110
no plume
distance (km)
-400
-200
0
200
400
1400
1300
1200
1100
1000
900
800
temp. (°C) at z = 53 km
b)
on TJ
ΔT = 200°C
r = 100 km
c)
on R3
ΔT = 200°C
r = 100 km
d)
on TJ
ΔT = 70°C
r = 300 km
e)
on R3
ΔT = 70°C
r = 300 km
distance (km)

Figure 11

Figure 12: Vertical slices of temperature along R_3. In panel a), no plume is present. Panels b) and c) show a hot, narrow plume centered at the triple junction and 200 km away from the triple junction along R_3, respectively, corresponding to panels b) and c) of Figure 11. Similarly, panels d) and e) show model predictions for the triple-junction-centered and R_3-centered broad, cool plume, respectively. Note the pronounced along-axis advection of the thermal anomaly, particularly in panel c). In all panels, the black line indicates the 1410°C contour.

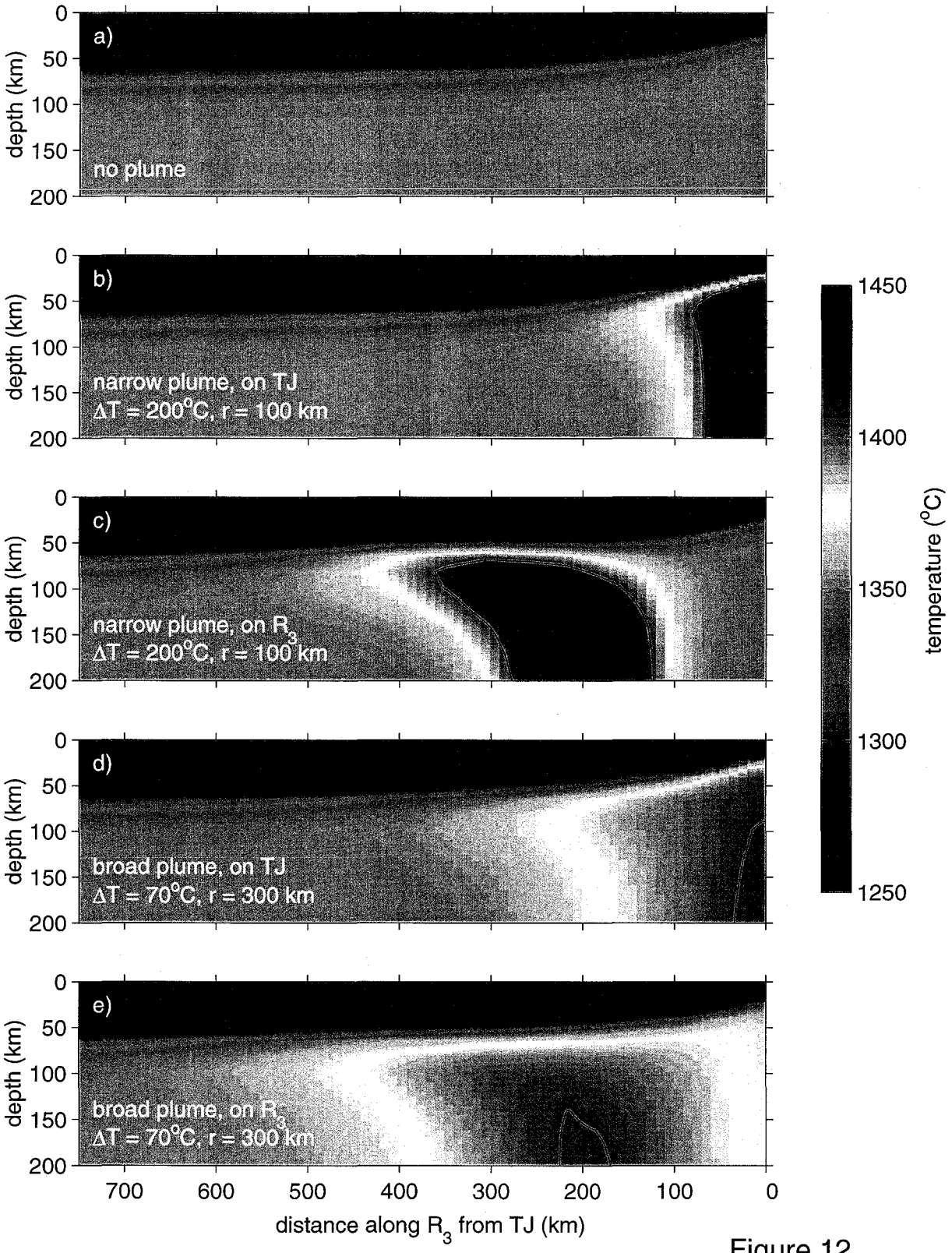
a)
no plume
b)
narrow plume, on TJ
ΔT = 200°C, r = 100 km
c)
narrow plume, on R3
ΔT = 200°C, r = 100 km
d)
broad plume, on TJ
ΔT = 70°C, r = 300 km
e)
broad plume, on R3
ΔT = 70°C, r = 300 km
depth (km)
0
50
100
150
200
700
600
500
400
300
200
100
0
distance along R3 from TJ (km)
1450
1400
1350
1300
1250
temperature (°C)

Figure 12

Figure 13: Along-axis temperature profiles at a depth of 32 km for a) R_3, b) R_2, and c) R_1, for each of the five plume configurations shown in Figure 11. In panels b) and c), the line for the no plume profile is offset slightly downwards to distinguish it from the line for the narrow, R_3-centered plume, which it would otherwise overlap. Panel d) shows the temperature increase along R_3 relative to the case with no plume.

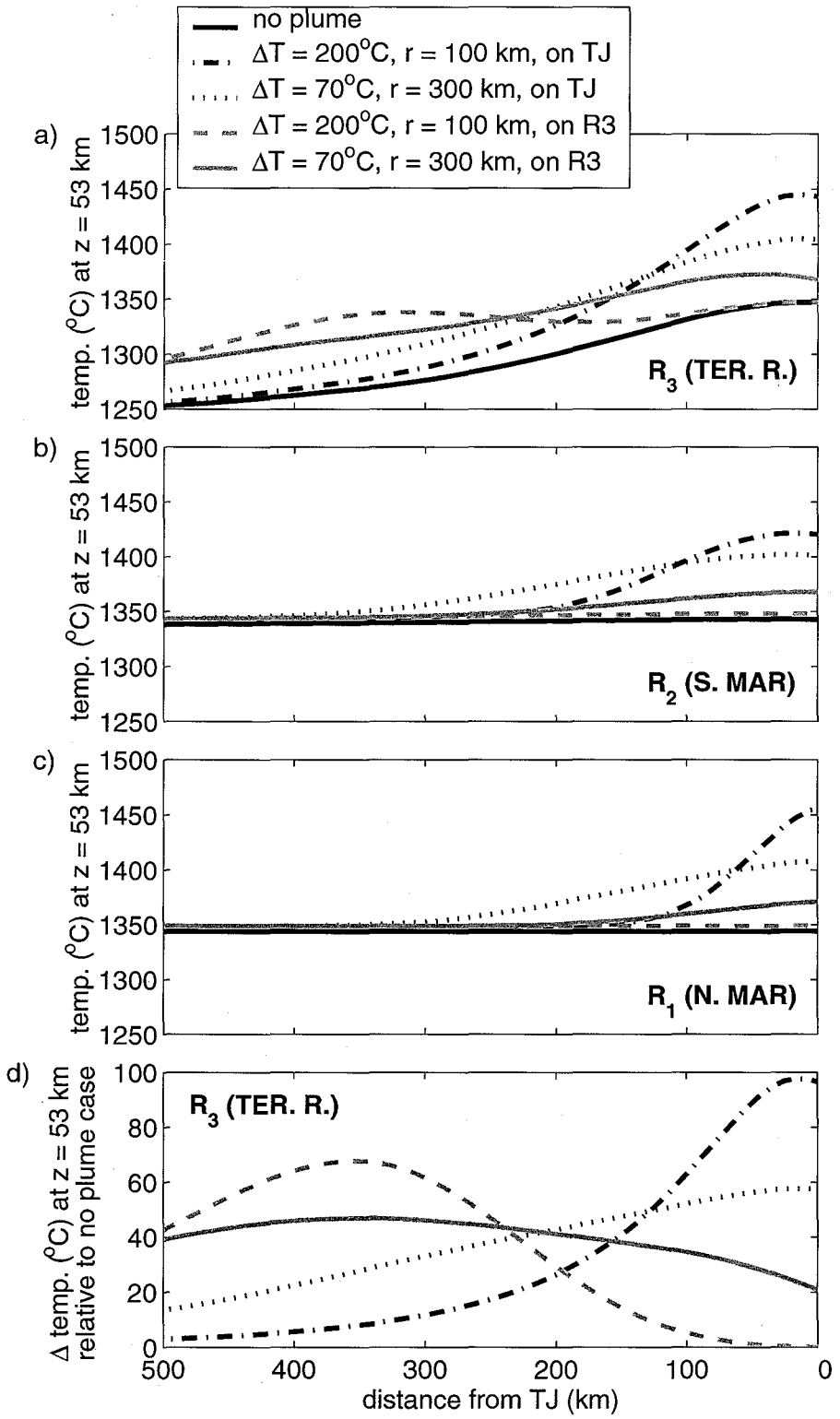
no plume
ΔT = 200°C, r = 100 km, on TJ
ΔT = 70°C, r = 300 km, on TJ
ΔT = 200°C, r = 100 km, on R3
ΔT = 70°C, r = 300 km, on R3
a)
b)
c)
d)
temp. (°C) at z = 53 km
Δ temp. (°C) at z = 53 km relative to no plume case
R3 (TER. R.)
R2 (S. MAR)
R1 (N. MAR)
distance from TJ (km)

Figure 13

Figure 14: Long-wavelength seafloor bathymetry around the Azores Triple Junction. Bathymetry map was generated by filtering predicted seafloor topography [*Smith and Sandwell*, 1997] using a lowpass filter with cutoff wavelength of 400 km. Note the pronounced long-wavelength bathymetric high over the Terceira Rift which extends to the portion of the Mid-Atlantic Ridge immediately to the south of the triple junction. As in Figure 1, the inferred center of the Azores plume is indicated with a white star.

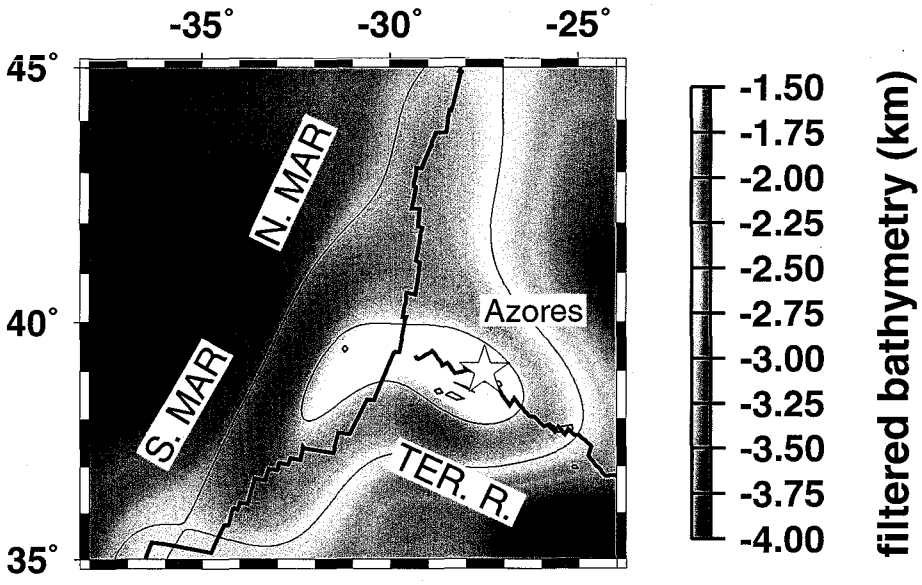
-35°
-30°
-25°
45°
40°
35°
N. MAR
S. MAR
Azores
TER. R.
-1.50
-1.75
-2.00
-2.25
-2.50
-2.75
-3.00
-3.25
-3.50
-3.75
-4.00
filtered bathymetry (km)

Figure 14

Figure 15: a) Profiles of along-axis long-wavelength seafloor topography for the Terceira Rift, southern Mid-Atlantic Ridge, and northern Mid-Atlantic Ridge, extracted from the bathymetry map of Figure 14. Portions of the profile along transform offsets have been omitted. b-e) Predicted isostatic topography along R_1, R_2, and R_3, resulting from the addition of a plume with a radius of 190 km and ΔT of 190°C to Model 2. The plumes were located 200 km from the triple junction, at positions of 1/15, 1/10, and 1/5 of the angle from R_3 to R_2. Isostatic topography profiles were calculated assuming that the mantle thermal contribution to seafloor bathymetry is 30%.

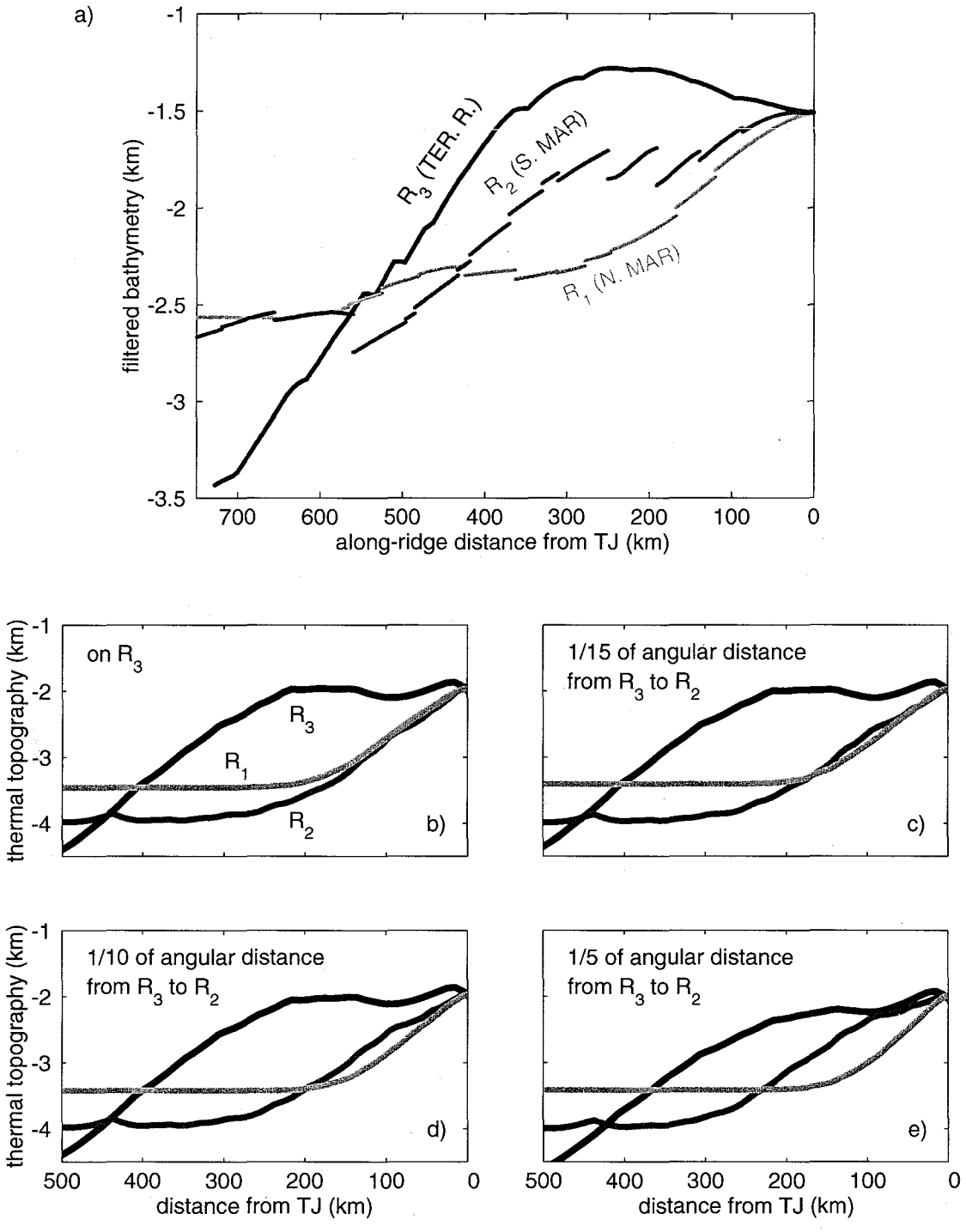
a)
filtered bathymetry (km)
-1
-1.5
-2
-2.5
-3
-3.5
R_3 (TER. R.)
R_2 (S. MAR)
R_1 (N. MAR)
700
600
500
400
300
200
100
0
along-ridge distance from TJ (km)
thermal topography (km)
on R_3
R_3
R_1
R_2
b)
1/15 of angular distance
from R_3 to R_2
c)
1/10 of angular distance
from R_3 to R_2
d)
1/5 of angular distance
from R_3 to R_2
e)
distance from TJ (km)

Figure 15

Chapter 6: Summary

This thesis explored plume-ridge interactions in geological settings with a variety of ridge geometries. We first investigated how a high degree of ridge segmentation along the Southwest Indian Ridge (SWIR) influences the dispersal of the near-ridge Marion and Bouvet plumes. We next quantified how transform offset length and spreading rate affect the along-axis flow of plume-driven mantle. Third, we explored how $^{3}He/^{4}He$ isotopic ratios vary along two supersegments of the western SWIR, one that is highly oblique to the regional spreading direction and another that is oriented perpendicular to the regional spreading direction and that has no transform offsets. Finally, we examined mantle flow and heat transfer beneath a triple junction plate boundary to determine how velocity structure and temperature patterns differ from the case of a single ridge, and to investigate how three-dimensional mantle flow advects a plume thermal anomaly.

Chapter 2 suggests that both Marion and Bouvet significantly affect crustal accretionary processes along the ultra-slow spreading SWIR (half-rate 0.7-0.8 cm/yr). Marion and Bouvet are associated with high-amplitude mantle Bouguer anomaly lows, implying pronounced crustal thickening and/or elevated mantle temperatures. Whereas Marion's influence is apparent over several segments of the central SWIR, the Bouvet gravity signal appears to largely be localized between the Bouvet and Islas Orcadas fracture zones, an along-axis distance or waist width of only several hundred kilometers. Off-axis, the Marion hotspot track inferred from gravity coincides with the Madagascar Ridge, consistent with earlier reconstructions of Marion's paleopositions from magnetic studies. In contrast, there is little evidence from gravity anomalies for the position of the Bouvet plume for ~30 - ~90 Ma.

Motivated by the observation that long-offset transform faults may limit the dispersion of the Marion and Bouvet plumes along the SWIR, Chapter 3 uses a 3D numerical model to quantify the along-axis flux driven by an on-axis plume as a function of transform offset length and spreading rate. Calculations using a pressure- and temperature-dependent mantle viscosity predict that the high upper mantle viscosity associated with long transform offsets in slow-spreading environments may significantly reduce along-axis asthenospheric flux. For example, for a 250-km transform offset and a half-spreading rate of 0.75 cm/yr, along-axis plume-driven asthenospheric flux is predicted to be reduced by 40% relative to the case with no transform offset. Consistent with earlier analytical studies that suggest that ridge offsets may limit axial asthenospheric flow, these model results predict that transforms in ultra-slow spreading environments like the SWIR may shorten the waist width of a near- or on-axis plume.

The influence of the Bouvet plume on the SWIR is further explored in Chapter 4. Chapter 4 reports more than 30 new helium isotope measurements for the SWIR between 9°E and 24°E. This portion of the SWIR may be divided into two supersegments, a western area between 9°E and 16°E that is oriented at a high angle to the regional spreading direction, and an eastern region between 16°E and 24°E that strikes roughly orthogonally to the direction of regional spreading. The effective spreading rate for the western oblique supersegment, or component of plate separation in the regional spreading direction, is very low, ~0.5 cm/yr. Despite the difference in effective spreading rate between the oblique and orthogonal supersegments, $^{3}He/^{4}He$ ratios for the two regions are very similar. The average $^{3}He/^{4}He$ ratio for the oblique supersegment is 6.6 R/R_a, whereas that for the orthogonal supersegment is 6.9 R/R_a. Overall, $^{3}He/^{4}He$ ratios through the entirety of the study area range from 6.3-7.3 R/R_a, lower than the normal MORB average ratio of 8±1 R/R_a. The favored explanation for these low ratios is addition of (U+Th) to the mantle

source through crustal and/or sediment recycling. Although earlier studies suggested that anomalous geochemistry in basalts dredged from the oblique supersegment may be due to influence from the high $^{3}He/^{4}He$ Bouvet plume, there is no evidence from elevated $^{3}He/^{4}He$ ratios for such influence.

Finally, Chapter 5 investigates mantle flow and temperature patterns for oceanic ridge-ridge-ridge triple junctions using numerical modeling. For triple junctions with a configuration similar to the Rodrigues Triple Junction in the central Indian Ocean, 3D solutions for passive, plate-driven flow of an isoviscous mantle predict a significant influence of the two faster-spreading ridge branches on the slowest-spreading branch. For spreading rates representative of the Rodrigues Triple Junction, both temperature and upwelling velocity along the slowest-spreading ridge are predicted to increase within a few hundred kilometers of the triple junction, to approach the conditions along the fastest-spreading ridge. Furthermore, because of the directions of plate divergence away from the triple junction, a strong component of along-axis flow, directed away from the triple junction, is predicted for the slowest-spreading ridge. When a thermal anomaly representing a plume source is added to the base of the model near the triple junction, the influence of the thermal anomaly is predicted to be greatest for the slowest-spreading ridge because of this along-axis flow. Such calculations help to constrain the deep source location of a plume near a triple junction such as the Azores.

The investigative approaches used in this thesis range from analysis and interpretation of bathymetry, gravity, and other geophysical data, to rare gas isotopic measurements, to computational geodynamics modeling. This thesis work points out several new lines for future investigations. For example, a program which couples seismic refraction experiments to measure crustal thickness variations with geochemical analysis of closely spaced rock dredges along the three branches of a triple junction could provide a direct test

of the mantle temperature and crustal accretion predictions of our models. Similarly, detailed axial dredge sampling along plume-affected segments proximal to a long transform offset would help to constrain how along-axis plume flow interacts with ridge discontinuities. Subsequent models could then incorporate these important constraints to further understanding of the complex processes of plume-ridge interactions.